#### INFORMATION TO USERS

This manuscript has been reproduced from the microfilm master. UMI films the text directly from the original or copy submitted. Thus, some thesis and dissertation copies are in typewriter face, while others may be from any type of computer printer.

The quality of this reproduction is dependent upon the quality of the copy submitted. Broken or indistinct print, colored or poor quality illustrations and photographs, print bleedthrough, substandard margins, and improper alignment can adversely affect reproduction.

In the unlikely event that the author did not send UMI a complete manuscript and there are missing pages, these will be noted. Also, if unauthorized copyright material had to be removed, a note will indicate the deletion.

Oversize materials (e.g., maps, drawings, charts) are reproduced by sectioning the original, beginning at the upper left-hand corner and continuing from left to right in equal sections with small overlaps.

ProQuest Information and Learning 300 North Zeeb Road, Ann Arbor, MI 48106-1346 USA 800-521-0600



# Portal imaging with a direct-detection active matrix flat panel imager

Martin Lachaîne

Department of Physics McGill University, Montreal February, 2001

A thesis submitted to the faculty of graduate studies and research in partial fulfillment of the requirements of the degree of Doctor of Philosophy

© Martin Lachaîne 2001



National Library of Canada

Acquisitions and Bibliographic Services

395 Wellington Street Ottawa ON K1A 0N4 Canada Bibliothèque nationale du Canada

Acquisitions et services bibliographiques

395, rue Wellington Ottom ON K1A 0N4 Canada

Your Sin Votes stiffeness

Cur illa Natra référence

The author has granted a nonexclusive licence allowing the National Library of Canada to reproduce, loan, distribute or sell copies of this thesis in microform, paper or electronic formats.

The author retains ownership of the copyright in this thesis. Neither the thesis nor substantial extracts from it may be printed or otherwise reproduced without the author's permission.

L'auteur a accordé une licence non exclusive permettant à la Bibliothèque nationale du Canada de reproduire, prêter, distribuer ou vendre des copies de cette thèse sous la forme de microfiche/film, de reproduction sur papier ou sur format électronique.

L'auteur conserve la propriété du droit d'auteur qui protège cette thèse. Ni la thèse ni des extraits substantiels de celle-ci ne doivent être imprimés ou autrement reproduits sans son autorisation.

0-612-75649-1



#### **Abstract**

The problem of charge creation by x-rays in amorphous selenium (a-Se) is studied. A quantitative theory is developed which includes collective and single electron-hole pair excitations by a passing electron. This theory is incorporated into a Monte Carlo code to calculate track structures in a-Se. The initial positions of the electron-hole pairs along these tracks are used to study the fraction of pairs which recombine versus incident x-ray energy and applied electric field. The experimentally-observed energy dependence of recombination is attributed to a spur size which is dependent on the velocity of the ionizing electrons. The theory and simulations agree with available experimental data in the energy range from 20 keV to 10 MeV.

The use of an a-Se based direct-detection active matrix flat-panel imager (AMFPI) is explored at megavoltage energies for use in the verification of radiotherapy treatments. As with most other megavoltage detectors, a metal front plate is used to reduce patient scatter and to act as a buildup layer. The Modulation Transfer Function (MTF), Noise Power Spectrum (NPS), and Detective Quantum Efficiency (DQE) are measured. The DQE for the direct detection AMFPI is compared with the published DQE of an indirect detection AMFPI for portal imaging. The direct detector has a lower DQE at zero frequency, but there is a cross-over at approximately 0.3 cycles/mm after which it has a higher DQE.

A theoretical expression for the DQE of medical imaging detectors with nonelementary cascade stages is derived. This formalism can be used in conjunction with Monte Carlo techniques to evaluate the DQE of megavoltage imaging detectors. The predictions of the theory agree with the experimental DQE results for the direct-detection AMFPI and also for published results for the DQE of both a metal/phosphor detector and an indirect-detection AMFPI.

The effect of scatter on image quality is modeled in terms of the scatter fraction (SF) and scatter-to-primary ratio (SPR) using Monte Carlo techniques. To validate these simulations, the SF is measured experimentally using a prototype a-Se detector which uses an electrostatic probe to measure the a-Se surface potential. The simulations are used, along with the DQE simulations, to study the effect of metal/a-Se or metal/phosphor thicknesses on image quality in direct and indirect AMFPIs at megavoltage energies. It is found that for a-Se or phosphor thicknesses less than about 300 µm, a front plate of about 1 mm copper is optimal whereas for larger a-Se/phosphor thicknesses a front plate of about 0.4 mm may in some situations lead to better image quality.

### Résumé

Le problème de la création de charges dans le sélenium amorphe (a-Se) est étudié. Une théorie quantitative est developée qui inclut non seulement la création de paires électron-trou par un électron ionisant mais aussi les effets collectifs. Cette théorie est incorporée dans un code Monte Carlo pour calculer les structures de traces dans le a-Se. Les positions initiales des paires électron-trou sont utilisées pour étudier le montant de recombinaison en fonction de l'énergie incidente et de champ électrique appliqué. La dépendence est attribuée à des sphères contenant plusieurs paires avec un diamètre qui dépend sur la vitesse de l'électron ionisant. La théorie et les simulations sont en accord avec les mesures disponibles pour les énergies de rayons-x entre 20 keV et 10 MeV.

L'utilisation d'un détecteur plan matriciel avec détection directe basée sur le a-Se est exploré pour l'imagerie numerique en radiothérapie. Pareillement à autres détecteurs pour la radiothérapie, une plaque de métal est utilisée pour réduire les rayons-x diffusés par le patient et pour convertir les rayons-x primaires en électrons. La fonction de transfers de modulation (modulation transfer function MTF), le spèctre en puissance du bruit (noise power spectrum NPS), et l'éfficacité quantique de détection (detective quantum efficiency DQE) sont mesurés. Le DQE est comparé avec le DQE d'un détecteur plan matriciel avec détection indirecte pour la radiotherapie. Le détecteur indirect a un DQE supérieur a zero-frequence, mais les DQE se croisent à l'entour de 0.3 cycles/mm après lequel le detecteur direct a un DQE supérieur.

Une expression théorique pour le DQE de détecteurs medicaux avec des stages non-élémentaires est dérivée. Ce formalisme peut être utilisé en conjonction avec des techniques Monte Carlo pour évaluer le DQE de détecteurs a hautes-énergies utilisés pour

la radiotherapie. Cette théorie est en accord avec les mesures pour les détecteurs à détection directe et indirecte.

L'effet des rayons-x et électrons diffusés par un patient est étudié en considérant la fraction de diffusion (scatter fraction SF) et la fraction diffusion-primaire (scatter to primary ratio SPR) en utilisant la méthode Monte Carlo. Le SF est mesuré experimentalement avec un détecteur électrostatique basé sur le a-Se. Les mesures sont en accord avec les simulations. Les résultats des simulations, combinés avec les simulations du DQE, sont utilisés pour étudier l'effet de l'épaisseur de la couche de métal sur la qualité de l'image pour les détecteurs à plan matriciel directs et indirects aux énergies utilisées pour la radiothérapie. Les résultats démontrent que pour une couche de a-Se ou de Gd<sub>2</sub>O<sub>2</sub>S:Tb plus mince qu'environ 300 µm, une plaque de métal de 1 mm est optimale, tandis que pour une épaisseur de a-Se ou de Gd<sub>2</sub>O<sub>2</sub>S:Tb plus large une plaque de 0.4 mm est optimale.

### **Original Contribution**

The mechanism of signal formation by x-rays in amorphous selenium (a-Se) has been debated for quite some time in terms of two competing models. This thesis puts forward a new model which is successful in explaining the observed energy and electric field dependencies of the x-ray induced signal in a-Se. This has involved the calculation of cross-sections for the creation of plasmons and their subsequent disintegration into multiple electron-hole pairs, the development of a Monte Carlo code to calculate track structures in a-Se, and the development of a method to extend a two-body formula for recombination (Onsager formula) into a many-body calculation, all of which are new developments in the field.

In this thesis, measurements of the MTF, NPS and DQE are reported for a directdetection AMFPI detector at megavoltage energies. These measurements are important in analyzing this new technology.

Linear systems cascade analysis has been used by a number of researchers to quantify the signal and noise characteristics of medical imaging detectors. This involves separating the imaging process into stages. The types of stages that can be used are limited, which poses a serious problem in using this formalism at megavoltage energies required for radiotherapy imaging. In this thesis a new cascade equation is derived which overcomes this limitation. In addition, Monte Carlo techniques are developed which use the new cascade equation to calculate the DQE of direct and indirect AMFPI detectors at megavoltage energies. This allows an investigation into the comparison and optimization of both techniques.

### Acknowledgements

I would like to thank my supervisor, Dr B. G. Fallone, for his guidance and support. I am grateful for the chance he has given me to pursue my interests, and for giving me the opportunity to continue my work in Edmonton when he moved to the Cross Cancer Institute. His insight, resourcefulness and commitment to this work have been invaluable.

I would also like to thank Dr E. B. Podgorsak, the Director of Medical Physics at McGill, for his many contributions to my education throughout the years. The illuminating lectures he has taught have proven to be of endless use throughout the course of this research.

I am thankful to the American Association of Physicists in Medicine (AAPM) for the fellowship I have received for the first two years of my Ph.D. studies, and to the University of Alberta and the Cross Cancer Institute for the Shell scholarship in Medical Physics in the final two years. I am also grateful for the additional support I have received at the Cross Cancer Institute.

I am indebted to everyone in the Medical Physics departments at both the Montreal General Hospital and the Cross Cancer Institute for making my time at each place pleasant and rewarding. In particular, I thank Dr Eugene Fourkal of the Cross Cancer Institute for the very fruitful collaboration in developing the theory of charge creation in amorphous selenium, Dr Tony Falco for many useful discussions and for the time he took to show me how to use the probe-based imager, and Mr François Deblois for helping me to learn how to program in C.

I am appreciative of the help provided by the people at Anrad Corp., especially Mr Vincent Loustauneau and Mr Kerwin Wong who helped me with the specifics of writing the necessary scripts to run the flat panel detector.

This thesis is dedicated to my family: my parents André and Carole, my brothers Alexis and Pierre-André, my Grand Maman, and of course my wife Carey. Your love, support and encouragement have been a source of inspiration.

This work is partly supported by the Natural Science and Engineering Research Council of Canada (NSERC) University-Industry Grant (CRD 215792-98).

# **List of Figures**

| Figure 1.1: Schematic diagram showing (a) indirect and (b) direct AMFPIs   |
|--|
| Figure 2.1: Schematic diagram of the model of Knights and Davis p.19   |
| Figure 2.2: Cross-sections for major photon interactions for atomic selenium (taken from the EPDL database)  |
| Figure 2.3: Cross-sections for photoelectric interactions with the subshells of atomic selenium, taken from the EPDL database  |
| Figure 2.4: Cross-sections for major electron interactions in atomic selenium (taken from the EEDL database)   |
| Figure 2.5: Differential cross-section of elastic scattering of electrons in atomic selenium for various energies (data taken from EEDL). Cross-sections are plotted versus an angular variable $x=1-\cos\theta$ |
| Figure 2.6: Cross-section for inelastic scattering of electrons in atomic selenium for individual subshells (outer shells are not shown). Data taken from the EEDL database                                      |
| Figure 2.7: Schematic diagram of (a) the columnar recombination model.and (b) pairs created along the track of ionizing radiation p.45   |
| Figure 2.8: Qualitative model of Mah et al to account for the observed energy dependence of $W_{\pm}$  |
| Figure 2.9: Schematic diagram of particles incident on a slab of material  |
|  |

| Figure 2.10: Spectrum of elementary excitations in the bulk electron gas.     |
|---|
| The plasmon dispersion line as well as the electron-hole pair domain are      |
| shown   |
| Figure 2.11: Energy loss function for a-Se, measured by Bell and Liang        |
|   |
| Figure 2.12: The n-particle excitation domains. Regions from $n=1$ to 4       |
| are explicitly shown on the graph whereas the other regions (n>4) are         |
| grouped together for clarity  |
| Figure 2.13: The n-particle excitation states in the $(B,T)$ plane, for $n=1$ |
| (single particle) and $n = 2$ (double particle). The solid line represents    |
| the energy-momentum conservation equation                                     |
| Figure 2.14: The calculated n-particle inelastic cross sections versus        |
| electron energyp.62   |
| Figure 2.15: The calculated inelastic cross sections versus electron          |
| energy for a-Se compared to the cross-sections taken from the EEDL            |
| database for isolated Se atoms  |
| Figure 2.16: The calculated Y-distributions, i.e., cumulative cross-          |
| sections as a function of energy transfer T normalized to the total cross-    |
| section for the creation of n electron-hole pairs in the inelastic cross      |
| section of an electron with a-Sep.65  |
| Figure 2.17: Coordinate system used in Monte Carlo transport code p.67        |
| Figure 2.18: Typical track structure for a 50 keV electron in a-Se p.75       |
| Figure 2.19: Typical track structure for a 1 MeV electron in a-Se p.75        |

| Figure 2.20: Average spur size versus photon energy. The a-Se thickness is 150 µm   |
|---|
| Figure 2.21: Average number of pairs per spur versus photon energy. The a-Se thickness is 150 µm  |
| Figure 2.22: Schematic diagram describing an example of transport, recombination and escape of electron-hole pairs to calculate the escape efficiency   |
| Figure 2.23: Comparison of recombination code (points) for the special case of a single electron-hole pair compared to the Onsager formula (lines)  |
| Figure 2.24: The dependence of $W_\pm$ on applied electric field along with experimental values measured by Blevis et al and Mah et al. The thickness of the a-Se layer is 150 $\mu$ m for the 40 and 140 keV photons, and 50 $\mu$ m for the 1.25 MeV (Co-60) photons                                      |
| Figure 2.25: The energy dependence of $W_{\pm}$ for photons (solid curve) and electrons (dashed curve). Also shown are experimental measurements by Blevis et al <sup>6</sup> and Mah et al <sup>13</sup> . The thickness of the a-Se layer is 150 $\mu$ m, and the applied electric field is 10 V/ $\mu$ m |
| Figure 2.26: The inter-spur separation distance plotted versus electron energy  |
| Figure 2.27: Dependence of $W_{\pm}$ on x-ray energy for various a-Se thicknesses   |
| Figure 2.28: Dependence of $W_{\pm}$ on a-Se thickness for a 6 MV beam (independent of metal thickness)   |

| Figure 3.1: Schematic representation of x-ray imaging geometry, labeling      |
|---|
| object, subject and image contrastp.97  |
| Figure 3.2: Schematic representation of sensitivity curve for film (H&L       |
| curve) and associated contrastp.99  |
| Figure 3.3: Detector viewed as a "black box"p.102                             |
| Figure 3.4: Schematic representation of a point spread function (PSF)         |
| p.104   |
| Figure 3.5: Schematic representation of (a) undersampling of LSF in           |
| cartesian space, (b) corresponding repetition of OTF in frequency space       |
| and (c) aliasing due to the overlap of the OTFp.117                           |
| Figure 3.6: Digital LSF is measured with input line incident on (a) the       |
| centre of a row of pixels and (b) between two rows of pixels. Also shown      |
| are the corresponding digital MTFs (the dashed lines correspond to the        |
| presampling LSFs and MTFs)p.119   |
| Figure 3.7: Angulated slit technique to determine the presampling LSF of      |
| an undersampled digital detector. The input line is slightly tilted relative  |
| to the pixel grid (tilt is exaggerated here for clarity), and the digital LSF |
| values for each row are recorded. These values are pieced together to         |
| build a finely sampled version of the presampling LSFp.120                    |
| Figure 3.8:(a) Picture of direct-detection AMFPI with cover removed (b)       |
| Schematic diagram showing interaction of x-rays with the direct-detection     |
| AMFPIp.123.   |
| Figure 3.9:(a) Schematic diagram and (b) micrograph of a pixel in the         |
| direct-detection AMFPIp.125   |
| Figure 3.10: (a) Schematic diagram of the active matrixp.126                  |

| Figure 3.11: Experimental setup for LSF/MTF measurementsp.129  |
|--|
| Figure 3.12: Sensitivity curve for the IMAM detector for 6 and 15 MV                                   |
| photon beams. Signal (ADC counts) is plotted versus dose measured in                                   |
| water at depth of dose maximum, with the same SSD as the detectorp.133                                 |
| Figure 3.13: Presampling Modulation Transfer Function for the metal/a-                                 |
| Se AMFPI for 6 MV and 15 MV beamsp.134   |
| Figure 3.14: Measured Noise Power Spectrum for the metal/a-Se AMFPI                                    |
| for 6 MV and 15 MV beamsp.135  |
| Figure 3.15: Detective Quantum Efficiency for the metal/a-Se AMFPI for                                 |
| (a) 6 MV and (b) 15 MV beamsp.136  |
| Figure 3.16: Detective Quantum Efficiency for the metal/a-Se based direct                              |
| AMFPI compared to a metal/phosphor based indirect AMFPIp.137   |
| Figure 4.1: Schematic diagram showing the interaction of a megavoltage                                 |
| x-ray photon with a metal/phosphor detector. The x-ray creates a cascade                               |
| of ionizing photons, electrons, and positrons which subsequently create                                |
| optical photons along their paths. The locations of the ith, $(i+1)th$ ,                               |
| (i+2)th, etc. optical photons are correlated to one another. The optical                               |
| photons created scatter within the phosphor until they either they escape                              |
| or they are absorbedp.149  |
| Figure 4.2: Schematic diagram showing the pixelization of the input and                                |
| output plane used in the statistical analysisp.150   |
| Figure 4.3: Schematic diagram showing modeling of detector using                                       |
| EGSnrc   |
| Figure 4.4: DQE for a 6MV x-ray beam interacting with a 1 mm Cu front                                  |
| plate above a 134 mg/cm <sup>2</sup> Gd <sub>2</sub> O <sub>2</sub> S:Tb phosphor calculated using the |
|  |

| cascade analysis developed in this work (without taking the Lubberts                                   |
|--|
| effect into account) compared to the DQE calculated using the cascade                                  |
| analysis of Bissonnette et al and of Drake et alp.175  |
| Figure 4.5: DQE for a 6MV x-ray beam interacting with a 1 mm Cu front                                  |
| plate above a 400 mg/cm <sup>2</sup> Gd <sub>2</sub> O <sub>2</sub> S:Tb phosphor calculated using the |
| cascade analysis developed in this work (with the Lubberts effect taken                                |
| into account) compared to the experimental measurements of Munro et al.                                |
| Also shown are the DQE calculated using the cascade analysis of  |
| Bissonnette et al and of Drake et alp.176  |
| Figure 4.6: Theoretical calculations of MTF for the direct-detection MTF                               |
| compared to measured values, for 6 MV and 15 MV x-ray beamsp.177                                       |
| Figure 4.7: Theoretical calculations of DQE for the direct-detection MTF                               |
| compared to measured values, for (a) 6 MV and (b) 15 MV x-raysp.178                                    |
| Figure 4.8: Theoretical calculations of DQE for the indirect-detection                                 |
| DQE compared to measured values described by Munro and Bouius. p.179                                   |
| Figure 4.9: Theoretical calculations of DQE for various mass thicknesses                               |
| for (a) direct-detection and (b) indirect-detection AMFPIs. Calculations                               |
| are for 6 MV with a 1 mm Cu front platep.180   |
| Figure 5.1: Schematic diagram of the EGSnrc user code geometry to                                      |
| simulate the SF and SPRp.194   |
| Figure 5.2: a) SF and b) SPR for a 20×20 cm <sup>2</sup> field versus metal thickness                  |
| for various metals, generated by EGSnrc, with a 20 cm phantom and SRD                                  |
| of 172 cm. Empty points (with error bars) correspond to measured values.                               |
| n 196  |

| Figure 5.3: Measurements of surface potential versus relative absorbed    |
|---|
| dose to a-Se, with four plates. Only one curve is shown for 1.0 mm Cu and |
| 1.5 mm Cu plates, since they were identical within experimental           |
| uncertainties. Measured on a Clinac 2300 C/D (6 MV, SRD=172 cm).p.197     |
| Figure 5.4: Measurements of relative dose to a-Se versus field size with  |
| phantom, without phantom and the corrected curve which represents the     |
| change due to patient scatter only. Measured on a Clinac 2300 C/D (6      |
| MV), SRD = 172 cm, 20 cm polystyrene phantom,p.198                        |
| Figure 5.5: DQE of metal/a-Se detectors at 6 MV for various front plate   |
| (copper) and a-Se thicknessesp.202  |
| Figure 5.6: DQE of metal/phosphor detectors at 6 MV for various front     |
| plate (copper) and Gd <sub>2</sub> O <sub>2</sub> S:Tb thicknesses        |
| Figure 5.7: Contrast degradation factor of (a) metal/a-Se and (b)         |
| metal/phosphor detectors at 6 MV plotted versus front plate (copper)      |
| thickness, for various sensitive layer thicknessesp.204                   |
| Figure 5.8: DSNR degradation factor of (a) metal/a-Se and (b)             |
| metal/phosphor detectors at 6 MV plotted versus front plate (copper)      |
| thickness, for various sensitive layer thicknessesp.205                   |
| Figure 5.9: DQE of metal/a-Se detectors at 15 MV for various front plate  |
| (copper) and a-Se thicknessesp.206  |
| Figure 5.10: DQE of metal/phosphor detectors at 15 MV for various front   |
| plate (copper) and Gd <sub>2</sub> O <sub>2</sub> S:Tb thicknessesp.207   |
| Figure 5.11: Contrast degradation factor of (a) metal/a-Se and (b)        |
| metal/phosphor detectors at 15 MV plotted versus front plate (copper)     |
| thickness, for various sensitive layer thicknessesp.208                   |

| Figure  | <i>5.12:</i> | DSNR     | degradation    | factor    | of (a)   | metal/a-Se  | and (b)  |
|---------|--------------|----------|----------------|-----------|----------|-------------|----------|
| metal/p | hospho       | r deteci | ors at 15 M    | V plotte  | d versus | front plate | (copper) |
| thickne | ss, for v    | arious   | sensitive laye | r thickne | esses    |             | p.209    |

# **Table of Contents**

| Abst | tract  | i        |
|------|--|----------|
| Résu | ımé  | iii      |
| Orig | ginal Contribution   | v        |
| Ackn | nowledgments   | vi       |
| List | of Figures   | viii     |
| Cha  | pter 1: Introduction   | 1        |
| 1.1  | X-ray imaging  |          |
| 1.2  | Portal Imaging   |          |
| 1.3  | Scope and organization of thesis                             |          |
| 1.4  | References   |          |
| Cha  | pter 2: Signal formation in <i>a</i> -Se                     | 14       |
| 2.1  | Introduction   |          |
| 2.2  | Background   | 17       |
|      | 2.2.1 Interaction of visible photons with a-Se               | 17       |
|      | 2.2.2 Interaction of ionizing radiation with matter          | 21       |
|      | 2.2.3 Generalized oscillator strength distribution in solids | 37       |
|      | 2.2.4 Interaction of x-rays with a-Se                        | 42       |
|      | 2.2.5 The Monte Carlo method                                 | 47       |
| 2.3  | Model for the creation of electron-hole pairs in a-Se        | 51       |
| 2.4  | Calculation of inelastic cross-sections                      | 58       |
| 2.5  | Determination of track structure                             |          |
| 2.6  | Determination of escape efficiency $\eta$                    |          |
| 2.7  | Conclusions  | 88       |
| 2.8  | References   | 90       |
| Cha  | pter 3: DQE Measurements of a direct AMFPI at megavoitage    | energies |
| ,    |  | 95       |
|      | Introduction   |          |
| 3.2  | Background   |          |
|      | 3.2.1 Contrast and Sensitivity                               |          |
|      | 3.2.2 Resolution and noise                                   |          |
|      | 3.2.3 Linear systems analysis                                |          |
|      | 3.2.4 Transfer characteristics of digital detectors          |          |
| 3.3  | Materials and Methods  |          |
|      | 3.3.1 Description of detector                                |          |
|      | 3.3.2 Sensitivity  | 127      |

| 3.3.3 Modulation Transfer Function   | 129  |
|--|--|
| 3.3.4 Noise Power Spectrum   | 130  |
| 3.3.5 Detective Quantum Efficiency   | 131  |
| 3.4 Results and Discussion   |  |
| 3.5 Conclusions  |  |
| 3.6 References   |  |
| Chapter 4: Theoretical calculations of DQE at megavoltage energies  4.1 Introduction | 141<br>142<br>147<br>147<br>150<br>158<br>160<br>164<br>167<br>167 |
| 4.5 Results and Discussion   |  |
| 4.6 Conclusion   |  |
| 4.7 References   |  |
| Chapter 5: Effect of front plate on image quality  5.1 Introduction                  | 185  |
| 5.2 Background: the effect of scattered radiation on image quality                   | 187  |
| 5.3 Materials and Methods  |  |
| 5.3.1 Description of Electrostatic probe a-Se detector                               |  |
| 5.3.2 Measurement of Scatter Fraction  |  |
| 5.3.3 Monte Carlo simulations of SF and SPR  |  |
| 5.4 Results and Discussion   |  |
| 5.4.1 SF and SPR: comparison of simulations with experiment                          |  |
| 5.4.2 Effect of front plate on DQE, contrast and DSNR                                |  |
| 5.5 Conclusions  |  |
| 5.6 References   | 210  |
| Chapter 6: Conclusions   | 211<br>213   |

| 1.1 X-ray imaging 1                  |
|--------------------------------------|
| 1.2 Portal Imaging                   |
| 1.3 Scope and organization of thesis |
| 1.4 References 9                     |

### 1.1 X-ray imaging

In medical x-ray imaging, x-ray photons are used to obtain a two-dimensional image of patient anatomy. The x-ray energies used for diagnostic purposes typically range from about 20 kVp\* for mammography to about 120 kVp for chest radiography. Some of the factors affecting the choice of energy for a particular application include consideration of the contrast required to detect the structures under study, minimization of patient dose, and penetration of x-rays through the patient.

In the diagnostic energy range, the dominant photon interaction is the photoelectric effect which depends strongly on atomic number.<sup>2</sup> This results in a large contrast between structures of different composition, and this contrast increases with

<sup>\* 20</sup> kVp refers to a spectrum of energies from 0 to 20 keV. At megavoltage energies, a spectrum of energies ranging from 0 to 6 MeV (for example) is commonly denoted by 6 MV.

decreasing photon energy. For example, low energies are used in mammography to obtain the high contrast required to differentiate between soft tissues and possible microcalcifications. In chest radiography on the other hand, where high contrast is not as critical, a higher energy is used to achieve more penetration and to reduce patient dose.

The most common detector used for x-ray imaging is radiographic film. A phosphor screen is often placed above the film to convert x-rays into optical photons which then expose the film. This approach increases sensitivity, but a trade-off is that the optical photons scatter within the phosphor leading to a degradation in image resolution.

X-ray detectors other than screen/film systems have been explored in the past. Xeroradiography was introduced into the medical imaging field in the 1950s by Schaffert.<sup>3</sup> This technique was based on the photoconductor amorphous selenium (a-Se), which is also used for optical imaging.<sup>4</sup> Selenium in the amorphous state is formed by evaporating crystalline selenium (atomic number Z = 34) and depositing it on a substrate in a controlled fashion. In this manner large, uniform a-Se layers can be formed. Energy deposited in a-Se by either optical photons or x-rays leads to the creation of electron-hole pairs. In the presence of an electric field, these pairs can be separated and collected to form a two-dimensional image.<sup>5</sup>

In xeroradiography, a uniform positive surface charge was placed on the a-Se surface by corona charging, in effect establishing an electric field within the a-Se. The electron-hole pairs generated by the x-rays would then result in the partial neutralization of the surface charge distribution. This distribution was recorded by applying charged toner particles to the a-Se surface, which would distribute themselves according to the

electric field lines above the surface. A hard copy of the image could then be obtained by pressing special coated paper over the attached toner particles.<sup>3</sup>

Xeroradiography gained interest in the field of mammography and in the imaging of extremities, but its use has declined partly due to a lower sensitivity than that of film-based detectors. It also seems likely that the image quality was severely degraded by the toner particles. Lately, however, with novel methods such as photoinduced discharge with a laser<sup>6</sup> to read out the surface charge distribution digitally, research into a-Se has been revitalized.

X-ray detectors which are inherently digital have many advantages, such as immediate viewing, the ability to digitally enhance image quality, and image archiving. In recent years, thin film transistor (TFT) technology has lead to the development of a new category of digital x-ray detectors. Such detectors, often called *active-matrix flat panel imagers* (AMFPIs), use either the *indirect*<sup>7-10</sup> or the *direct*<sup>11-13</sup> approach to detect x-rays. Indirect detection AMFPIs, shown schematically in Fig. 1.1(a), convert x-rays to visible light using a phosphor screen. The visible light is then converted to charge with a photosensitive pixel array, and the charge is subsequently read out to form a digital image. For direct detection AMFPIs, shown schematically in Fig. 1.1(b), the x-rays are directly converted to charge within a photoconductor, such as a-Se. The charge is collected though the use of an applied electric field by an array of pixel electrodes, where it is stored by capacitors and subsequently read out to form the digital image.

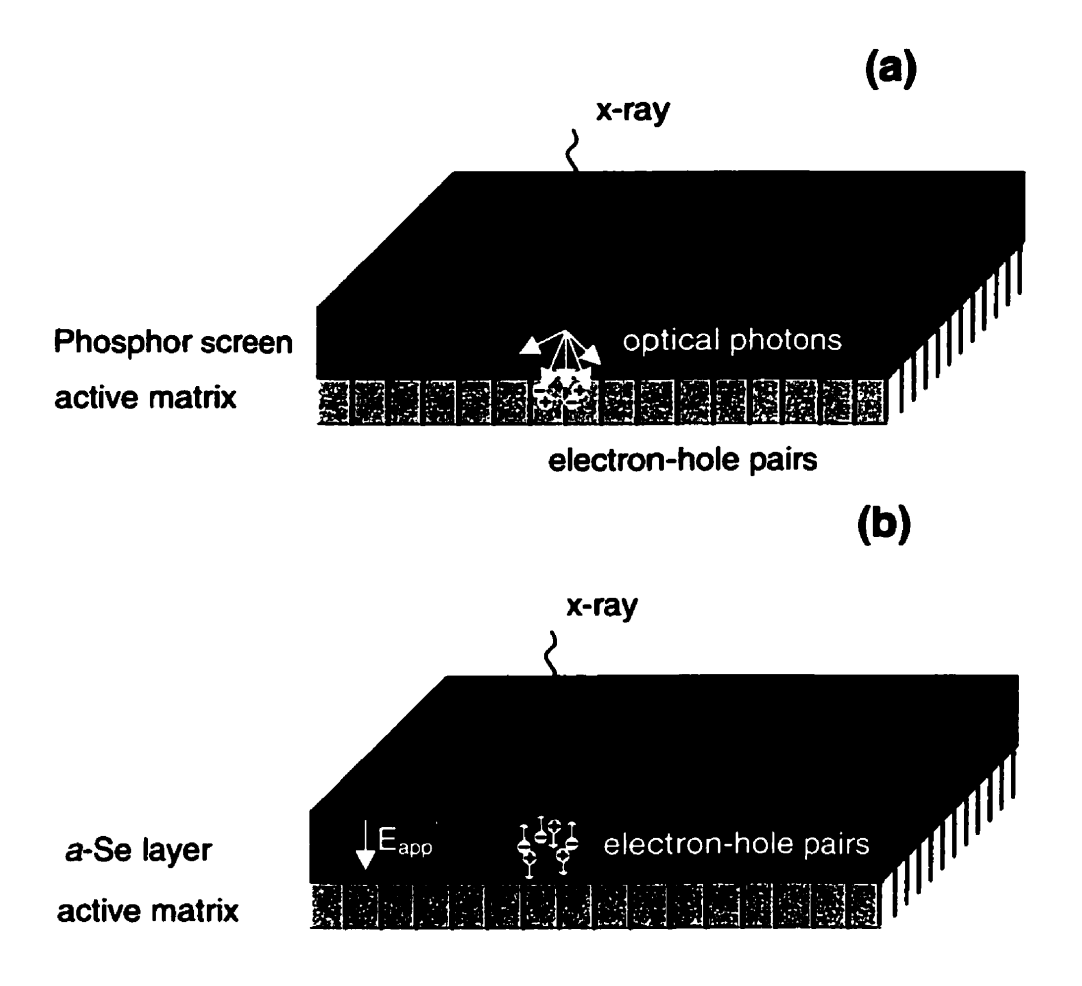


Figure 1.1: Schematic diagram showing (a) indirect and (b) direct AMFPIs.

Both indirect and direct AMFPIs have been developed and studied for various modalities, such as mammography, fluoroscopy and chest radiography. Results so far have been very promising, and detectors are now beginning to be available commercially. Of particular help in the optimization of these detectors has been the development of theoretical models to explore the effects of design characteristics on image quality. These models are based on linear systems cascade analysis, <sup>14</sup> which allows one to follow the

propagation of signal and noise within the detector through various stages of signal formation. The effect of characteristics, such as detector thickness, pixel size, and electronic noise on the image quality, have been studied using this formalism, 9.13 and along with technological advances are leading to improved detector performance.

## 1.2 Portal imaging

In the treatment of cancer with radiation, the goal is to maximize the absorbed dose to the treatment volume while minimizing the dose to healthy tissues.<sup>2</sup> During treatment, many factors may influence the proper delivery of a calculated dose distribution. Some of these factors include misalignment of the treatment beam with respect to the patient, external or internal patient motion, or inaccurate positioning of beam-modifying devices.<sup>15</sup> In order to quantify these geometric inaccuracies during treatment, the megavoltage treatment beam which is transmitted through the patient is imaged on the beam exit side of the patient by a two-dimensional detector. In this manner it is possible to verify the position of the radiation field relative to the bony anatomy.

The extraction of an image from a megavoltage (1~20 MeV) photon beam has inherent problems. As opposed to the diagnostic energy range, where the photoelectric effect is dominant, in megavoltage imaging the Compton effect is more probable. Compton interactions vary little with atomic number, resulting in very poor contrast. This contrast is degraded even further by a large amount of scattered photons and electrons originating from the patient which reach the receptor. Furthermore, the sensitivity of

detectors at megavoltage energies is very low, since typically 98-99% of x-rays pass through the detector without interacting.<sup>17</sup>

To increase the sensitivity and to reduce scatter, a metal plate is usually placed directly above the portal imager. 16 X-ray photons interact with the metal and transfer some of their energy to electrons, which subsequently deposit their energy in the sensitive layer of the detector to generate a signal. For this reason the metal is often referred to as a *front plate*, *conversion plate*, or *build-up plate*. Since the energy of scattered photons is on average lower than the energy of the primary beam, scattered photons are preferentially attenuated by the front plate resulting in less scatter from the patient reaching the sensitive layer.

Traditionally, film has been used as the portal imaging detector. Over the past decade, several electronic portal imaging devices (EPIDs) have been developed for the purpose of replacing film. Some of these detectors have been developed commercially, while others are still in the research stage. The advantages of such inherently digital detectors include immediate viewing, the ability to use contrast-enhancing algorithms to improve image quality, and the ability to verify dynamic treatments as they are delivered, with the potential of halting treatment if the setup is incorrect. Despite these advantages, however, EPIDs have not yet widely replaced portal films. This has been attributed to poor image quality, limited field of view, and bulkiness. In

In 1973, Wolfe *et al*<sup>20</sup> reported an a-Se based detector for portal imaging which used xeroradiographic toner to extract the latent image. In this system, the metal plate on which a-Se is deposited faces away from the treatment beam, and as a result the images

acquired were unsatisfactory. Our laboratory has investigated the use of a-Se for megavoltage portal imaging, with the metal substrate facing the x-ray beam to act as a conversion plate.<sup>21,22</sup> A rudimentary method of measuring the surface voltage with a coupled electrostatic probe was used to study the imaging prospects of the system. The prototype detector was shown to produce portal images of higher quality than other available detectors, suggesting the use of an a-Se based direct-detection AMFPI for megavoltage imaging. Although indirect-detection AMFPIs have been studied for megavoltage imaging,<sup>8,23</sup> there has been no study of a direct detection AMFPI at megavoltage energies.

## 1.3 Scope and organization of thesis

The main goal of this thesis is to study the use of an a-Se based direct-detection AMFPI for megavoltage imaging. Although a-Se has been studied in medical imaging since the 1970s, no theory is available for describing the signal produced by x-rays in this material. The first step of this thesis is thus to develop a quantitative method of predicting the creation of electron-hole pairs by x-rays in a-Se and this work<sup>24-30</sup> is described in Chapter 2. A theoretical formalism is developed for the inelastic interactions of electrons in solids in terms of the dielectric properties of the medium. This formalism is used to calculate the cross-sections for the excitation of multiple electron-hole pairs by fast electrons in a-Se. These cross-sections are then used to develop a simulation technique which describes the observed signal produced by x-rays in a-Se.

In Chapter 3, experimental measurements<sup>31</sup> of the signal and noise properties of an a-Se based direct AMFPI at megavoltage energies are presented. This includes measurements of the Modulation Transfer Function (MTF), Noise Power Spectrum (NPS), and Detective Quantum Efficiency (DQE).

In Chapter 4, a theoretical formalism based on linear systems cascade analysis is developed<sup>30-35</sup> to describe the signal and noise transfer characteristics of medical imaging detectors. This theory is then used in conjunction with Monte Carlo techniques to explain published results for metal/phosphor detectors at megavoltage energies and also the experimental results from Chapter 3 for the metal/a-Se detector. The formalism is also used to explore some issues related to the design of direct and indirect AMFPI detectors for portal imaging.

In Chapter 5 the effect of scatter on image quality is considered for direct and indirect AMFPIs using Monte Carlo methods. 30,33,36-38 Specifically, the scatter fraction (SF) and scatter-to-primary ratio (SPR) are modeled and the SF is measured experimentally with a prototype electrostatic probe-based detector. The simulations are then used to study the optimal front plate thickness for AMFPI detectors.

The conclusions of the thesis are summarized in Chapter 6. In addition, Chapters 2-5 have their own individual Introduction, Background and Conclusion sections.

#### 1.4 References

[1] P. Sprawls, "X-ray imaging concepts: basic considerations" in *Proceedings of the* 1991 AAPM Summer School: Specification, Acceptance Testing and Quality Control of Diagnostic X-ray Imaging Equipment edited by J.A. Siebert, G.T. Barnes, and R.G. Gould (AAPM, New York, 1991).

- [2] H.E. Johns and J.R. Cunningham, *The Physics of Radiology* (Thomas, Springfield, 1983).
- [3] R. M. Schaffert, U.S. Patent 2666144 (1950).
- [4] C.F. Carlson, U.S. Patent 221776 (1938).
- [5] J.W. Boag, "Xeroradiography (review)," Phys. Med. Biol. 18 3-37 (1973).
- [6] J.A. Rowlands and D.M. Hunter, "X-ray imaging using amorphous selenium: photoinduced discharge (PID) readout for digital general radiography," Med. Phys. 22 1983-2005 (1995).
- [7] L.E. Antonuk, Y. El-Mohri, J.H. Siewerdsen and J. Yorkston, "Empirical investigation of the signal performance of a high-resolution, indirect detection, active matrix flat-panel imager (AMFPI) for fluoroscopic and radiographic operation," Med. Phys. 24 51-70 (1997).
- [8] L.E. Antonuk, Y. El-Mohri, W. Huang, K.-W. Jee, J. Siewerdsen, M. Maolinbay, V. Scarpine, H. Sandler and J. Yorkston, "Initial Performance Evaluation of an indirect-detection, active matrix flat-panel imager (AMFPI) prototype for megavoltage imaging," Int. J. Rad. Onc. Biol. Phys. 42 437-452 (1998).

[9] J.H. Siewerdsen, L.E. Antonuk, Y. El-Mohri, J. Yorkston, W. Huang and J.M. Boudry, "Empirical and theoretical investigation of the noise performance of indirect detection, active matrix flat-panel imagers (AMFPIs) for diagnostic radiology," Med. Phys. 24 71-89 (1997).

- [10] J.H. Siewerdsen, L.E. Antonuk, Y. El-Mohri, J. Yorkston and W. Huang, "Signal, noise power spectrum, and detective quantum efficiency of indirect-detection flat-panel imagers for diagnostic radiology," Med. Phys. **25** 614-628 (1998).
- [11] W. Zhao, I. Blevis, S. Germann and J.A. Rowlands, "Digital radiology using active matrix readout of amorphous selenium: Construction and evaluation of a prototype real-time detector," Med. Phys. **24** 1834-1843 (1997).
- [12] W. Zhao and J.A. Rowlands, "X-ray imaging using amorphous selenium: Feasibility of a flat panel self-scanned detector for digital radiology," Med. Phys. 22 1595-1604 (1995).
- [13] W. Zhao and J.A. Rowlands, "Digital radiology using active matrix readout of amorphous selenium: Theoretical analysis of detective quantum efficiency," Med. Phys. 24 1819-1833 (1997).
- [14] I.A. Cunningham, M.S. Westmore and A. Fenster, "A spatial-frequency dependent quantum accounting diagram and detective quantum efficiency model of signal and noise propagation in cascaded imaging systems," Med. Phys. 21 417-427 (1994).
- [15] G.J. Kutcher, G.S. Mageras and S.A. Leibel, "Control, correction and modeling of setup errors and organ motion," Semin. Radiat. Oncol 5 143-145 (1995).
- [16] R.T. Droege and B.E. Bjarngard, "Influence of metal screens on contrast in megavoltage x-ray imaging," Med. Phys. 6 487-493 (1979).

[17] D.A. Jaffray, J.J. Battista, A. Fenster and P. Munro, "Monte Carlo studies of x-ray energy absorption and quantum noise in megavoltage transmission radiography," Med. Phys. 22 1077-1088 (1995).

- [18] A.L. Boyer, L. Antonuk, A. Fenster, M. Van Herk, H. Meertens, P. Munro, L.E. Reinstein and J. Wong, "A review of electronic portal imaging devices (EPIDs)," Med. Phys. 19 1-16 (1992).
- [19] P. Munro, "Portal imaging technology: Past, present and future," Semin. Radiat. Oncol. 5 115-133 (1995).
- [20] L. Wolfe, L. Kalisher and B. Considine, "Cobalt-60 treatment field verification by xeroradiography," A. J. R. 18 1973 (1973).
- [21] B.G. Fallone and T. Falco, "Megavoltage imaging method using a combination of a photoreceptor with a high energy photon converter and intensifier," U.S. Patent (1997).
- [22] T. Falco, H. Wang and B.G. Fallone, "Preliminary study of a metal/a-Se-based portal detector," Med. Phys. **25** 814-823 (1998).
- [23] P. Munro and D.C. Bouius, "X-ray quantum limited portal imaging using amorphous silicon flat-panel arrays," Med. Phys. **25** 689-702 (1998).
- [24] M. Lachaine and B.G. Fallone, "Calculation of inelastic cross-sections for the interaction of electrons with amorphous selenium," J. Phys. D 33 551-555 (2000).
- [25] M. Lachaine and B.G. Fallone, "Monte Carlo simulations of x-ray induced recombination in amorphous selenium," J. Phys. D 33 1417-1423 (2000).
- [26] E. Fourkal, M. Lachaine and B.G. Fallone, "Signal formation in amorphous-Sebased x-ray detectors," Phys. Rev. B 63, 195204 (2001).

[27] M. Lachaine and B.G. Fallone, "Monte Carlo simulations of recombination in amorphous selenium," Proceedings of the Canadian Organization of Physicists in Medicine 92-94 (1999).

- [28] B.G. Fallone and M. Lachaine, "X-ray interactions in a-Se based diagnostic and portal imagers," Proceedings of the Chicago 2000 World Congress on Medical Physics and Biomedical Engineering 3294-76031.pdf (2000).
- [29] M. Lachaine and B.G. Fallone, "Quantitative analysis of signal formation in a-Se based diagnostic imagers," Proceedings of the Chicago 2000 World Congress on Medical Physics and Biomedical Engineering 3769-22590.pdf (2000).
- [30] M. Lachaine, E. Fourkal and B.G. Fallone, "Investigation into the physical properties of direct and indirect active matrix flat panel imagers for radiotherapy," Med. Phys. (in press).
- [31] M. Lachaine, E. Fourkal and B.G. Fallone, "Detective quantum efficiency of a direct-detection active matrix flat panel imager," Med. Phys. (in press) 28 (2001).
- [32] M. Lachaine and B.G. Fallone, "Cascade analysis for medical imaging detectors with stages involving both amplification and dislocation processes," Med. Phys. 28 501-507 (2001).
- [33] M. Lachaine and B.G. Fallone, "Monte Carlo detective quantum efficiency and scatter studies of a metal/a-Se portal detector," Med. Phys. 25 1186-1194 (1998).
- [34] M. Lachaine and B.G. Fallone, "Design characteristics of direct and indirect active matrix flat panel portal imagers," Radiology and Oncology 35, 67-75 (2001).
- [35] M. Lachaine and B.G. Fallone, "Characteristics of direct and indirect active matrix flat-panel portal imagers," Proceedings of the Chicago 2000 World Congress on Medical Physics and Biomedical Engineering, Chicago IL 3295-53559.pdf (2000).

[36] M. Lachaine and B.G. Fallone, "Front plate optimization of an a-Se based portal imager," Proceedings of the conference of the Canadian Organization of Medical Physicists (COMP), Charlottetown, PEI 165-167 (1997).

[37] M. Lachaine and B.G. Fallone, "Monte Carlo optimization of a metal-plate/a-Se portal imager," Med. Phys. (abstract) 24 1003 (1997).

[38] M. Lachaine and B.G. Fallone, "Front-plate optimization of an a-Se based portal imager," Med. Phys. (abstract) 24 1207 (1997).

# Chapter 2: Signal formation in a-Se

| 2.1 Introduction   | 14 |
|--|----|
| 2.2 Background   | 17 |
| 2.2.1 Interaction of visible photons with a-Se               |    |
| 2.2.2 Interaction of ionizing radiation with matter          |    |
| 2.2.3 Generalized oscillator strength distribution in solids | 37 |
| 2.2.4 Interaction of x-rays with a-Se                        | 42 |
| 2.2.5 The Monte Carlo method                                 | 47 |
| 2.3 Model for the creation of electron-hole pairs in a-Se    | 51 |
| 2.4 Calculation of inelastic cross-sections                  | 58 |
| 2.5 Determination of track structure                         | 66 |
| 2.6 Determination of escape efficiency $\eta$                | 74 |
| 2.7 Conclusions  |    |
| 2.8 References   |    |

### 2.1 Introduction

Although the signal produced by the interaction of visible light in a-Se is reasonably well understood, the mechanism of signal formation due to the interaction of x-rays with a-Se has never been quantitatively explained. The quantity which is usually measured to describe the signal produced by x-rays is  $W_{\pm}$ , defined as the energy required to create a detectable electron-hole pair.  $W_{\pm}$  has been measured by many investigators, 1-7 but until recently results have been unreliable due to a limited range of energies, the use of indirect measurement techniques, and different sample preparations.

It has been known for some time that  $W_{\pm}$  is mainly governed by recombination,<sup>8</sup> and various recombination mechanisms have been invoked to explain the limited data sets that were available at the time. Hirsch and Jahankhani<sup>9</sup> suggested that recombination occurred within a dense, uniform column of electron-hole pairs and that the columnar recombination model, first introduced by Jaffé for ionization chambers,<sup>10</sup> was applicable to recombination in a-Se. Later, Que et al<sup>11</sup> argued that the geminate theory of recombination, which is the accepted mechanism for the interaction of visible photons with a-Se,<sup>12</sup> seemed to best explain the observed trends. They stated, however, that more data was needed to make any definitive conclusions.

Recently, Blevis et al<sup>6</sup> have directly measured  $W_{\pm}$  using a pulse height spectroscopy technique over a relatively wide range of monoenergetic energies, from 40 keV to 140 keV. Their results indicate a clear energy dependence, and cannot be explained in terms of either the columnar or geminate models of recombination. Mah et al<sup>13</sup> have used a xerographic discharge method to measure  $W_{\pm}$  up to megavoltage energies, and have observed a decrease of  $W_{\pm}$  up to the MeV photon range, after which their measured values reached a plateau. They offered a qualitative description in terms of a simple microdosimetric mechanism and they suggested that the high energy electrons generated by the incident x-ray photons deposit their energy in discrete spurs, a concept first introduced in radiation chemistry. The spurs consist of charge clouds created by inelastic collisions with outer atomic shells, which typically occur at the resonant energies of these shells which has been estimated to lie between 20 eV and 80 eV. In this simple model the spur size is assumed to be independent of the energy of the ionizing

electron. At low photon energies, the mean free path between spurs is assumed to be smaller than the spur size, so that the pairs are formed in a column surrounding the ionizing electron track, resulting in a high recombination probability. As the photon energy increases, the spurs are formed farther apart resulting in less recombination. At megavoltage energies, the spurs are assumed to be isolated from each other so that the escape probability is no longer dependent on the incident energy.

Although the model of Mah et  $al^{13}$  sheds some insight into the mechanisms at work, it is not sufficient to properly explain the signal formation in a-Se in a quantitative manner. In this work we develop a mechanism for the recombination in a-Se in order to describe the energy and applied field dependencies of  $W_{\pm}$ . We first develop cross-sections for the creation of multiple electron-hole pairs in a-Se and then develop a coupled photon/electron transport code which uses these cross-sections to determine the positions of electron-hole pairs along the tracks of ionizing radiation. We follow the positions of the electron-hole pairs through time in order to calculate the fraction that escapes recombination and contributes to the detectable signal. From these simulations we calculate  $W_{\pm}$  as a function of both the applied electric field and incident x-ray energy, and compare our calculations to the previously unexplained measurements of Blevis et  $al^6$  and Mah et  $al.^{13}$  We use our simulations to explore the effect of energy, electric field and sample thickness on the signal formation in a-Se.

# 2.2 Background

## 2.2.1 Interaction of visible photons with a-Se

The interaction of visible light with a-Se leads to the creation of electron-hole pairs, typically one pair per photon. The number of pairs collected increases with increasing applied electric field and also with increasing incident photon energy. Historically, various models have been invoked to explain the experimental measurements. Poole-Frenkel recombination theory was initially used in an attempt to explain the observed results. Knights and Davis  $^{14}$  modeled the situation by postulating that a photon with energy hv will lead to the creation of an electron-hole pair with kinetic energy  $hv - E_g$ , where  $E_g$  is the band-gap of a-Se (2.3 eV). The pair will lose this excess kinetic energy by interaction with phonons, and the process is called the *thermalization* process. They assumed the motion to be diffusive and that the separation  $r_o$  at the end of the thermalization time t would be given by

$$r_o = \sqrt{Dt} \tag{2.1}$$

where D is the sum of the diffusion coefficient for electrons and holes.

Due to the amorphous state of a-Se, Knights and Davis assumed that there is no wave vector conservation and that the rate of energy loss during thermalization will reach its maximum of a typical phonon frequency  $v_p$  times a typical phonon energy  $hv_p$ . The time required to dissipate the pair's energy was taken to be

$$t = \frac{(hv - E_g) + \frac{e^2}{4\pi\varepsilon r_o} + eE_{app}r_o\cos\theta}{hv_p^2},$$
 (2.2)

where  $E_{app}$  is the applied electric field and  $\theta$  is the orientation of the pair relative to the field. By equating Eqs. (2.1) and (2.2), the electron-hole separation at the end of the thermalization process is given by the solution of the equation

$$\frac{r_o^2}{D} = \frac{hv - E_g + \frac{e^2}{4\pi\varepsilon r_o} + eE_{app}r_o\cos\theta}{hv_p^2},$$
 (2.3)

which is a cubic equation in  $r_o$ , and leads to a binding energy  $E_o$  for the pair of

$$E_o = \frac{e^2}{4\pi\varepsilon r_o} + eE_{app}r_o . ag{2.4}$$

A schematic diagram of the Knights and Davis model is shown in Fig. 2.1. Following the thermalization process, the hole is placed at r=0, and the electron at  $r=r_o$ . The electron experiences a potential which is the Coulomb potential lowered by the applied field, which forms an effective barrier. The electron must escape this barrier to contribute to the measured signal, with a probability which can be calculated with a formula derived by Frenkel. The model of Knights and Davis incorporated further factors, such as an "attempt-to-escape" frequency, but was unable to quantitatively account for the observed results.

Pai and Enck<sup>12</sup> took a different approach to calculate the recombination of electron-hole pairs produced by optical photons. They did not explicitly model the

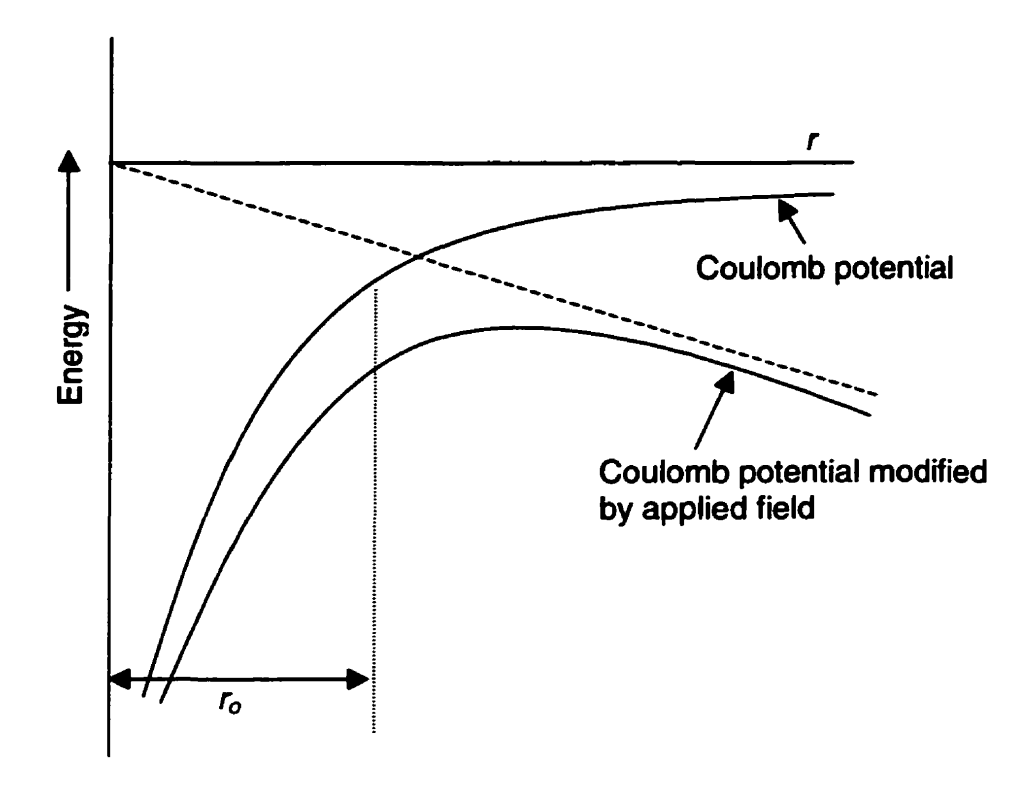


Figure 2.1: Schematic diagram of the model of Knights and Davis. 14

thermalization process, but assumed that the pair would initially be separated by a distance  $r_o$  once it had lost its initial kinetic energy. The pair would subsequently undergo an average drift in the applied field, defined by the mobilities  $\mu_-$  and  $\mu_+$  for electrons and holes, respectively, and would also undergo random diffusion with diffusion constants given by the Einstein equation

$$D_{\pm} = \frac{\mu_{\pm}kT}{e} , \qquad (2.5)$$

where k is the Boltzmann's constant and e is the charge of an electron. The differential equation governing the motion is then given by a Smoluchowski-type equation

$$\frac{\partial P^{\pm}}{\partial t} = \pm \mu_{\pm} E \cdot \nabla P^{\pm} + D_{\pm} \nabla^{2} P^{\pm} , \qquad (2.6)$$

where  $P^{\pm}(\mathbf{r},t)$  is the probability that the electron or hole is at a position  $\mathbf{r}$  at time t, and  $\mathbf{E}$  is the sum of the applied field and the Coulomb potential between the electron and the hole. The first term of Eq. (2.6) describes the drift in the total electric field, and the second term describes the diffusion.

A particle separation of zero corresponds to recombination, whereas an infinite separation corresponds to escape. The differential equation of Eq. (2.6) has been solved in the steady-state by Onsager, 15 and the solution for the escape efficiency  $\eta$  (i.e., the probability of escape) is given by

$$\eta = e^{-a-b} \frac{1}{b} \sum_{l=1}^{\infty} l \left( \frac{b}{a} \right)^{l/2} I_l(2\sqrt{ab})$$
 (2.7)

where  $a = e^2 / (\varepsilon \varepsilon_0 r_0 kT)$ ,  $b = e E_{ann} r_0 / (kT)$ , and  $I_l(x)$  are modified Bessel functions.

Pai and Enck applied Eq. (2.7) to the creation of electron-hole pairs by visible light in a-Se, using  $r_o$  as a free parameter which they fit to experimental data. They observed excellent agreement between experiment and theory for applied fields above 1 V/ $\mu$ m (typically a field of 10 V/ $\mu$ m is used in a-Se based detectors). The theory overestimates the measured values of  $\eta$  below 1 V/ $\mu$ m because bulk trapping becomes important at these low fields. The parameter  $r_o$  was seen to increase with photon energy as expected. The Onsager recombination mechanism is now the accepted theory used to describe the signal produced by the interaction of optical photons with a-Se.

## 2.2.2 Interaction of ionizing radiation with matter

In this section some relevant concepts pertaining to the general interaction of ionizing radiation with matter are summarized. An ionizing particle impinging on matter has a probability of interacting with the medium which depends on the type of particle, its kinetic energy E, and the physical characteristics of the constituents of the medium (e.g., atomic number Z and density  $\rho$ ). The probability is usually defined in terms of a cross-section  $\sigma$ , equal to the probability of interaction per unit fluence  $\Phi$ . The cross-section can be thought of as the effective area presented by the target per unit interaction probability.

There are various types of interactions which can occur, depending on the nature of the incident particle, each with its own cross-section. For each type of interaction, there also exists differential cross-sections in scattering angle and in energy transfer, which describe the state after collision of both the incident particle and the target atom (or molecule). The important interactions for photons, electrons and positrons are summarized below.

## 2.2.2.1 **Photons**

Photons typically have large mean free paths (small cross-sections) compared to charged particles and the predominant interactions for x-rays are coherent scattering, incoherent scattering, photoelectric interactions and pair (or triplet) production. The cross-sections for isolated selenium atoms, taken from the Evaluated Photon Data Library (EPDL), <sup>16</sup> are shown in Fig. 2.2. The photoelectric effect is seen to be the dominant interaction up to about 100 keV (diagnostic range), after which incoherent

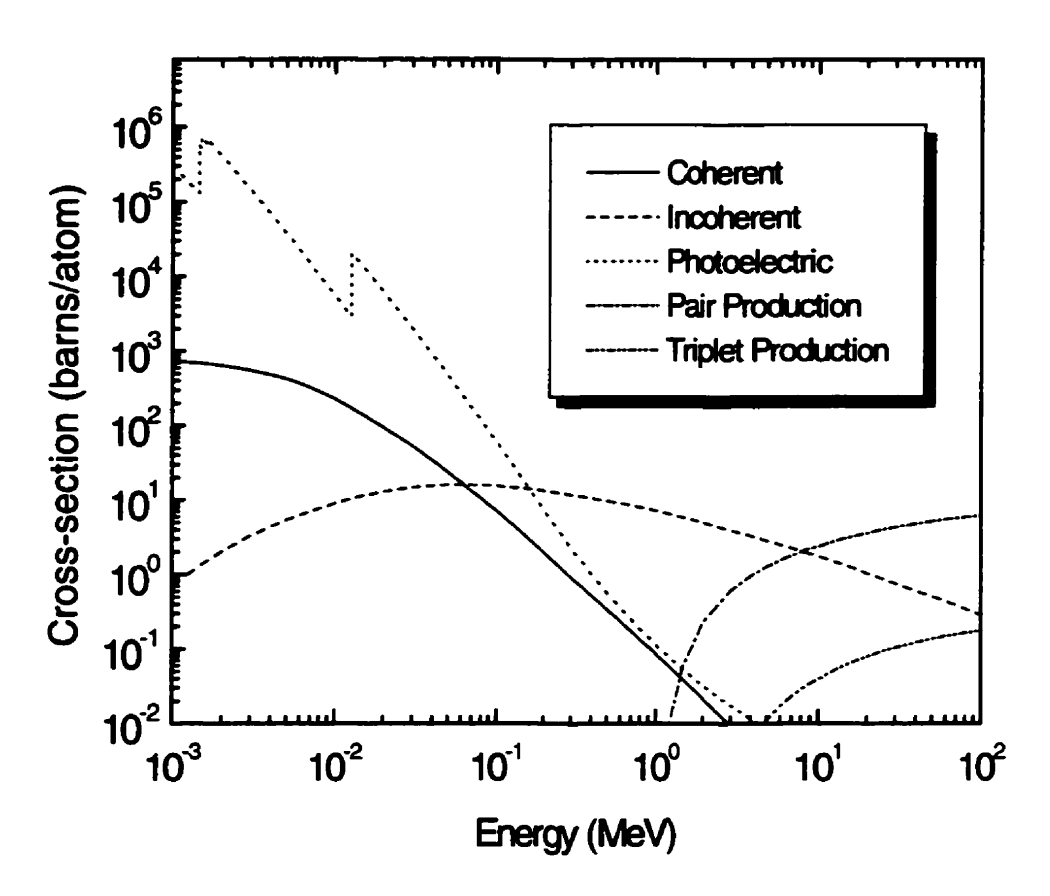


Figure 2.2: Cross-sections for major photon interactions for atomic selenium (taken from the EPDL database).

scattering takes over (therapy range). Above 10 MeV, pair production becomes the most important process. The types of interactions are summarized below.

## 2.2.2.1.1 Coherent scattering

Coherent scattering,  $^{17}$  also known as Rayleigh scattering, results from the interaction of a photon with an atom. The scattering involves contributions from the atom as a whole, and results in a change of photon direction but no energy is transferred to the atom. The differential cross-section in angle  $\theta$  is given by

$$\frac{d\sigma_{coh}}{d\theta} = \frac{r_e^2}{2} (1 + \cos^2 \theta) [F(x, Z)]^2 2\pi \sin \theta , \qquad (2.8)$$

where the parameter x is defined as

$$x = \frac{\sin\frac{\theta}{2}}{\lambda} \,, \tag{2.9}$$

 $\lambda$  is the photon wavelength, and  $r_e$  is the classical electron radius (2.82 fm). Here F(x,Z) is the *atomic form factor*, which can be found in tabulated form. Coherent scattering is predominant at low energies and high atomic number Z.

#### 2.2.2.1.2 Incoherent scattering

In an incoherent scattering interaction,  $^{17}$  also known as *Compton scattering*, a photon transfers some of its energy to an atomic electron. In the process, the photon changes direction and the electron is set in motion. By applying conservation of energy and momentum, it can be shown that energy of the photon decreases from  $h\nu$  to

$$hv'=hv\frac{1}{1+\alpha(1-\cos\theta)},\qquad(2.10)$$

where  $\alpha = hv/mc^2$  and  $\theta$  is the scattering angle of the photon. The kinetic energy K of the secondary electron is given by

$$K = hv \frac{\alpha(1 - \cos \theta)}{1 + \alpha(1 - \cos \theta)}, \qquad (2.11)$$

and the scattering angle  $\phi$  of the electron can be calculated by the relation

$$(1+\alpha)\tan\frac{\phi}{2} = \cot\theta . (2.12)$$

The differential angular cross-section in terms of the photon scattering angle  $\theta$  is

$$\frac{d\sigma}{d\theta} = \frac{r_e^2}{2} (1 + \cos^2 \theta) \cdot 2\pi \sin \theta \cdot F_{KN} \cdot S(x, Z) , \qquad (2.13)$$

where the  $F_{KN}$  are Klein-Nishina coefficients given by

$$F_{KN} = \left\{ \frac{1}{1 + \alpha (1 - \cos \theta)} \right\}^2 \left\{ 1 + \frac{\alpha^2 (1 - \cos \theta)^2}{\left[ 1 + \alpha (1 - \cos \theta) \right] (1 - \cos \theta)^2} \right\}, \qquad (2.14)$$

and x is the parameter defined by Eq. (2.9). The factor S(x,Z) is called the *scattering* function, which takes into account in an approximate way the fact that the atomic electrons are neither completely free nor stationary. The scattering function is available in tabular form.<sup>18</sup>

#### 2.2.2.1.3 Photoelectric effect

The photoelectric effect involves the complete absorption of a photon by an atom, resulting in the emission of a bound electron from a given subshell. The kinetic energy K of the photoelectron is given by

$$K = h v - B \tag{2.15}$$

where B is the binding energy of the photoelectron's original subshell. For a photoelectric interaction to occur with a given subshell, the photon energy must be greater than the binding energy of the subshell. The cross-section is greatest for the innermost shell

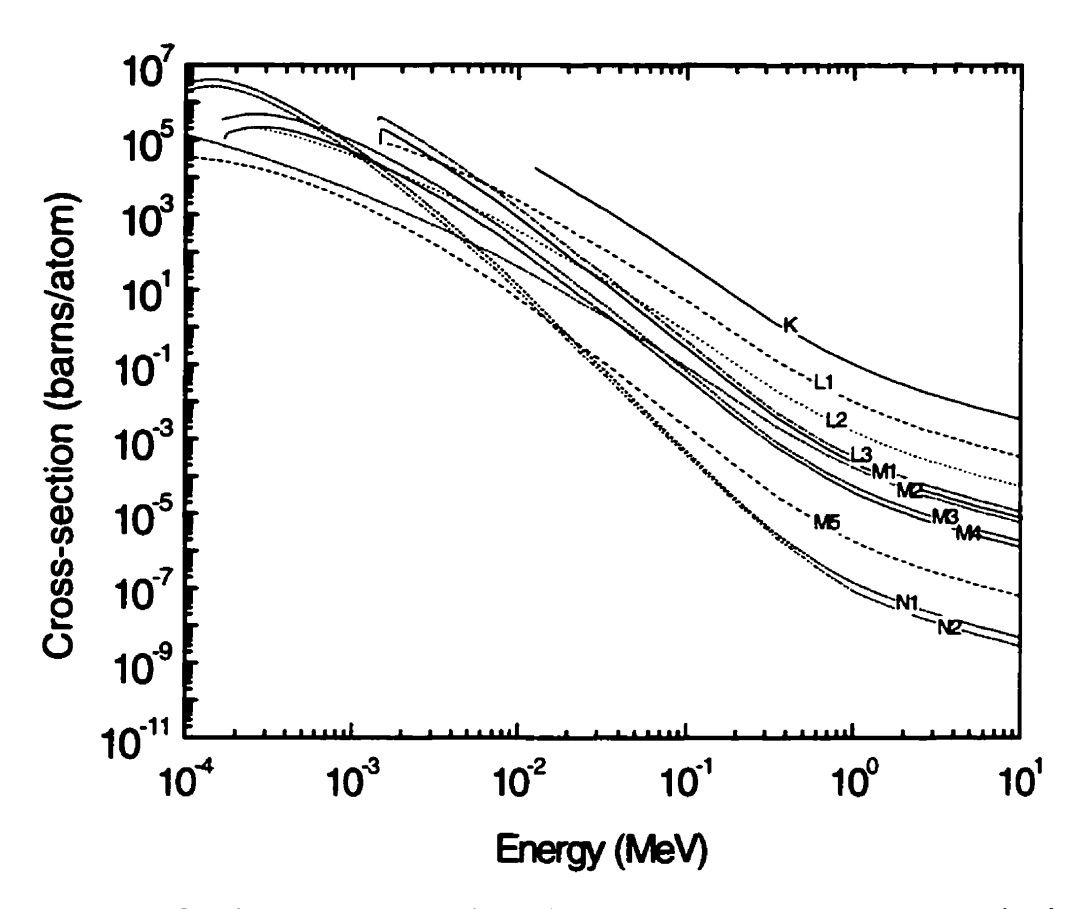


Figure 2.3: Cross-sections for photoelectric interactions with the subshells of atomic selenium, taken from the EPDL library. 16

(K-shell) and smallest for the outermost shell. The photoelectric cross-sections for each individual subshell in atomic Se are shown in Fig. 2.3.

For low energy electrons, the angular distribution of photoelectron emission tends to form lobes which are peaked at right angles to the incident direction. As the energy increases, these lobes tend to be more forward peaked.

### 2.2.2.1.4 Pair and triplet production

An x-ray photon can be absorbed in the nuclear field of an atom, with the energy being converted into an electron and a positron. This is referred to as *pair production*, and conservation of energy requires that the photon must have energy greater than a threshold

$$E_{thresh} = 2mc^2 \left( 1 + \frac{m_c c^2}{m_u c^2} \right), \tag{2.16}$$

where  $m_e$  is the mass of an electron and  $m_a$  is the mass of the atom. The second term in the bracket is small and thus to a good approximation the threshold is 1.022 MeV. Another possibility is that the photon is absorbed by the field of an atomic electron, which transfers energy to the atomic electron and leads to the creation of an electron/positron pair. This is called triplet production since it results in two electrons and one positron. The threshold for this effect is 2.044 MeV  $(4m_e c^2)$ .

#### 2.2.2.2 Electrons

Unlike photons, electrons moving in a medium typically undergo many collisions with orbital electrons and nuclei. The main interactions are *elastic scattering*, bremsstrahlung and inelastic scattering. The cross-sections for a-Se, taken from the Evaluated Electron Data Library (EEDL), 19 are shown in Fig. 2.4. The types of interactions are summarized below.

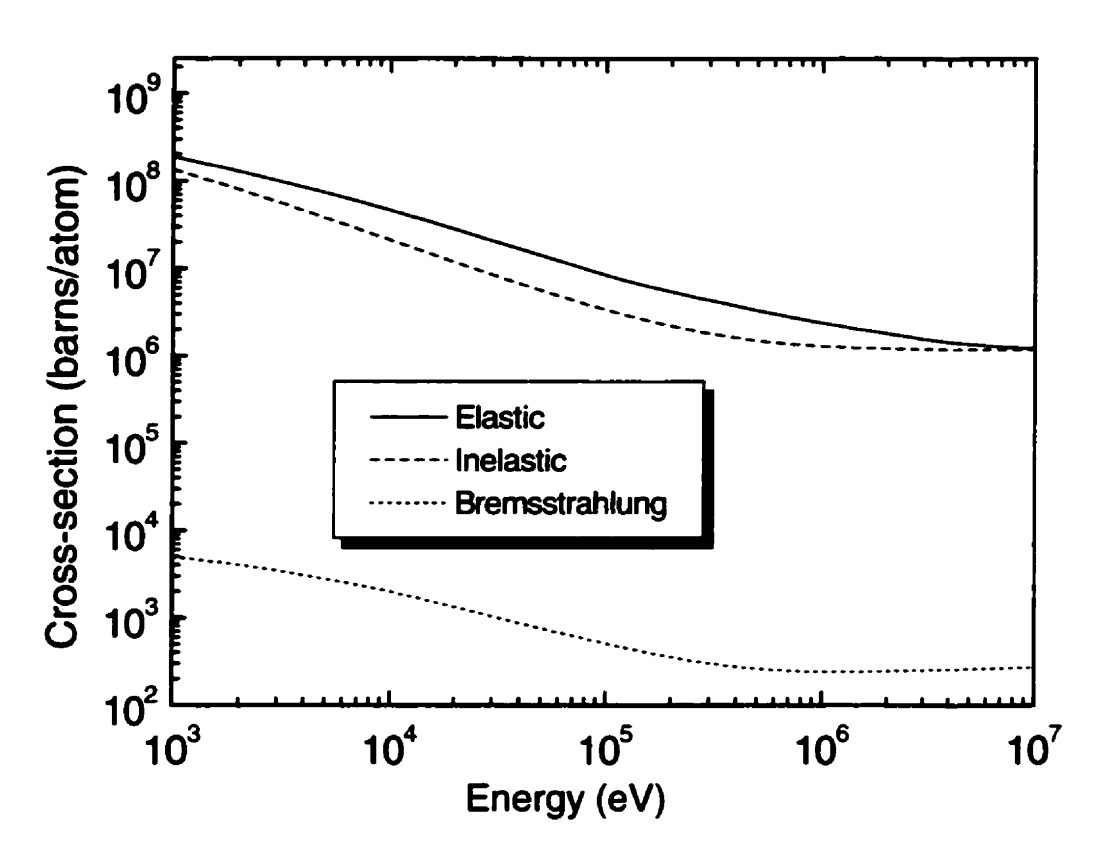


Figure 2.4: Cross-sections for major electron interactions in atomic selenium (taken from the EEDL database 19)

#### 2.2.2.1 Elastic scattering

In elastic scattering, an electron interacts primarily with the atomic nucleus, resulting in a change of direction with negligible energy loss. The total cross-section increases with increasing atomic number. The differential cross-section is available in tabular form and is shown in Fig. 2.5 for atomic selenium in terms of an angular variable  $x = 1 - \cos \theta$ , where  $\theta$  is the scattering angle. Larger scattering angles become increasingly probable with increasing atomic number.

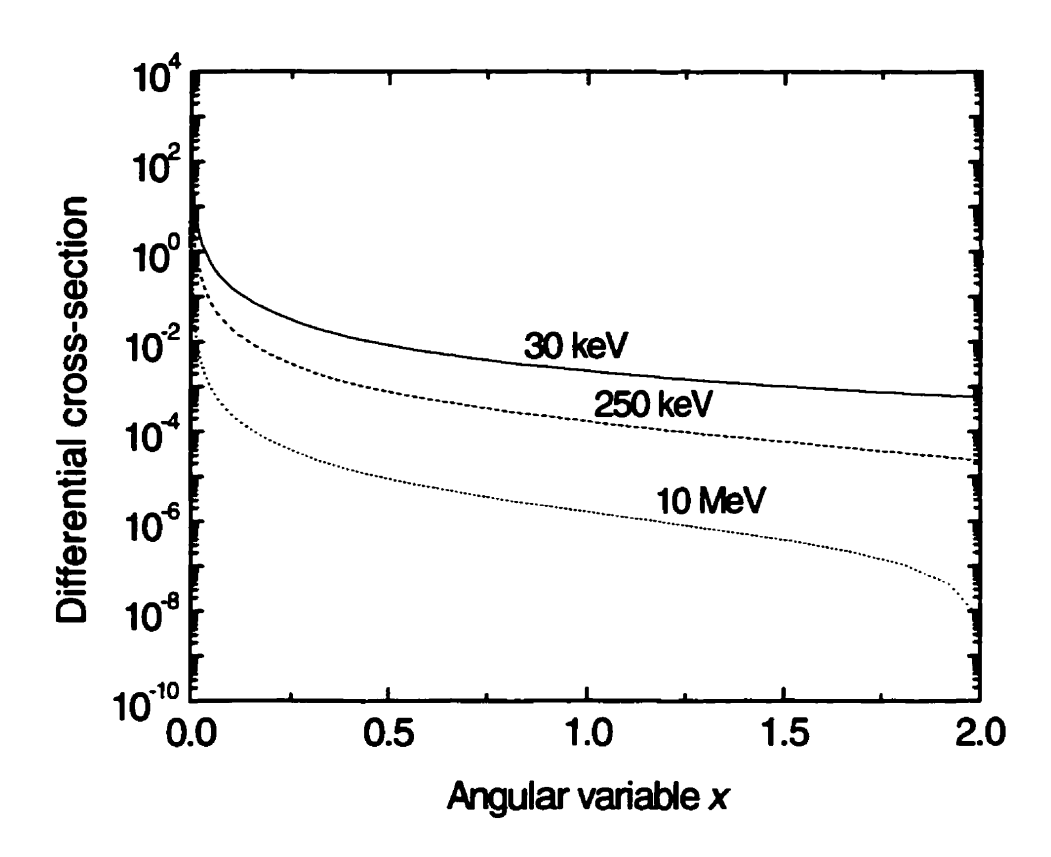


Figure 2.5: Differential cross-section of elastic scattering of electrons in atomic selenium for various energies (data taken from  $EEDL^{19}$ ). Cross-sections are plotted versus an angular variable  $x=1-\cos\theta$ .

#### 2.2.2.2. Bremsstrahlung

In a bremsstrahlung interaction, electrons are accelerated by the Coulomb field of the nucleus which results in the emission of x-ray radiation. It can be seen in Fig. 2.4 that the cross-section for bremsstrahlung is very small in atomic selenium compared to cross-sections for elastic and inelastic interactions. It is more important in high-Z materials such as tungsten.

### 2.2.2.3 Inelastic scattering

In an inelastic scattering interaction, an electron interacts with the Coulomb potential of atomic electrons which results in a transfer of energy. This energy transfer leads to ionization or excitation of the atom. Inelastic collisions are often grouped into either hard or soft collisions. Hard collisions are catastrophic interactions, where the incident electron "knocks out" an atomic electron, resulting in two high-energy electrons (the original electron and the secondary electron). For inner-shell electrons, these cross-sections can be reasonably approximated using tabulated cross-sections for isolated atoms. Cross-sections for hard inelastic collisions with the subshells of atomic selenium, taken from the EEDL database, are shown in Fig. 2.6.

The other category of inelastic collisions, soft collisions, occurs predominantly with outer-shell electrons. The energy levels of these electrons depend strongly on the dielectric properties of the medium, and the cross-sections cannot be approximated using data for isolated atoms.

In the following a formula for these cross-sections is explicitly derived, since the result is central to the work presented in this Chapter. The derivation is a modified version of that described by Rossi and Zaider.<sup>20</sup>

In an inelastic scattering interaction, an electron with momentum  $\hbar k_i$  transfers energy  $\hbar \omega$  and momentum  $\hbar q$  to the medium, after which it has momentum  $\hbar k_f$ . We wish to calculate the differential cross-section for inelastic scattering in terms of  $\omega$  and q. Using the fact that

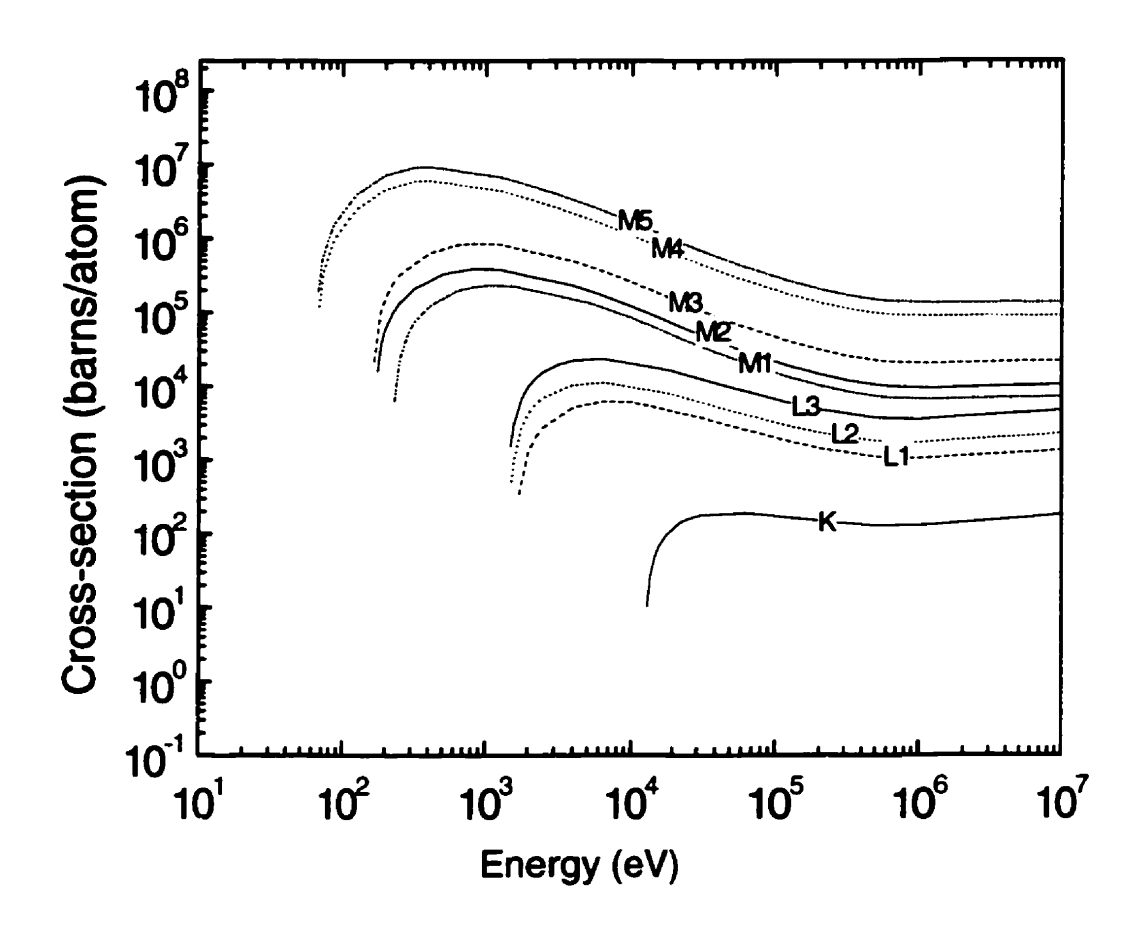


Figure 2.6: Cross-section for inelastic scattering of electrons in atomic selenium for individual subshells (outer shells are not shown). Data taken from the EEDL database.

$$q^{2} = \left| \mathbf{k}_{f} - \mathbf{k}_{i} \right|^{2} = k_{f}^{2} + k_{i}^{2} - 2k_{i}k_{f}\cos\theta , \qquad (2.17)$$

this cross-section can be expressed in terms of solid angle through the relation

$$\frac{d^2\sigma}{dqd\omega} = \frac{2\pi q}{k_i k_f} \frac{d^2\sigma}{d\Omega d\omega}.$$
 (2.18)

We begin by considering the differential cross-section in solid angle,  $d\sigma/d\Omega$ , which is given by the fluence through an area  $dA = r^2 d\Omega$  normalized to the incident fluence. The fluence j for a particle with wavefunction  $\psi$  is given by

$$j = \frac{i\hbar}{2m} \left( \psi^* \nabla \psi - \psi \nabla \psi^* \right). \tag{2.19}$$

To find an expression for the cross-section we thus need to calculate the wavefunction  $\psi(r) = \langle r | \psi \rangle$  such that  $H | \psi \rangle = E | \psi \rangle$ , where H is the total Hamiltonian of the interaction expressed as

$$\boldsymbol{H} = \boldsymbol{H}_{L} + \boldsymbol{H}_{R} + \boldsymbol{V} , \qquad (2.20)$$

where  $H_p = p^2 / 2m$  is the Hamiltonian of the *projectile* (i.e., the ionizing electron),  $H_i$  is the Hamiltonian of the *target* (i.e., the medium) and V is the interaction potential. The isolated eigenstates of the target are represented by

$$\boldsymbol{H}_{t}|\boldsymbol{E}_{n}\rangle = \boldsymbol{E}_{n}|\boldsymbol{E}_{n}\rangle \tag{2.21}$$

and of the projectile by

$$\boldsymbol{H}_{p}|\boldsymbol{k}\rangle = \frac{\hbar^{2}k^{2}}{2m}|\boldsymbol{k}\rangle . \tag{2.22}$$

The total wavefunction lies in the space which is the direct product of the spaces spanned by  $|E_n\rangle$  and  $|k\rangle$ . We expand it in terms of the eigenstates of the target  $|E_n\rangle$ 

$$|\psi\rangle = \sum_{n} |\Phi_{n}\rangle |E_{n}\rangle , \qquad (2.23)$$

where the coefficients  $|\Phi_n\rangle$  lie in the projectile space. Applying Eq. (2.20) to Eq. (2.23) leads to

$$\sum_{n} (\boldsymbol{H}_{t} + \boldsymbol{H}_{p}) |\boldsymbol{\Phi}_{n}\rangle |\boldsymbol{E}_{n}\rangle + V |\boldsymbol{\psi}\rangle = E \sum_{n} |\boldsymbol{\Phi}_{n}\rangle |\boldsymbol{E}_{n}\rangle , \qquad (2.24)$$

and multiplying both sides by the final target state  $\langle E_f |$  gives

$$\left(E - E_f - H_p\right) \left|\Phi_f\right\rangle = \sum_n \left\langle E_f \left|V\right|E_n\right\rangle \left|\Phi_n\right\rangle. \tag{2.25}$$

The solution to this, in the position representation and at a distance r which is far away from the interaction site, is given by

$$\Phi_{f}(\mathbf{r}) = \frac{1}{(2\pi L)^{3/2}} e^{i\mathbf{k}_{f} \cdot \mathbf{r}} - \frac{e^{i\mathbf{k}_{f} \cdot \mathbf{r}}}{r} \left[ \frac{m}{2\pi \hbar^{2}} \left\langle k_{f}, E_{f} \middle| V \middle| \psi \right\rangle \right], \qquad (2.26)$$

where  $\langle k_f, E_f |$  represents the final state where the projectile has momentum  $\hbar k_f$  and the target has energy  $E_f$ , and L is the length of the side of a square box used for normalization of the plane wave. Since the solution depends on  $|\psi\rangle$  which is not known,  $|\psi\rangle$  is replaced in the first Born approximation with  $|\psi\rangle\approx|k_i,E_i\rangle$  leading to

$$\Phi_{f}(\mathbf{r}) = \frac{1}{(2\pi L)^{3/2}} e^{i\mathbf{k}_{i}\mathbf{r}} - \frac{e^{i\mathbf{k}_{f}\mathbf{r}}}{r} \left[ \frac{mL^{3/2}}{2\pi\hbar^{2}} \left\langle k_{f}, E_{f} \middle| V \middle| k_{i}, E_{i} \right\rangle \right]. \tag{2.27}$$

The solution is seen to be the sum of the incident plane wave and a spherical wave with amplitude proportional to the matrix element of the interaction potential with the total wavefunction. This matrix element can be re-written as

$$\left\langle \boldsymbol{k}_{f}, E_{f} \left| \boldsymbol{V} \right| \boldsymbol{k}_{i}, E_{i} \right\rangle = \frac{1}{\left(2\pi\right)^{3} L^{3}} \int d\boldsymbol{r} e^{i\boldsymbol{q}\cdot\boldsymbol{r}} \left\langle E_{f} \left| \boldsymbol{V}(\boldsymbol{r}) \right| E_{i} \right\rangle = \frac{1}{\left(2\pi\right)^{3} L^{3}} \left\langle E_{f} \left| \boldsymbol{V}(\boldsymbol{q}) \right| E_{i} \right\rangle, (2.28)$$

where V(q) is the Fourier Transform of the potential evaluated at  $q = k_f - k_i$ . This leads to an expression for the differential angular cross-section

$$\frac{d\sigma}{d\Omega} = \frac{k_f}{k_i} \left| \frac{m}{2\pi \hbar^2} \left\langle E_f \left| V(q) \right| E_i \right\rangle \right|^2. \tag{2.29}$$

Since energy must be conserved, i.e.,  $\hbar \omega = E_f - E_i$ , then

$$\frac{d^2\sigma}{d\Omega d\omega} = \frac{k_f}{k_i} \hbar \left| \frac{m}{2\pi\hbar^2} \left\langle E_f \left| V(\mathbf{q}) \right| E_i \right\rangle \right|^2 \delta(\hbar\omega + E_f - E_i) , \qquad (2.30)$$

which, substituted into Eq. (2.18), gives an expression for the differential cross-section

$$\frac{d^2\sigma}{dqd\omega} = \frac{2\pi q}{k_i^2} \hbar \left| \frac{m}{2\pi \hbar^2} \left\langle E_f \left| V(q) \right| E_i \right\rangle \right|^2 \delta(\hbar\omega + E_f - E_i) . \tag{2.31}$$

In an inelastic collision, energy and momentum transfer by the incident electron (projectile) lead to density fluctuations in the medium (target). If the medium is assumed to consist of a number of particles at positions  $\mathbf{r}_j$ , then the density of the target can be expressed as a sum of delta functions

$$\rho(\mathbf{r}) = \sum_{j} \delta(\mathbf{r} - \mathbf{r}_{j}) , \qquad (2.32)$$

and the interaction potential as

$$V(\mathbf{r}) = \frac{e^2}{4\pi\varepsilon_0} \sum_{j} \frac{1}{|\mathbf{r} - \mathbf{r}_j|}, \qquad (2.33)$$

where r is the position of the projectile. Under this assumption the Fourier Transform of the potential can be expressed in terms of the Fourier Transform of the density through

$$V(q) = \frac{e^2}{\varepsilon_0 q^2} \rho^+(q) , \qquad (2.34)$$

which leads to an expression

$$\frac{d^2\sigma}{dqd\omega} = \frac{q}{v^2} \frac{e^2}{\varepsilon_0 q^2} \sum_{f} \left| \left\langle E_f \left| \rho^+(q) \right| E_i \right\rangle \right|^2 \delta(\hbar\omega + E_f - E_i) , \qquad (2.35)$$

where  $\hbar k_i = mv$  and where we have summed over the final states. The generalized oscillator strength distribution (GOSD) is defined as

$$f(q,\omega) = \frac{2m}{(\hbar q)^2} \hbar \omega \sum_{f} \left| \left\langle E_f \left| \rho^+(q) \right| E_i \right\rangle \right|^2 \delta(\hbar \omega + E_f - E_i) , \qquad (2.36)$$

which gives the following concise result for the cross-section in terms of the GOSD,

$$\frac{d^2\sigma}{dqd\omega} = \frac{4\pi}{mv^2} \left(\frac{e^2}{4\pi\varepsilon_0}\right)^2 \frac{1}{q\omega} f(q,\omega) . \qquad (2.37)$$

It can be shown<sup>21</sup> that the GOSD satisfies the relation

$$\int_{0}^{\infty} f(q,\omega)d\omega = Z \tag{2.38}$$

for all q, where Z is the atomic number of the medium, which is known as *Bethe's sum* rule. In section 2.2.3.1 we will discuss how to calculate the GOSD from the dielectric properties of a medium.

#### **2.2.2.2.4 Positrons**

Positrons undergo elastic, inelastic and bremsstrahlung collisions in a manner similar to electrons. They do so until they annihilate with an electron, leading to the creation of two gamma rays with combined energy  $2mc^2$ . The total cross-section is given by<sup>22</sup>

$$\sigma = \frac{\pi r_e^2}{E + 2mc^2} \left[ \frac{E^2 + 5mc^2 E + 6m^2 c^4}{E(E + 2mc^2)} + \ln\left(E + mc^2 + \sqrt{E(E + 2mc^2)} - \frac{E + 4}{\sqrt{E(E + 2)}} \right], \quad (2.39)$$

where E is the kinetic energy of the incident positron. The differential cross-section in energy  $h\nu_1$  of one of the annihilation photons is

$$\frac{d\sigma}{dhv_1} = \frac{\pi r_e^2}{E(E + 2mc^2)} \left[ S_1(hv_1) + S_1(E + 2mc^2 - hv_1) \right], \qquad (2.40)$$

where

$$S(x) = \frac{1}{x} \left( E + 2mc^2 + 2\frac{E + mc^2}{E + 2mc^2} - \frac{1}{x} \right) - 1.$$

It is also of note that annihilation into a single photon or into three photons are also possible, but not as likely as annihilation into two photons.

### 2.2.2.3 Atomic reorganization

The photoelectric effect, incoherent scattering, and inelastic scattering processes can lead to the ionization of an atom in the medium. The result is a vacancy in one of the subshells of the atom. This vacancy can be filled by an electron from a higher energy level and the transition can either be *radiative* or *non-radiative*.

For the radiative case, the transition results in the emission of a fluorescent photon with energy  $hv = E_n - E_m$ , where  $E_m$  is the energy of the original vacancy and  $E_n$  is the energy of the subshell of the electron which fills the vacancy. For the non-radiative case, the transition causes an atomic electron to be emitted. The kinetic energy of this electron is given by  $K = E_n - E_m - E_k$ , where  $E_k$  is the binding energy of the shell whose electron is emitted. The case  $E_k = E_n$  is often called the Auger effect, and the case  $E_k \neq E_n$  is often called the Coster-Kronig effect.

Relative probabilities of radiative and nonradiative transitions can be found in tabular form<sup>18</sup> (the probability of a radiative transition is often called the *fluorescent* yield). The result of one of these transitions is one or two new vacancies in the atom, in subshells with lower binding energy than the original vacancy. These new vacancies are then filled by electrons in higher subshells through new radiative or nonradiative transitions, and the process is repeated until the atom reaches its ground state.

## 2.2.3 Generalized oscillator strength distribution in solids

## 2.2.3.1 Relation between dipole strength and dielectric response function

Eq. (2.37) gives the cross-section for inelastic scattering of electrons in terms of the density fluctuations in the medium caused by the passing electron. In this section we derive the relation between these fluctuations and the dielectric response function  $\varepsilon(q,\omega)$  of the medium in question, which governs the relation between the electric field E and the dielectric displacement D in the medium through the relation

$$D(q,\omega) = \varepsilon(q,\omega)E(q,\omega) . \tag{2.41}$$

The derivation is again similar to that described by Rossi and Zaider.<sup>20</sup>

From Maxwell's equations,

$$\nabla \boldsymbol{D}(\boldsymbol{r},t) = \frac{1}{\varepsilon_0} \rho_p(\boldsymbol{r},t) \tag{2.42}$$

and

$$\nabla E(\mathbf{r},t) = \frac{1}{\varepsilon_0} \left[ \rho_p(\mathbf{r},t) + \left\langle \Delta \rho_t(\mathbf{r},t) \right\rangle \right], \qquad (2.43)$$

where  $\langle \Delta \rho_{t}(\mathbf{r},t) \rangle$  is the average charge fluctuation induced in the medium (target) by the passing electron. This leads to a relation between the charge fluctuations and the dielectric response function

$$\frac{1}{\varepsilon(\boldsymbol{q},\boldsymbol{\omega})} = 1 + \frac{\left\langle \Delta \rho_{t}(\boldsymbol{q},\boldsymbol{\omega}) \right\rangle}{\rho_{p}(\boldsymbol{q},\boldsymbol{\omega})}.$$
 (2.44)

To express the inelastic cross-section in terms of  $\varepsilon(q,\omega)$  the projectile density distribution is taken to be

$$\rho_{p}(\mathbf{r},t) = \rho_{p}(\mathbf{q})e^{i(\mathbf{q}\cdot\mathbf{r}-\alpha\mathbf{r})-\delta} + complex \ conjugate \tag{2.45}$$

(where  $\delta \to 0$  is used to make sure that the target does not interact with the particle at infinite times). The potential  $V(\mathbf{r},t)$  induced by the passing projectile,

$$V(\mathbf{r},t) = \int \frac{\rho_p(\mathbf{r},t)\rho_t(\mathbf{r}')}{|\mathbf{r}-\mathbf{r}|} d\mathbf{r} d\mathbf{r}' , \qquad (2.46)$$

is treated as a time-dependent pertubation. Substitution of Eq. (2.45) into (2.46) can be manipulated to yield

$$V(\mathbf{r},t) = \frac{e^2}{\varepsilon_0} \frac{1}{q^2} \rho_p(\mathbf{q}) \rho_i(\mathbf{q}) e^{-i\alpha \mathbf{r}) - \delta \mathbf{r}}.$$
 (2.47)

We wish to calculate the charge fluctuation

$$\langle \Delta \rho_{l}(\mathbf{q}, \omega) \rangle = \langle \Psi | \rho_{l}(\mathbf{q}, \omega) | \Psi \rangle \tag{2.48}$$

caused by this potential, and this requires knowledge of the wavefunction  $\Psi(r,t)$  of the target. We represent the eigenstates of the target in the absence of the pertubation to be

$$H_i \Phi_j(\mathbf{r}) = E_j \Phi_j(\mathbf{r}) . \qquad (2.49)$$

When the pertubation is turned on, the wavefunction is governed by the time-dependent Schrödinger equation

$$i\hbar \frac{\partial}{\partial t} \Psi(\mathbf{r}, t) = [H_t + V(\mathbf{r}, t)] \Psi(\mathbf{r}, t)$$
, (2.50)

which has the formal solution

$$\Psi(\mathbf{r},t) = \Phi(\mathbf{r},t) + \frac{1}{2\pi\hbar} \sum_{j} \int dE d\mathbf{r}' dt' e^{-iE(t-t')} \frac{\Phi_{j}^{*}(\mathbf{r}')V(\mathbf{r}',t')\Psi(\mathbf{r}',t')}{E-E_{j}} \Phi_{j}(\mathbf{r}) . \qquad (2.51)$$

The wavefunction  $\Psi(r',t')$  on the right-hand side is approximated by its unperturbed value  $\Phi_0(r,t)$  which is assumed to be in a pure state given by

$$\Phi_0(\mathbf{r},t) = \Phi_0(\mathbf{r})e^{-iE_0t}. \tag{2.52}$$

Substitution and reorganization gives

$$\Psi(\mathbf{r},t) = \Phi(\mathbf{r},t) - \frac{e^2}{4\pi\varepsilon_0} \frac{4\pi}{q^2} \rho_p(\mathbf{q}) \sum_{i} \langle \Phi_i | \rho_i^+(\mathbf{q}) | \Phi_0 \rangle \frac{e^{-i\omega t + \delta t}}{\hbar\omega_{i0} - \hbar\omega - i\hbar\delta} \Phi_i(\mathbf{r}') e^{-i\varepsilon_0 t}, (2.53)$$

where  $\hbar\omega_{j0} = E_j - E_0$  and the term corresponding to the complex conjugate of Eq. (2.45) has been omitted for clarity.

Substitution of Eq. (2.53) into Eq. (2.44) and using (2.48) gives the expression

$$\frac{1}{\varepsilon(q,\omega)} = 1 - \frac{e^2}{4\pi\varepsilon_0} \frac{4\pi}{q^2} \rho_p(q) \sum_j \left| \left\langle \Phi_j \left| \rho_i(q) \right| \Phi_0 \right\rangle \right|^2 \left[ \frac{1}{\hbar\omega_{j0} - \hbar\omega - i\hbar\delta} + \frac{1}{\hbar\omega_{j0} + \hbar\omega + i\hbar\delta} \right], \quad (2.54)$$

which relates the dielectric response function to the matrix elements of the density distribution of the medium. Using the identity

$$\lim_{\delta \to 0} \frac{1}{x \pm i\delta} = P\left(\frac{1}{x}\right) \mp i\pi\delta(x),$$

(where P represents the principal value) it can now be related back to Eq. (2.36) to obtain the expression for  $f(q,\omega)$  in terms of the dielectric response for positive energy transfers  $(\omega > 0)$ :

$$f(q,\omega) = \frac{2m}{h^2 N(e^2 / 4\pi\varepsilon_0)} \hbar \omega \operatorname{Im} \left\{ \frac{-1}{\varepsilon(q,\omega)} \right\}. \tag{2.55}$$

The quantity  $Im\{-1/\varepsilon(q,\omega)\}$  is often referred to as the *energy loss function*. Using Eq. (2.37), the cross-section for inelastic collisions can now be expressed in terms of the dielectric properties of the medium as

$$\frac{d^2\sigma(q,\omega)}{dqd\omega} = \frac{2e^2}{h^2N\varepsilon_0} \frac{1}{v^2} \frac{1}{q} \operatorname{Im} \left\{ \frac{-1}{\varepsilon(q,\omega)} \right\}. \tag{2.56}$$

This expression is correct at relativistic energies<sup>23</sup> as long as the energy transfers are small ( $\hbar\omega << mc^2$ ), and since we are dealing with soft collisions this is an excellent approximation.

## 2.2.3.2 Ashley's approximation for the dipole strength

The cross-section of Eq. (2.56) relies on knowledge of the dielectric response function  $\varepsilon(q,\omega)$ . Theoretical calculations of this function have been performed for only the simplest cases, and experimental data is typically only available in the *optical limit*  $q \sim 0$ . Using an approximation due to Ashley,<sup>24</sup> it is possible to extract information about

the generalized oscillator strength distribution in terms of its value at q = 0 through the relation

$$f(q,\omega) = \int_{0}^{\infty} d\omega' f(\omega) \delta\left(\omega - (\omega' - \frac{q^{2}}{2m})\right), \qquad (2.57)$$

where  $f(\omega) = f(0, \omega)$  is simply referred to as the oscillator strength distribution. This simple relation relies on the extrapolation of the oscillator strength distribution into the  $(q, \omega)$  along quadratic dispersion lines, and has been shown to be a good approximation for a variety of materials. In terms of the energy loss function, Ashley's approximation is expressed as

$$\omega \operatorname{Im} \left\{ \frac{-1}{\varepsilon(q,\omega)} \right\} = \int_{0}^{\infty} d\omega' \omega' \operatorname{Im} \left\{ \frac{-1}{\varepsilon(0,\omega)} \right\} \delta \left( \omega - (\omega' - \frac{q^{2}}{2m}) \right). \tag{2.58}$$

The oscillator strength distribution  $f(\omega)$  is related to the photoelectric crosssection  $\kappa(E)$  for the interactions of photons with matter through the relation<sup>25</sup>

$$f(E) = \frac{mc}{\pi h e^2} \kappa(E) \tag{2.59}$$

in the dipole approximation,  $qx \ll 1$ . The dipole limit is adequate, if the photon wavelength is much smaller than the interatomic distance. In this limit the oscillator strength distribution is often referred to as the dipole oscillator strength distribution.

## 2.2.4 Interaction of x-rays with a-Se

The interaction of x-rays with a-Se has been qualitatively described by many authors. 8.11.13 X-rays lead to the creation of high-energy secondary electrons, which subsequently create many electron-hole pairs within the medium. The average energy required to create one pair,  $W_o$ , is given in many materials by a semi-empirical formula due to Klein,  $^{26}$ 

$$W_{o} = 2.8E_{g} + rhv_{p} , \qquad (2.60)$$

where the second term is a phonon contribution and is between 0.5 and 1, or the alternate formula<sup>11</sup>

$$W_{o} = 2.2E_{o} + rhv_{n} , \qquad (2.61)$$

which lead to a value of approximately 4-7 eV for a-Se. In practice, however, what is measured is  $W_{\pm}$ , the average energy required to collect a *detectable* pair. Assuming that losses of electron-hole pairs result only from recombination (trapping is another possibility, which may be neglected above 1 V/ $\mu$ m, as discussed in Section 2.2.1), the two definitions of pair creation energy are related by

$$W_{\pm} = \frac{W_o}{\eta} . \tag{2.62}$$

where  $\eta$  is the escape efficiency, *i.e.*, the fraction of electron-hole pairs which escape recombination. A description of  $W_{\pm}$  thus requires a model for recombination in a-Se.

The main difference between recombination due to visible and x-ray photons is that in the former case only one pair is created, whereas in the latter many pairs are created. In principle, two types of recombination are possible: *general* and *initial* recombination. General recombination refers to recombination between any charges generated within a volume (in this case, the a-Se layer). General recombination in a-Se has been shown<sup>27</sup> to be consistent with Langevin recombination theory.<sup>28</sup> For general recombination in a volume bounded by parallel semi-infinite planes, the escape efficiency can be calculated using the formula<sup>17</sup>

$$\eta = 1 - \frac{1}{6} \frac{\alpha \dot{\rho} d^4}{e \mu_e \mu_b V^2} , \qquad (2.63)$$

where  $\dot{\rho}$  is the rate of charge creation in the layer, d is the thickness of the layer, e is the charge of an electron, V is the potential applied across the layer,  $\mu_e$  and  $\mu_h$  are the electron and hole mobilities, respectively, and  $\alpha$  is the Langevin recombination coefficient, given by

$$\alpha = \frac{e(\mu_e + \mu_h)}{\varepsilon_0 \varepsilon} \ . \tag{2.64}$$

Here  $\varepsilon_0$  is the permittivity of vacuum and  $\varepsilon$  is the relative dielectric constant of the material. This result shows that the amount of general recombination varies linearly with dose rate. To achieve 1% recombination in a-Se, a dose rate of  $10^8$  cGy/s would be needed, which is much larger than dose rates used for medical applications. <sup>13</sup> General recombination in a-Se can for this reason be ignored for practical purposes.

Initial recombination refers to recombination between charges which were created along a single track of ionizing radiation, and hence does not depend on dose rate. Since general recombination is negligible in a-Se, only initial recombination needs to be considered. It will be assumed in the remainder of this thesis, unless otherwise specified, that "recombination" refers to initial recombination only.

In the past, two competing models for initial recombination have been used to describe the experimental results. Hirsch and Jahankhani<sup>9</sup> used the columnar model of recombination, which assumes that the pairs are generated uniformly along a cylindrical track, as shown in Fig. 2.7(a). The original columnar model, due to Jaffé, <sup>10</sup> assumes that drift in the electric field is negligible which results in a diffusion equation in cylindrical coordinates, modified by an effective recombination coefficient  $\alpha$  given by Eq. (2.64):

$$\frac{\partial n}{\partial t} = D \left[ \frac{\partial^2 n}{\partial t^2} + \frac{1}{r} \frac{\partial n}{\partial r} \right] - \alpha n^2 , \qquad (2.65)$$

where n(r,t) is the number density of electron-hole pairs in the column. The columnar model was later extended to include an electric field,<sup>29</sup> but there is no solution in closed form and various numerical techniques have been used to extract results.

In 1991, Que and Rowlands<sup>11</sup> argued that, based on the experimental evidence at the time, that geminate recombination could not be ruled out as a possible model for recombination in a-Se. For the Onsager theory to hold, the pairs created along the ionizing track (shown schematically in Fig. 2.7(b)) would need to be so far apart that they could only recombine with their geminate pair, and not with other pairs along the track. The debate as to whether the columnar or geminate recombination models were better

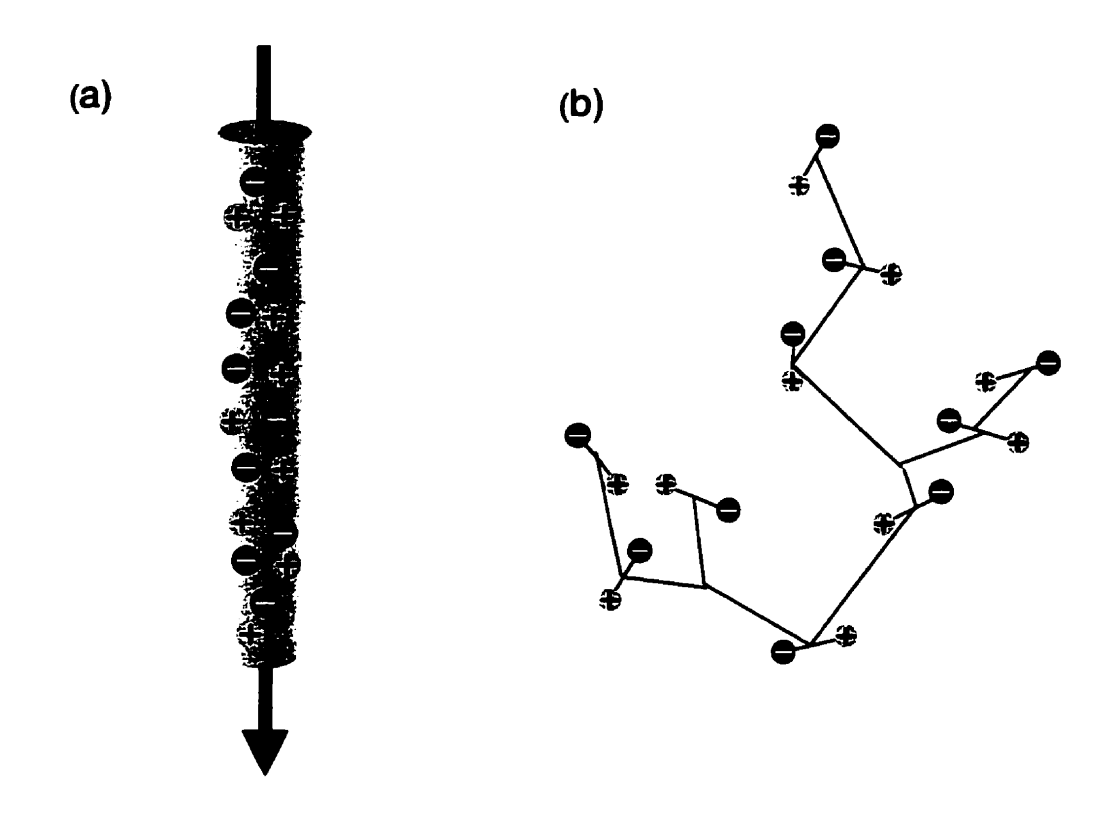


Figure 2.7: Schematic diagram of (a) the columnar recombination model and (b) pairs created along the track of ionizing radiation.

suited to recombination in a-Se was never resolved, since neither model could adequately explain the observed experimental results. It was noted by Que and Rowlands, however, that more reliable measurements of  $W_{\pm}$  than those which were available at the time were needed to demonstrate whether or not  $W_{\pm}$  exhibited an energy dependence. Recent measurements by Blevis  $et\ al^6$  have demonstrated that such a dependence indeed exists, indicating that the Onsager model is clearly not acceptable, since it does not depend on the energy in any way.

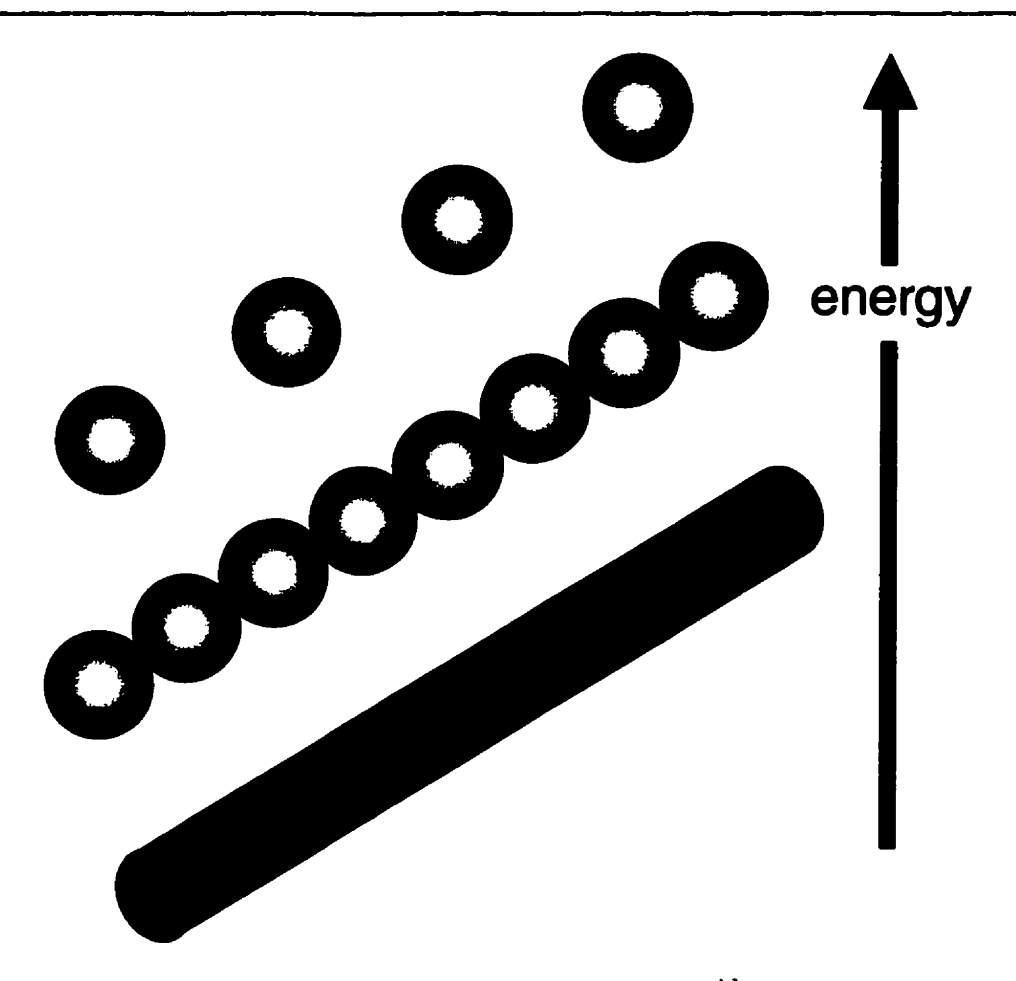


Figure 2.8: Qualitative model of Mah et al<sup>13</sup> to account for the observed energy dependence of  $W_{\pm}$ .

Mah et al<sup>13</sup> have recently extended measurements of  $W_{\pm}$  to megavoltage energies, where they found that  $W_{\pm}$  reaches a plateau and becomes energy independent. The qualitative picture put forward to explain their results is shown in Fig. 2.8. They assume that an ionizing electron loses its energy in many small collisions called *spurs*, a term borrowed from radiation chemistry. They assume that these spurs have a fixed energy of about 40 eV, which lead to the creation of a small group of electron-hole pairs. At high incident energies, the spurs are created sufficiently far apart that they can be treated as

more or less independent. For this reason the Onsager theory is more or less applicable at high energies, resulting in an energy-independent  $W_{\pm}$ . As the energy is decreased, the spurs become closer together and begin to interact with each other, and thus  $W_{\pm}$  becomes energy dependent. At very low energies the spurs completely overlap and form a column, in which case the columnar theory becomes valid. This qualitatively explains the observed trends and gives some insight to the mechanisms at work, but is unable to explain the results in a quantitative manner.

## 2.2.5 The Monte Carlo method

In order to calculate  $W_{\pm}$  we will rely extensively on Monte Carlo methods to simulate random physical processes. The Monte Carlo method is widely used in many fields by a large number of investigators. In this section we briefly introduce the basic concept behind the method.

The Monte Carlo method consists of sampling random numbers which directly simulate the physical processes of the problem at hand, and of extracting the relevant information from these random numbers. Mathematically, if we wish to sample a random physical variable X with probability density f(x), the Monte Carlo method substitutes X for another random variable Y with probability density g(y) given by

$$g(y) = 1 for 0 \le y \le 1$$
  

$$g(y) = 0 otherwise , (2.66)$$

such that the cumulative probabilities are the same, i.e.,

$$\int_{-\infty}^{x} f(x)dx = \int_{-\infty}^{y} g(y)dy , \qquad (2.67)$$

which establishes a relation between the random variables X and Y.

The function g(y) can then simply be simulated by sampling random numbers R between 0 and 1. For a given R, Eq. (2.67) leads to

$$\int_{-\infty}^{X} f(x)dx = \int_{-\infty}^{Y} g(y)dy = Y = R$$
 (2.68)

and

$$X = F^{-1}(R) (2.69)$$

Eq. (2.69) relates a physical process represented by the variable X to a random number between 0 and 1. The function F' is the inverse function of the cumulative distribution F(x) of f(x). In this manner complicated physical processes can be reduced to sampling a uniform random number.

The trajectory of a photon or an electron in a medium is a succession of interactions which result in a change of energy and/or direction of the interacting particles, and often lead to the creation of new particles along the track. The particle transport can thus be described by sampling the distance, or *free path*, between successive interactions and then determining the type of interaction.

Consider a beam of monoenergetic particles of energy E and intensity  $I_o$  incident on a semi-infinite plane, as shown in Fig. 2.9. As the beam travels though an element of the slab dx at a depth x, its decrease in intensity dI is proportional to its intensity I(x), to

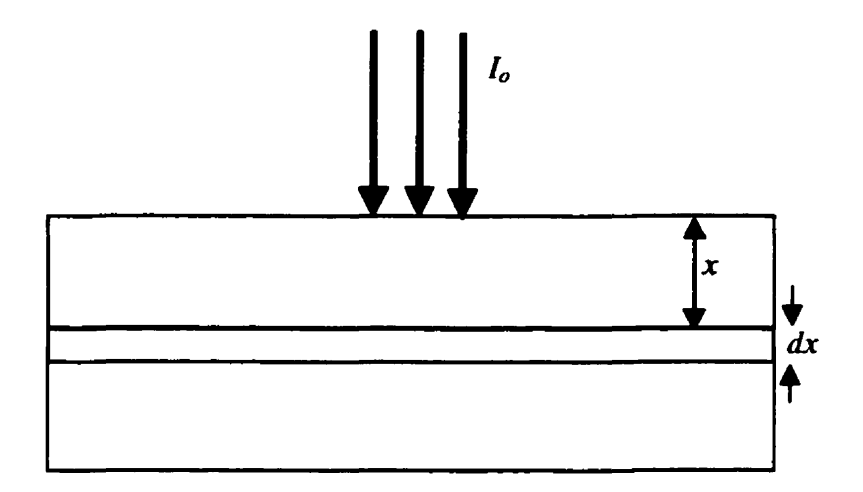


Figure 2.9: Schematic diagram of particles incident on a slab of material.

the element dx, to the total interaction cross-section  $\sigma(E)$ , and to the number of atoms (or molecules) per unit volume, N, and is given by

$$dI = -I(x)\sigma(E)Ndx . (2.70)$$

If we consider that a particle is excluded from the beam after a single collision, the probability that a particle of the beam suffers an interaction between x and x+dx is proportional to I(x) and we may write

$$dP = -P(x)\sigma(E)Ndx , \qquad (2.71)$$

where P(x) is the probability density of such an occurrence which must satisfy the condition

$$\int_{0}^{\infty} P(x)dx = 1. \tag{2.72}$$

Integrating Eq. (2.71) and fixing P(x) with Eq. (2.72) leads to

$$P(x) = \sigma(E)Ne^{-\sigma(E)Nx}.$$
 (2.73)

To say that a particle suffers its first interaction at a depth x is equivalent to saying that it travels a distance x without interaction; therefore, P(x) also represents the probability of a free path equal to x, and Eq. (2.73) may serve as a distribution function of free paths. The mean free path  $\overline{\lambda}(E)$  for a particle of energy E is given by

$$\overline{\lambda}(E) = \frac{\int_{0}^{\infty} xP(x)dx}{\int_{0}^{\infty} P(x)dx} = \frac{1}{\sigma(E)N} . \tag{2.74}$$

In order to sample the distance between interactions, one can sample the distribution (2.73), which, using the relation (2.68), leads to

$$\int_{0}^{\lambda} P(x)dx = R . \qquad (2.75)$$

Since a uniform random number 1-R is equivalent to R, the distance to the next interaction can thus be determined from a random number R between 0 and 1 by the equation

$$\lambda(E) = -\overline{\lambda}(E) \ln R \quad . \tag{2.76}$$

This is a standard equation used in Monte Carlo transport codes.

Knowing that an interaction will occur at a distance  $\lambda$ , if there exists k types of interactions with the cross-section for jth interaction given by  $\sigma_j(E)$ , the probability of occurrence for an interaction of type j is given by

$$P_{j} = \frac{\sigma_{j}(E)}{\sum_{i=1}^{k} \sigma_{j}(E)} . \tag{2.77}$$

Thus during the simulation, once the position of interaction is fixed, an interaction of type *j* will occur if

$$\sum_{i=1}^{j-1} P_i < R \le \sum_{i=1}^{j} P_i \quad , \tag{2.78}$$

where R is a random number evenly distributed between 0 and 1.

# 2.3 Model for the creation of electron-hole pairs in a-Se

Our goal is to model the signal produced by x-rays in a-Se. For this we require a model relating energy deposited in a-Se to the creation of electron-hole pairs. In this section we develop such a model which we will use in subsequent sections.

As an electron traverses a medium, it may undergo elastic, radiative (bremsstrahlung), and inelastic interactions. We focus on the latter, since it is the main mechanism for the creation of electron-hole pairs. Inner-shell electrons are tightly bound to the atomic core and thus can be approximated reasonably by known cross-sections for isolated atoms. Inelastic collisions with outer-shell electrons, on the other hand, typically

involve low energy transfers and are strongly influenced by the structure of the medium.

The differential cross-section in energy transfer can be calculated by integrating Eq. (2.56) over momentum transfers to give

$$\frac{d\sigma}{d\omega} = \frac{2e^2}{h^2 N v^2 \varepsilon_0} \int_{hq_-}^{hq_+} \frac{dq}{q} \operatorname{Im} \left\{ \frac{-1}{\varepsilon(q,\omega)} \right\}. \tag{2.79}$$

In general,  $\varepsilon$  may be a tensor which depends on the direction of q. In this work it is assumed that the medium is homogeneous and isotropic so that  $\varepsilon(q,\omega)$  depends on only the magnitude of q. This assumption is consistent with the experimental work of Bell and Liang.<sup>30</sup> The quantities  $\hbar q_-$  and  $\hbar q_+$  are the minimum and maximum momentum transfers, respectively, and they are found from the relativistic energy/momentum conservation equations

$$\hbar q_{\pm} = \sqrt{2m} \left( \sqrt{E(1 + E/2mc^2)} \pm \sqrt{E(1 + E/2mc^2) - \hbar\omega(1 + E/mc^2)} \right),$$
 (2.80)

where E is the incident electron energy and  $\hbar\omega$  is the energy transferred to the medium. In Eq. (2.80) we have ignored terms of the order of  $\hbar\omega/mc^2$ . Eqs (2.80) determine the plane of all possible momentum and energy transfers to the system.

Energy transferred goes into excitation of different degrees of freedom of the medium determined by the spectrum of elementary excitations. There is a certain probability that the energy transfer goes into the creation of a single electron-hole pair. If the initial momentum of the outer-shell electron is assumed to be equal to the Fermi

momentum  $\hbar q_F$  and to be below the energy gap  $E_g$ , then energy transferred to the electron-hole pair for a given momentum transfer  $\hbar q$  is given by

$$\hbar\omega(q) - E_g = \frac{\hbar^2 (q + q_F)^2}{2m} - \frac{\hbar^2 q_F^2}{2m} \ . \tag{2.81}$$

This bounds the possible transfers for the creation of a single electron-hole pair in the energy/momentum plane by the two parabolas

$$\hbar\omega(q) - E_g = \frac{\hbar^2 q^2}{2m} \pm \frac{\hbar^2 q q_F}{m} . \qquad (2.82)$$

This electron-hole domain is shown in Fig. 2.10.

Another probable mechanism is that the energy transferred by the passing electron may induce collective oscillations of electrons in the medium, *i.e.*, plasma waves. The dispersion relation for these waves is given by<sup>31</sup>

$$\omega_p(q) = \omega_{pe} + \alpha q^2 + \dots , \qquad (2.83)$$

where  $\omega_{pe} = \sqrt{Ne^2/\varepsilon_0 m}$  is a plasma frequency, and  $\alpha = \frac{3}{5}v_F^2$ . This dispersion line is shown in Fig. 2.10. It intersects the electron-hole domain at  $\hbar q_c$ , which is determined by the relation

$$\hbar\omega_{p}(q_{c}) = E_{g} + \frac{\hbar^{2}q_{c}^{2}}{2m} + \frac{\hbar q_{c}q_{F}}{m}$$
 (2.84)

For  $q > q_c$ , the plasmon decays into a single particle excitation state. This implies that in this case a plasmon lives for a limited time  $\tau$  after it has been created. If this time

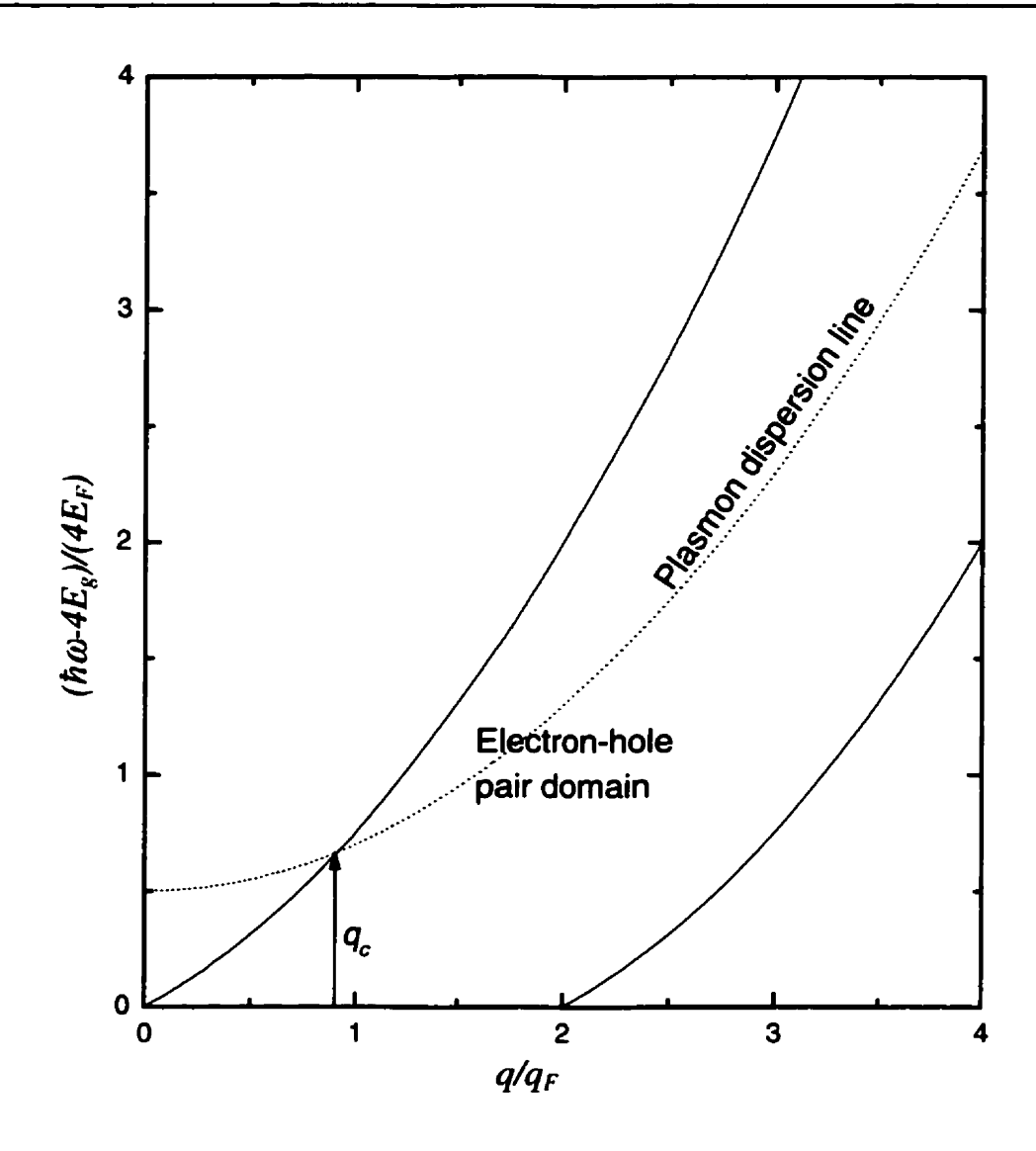


Figure 2.10: Spectrum of elementary excitations in the bulk electron gas. The plasmon dispersion line and the electron-hole pair domain are shown.

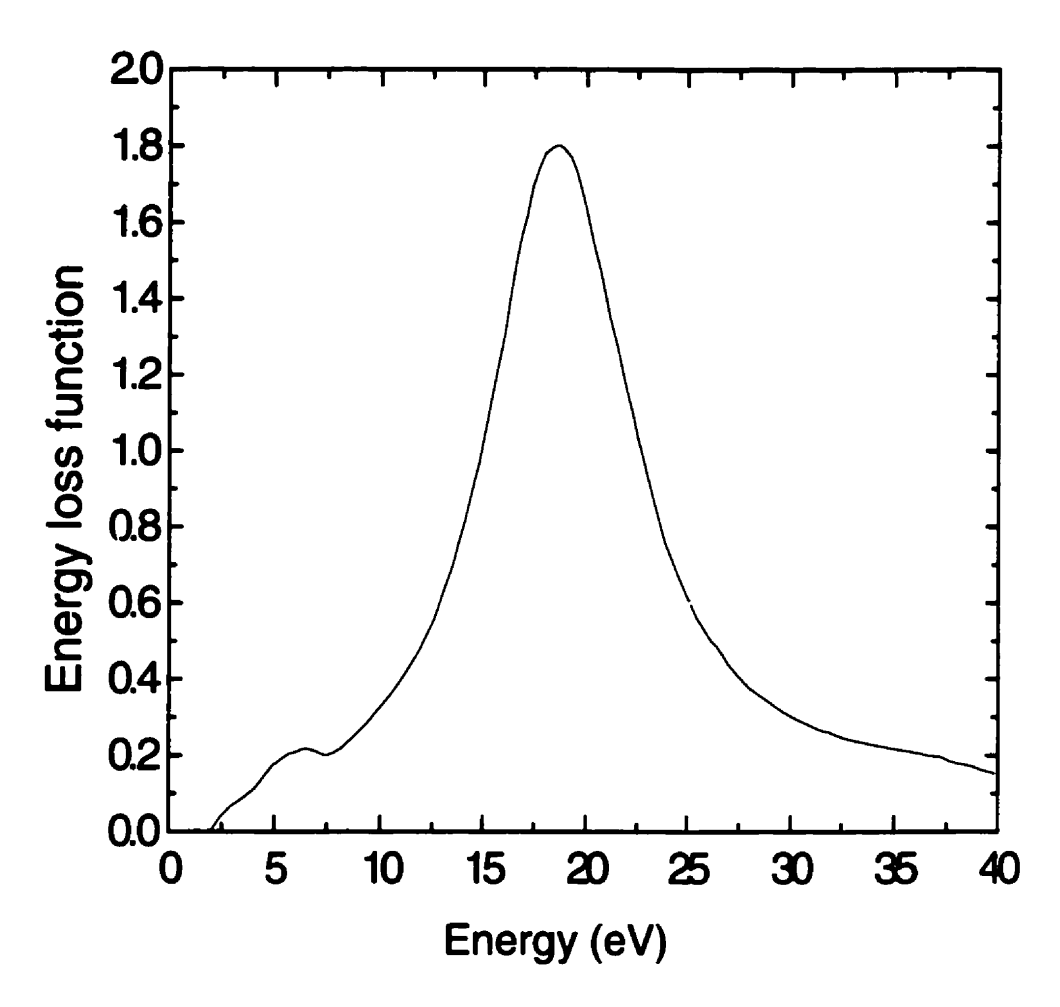


Figure 2.11: Energy loss function for a-Se, measured by Bell and Liang.<sup>29</sup>

is smaller than the characteristic oscillation time of a plasmon  $2\pi/\omega_{pe}$ , then the plasmon cannot exist as a coherent motion of all electrons in the charge cloud and it will no longer be an observable entity. On the other hand, for the  $q < q_c$  regime, the arguments presented above would predict that plasmons are undamped. Experiments, however, indicate that this is not always so and therefore sources of damping different from the single pair excitations must be invoked in order to explain the observations. Fig. 2.11 shows the experimentally measured optical  $(q \sim 0)$  energy loss function  $Im\{-1/\varepsilon(0,\omega)\}$ 

for a-Se (the data has been taken from Bell and Liang<sup>30</sup>). One can see that the energy loss function is not in the form  $\delta(\omega-\omega_{pe})$ , as it is for media in which plasma waves are undamped once created. It exhibits a spread about its peak, indicating a finite damping rate  $(\gamma-\omega_{pe}/2)$  and a finite lifetime  $(\tau-2/\omega_{pe})$  for plasma waves in this material. This indicates that in a-Se energy transfers to collective excitations are not constrained to exist along the plasmon dispersion line.

One of the sources of plasma damping is the simultaneous excitation of several electron-hole pairs. These multiparticle excitations are no longer confined to lie in the strip of the  $(q, \omega)$  plane defined by Eq. (2.82). The possibility that plasma waves decay into several (more than one) electron-hole pairs has also been qualitatively discussed by other authors.<sup>32,33</sup> Another source of damping is the interaction of the electrons with the lattice periodic potential (electron-phonon interaction), resulting in the decay of plasmons into phonons.

In the present section we will concentrate on the effect of plasmon decay into several electron-hole pairs and its manifestation in the studies of charge formation and transport in a-Se. Our goal is to obtain the n-particle excitation inelastic cross-sections and implement them in a Monte Carlo code to study the charge transport.

In the physical model presented in this work, energy/momentum transferred in inelastic collisions with outer-shell electrons goes into either the creation of a single electron-hole pair or the excitation of plasma waves. The plasma waves quickly decay into n electron-hole pairs. Since the lifetime of the plasmon is short, the whole picture looks as if the ionizing electron created n electron-hole pairs in the vicinity of the

interaction point. These pairs constitute a spur. The number n of electron-hole pairs in a given spur is a stochastic quantity which we model in terms of cross-sections for the creation of n pairs in an inelastic collision,  $\sigma_n(E)$ . To calculate these cross-sections, we must determine the regions of integration in the  $(q, \omega)$  plane for each individual n, and integrate Eq. (2.79) over the regions of interest. The integration regions can be found by considering the relation between the energy and momentum transfer to the system for the case when n electrons are excited from the Fermi surface to the conduction band. For a given n, the region of allowed excitations is bound by the lines

$$\hbar\omega = n \left( E_g + \frac{\hbar^2 q_c^2}{2m} \pm \frac{\hbar q_c q_F}{m} \right). \tag{2.85}$$

In Eq. (2.85) we have assumed that the density of electron states in the Fermi surface is large, so that the initial momenta of the electrons that are subsequently excited into the conduction band are close to the Fermi momentum  $\hbar q_F$  (the number of the excited particles is much smaller than the number of the electrons in the Fermi surface). Eq. (2.85) together with Eq. (2.80) constitutes the domains of the *n*-particle excitations allowed in the system. Fig. 2.12 shows the dispersion relation diagram for the *n*-particle excitation domains. The domain above the single-particle excitation state (plasmon domain) is split into subdomains for the *n*-particle excitation states. In general, there exists overlapping between different domains, *i.e.*, the single electron-hole domain contains part of the two-particle excitation domain, the two-particle excitation domain

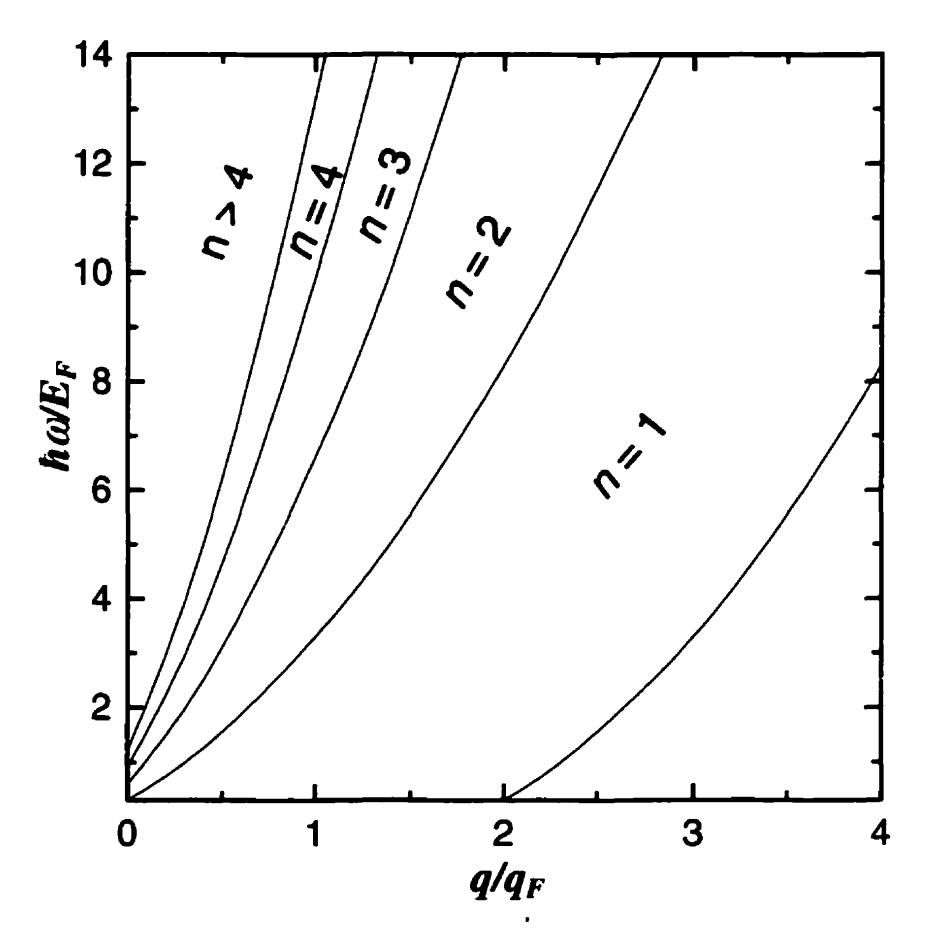


Figure 2.12: The n-particle excitation domains. Regions from n=1 to 4 are explicitly shown on the graph whereas the other regions (n>4) are grouped together for clarity.

contains part of the three-particle excitation, etc. As a first approximation we shall neglect the effect of overlapping in the calculation of the cross-sections.

# 2.4 Calculation of inelastic cross-sections

Having identified the integration regions, we can proceed to calculate the *n*-particle excitation cross-sections. Eq. (2.79) contains the energy loss function  $Im\{-1/\varepsilon(q,\omega)\}$ . As discussed in Section 2.2.3.2, the optical data, shown in Fig. 2.11,

only gives us the long wavelength response of the medium. The extension of the energy loss function to q>0 from the optical limit is made using Ashley's approximation given by Eq. (2.58). To simplify the integration in Eq. (2.79) we map the  $(q,\omega)$  plane into the (B,T) plane, using the transformation  $\hbar^2q^2/2m = T - B$  and  $T = \hbar\omega$ . The *n*-particle cumulative inelastic cross-section for all energy transfers up to  $T = T^-$  can be found by substituting Eq. (2.58) into Eq. (2.79) and reversing the order of integration, leading to

$$\sigma_n(E,T) = \int_0^T dT' \frac{d\sigma}{dT'} = \chi \int_0^T dT' \int_0^{B_1} dB f(B) g(T',B) , \qquad (2.86)$$

where  $\chi = 2\pi r_e^2 mc^2 / \beta^2$ ,  $\beta = v/c$ ,

$$g(T',B) = \frac{1}{T'(T'-B)}$$
, (2.87)

and f(B) is the dipole oscillator strength distribution, which is related to the energy loss function by

$$f(B/\hbar) = \frac{2m}{h^2 N(e^2/4\pi\varepsilon_0)} B \operatorname{Im} \left\{ \frac{-1}{\varepsilon(0, B/\hbar)} \right\}, \qquad (2.88)$$

which is simply the optical limit of Eq. (2.55). The integration regions for *n*-particle excitation states in the new (B,T) plane are shown in Fig. (2.13) and for a given *n* are defined by the equation

$$B_n = \frac{\sqrt{\beta^2 - 4\alpha\gamma - \beta}}{2\gamma} , \qquad (2.89)$$

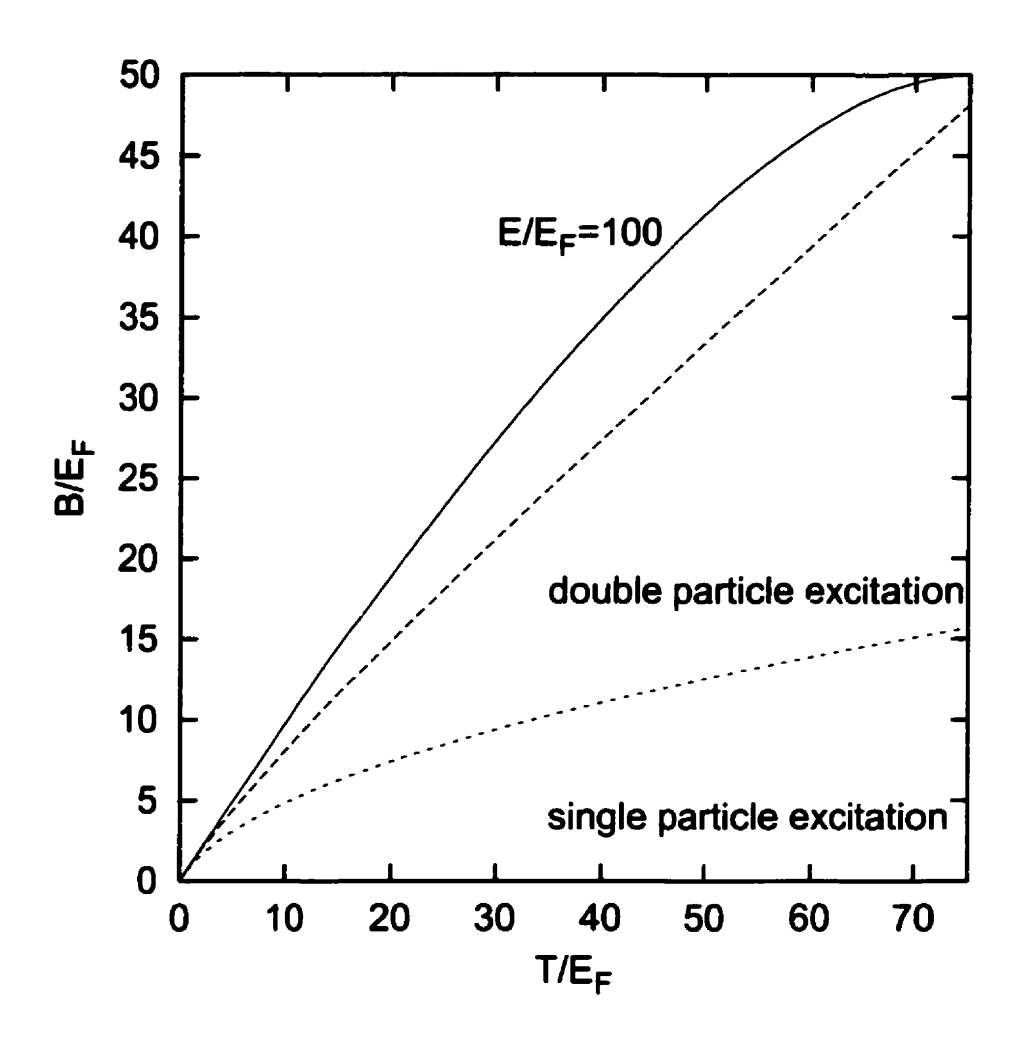


Figure 2.13: The n-particle excitation states in the (B,T) plane, for n=1 (single particle) and n=2 (double particle). The solid line represents the energy-momentum conservation equation.

where 
$$\alpha = n^2$$
,  $\beta = 2n[n(2E_F - E_{gap} - T) + T]$  and  $\delta = (T(1-n) - nE_{gap})^2 - 4n^2E_FT$ .

Eq. (2.86) requires knowledge of the oscillator strength up to high energies, while the energy loss function data of Bell and Liang<sup>30</sup> extends only up to 40 eV. For high energies, however, the atoms can be approximated as independent and therefore the dipole strength at these energies is independent of the state of the material. It can thus be

calculated from the photoelectric cross-section for isolated atoms using Eq. (2.59). For energies greater than 100 eV, we use the outer-shell photoelectric data from EPDL<sup>16</sup> to calculate the oscillator strength distribution. Below ~100 eV,  $f(\omega)$  will begin to be affected by the amorphous state and cross-sections of independent atoms will no longer be accurate. Note that we do not include the inner-shell photoelectric cross-sections in the calculation, since we are concerned only with outer shell electrons. In order to bridge the gap between 40 eV and 100 eV, we follow the procedure of Laverne and Pimblott<sup>34</sup> and interpolate the data sets with an inverse power law. For consistency, we check that our constructed oscillator strength data satisfies Bethe's sum rule, Eq. (2.38). For this, however, we need the total dipole strength  $f_{int}(\omega)$  which includes not only the outer-shell electrons but the inner-shell electrons as well. This is accomplished by using the innershell photoelectric effect cross-sections from EPDL. Integration yields a value of 34.2, which we deem satisfactorily close to the atomic number of a-Se, i.e. Z = 34. We also integrate the oscillator strength distribution for the outer electrons and obtain a value of 6.02 which is surprisingly close to the number of outer electrons ( $Z_{outer} = 6$ ).

Having constructed the dipole oscillator strength, we are now in a position to integrate over each region of the (B,T) plane, corresponding to the appropriate n. Integration is carried out numerically with a computer algorithm. The resulting crosssections  $\sigma_n(E)$  for the creation of n electron-hole pairs in an inelastic collision by an ionizing electron with a-Se are shown in Fig. 2.14 for various n. With increasing electron

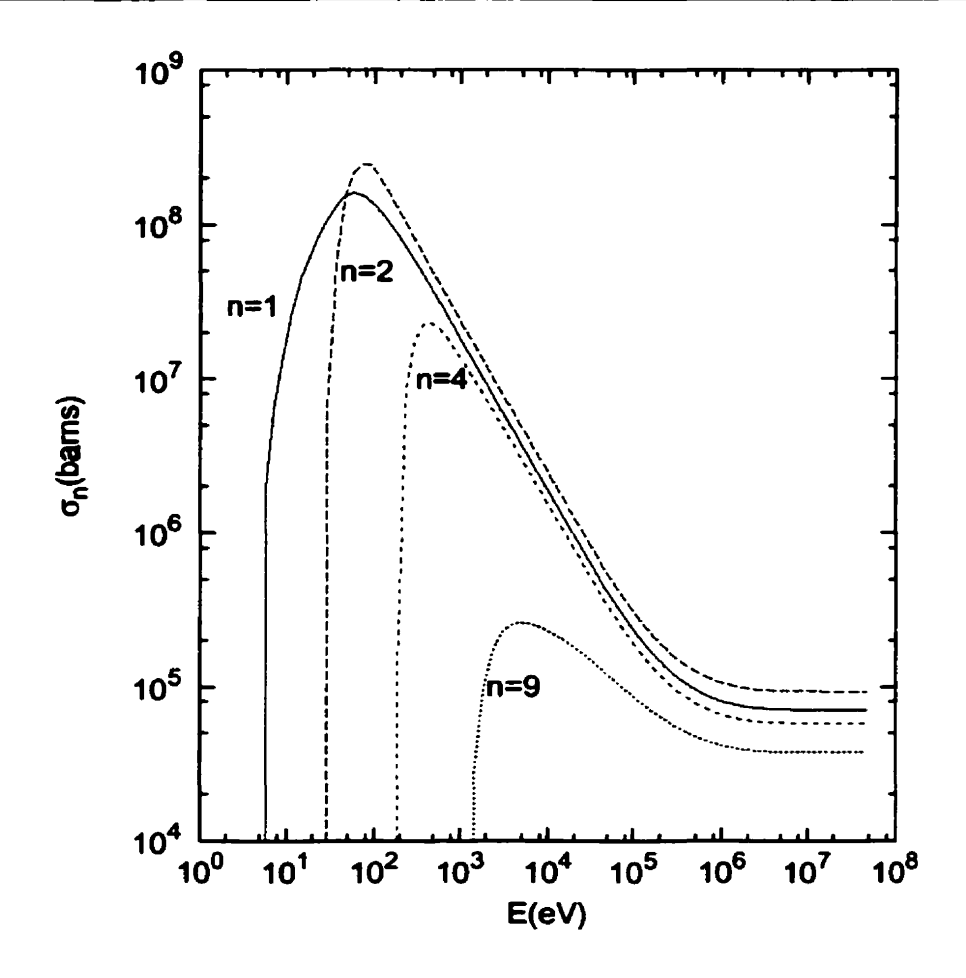


Figure 2.14: The calculated n-particle inelastic cross sections versus electron energy.

energy the possibility of creating n > 1 electron-hole pairs increases. For this reason, since an ionizing electron loses kinetic energy along its path, it has a greater probability of creating more electron-hole pairs in a given spur at the beginning of its track than at the end of its track. The total inelastic cross-section, summed over all n, is shown in Fig. 2.15. Also shown for comparison are the inelastic cross-sections for isolated atoms taken from the EEDL database. Agreement is excellent above about 100 eV, since at

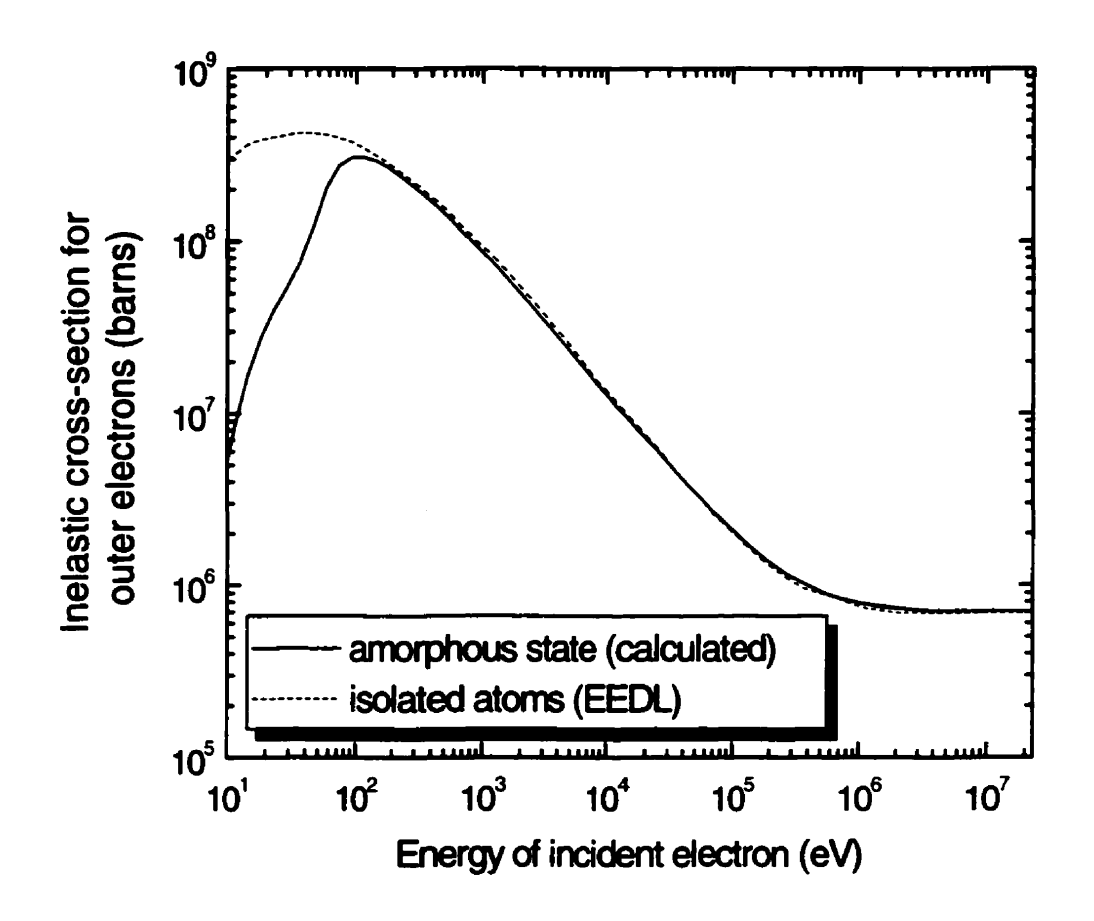


Figure 2.15: The calculated inelastic cross sections versus electron energy for a-Se compared to the cross-sections taken from the EEDL database<sup>19</sup> for isolated Se atoms.

these energies the physical state does not strongly affect the interactions. The normalized cumulative n-particle cross-sections  $Y_n(E,T)$  versus energy transfer T, defined as

$$Y_n(E,T) = \frac{\sigma_n(E,T)}{\sigma_n(E)} , \qquad (2.90)$$

are shown in Fig. 2.16 for some representative values of n, and for an incident electron energy of 10 keV. We have found the Y-distributions are relatively insensitive to the electron energy.

A question which needs to be addressed is the initial size of a spur. Obviously, energy transferred to the system is not concentrated at one point. One way to approach this problem is as follows.<sup>32</sup> From the viewpoint of the outer atomic electrons, a passing charged particle constitutes an electrical impulse. The duration of the impulse increases with distance r from the particle trajectory as r/v, where v is the charged particle velocity. When the pulse duration becomes much longer than the response time of the bound outer shell electrons ( $\sim 1/\omega_{pe}$ ), then these electrons follow the electrical field adiabatically. In this case the medium merely polarizes under the influence of the charged particle with negligible energy absorption. The resonant condition  $r = v/\omega_{pe}$ , Bohr's adiabatic criterion,<sup>35</sup> determines the distance of maximum energy deposition from the path of the ionizing particle. This region constitutes the spur core, which increases with increasing velocity of the ionizing electron. Qualitatively, this effect would lead to an escape efficiency  $\eta$  which increases with the energy of the ionizing electron.

Electron-hole pairs created in the spur core lose their initial kinetic energy in a thermalization process, after which they are separated by a finite distance  $r_0$ . This

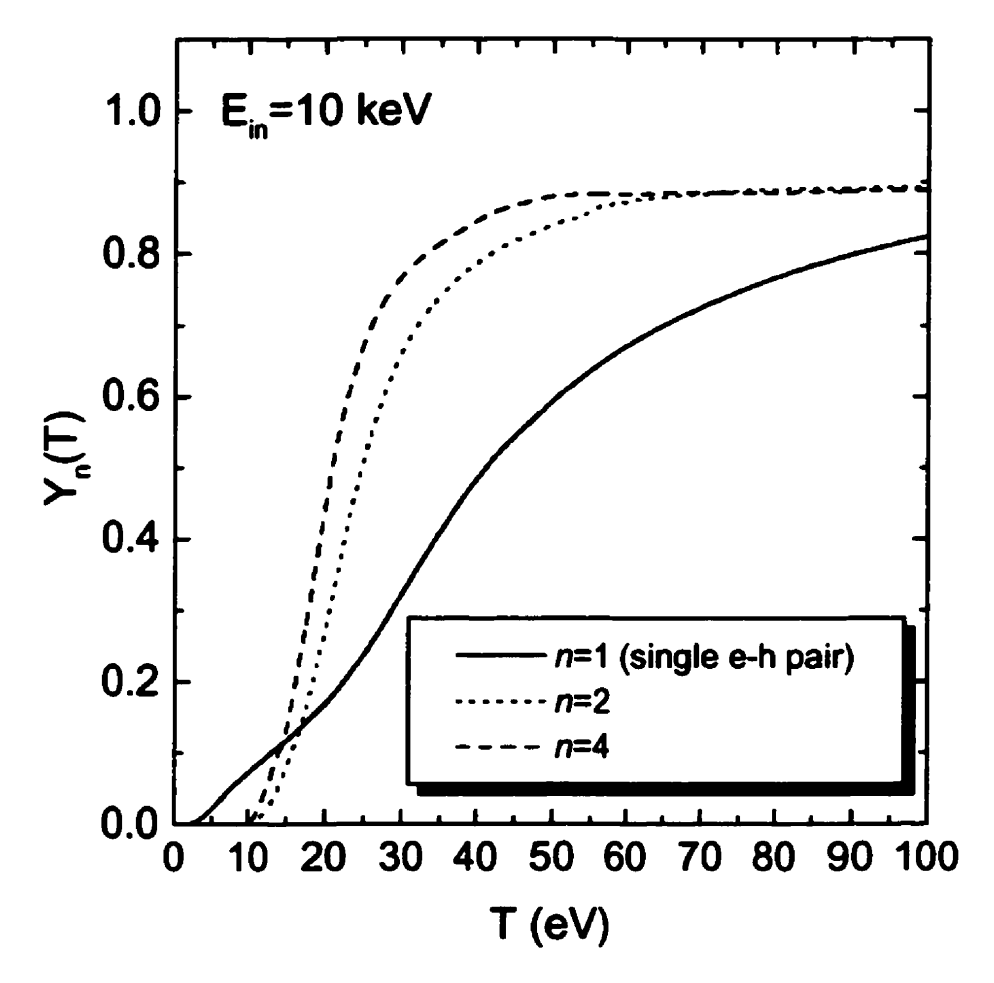


Figure 2.16: The calculated Y-distributions, i.e., cumulative cross-sections as a function of energy transfer T normalized to the total cross-section for the creation of n electron-hole pairs in the inelastic cross section of an electron with a-Se.

distance can be estimated for a given initial kinetic energy using the Knights and Davis equation (Eq. (2.3)). We define the *spur size* as the spur core size plus the thermalization distance  $r_0$ . In the next section we model the physics described in this section using Monte Carlo techniques to calculate the escape efficiency  $\eta$  and the pair creation energy  $W_{\pm}$ .

# 2.5 Determination of track structure

In order to calculate the recombination of electron-hole pairs, we first need to determine the track structure in a-Se. Standard Monte Carlo transport codes such as EGSnrc<sup>22</sup> can not be used for this purpose, since they do not follow individual collisions. We have thus developed our own *single-collision* Monte Carlo code for the transport of photons, electrons and positrons in a-Se, which we now describe.

To simulate particle transport, we need a way to keep track of the direction each particle is travelling. Consider a particle with energy E and velocity v in a fixed cartesian frame of reference with axes (x,y,z), shown in Fig. 2.17. We characterize the direction of its trajectory by direction cosines which are defined by

$$u = \sin \theta \cos \phi ,$$

$$v = \sin \theta \sin \phi ,$$

$$w = \cos \phi ,$$
(2.91)

where  $\theta$  and  $\phi$  are the angles in spherical polar coordinates relative to the (x,y,z) axes. Consider that the particle being transported interacts at a point M with an atom in the medium. Following the interaction, the incident particle will have a new direction defined by a velocity  $\mathbf{v}_1$ , and a secondary particle may be created with a velocity  $\mathbf{v}_2$ . Let  $\theta$  and  $\theta$  be the angles that  $\mathbf{v}_1$  and  $\mathbf{v}_2$  make with  $\mathbf{v}_2$ , and  $\mathbf{v}_3$  and  $\mathbf{v}_4$  and  $\mathbf{v}_5$  make on a plane perpendicular to  $\mathbf{v}_4$  (referenced to an arbitrary angle). The

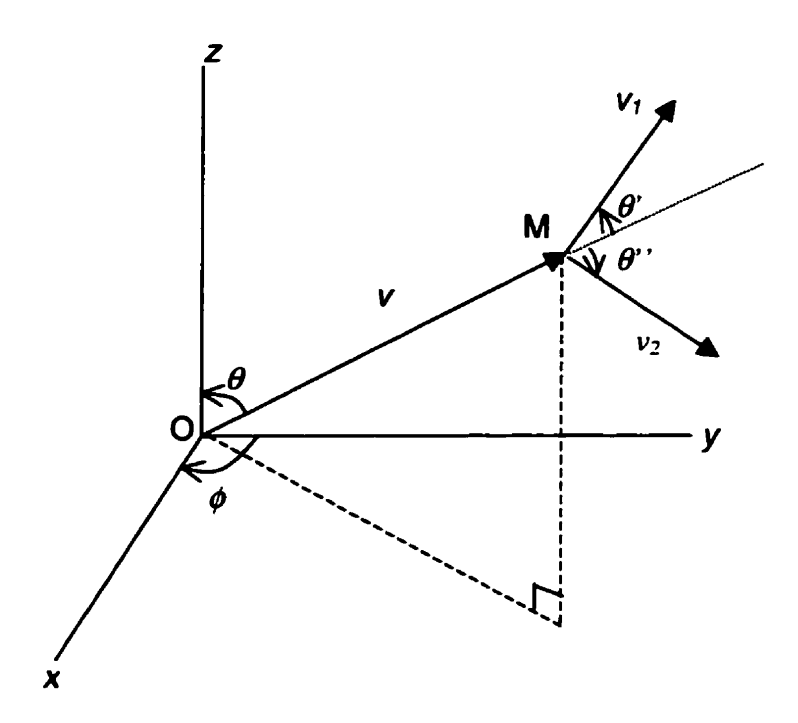


Figure 2.17: Coordinate system used in Monte Carlo transport code.

angles  $\phi'$  and  $\phi''$  are the azimuthal deflections and are in general evenly distributed between 0 and  $2\pi$ .

The new particle directions, referenced in the frame of the incident particle, must be referenced back to the (x,y,z) frame. Using rotation matrices, one can show that the new angles which characterize the velocities  $\mathbf{v}_1$  and  $\mathbf{v}_2$ , given in the frame of reference (x,y,z), are given by

$$\cos \theta_{1} = \cos \theta \cos \theta' - \sin \theta \sin \theta' \cos \phi$$

$$\cos \phi_{1} = \frac{\cos \phi(\sin \theta' \cos \phi' \cos \theta + \sin \theta \cos \theta') - \sin \theta' \sin \phi' \sin \phi}{\sin \theta_{1}}$$
(2.92)

and

$$\cos \theta_2 = \cos \theta \cos \theta'' - \sin \theta \sin \theta'' \cos \phi''$$

$$\cos \phi_2 = \frac{\cos \phi(\sin \theta'' \cos \phi'' \cos \theta + \sin \theta \cos \theta'') - \sin \theta'' \sin \phi'' \sin \phi}{\sin \theta_2}$$
 (2.93)

The direction cosines of  $v_1$  and  $v_2$  then become

$$u_1 = \sin \theta_1 \cos \phi_1 ,$$

$$v_1 = \sin \theta_1 \sin \phi_1 ,$$

$$w_1 = \cos \phi_1 ,$$
(2.94)

and

$$u_2 = \sin \theta_2 \cos \phi_2 ,$$

$$v_2 = \sin \theta_2 \sin \phi_2 ,$$

$$v_3 = \cos \phi_2 .$$
(2.95)

We have chosen to write our transport code in the C programming language to take advantage of speed and flexible memory management. The geometry is taken to be a Copper layer (optional) above an a-Se layer, both of variable thickness. We use a linked list structure to keep track of the particles. A linked list is a set of nodes in memory which is linked together with pointers. Each node represents a particle, and holds the particle's parameters: its charge Q (0 for photons, -1 for electrons, 1 for positrons), its kinetic energy E, its x, y, and z positions, and its direction cosines u, v and w. We have used this structure because the links can be created and destroyed, depending on how many particles are being followed at any given time, which saves space in memory.

We begin a particle history by creating an incident photon or electron with a specific energy E. We then interpolate from tables of the total interaction cross-sections

for the given energy and type of particle, and for the given medium (a-Se or Cu). These cross-sections are assumed to be the same as for isolated atoms, and are taken from the EPDL and EEDL databases, with the exception of inelastic collisions with outer-shell electrons for a-Se. In the latter case our calculated results are used (see Fig. 2.15). We calculate the mean free path from the total cross-section using Eq. (2.74), and sample the distance to the next interaction  $\lambda$  using Eq. (2.76).

If the free path  $\lambda$  is larger than the distance d to the closest interface (e.g., Cu/a-Se interface) along the path of the particle, then  $\lambda$  is replaced by  $\lambda = d$ . We then change the coordinates of the particle from its original location (x, y, z) to (x', y', z') given by

$$x' = x + \lambda u ,$$

$$y' = y + \lambda v ,$$

$$z' = z + \lambda w .$$
(2.96)

The next step is to determine which type of interaction is to occur. This is done by sampling a uniform random number and using Eq. (2.78). Depending on the type of interaction chosen, one of the following then occurs:

#### a) coherent interaction

The angular differential cross-section of Eq. (2.8) is integrated and inverted. The Form Factor data is interpolated from tables taken from the Evaluated Atomic Data Library (EADL). A uniform pseudo-random number R is generated and the corresponding scattering angle is calculated through Eq. (2.69). The direction cosines of the photon are updated to reflect this change using Eqs. (2.92) and (2.94).

#### b) incoherent interaction

The photon scattering angle is sampled similarly to coherent interactions except Eq. (2.13) is used instead. The atomic scatter function values are taken from the EADL database. The kinetic energy and angle of the Compton electron are calculated by Eqs (2.11) and (2.12), respectively. A new node is added to the end of the linked list reflecting the creation of the secondary electron. The direction cosines of this new electron are calculated from the electron scattering angle using Eqs. (2.93) and (2.95), and the direction cosines of the original photon are changed using the photon scattering angle along with Eqs. (2.92) and (2.94).

### c) photoelectric effect

The subshell of interaction is first determined by sampling the subshell cross-sections, taken from EPDL (see Fig. 2.15). The photon is then removed from the linked list and a new node is added to account for the creation of the photoelectron. The kinetic energy of the photoelectron is equal to that of the incident photon minus the binding energy of the subshell in question. As is common practice in most Monte Carlo transport codes, the angular distribution of the photoelectron is ignored; its direction is assumed to be the same as that of the incident photon.

## d) pair production

The kinetic energy and angles of the electron and positron are sampled using an algorithm described in the EGSnrc manual.<sup>22</sup> The photon is removed from the linked list and nodes are created for the new electron and positron. The scattering angles are used to find the new direction vectors using Eqs. (2.93) and (2.95).

#### e) Elastic collision

Elastic collisions are treated the same as coherent interactions except that the angular distribution is taken from tables provided in the EEDL database.

#### f) Inelastic collisions with inner-shell electrons

The subshell is determined by sampling the individual subshell cross-sections, taken from EEDL.<sup>19</sup> The differential cross-sections in terms of kinetic energy for the appropriate subshell and electron energy are read in from data tables taken from EEDL. Cumulative distributions are constructed from this data and inverted, and a random number is generated to sample the kinetic energy K from these distributions. A new node is added to the end of the linked list reflecting the creation of the secondary electron. The scattering angles of the incident and secondary electrons,  $\theta$  and  $\theta$ , are calculated using classical mechanics:

$$\cos^2 \theta = \frac{(E - T)(E + 2mc^2)}{2E + (E - T)E} , \qquad (2.97)$$

$$\cos^2 \theta' = \frac{2T + TE}{2E + TE} , \qquad (2.98)$$

which is an adequate approximation, if the incident electron energy is much larger than the velocities of the target electrons. The direction cosines of the new electron are calculated from  $\theta$  using Eqs. (2.93) and (2.95), and the new direction cosines of the original electron are calculated from  $\theta$ ' using Eqs. (2.92) and (2.94).

## g) Inelastic collisions with outer-shell electrons

We only distinguish between outer and inner shell collisions for the a-Se layer. For the Cu layer we treat all subshells as described above in f). When an inelastic collision with the outer shell in a-Se occurs, we sample the cross sections for n-particle excitation for the given electron energy E (see Fig. 2.14) to determine the number of electron-hole pairs generated at the interaction site. We subsequently sample the energy T transferred to the medium from the cumulative cross sections (see Fig. 2.16). This kinetic energy is assumed to be equally distributed among the n electron-hole pairs. The direction of the ionizing electron is assumed to remain unchanged, since energy transfers are typically small (about 20 eV).

The thermalization distance is calculated using the Knights and Davis equation (Eq. (2.3)). For the spur core, we assume a Gaussian distribution with a full width at half-maximum given by  $r = \gamma v/\omega_{pe}$ , where  $\gamma$  is a parameter we have introduced to obtain agreement with experimental data. The parameter is required because Bohr's adiabatic criterion is only an approximate length scale. In our simulations, we use a value of

 $\gamma$ =1.6. The positions of the electron-hole pairs are recorded in a file so that they may be used later to study recombination.

#### h) Bremsstrahlung

We neglect bremsstrahlung in our simulations, since, as can be seen in Fig. 2.4, its cross-section is very small for a-Se.

#### i) Annihilation

If a positron undergoes annihilation, then Eq. (2.40) is used to sample the cross-section using an algorithm developed for EGSnrc.<sup>22</sup> The angle of emission of one of the photons is randomly sampled in the full  $4\pi$  solid angle, and the second photon is sent in the opposite direction. The incident positron is removed from the linked list and two nodes are added to accommodate the newly created photons.

After an ionization event, radiative and nonradiative probabilities are sampled from probabilities provided in the EADL database.<sup>18</sup> This is repeated in a recursive fashion until the vacancy reaches the outer shell. The photons and electrons created by these transitions are sent in a direction sampled from an isotropic distribution.

We follow all photons, electrons, and positrons until they reach a cut-off energy  $E_{cut}$ . We use a value of  $E_{cut} = 50$  eV, since Eq. (2.37) for the inelastic cross section is derived in the first Born approximation. We found that this particular energy was a threshold value above which the simulation results did not vary substantially. Another

reason for introducing the cutoff energy is the possible inelastic collisions of low energy electrons with phonons, the physics of which is not well understood for amorphous materials. As the electron's kinetic energy falls beyond the cutoff energy, the electron is removed from the simulation.

For each inelastic outer-shell collision we record the energy deposited  $E_{dep}$  and the number of pairs created n, and calculate  $W_0 = E_{dep} / n$ . After averaging over many histories, the simulated energy required to create an electron-hole pair was found to be  $W_0 \approx 4.8 \, \text{eV}$ , which lies within the range of accepted values of 4-7 eV. Figs. 2.18 and 2.19 show typical track structures for a 50 keV and 1 MeV electron traversing the a-Se detector, respectively. The spur core size, averaged over the track structures, is plotted versus incident photon energy in Fig. 2.20 for an a-Se thickness of 150  $\mu$ m. As the photon energy increases, the average size of the core is seen to increase due to the higher kinetic energies of the secondary ionizing electrons produced by the primary photons. As shown in Fig. 2.21, the number of pairs in a spur, averaged over the track structures, increases only mildly with the incident photon energy over the range of energies shown.

# 2.6 Determination of escape efficiency $\eta$

Once the initial positions of the electron-hole pairs are found for a large number of particle histories, the subsequent motion of the pairs must be known in order to determine the amount of recombination. In essence, the Onsager model, which describes a two-body problem, must be extended to a 2N-body problem, where N is the number of pairs created along the track. The differential equation governing the motion is given by

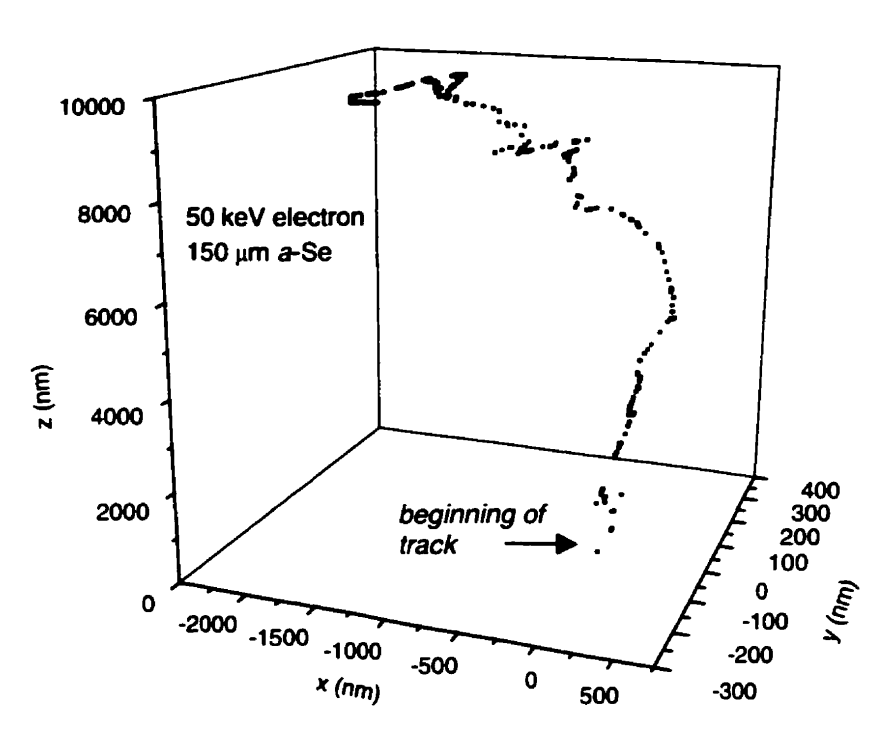


Figure 2.18: Typical track structure for a 50 keV electron in a-Se.

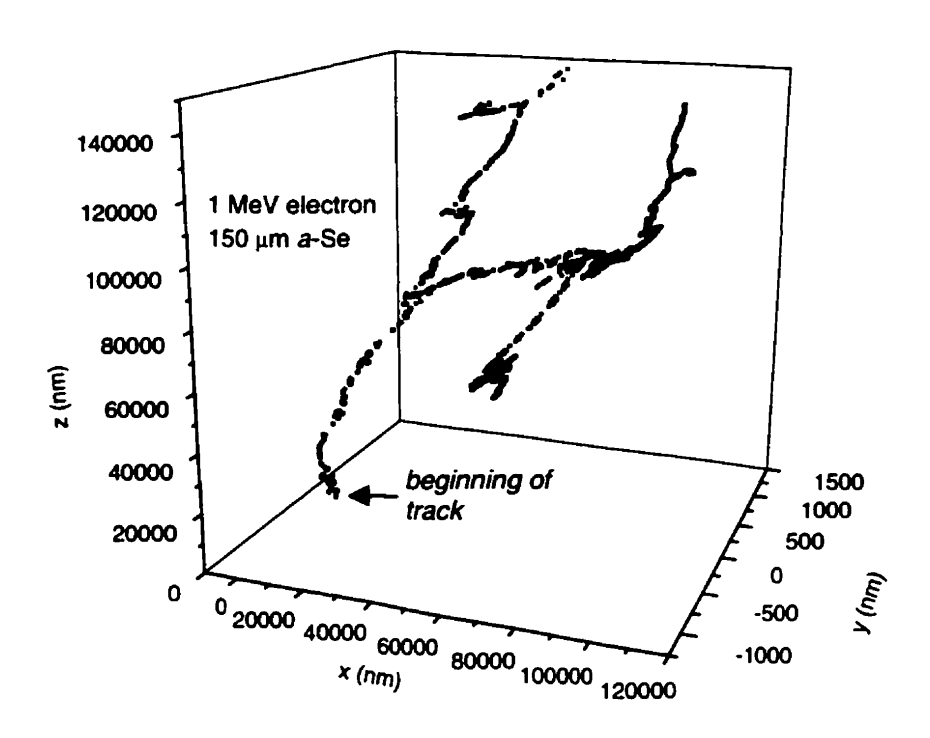


Figure 2.19: Typical track structure for a 1 MeV electron in a-Se.

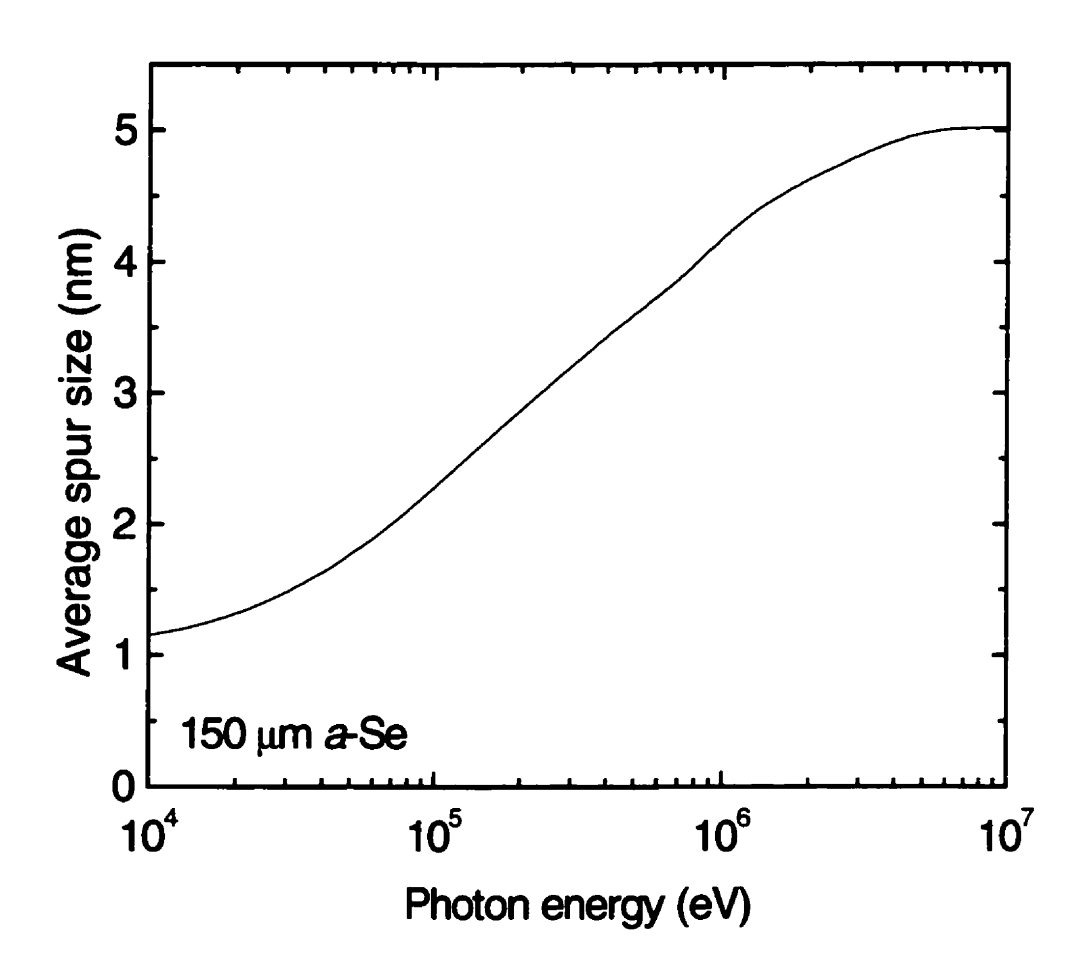


Figure 2.20: Average spur size versus photon energy. The a-Se thickness is 150  $\mu m$ .

$$\frac{\partial P_i^{\pm}}{\partial t} = \pm \mu_{\pm} E_i \cdot \nabla P_i^{\pm} + D_{\pm} \nabla^2 P_i^{\pm} \quad , \quad i = 1..2N$$
 (2.99)

where  $P^{\pm}(r,t)$  is the probability that the  $i^{th}$  carrier is found at a position r at a time t (the  $\pm$  referring to the carrier's charge),  $\mu_{\pm}$  is the mobility of the  $i^{th}$  carrier, and  $D_{\pm}$  is its diffusion constant which can be assumed related to the mobility through Eq. (2.5). The electric field is given by the sum of the applied field and the self-consistent Coulomb field due to the rest of the carriers, *i.e.*,

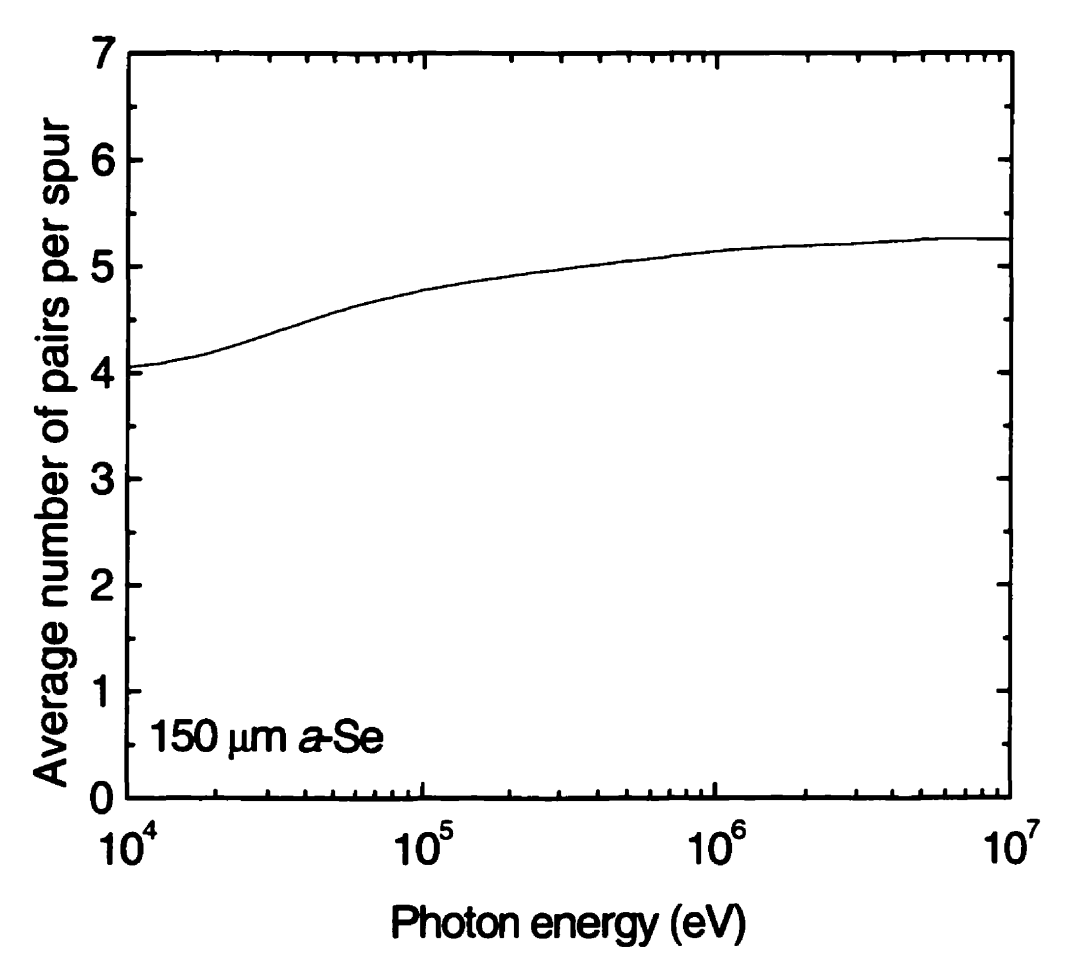


Figure 2.21: Average number of pairs per spur versus photon energy. The a-Se thickness is 150  $\mu$ m.

$$\boldsymbol{E}_{i} = \boldsymbol{E}_{app} + \sum_{j \neq i} \frac{1}{4\pi\varepsilon\varepsilon_{0}} \frac{q_{j}}{r_{ij}^{2}} \hat{\boldsymbol{r}}_{ij} . \qquad (2.100)$$

The mobilities for electrons and holes in a-Se have been measured to be  $3\times10^{-3}$  cm<sup>2</sup>/(Vs) and 0.12 cm<sup>2</sup>/(Vs), respectively, <sup>13</sup> and to be dominated by the presence of shallow traps.

Eq. (2.99) consists of 2N partial differential equations which are coupled by the presence of the self-consistent field. The initial conditions are determined by the track

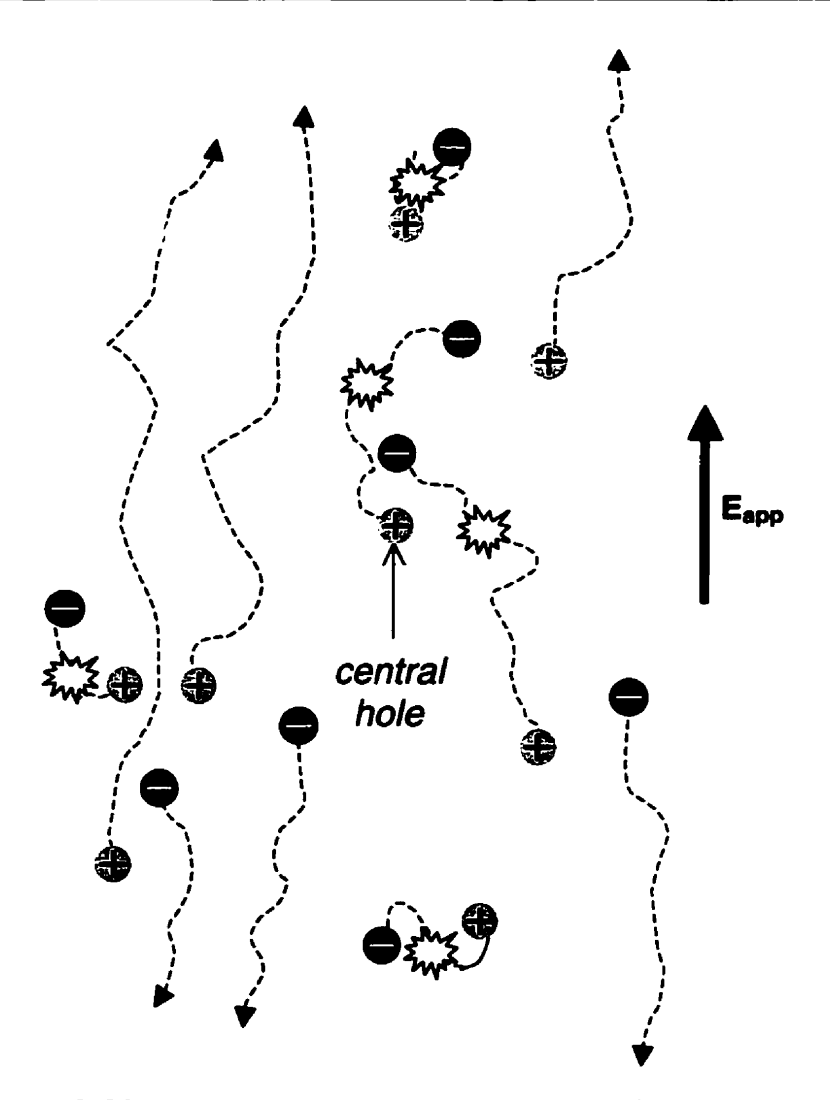


Figure 2.22: Schematic diagram describing an example of transport, recombination and escape of electron-hole pairs to calculate the escape efficiency.

structures calculated in Section 2.5. We solve for the escape fraction using a computer simulation code similar to a technique previously used in radiation chemistry.<sup>36</sup> The code, written in the C programming language, works as described below. A schematic diagram is shown in Fig. 2.22.

We initially place electrons and holes at locations along a particular track structure (for a given photon energy and metal/a-Se thickness). The trajectory of each charge is subdivided into discrete time steps  $\Delta t$ . For each step, the displacement is calculated by taking into account the Coulomb field due to the other charges, the applied field, and the random diffusion.

A cartesian coordinate system is used for the transport, with the applied field in the z-direction. The electric field is determined by adding the applied field and the Coulomb fields due to all the other particles. The displacements are then calculated by

$$\Delta x_{drift} = \mu_i E_{r,i} \Delta t , \qquad (2.101)$$

where  $\mu_i$  is the mobility of the  $i^{th}$  particle, and  $E_{x,i}$  is the x component of the self-consistent field; the displacement in the y- and z-directions are calculated in a similar fashion. The diffusion components  $\Delta x_{diff}$ ,  $\Delta y_{diff}$ , and  $\Delta z_{diff}$  must be sampled from a distribution which represents the physical properties of diffusion. Only the mean and variance of the displacement distribution are important when averaged over a large number of histories. The displacements are thus sampled from a uniform distribution between the limits  $-L_i$  and  $+L_i$ . In order to fix the standard deviation, the value of  $L_i$  is given by

$$L_i = \sqrt{6D_i \Delta t} \quad , \tag{2.102}$$

where  $D_i$  is the diffusion constant of the  $i^{th}$  particle. The total displacement in the x-direction in time  $\Delta t$  is then given by

$$\Delta x = \Delta x_{drift} + \Delta x_{diff} \tag{2.103}$$

and similarly for the other directions.

The displacements are calculated for each particle, and particles are discarded along the way if l) they approach a charge of opposite sign within a distance a, called the recombination radius, in which case both particles are counted as having recombined, or 2) the central hole is a distance of at least  $R_{min}$  away from all of the other negative charges. If the central hole recombines or escapes, the history is terminated. If it has recombined, the escape efficiency for the history is given a value of 0, and if it has escaped it is given a value of 1. The escape efficiency is averaged over at least  $10^4$  histories, to obtain a standard deviation within 5%. This took approximately 4 hours for a given energy and electric field.

Since our simulation code is an extension of the Onsager formula, we verified that it agrees with Eq. (2.7) for the case of a single initial electron-hole pair. We place this pair with a distance  $r_0$  at a random direction relative to the electric field. The simulation results are shown in Fig. 2.23 as a function of electric field for various  $r_0$  and temperatures T. The simulations are seen to fit the Onsager theory within the statistical uncertainties, which gives credence to our results. A recombination radius a of 1 nm, a distance  $R_{min}$  of 100 nm, and a time interval  $\Delta t$  of  $1 \times 10^{-16}$  s were sufficient in the one-pair simulations, and we therefore used these values in the multi-pair simulations as well.

We ran simulations for various a-Se thicknesses in the absence of a front Cu plate. Results for  $W_{\pm} = W_0 / \eta$ , where  $W_0$  was taken from our simulations to be 4.8 eV,

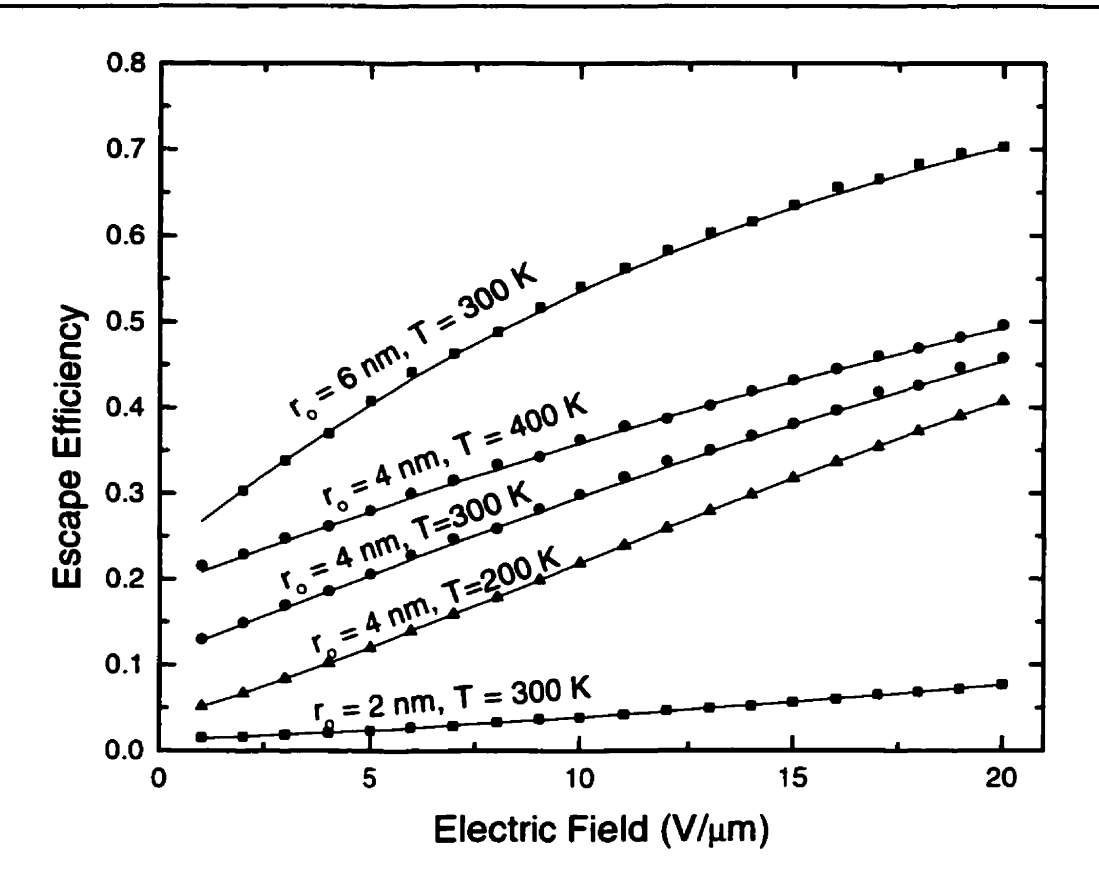


Figure 2.23: Comparison of recombination code(points) for the special case of a single electron-hole pair compared to the Onsager formula (lines).

are shown in Fig. 2.24 for three photon energies (40 keV, 140 keV and 1.25 MeV) along with the experimental data points measured by Mah et al<sup>13</sup> (Co-60) and by Blevis et al<sup>6</sup> (40 and 140 keV). As one can see, there is a good agreement between the theoretical and experimental values within uncertainties. As previously discussed, the electric field dependence is due to the fact that more particles will escape recombination with increased electric field, which will lead to higher  $\eta$  and lower  $W_{\pm}$ . The scaling with electric field, however, depends on both the number of electron-hole pairs and their spatial distribution within a spur. The dependence of  $W_{\pm}$  on electron energy, for an

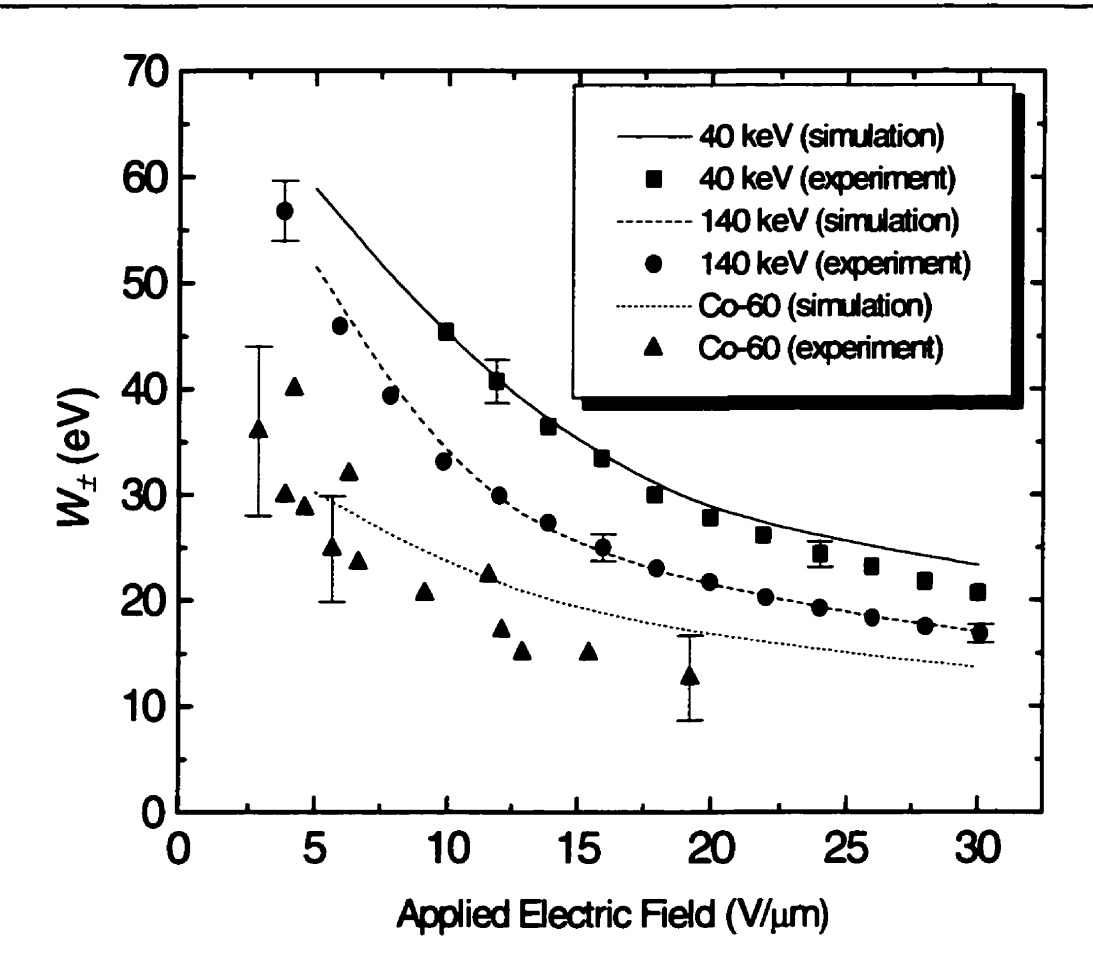


Figure 2.24: The dependence of  $W_{\pm}$  on applied electric field along with experimental values measured by Blevis et al<sup>6</sup> and Mah et al.<sup>13</sup> The thickness of the a-Se layer is 150  $\mu$ m for the 40 and 140 keV photons, and 50  $\mu$ m for the 1.25 MeV (Co-60) photons.

applied electric field of 10 V/ $\mu$ m, is shown in Fig. 2.25.  $W_{\pm}$  is seen to decrease with increasing energy and to reach a plateau at approximately 600 keV. The energy dependence is due to the fact that the spur size is proportional to the electron velocity v. As the spur size increases, electron-hole pairs are farther apart on average, resulting in less recombination and a correspondingly lower  $W_{\pm}$ . The plateau arises because v saturates at relativistic energies.

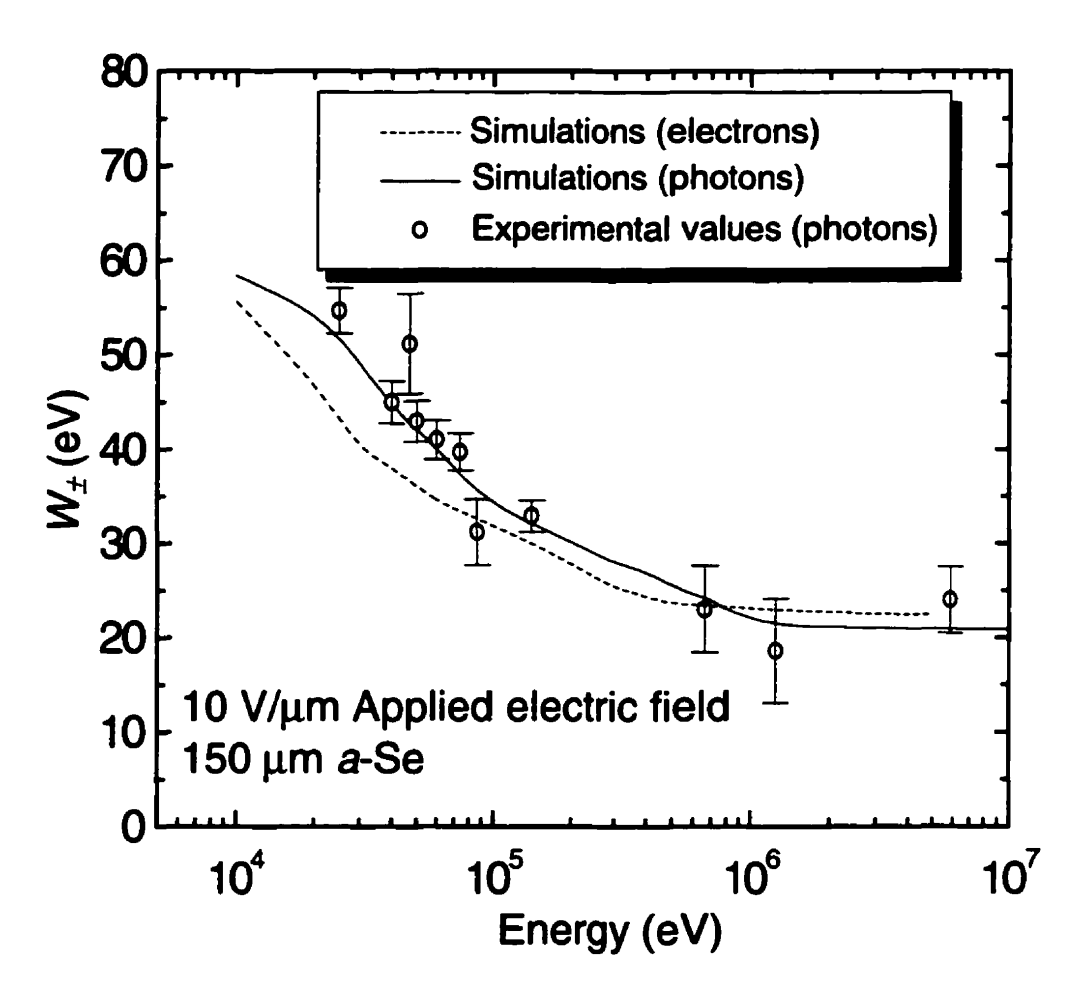


Figure 2.25: The energy dependence of  $W_{\pm}$  for photons (solid curve) and electrons (dashed curve). Also shown are experimental measurements by Blevis et al<sup>6</sup> and Mah et al<sup>13</sup> The thickness of the a-Se layer is 150  $\mu$ m, and the applied electric field is 10  $V/\mu$ m.

In Fig. 2.25 we also show the dependence of  $W_{\pm}$  on photon energy. The trend is similar to that of electrons, except that  $W_{\pm}$  is higher and the plateau is reached at about 1 MeV instead of 600 keV. This occurs because the ionizing secondary electrons are of lower energy than their parent photons. Also shown in Fig. 2.25 are experimental values

measured by Mah et al and by Blevis et al. The simulations agree with the measurements within experimental uncertainties.

The energy dependence of  $W_{\pm}$  in a-Se has been debated by various authors for quite some time.<sup>9,11,37</sup> The two main competing models have been the Onsager model of geminate recombination and the Jaffé model of columnar recombination. In the Jaffé model, it is assumed that the ionizing electrons produced by x-rays create electron-hole pairs continuously in a column surrounding their tracks. For this to hold the separation between spurs would have to be smaller than the spur size. The interspur separation, calculated from the total outer inelastic cross-sections, is plotted in Fig. 2.26. Assuming that on average the spur size is 5-6 nm, the overlapping only becomes important when the electron energy is less than 5 keV. The columnar model is therefore too simplistic a model to describe recombination over a wide range of incident energies. In the Onsager model, on the other hand, it is assumed that charges can only recombine with their geminate pair. This model leads to a dependence of  $W_{\pm}$  on electric field, albeit not with the proper slope, but does not predict a dependence on x-ray energy. The reason for the failure of this model is twofold: first, it takes into account only a single electron-hole pair while there are on average about 4-5 pairs in a spur, and secondly the distance between pairs does not vary with energy of the ionizing electron, since only thermalization is taken into account which only depends on energy transfer.

Our model can perhaps be seen as an extension of the Onsager theory. The model is extended to include multiple electron-hole pairs in a spur. The energy dependence of  $W_{\pm}$  comes from the velocity-dependent spur size. Our results suggest that although

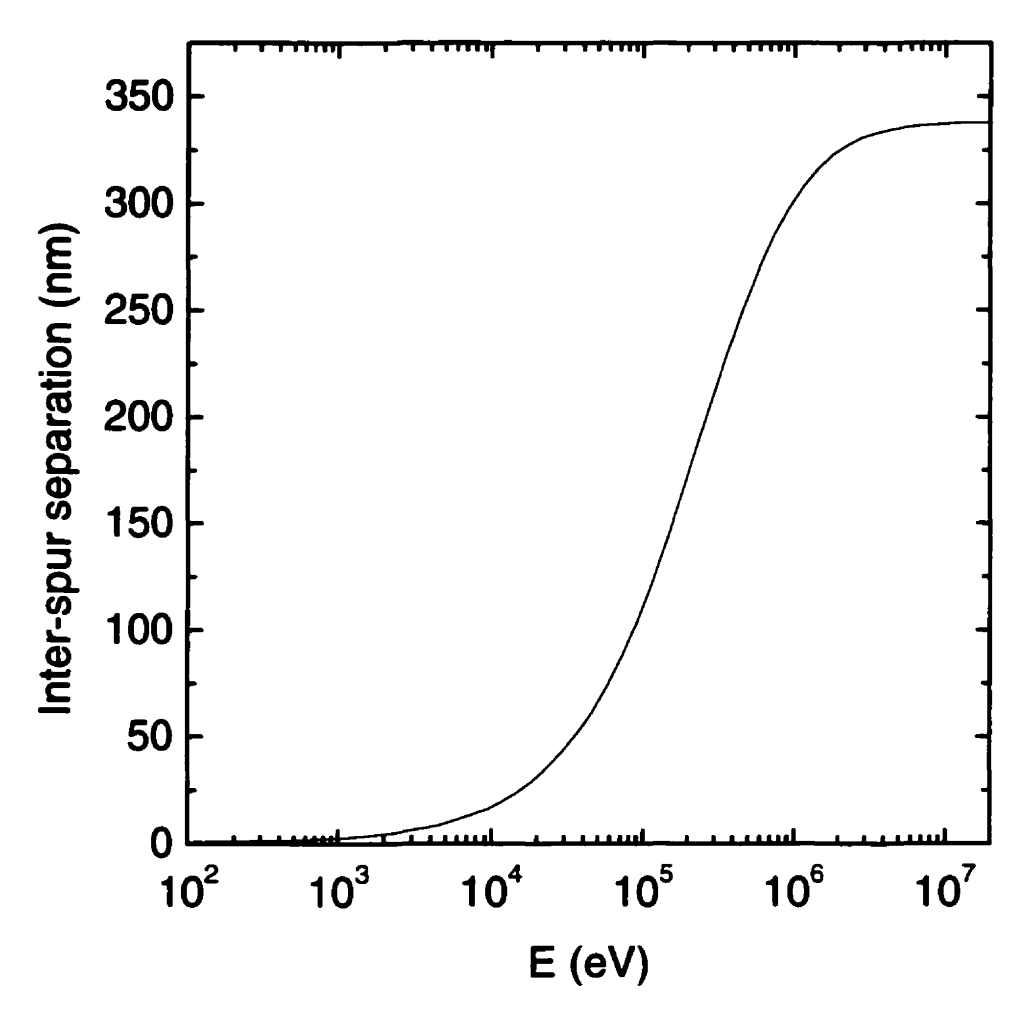


Figure 2.26: The inter-spur separation distance plotted versus electron energy.

interspur separation can influence the energy dependence, it does not play as significant a role as the size of the spur.

On a minor note, the temperature dependence of  $W_{\pm}$  has sometimes been used to distinguish between recombination models. The Onsager model predicts a temperature dependence, while the columnar model does not. Experimental evidence about the temperature dependence of  $W_{\pm}$ , however, is contradictory. Hirsch and Jahakhani<sup>9</sup> have

found that  $\eta$  increases by more than a factor of two between 200-300 K, while recent measurements by Haugen *et al*<sup>37</sup> have shown that there is no temperature dependence in the range 260-300 K. We have run simulations for various temperatures with our code and have found no significant dependence (less than 5%) within the range 200-300 K. Further experimental evidence must be acquired before the temperature dependence can be properly understood.

We have also explored the dependence of  $W_{\pm}$  on the a-Se thickness. Simulation results are shown in Fig. 2.27. At low x-ray energies there is no thickness dependence, because the electrons generated in a-Se are completely absorbed in the layer. At megavoltage energies, we observe an increase of  $W_{\pm}$  with a-Se thickness. This is because the electrons generated in the a-Se lose their energy as they traverse the layer, and there will be greater proportion of electron-hole pairs generated by low energy electrons for larger a-Se thicknesses, leading to an increase in  $W_{\pm}$ .

For megavoltage imaging, the x-rays are usually generated from a linear accelerator and thus have a spectrum of energies. We have run simulations for a typical 6 MV spectrum<sup>38</sup> for various a-Se thicknesses, shown in Fig. 2.28. It is seen that with this spectrum  $W_{\pm}$  increases with thickness until about 200  $\mu$ m, after which a saturation is reached.

We have investigated the effect of a Cu front plate on  $W_{\pm}$ . X-rays are mostly converted to electrons through Compton scattering in the plate, and these electrons create the electron-hole pairs in a-Se. Conceptually, since these electrons are of lower energy

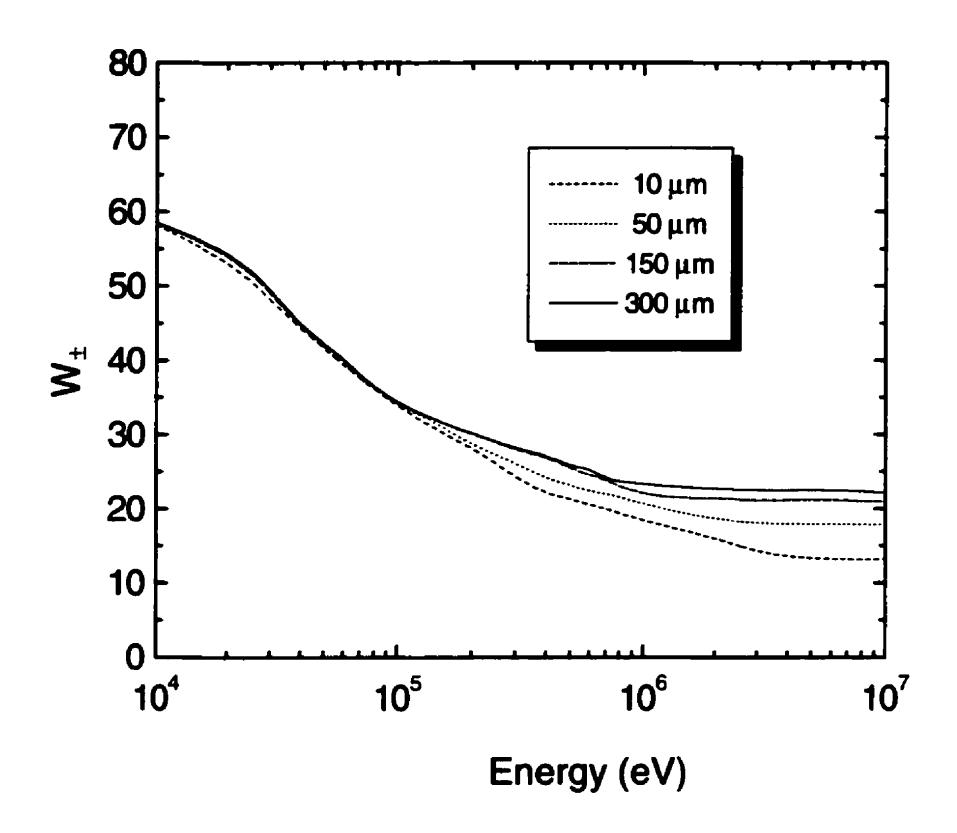


Figure 2.27: Dependence of  $W_{\pm}$  on x-ray energy for various a-Se thicknesses.

than the primary x-rays, the presence of the plate could increase  $W_{\pm}$ . We have run simulations with various metal thicknesses and have found that  $W_{\pm}$  is independent of the metal plate thickness, showing that this effect is negligible.

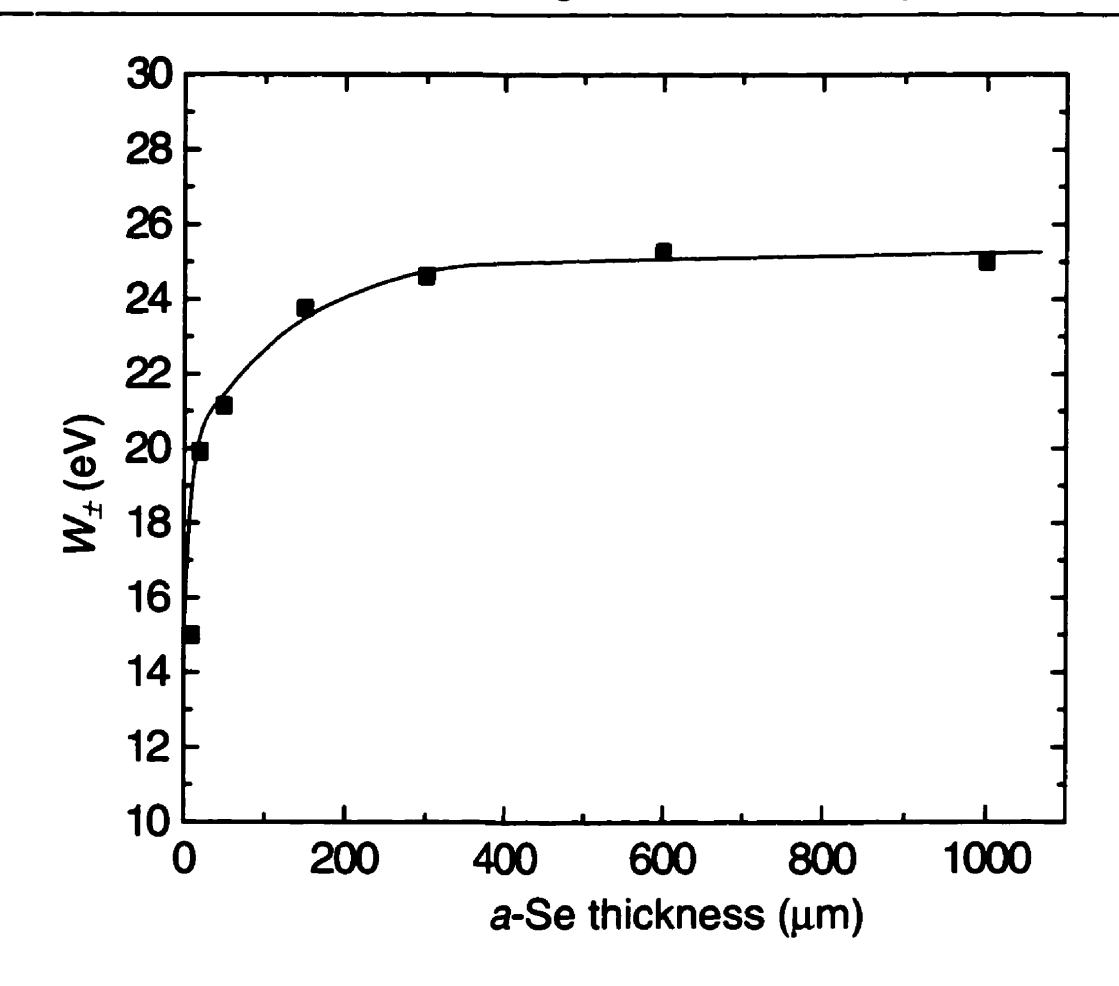


Figure 2.28: Dependence of  $W_{\pm}$  on a-Se thickness for a 6 MV beam (independent of metal thickness).

# 2.7 Conclusions

The signal generated by x-rays in the photoconductor a-Se is not well understood. It is primarily governed by recombination, which is very sensitive to the positions of the electron-hole pairs generated along the photon/electron/positron track structures. In this work, we develop a theoretical description of the charge formation in a-Se. In our model,

high energy electrons created by the interacting x-rays undergo interactions with atomic electrons, exciting collective (plasma) oscillations as well as single electron-hole pairs. We develop cross sections for the decay of plasma oscillations into the creation of n electron-hole pairs. These cross sections are integrated into a Monte Carlo code which simulates the stochastic track structures in a-Se. From these tracks, we determine the initial positions of electrons and holes in the medium. We subsequently follow their time evolution using a simulation code which effectively solves the many-body transport equation. From these simulations we calculate  $W_{\pm}$  which depends on both the pair creation energy  $W_0$  and the escape efficiency  $\eta$ .

Using our model, we calculate  $W_{\pm}$  as a function of incident energy and electric field for both electrons and photons. We compare to available experimental data and show good agreement.  $W_{\pm}$  decreases with electric field because a higher fraction of particles escape recombination, thus increasing  $\eta$ .  $W_{\pm}$  decreases with increasing photon energy up to about 1 MeV, after which it approaches a constant plateau. In another paper this has been qualitatively described by an inter-spur recombination mechanism. In our model, the energy dependence is not due to inter-spur recombination, since spurs are only close enough to affect each other at energies less than about 5 keV. Instead, the energy dependence is attributed to an energy-dependent spur size. This arises because energy is deposited within a sphere whose size is proportional to the incident velocity of the ionizing particle. The escape efficiency increases with increasing spur size because electron-hole pairs in the spur are farther apart, resulting in a greater probability of

escaping recombination. This mechanism seems to explain the observed energy dependence of  $W_{\pm}$  in a-Se.

The results presented in this work can be used to calculate the signal in a-Se-based x-ray detectors for applications in diagnostic radiology and portal imaging. Better understanding of the signal generation in these detectors may lead to further optimization of both detector design and the choice of x-ray energy spectra used for imaging with these detectors.

# 2.8 References

- [1] J.L. Donovan, "X-ray sensitivity of selenium," J. Appl. Phys. **50** 6500-6504 (1979).
- [2] G. Borasi and R. Cubeddu, "Some remarks on selenium plates for xeroradiography," J. Appl. Phys. 48 1375-1379 (1977).
- [3] W.D. Fender, "Quantification of the xeroradiographic discharge curve," SPIE 70 364-371 (1975).
- [4] J.A. Rowlands and D.M. Hunter, "X-ray imaging using amorphous selenium: photoinduced discharge (PID) readout for digital general radiography," Med. Phys. 22 1983-2005 (1995).
- [5] H. Fiedler and F. Laugwitz, "Zur Quantenausbeute elektroradiographischer Selenschichten," J. Signal AM 9 229-235 (1981).
- [6] I.M. Blevis, D.C. Hunt and J.A. Rowlands, "Measurement of x-ray photogeneration in amorphous selenium," J. Appl. Phys. **85** 7958-7963 (1999).

- [7] S.O. Kasap, V. Aiyah., B. Polischuk and A. Baillie, "X-ray sensitivity of stabilized a-Se for x-ray imaging with electrostatic readout," J. Appl. Phys. 83 2879-2887 (1998).
- [8] J.W. Boag, "Xeroradiography (review)," Phys. Med. Biol. 18 3-37 (1973).
- [9] J. Hirsch and H. Jahankhani, "The carrier yield in a-Se under electron bombardment," J. Phys.: Condens. Matter 1 8789 (1989).
- [10] G. Jaffé, "Columnar ionization," Le Radium 10 126-134 (1913).
- [11] W. Que and J.A. Rowlands, "X-ray photogeneration in amorphous selenium: Geminate versus columnar recombination," Phys. Rev. B 51 10500-10507 (1995).
- [12] D.M. Pai and R.C. Enck, "Onsager mechanisms of photogeneration in amorphous selenium," Phys. Rev. B 11 5163-5174 (1975).
- [13] D. Mah, J.A. Rowlands and J.A. Rawlinson, "Sensitivity of amorphous selenium to x rays from 40 kVp to 18 MV: Measurements and implications for portal imaging," Med. Phys. 25 444-456 (1998).
- [14] J.C. Knights and E.A. Davis, "Photogeneration of charge carriers in amorphous selenium," J. Phys. Chem. Solids 35 543-554 (1975).
- [15] L. Onsager, "Initial recombination of ions," Phys. Rev. 54 554 (1938).
- [16] D.E. Cullen, S.T. Perkins and S.M. Seltzer, Tables and graphs of photon-interaction cross sections from 10 eV to 100 GeV derived from the LLNL evaluated photon data library (EPDL), parts A&B, Lawrence Livermore National Laboratory (1989).
- [17] H.E. Johns and J.R. Cunningham, *The Physics of Radiology* (Thomas, Springfield, 1983).
- [18] S.T. Perkins, D.E. Cullen, M.H. Chen, J.H. Hubbell, J.Rathkopf and J.Scofield, Tables and Graphs of Atomic Subshell and Relaxation Data Derived from the LLNL

- Evaluated Atomic Data Library (EADL), Z = 1-100, Lawrence Livermore National Laboratory (1991).
- [19] D.E. Cullen, S.T. Perkins and S.M. Seltzer, Tables and Graphs of Electron Interaction Cross Sections from 10 eV to 100 GeV Derived from the LLNL Evaluated Electron Data Library (EEDL), Z = 1 100, Lawrence Livermore National Laboratory (1991).
- [20] H.H. Rossi and M. Zaider, *Microdosimetry and its applications* (Springer, New York, 1995).
- [21] H. Bethe, "Theory of the passage of fast corpuscular rays through matter," Annal der Physik 5 325 (1930).
- [22] I. Kawrakow and D.W.O. Rogers, "The EGSnrc Code System: Monte Carlo Simulation of Electron and Photon Transport," NRCC Report PIRS-701 (2000).
- [23] M. Lachaine and B.G. Fallone, "Calculation of inelastic cross-sections for the interaction of electrons with amorphous selenium," J. Phys. D 33 551-555 (2000).
- [24] J.C. Ashley, "Interaction of low-energy electrons with condensed matter: stopping powers and inelastic mean free paths from optical data," Journal of Electron Spectroscopy and Related phenomena, 46 199-214 (1988).
- [25] U. Fano and J.W. Cooper, "Spectral distribution of atomic oscillator strengths," Rev. Mod. Phys. 40 441-507 (1968).
- [26] C.A. Klein, "Band gap dependence and related features of radiation ionization energies in semiconductors," J. Appl. Phys. 39 2029 (1968).
- [27] C. Haugen and S.O. Kasap, "Langevin recombination of drifting electrons and holes in stabilized a-Se (Cl-doped a-Se: 0.3% As)," Phil. Mag. B 71 91-96 (1995).

- [28] P. Langevin, "Recombinaison et mobilités des ions dans les gaz," Ann. Chim. Phys. 28 287-433 (1903).
- [29] H.A. Kramers, "On a modification of Jaffé's theory of column ionization," Physica (Utrecht) 18 665-675 (1952).
- [30] M.G. Bell and W.Y. Liang, "On determination of the dielectric functions of a-Se and trig-Se by electron energy loss spectroscopy," in 5th International Conference on Amorphous and Liquid Semiconductors (1973).
- [31] W. Jones and N. March, *Theoretical solid state physics, Vol. 1* (Dover, New York, 1973).
- [32] R.H. Ritchie and W. Brandt, "Primary processes and track effects in irradiated media" in *Radiation research: biomedical, chemical and physical perspectives* edited by O.F. Nygaard, H.I. Adler, and W.K. Sinclair (Academic Press, New York, 1975).
- [33] R.N. Hamm, J.E. Turner, R.H. Ritchie and H.A. Wright, "Calculation of heavy-ion tracks in liquid water," Radiat. Res. 104 S5-S20 (1985).
- [34] J.A. Laverne and S.M. Pimblott, "Energy loss distributions in hydrocarbons," The Journal of Physical Chemistry **99** 10541-10548 (1995).
- [35] N. Bohr, Mat. Fys. Medd. K. Dan. Vidensk. Selsk. 18 1 (1948).
- [36] W.M. Bartczak and A. Hummel, "Computer simulation of ion recombination in irradiated nonpolar liquids," J. Chem. Phys 87 5222-5228 (1987).
- [37] C. Haugen, S.O. Kasap and J. Rowlands, "Charge transport and electron-hole pair creation energy in stabilized a-Se x-ray photoconductors," J. Phys. D: Appl. Phys. 32 200-207 (1999).

[38] S. Kubsad, R. Mackie, B. Gehring, D. Misisco, B. Paliwal, M. Mehta and T. Kinsella, "Monte Carlo and convolution dosimetry for stereotactic radiosurgery," Int. J. Rad. Onc. Biol. Phys. 19 1027-1035 (1990).

| 3.1 Introduction                                    | 96  |
|---|-----|
| 3.2 Background                                      | 96  |
| 3.2.1 Contrast and Sensitivity                      |     |
| 3.2.2 Resolution and noise                          |     |
| 3.2.3 Linear systems analysis                       | 101 |
| 3.2.4 Transfer characteristics of digital detectors | 113 |
| 3.3 Materials and Methods                           | 122 |
| 3.3.1 Description of detector                       | 122 |
| 3.3.2 Sensitivity                                   | 127 |
| 3.3.3 Modulation Transfer Function                  | 129 |
| 3.3.4 Noise Power Spectrum                          | 130 |
| 3.3.5 Detective Quantum Efficiency                  | 131 |
| 3.4 Results and Discussion.                         | 132 |
| 3.5 Conclusions                                     | 138 |
| 3.6 References                                      | 138 |

# 3.1 Introduction

In this Chapter, we report the measurement of the imaging characteristics of a metal/a-Se based direct AMFPI for portal imaging. We first define parameters used to describe imaging detectors, such as the sensitivity, modulation transfer function (MTF), noise power spectrum (NPS), and Detective Quantum Efficiency (DQE). We then measure these quantities and compare the DQE of the direct AMFPI to published values for an indirect AMFPI.

# 3.2 Background

In this section we introduce some basic concepts of medical imaging to define the quantities measured in this Chapter. In-depth descriptions have been given in a number of books on the subject.<sup>1-3</sup>

# 3.2.1 Contrast and Sensitivity

In x-ray imaging, photons emanating from a point source are detected on the exit side of a patient by a detector to form a two-dimensional image. Consider the schematic representation of Fig. 3.1, where a uniform spherical object with attenuation coefficient  $\mu_1$  embedded in a uniform material of attenuation coefficient  $\mu_2$  is imaged with x-rays. The two-dimensional distribution of x-ray quanta per unit area  $q_0(x, y)$  impinging on the

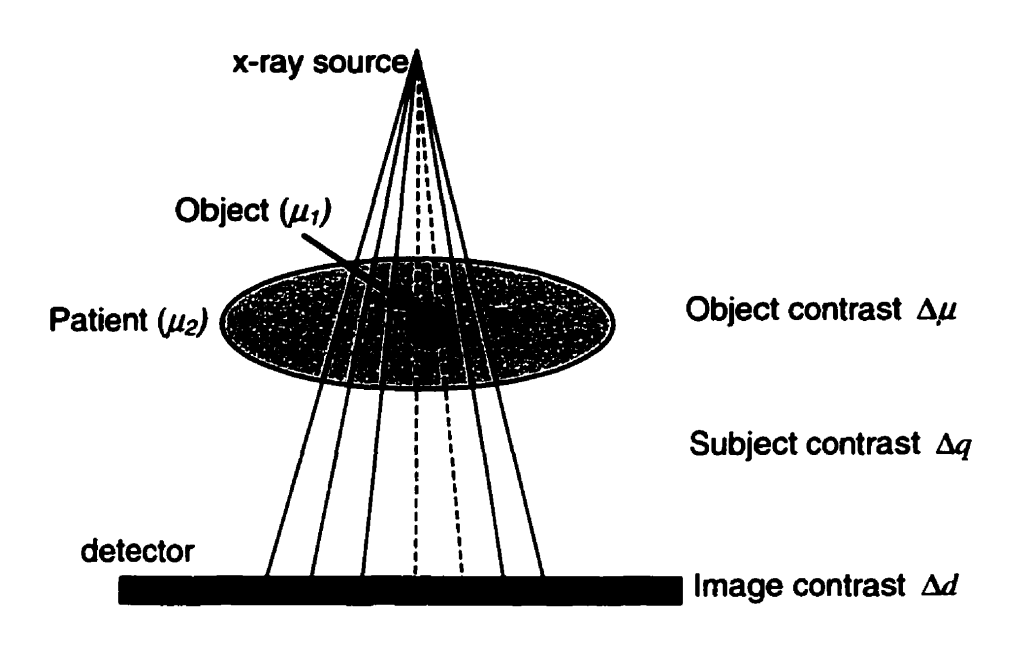


Figure 3.1: Schematic representation of x-ray imaging geometry, labeling object, subject and image contrast.

detector plane is the detector *input*, which, for a monoenergetic beam neglecting scattered radiation, is proportional to

$$q_0(x,y) \propto e^{-\int \mu dl} , \qquad (3.1)$$

where the integration is over the straight line subtended between the source and the point (x,y) in the detector plane. The role of the detector is to convert  $q_0(x,y)$  into a two-dimensional image d(x,y).

For a given x-ray energy the visibility of the spherical object will be related to both the size of the object and the difference in attenuation coefficient  $\Delta \mu = \mu_1 - \mu_2$ 

between the object and its surroundings, which is related to their atomic numbers and densities. This inherent physical difference in x-ray attenuation properties is referred to as the *object contrast*.<sup>3</sup> Consider two points in the detector plane: point  $P_1$  at location  $(x_1, y_1)$  which is in the "shadow" of the spherical object, and a point  $P_2$  at location  $(x_2, y_2)$  which is not in the shadow. The *subject contrast* of the spherical object can be defined as

$$C_{sub} = \frac{q_0(x_1, y_1) - q_0(x_2, y_2)}{q_0(x_2, y_2)} . \tag{3.2}$$

Similarly, the image contrast for the simple spherical object can be defined as

$$C_{image} = \frac{d(x_1, y_1) - d(x_2, y_2)}{d(x_2, y_2)} . \tag{3.3}$$

The image contrast will depend on the subject contrast (which in turn depends on the object contrast), as well as on the *sensitivity* of the detector. The sensitivity  $\Gamma$  is a function which governs how the large-area input to the detector is mapped to a signal in the image (the input must have a large uniform area so that imperfect resolution, which will be discussed in the next section, does not affect the response). For an average input q the detector signal is given by

$$d = \Gamma(q_0) . \tag{3.4}$$

The sensitivity curve may or may not be linear, and can be determined by exposing the detector to various inputs. In general the sensitivity may depend on the x-ray energy spectrum.

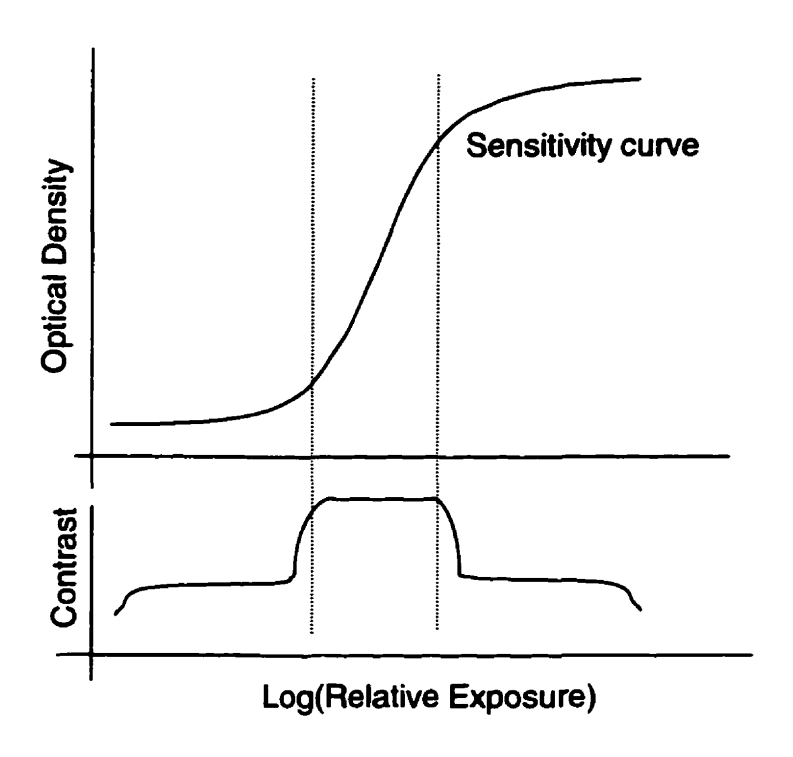


Figure 3.2: Schematic representation of sensitivity curve for film (H&D curve) and associated contrast.

In the above, the contrast was defined using an analogy to a spherical object. Another, perhaps more general, definition of image contrast describes how a variation of the input  $dq_0$  is converted into a signal variation which is given by the derivative of the sensitivity curve,

$$C_{image}(q_0) = \frac{d\Gamma(q_0)}{dq_0} . {3.5}$$

To illustrate the concept, consider the schematic diagram for the sensitivity curve of film (usually called a H&D curve) shown in Fig. 3.2. In this case the input  $q_0$  is defined as the relative logarithm of the exposure, and the output as the optical density (O.D.) of the

film. At low and high exposures, the O.D. varies little with exposure whereas in the middle region the O.D. is approximately linear with the log of the exposure. The contrast, defined as the derivative of the sensitivity curve, is also shown. This shows that outside the linear region there is low contrast (since the sensitivity curve is constant), and that there is high contrast in the linear region. For this reason it is important, when using film, to use exposures in the linear range of the film in question. A film with a high slope in the linear region of its sensitivity curve will subsequently have a high image contrast usually at the expense of the *latitude* (*i.e.*, the range of exposures for which the sensitivity curve is linear).

# 3.2.2 Resolution and noise

The image quality discussed in the previous section pertains to signals which do not vary drastically with position. Ideally, each input point  $q_0(x, y)$  is represented by a point in the image  $d(x, y) = \Gamma[q_0(x, y)]$ . Inputs  $q_0(x, y)$  with high spatial variations, however, may not be well reproduced due to a lack of detector resolution.<sup>3</sup> Resolution is sometimes defined as the minimum separation between two points or lines which can be distinguished in the image. Alternatively, it can be defined as the smallest object size which can be viewed in the image. The mechanism which limits the resolution is often called blur, and arises because the detector "smears out" information.

X-ray interactions are stochastic processes and thus there will always be noise present in images. Furthermore, components such as electronic amplifiers in the detector

may increase the noise in the image. If the noise is of the same order of magnitude as the contrast between an object and its background, the object will be obscured.<sup>3</sup>

Although contrast, resolution and noise are usually discussed as the most important quantities affecting image resolution, there are other unwanted effects which may be present in an image. Distortion, for example, alters the size, shape or relative position of an object, but this does not affect its visibility. Detectors may also produce artifacts, i.e., objects, which appear in the image but are not present in the input x-ray distribution. Although artifacts are often recognizable, they may be confused with actual objects and lead to misinterpretation.

## 3.2.3 Linear systems analysis

#### 3.2.3.1 Modulation Transfer Function

In the previous sections we have discussed imaging characteristics in a qualitative sense. In order to characterize a detector, it is often useful to regard it as a "black box" which maps a two-dimensional input  $q_0(x, y)$  into a two-dimensional output d(x, y), as shown in Fig. 3.3. The effect of the system can then be represented mathematically by an operator S, *i.e.*,

$$d(x, y) = S\{q_0(x, y)\}. (3.6)$$

In this section we neglect noise and assume that the input and output are deterministic; noise will be treated in the Section 3.2.3.2.

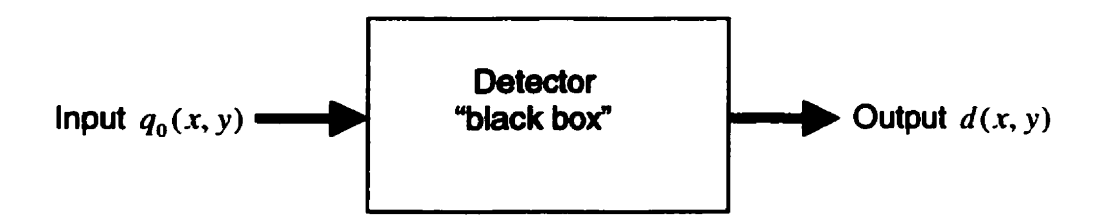


Figure 3.3: Detector viewed as a "black box".

The input/output characteristics of a system are usually treated in the framework of *linear systems analysis*.<sup>2,4</sup> This assumes the following about the system under investigation:

(a) Linearity: if two inputs, A and B, give outputs  $d^A(x, y) = S[q_0^A(x, y)]$  and  $d^B(x, y) = S[q_0^B(x, y)]$ , then

$$S\{aq_0^A(x,y) + bq_0^B(x,y)\} = ad^A(x,y) + bd^B(x,y), \qquad (3.7)$$

where a and b are arbitrary constants. This implies that if the input is broken down into a weighted sum of elementary inputs, the output will be a weighted sum of the outputs.

(b) Shift invariance: shifting the input by (x',y') will merely lead to a corresponding shift in the output, but not change its shape. Mathematically this can be written as

$$d(x-x',y-y') = S\{q_0(x-x',y-y')\}.$$
 (3.8)

The linearity requirement is not always satisfied with practical detectors, since according to Eq. (3.4) the output is related to the input by the sensitivity curve  $d = \Gamma(q_0)$  which may be non-linear. This can be overcome, if the output is "linearized"

by applying the inverse function  $d_{linear} = \Gamma^{-1}(d)$  to the image data. The requirement of shift invariance, on the other hand, will not hold, if the sensitivity is not uniform over the detector, if there is distortion, or if the detector produces artifacts. It is usually possible, however, to either correct for these or to limit measurements to a small area of the detector. Even if these effects are insurmountable, useful information can nonetheless be determined using linear systems analysis. For example, as will be discussed in Section 3.2.4, digital detectors are not shift invariant due to the finite size of the pixels; in this case linear systems analysis must be used with caution, but the technique remains extremely useful.

It is useful to consider a "point-like" input at coordinates (x',y'), which can be represented as a two-dimensional delta function  $\delta(x-x',y-y')$ . The corresponding output (normalized to unit area), denoted as p(x,y;x',y'), will have a finite width due to imperfect detector resolution and is referred to as the point spread function (PSF), shown schematically in Fig. 3.4. Since the system is assumed to be shift-invariant, the PSF must only depend on the differences x-x' and y-y', and is denoted by p(x-x',y-y').

Using the shifting property of the delta function, any input can be expressed as a sum of delta functions, implying that any output distribution is related to its corresponding input by

$$d(x, y) = S\left\{ \int_{-\infty}^{\infty} \int_{-\infty}^{\infty} q_0(x', y') \delta(x' - x, y' - y) dx' dy' \right\}. \tag{3.9}$$

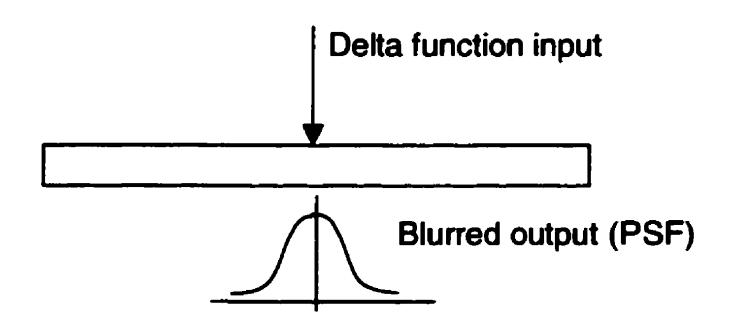


Figure 3.4: Schematic representation of a point spread function (PSF).

Using the linearity assumption, the operator S can be moved inside the integral so that it acts only on the delta function. Since the response of a delta-function input has been defined as the PSF, Eq. (3.9) becomes

$$d(x, y) = \int_{-\infty}^{\infty} \int_{-\infty}^{\infty} q_0(x', y') p(x'-x, y'-y) dx' dy'.$$
 (3.10)

This is a two-dimensional convolution integral, which can be represented in shorthand notation as

$$d(x, y) = q_0(x, y) \otimes \otimes p(x, y) . \tag{3.11}$$

This shows that the system blurs the input by convolving it with a PSF. A wide PSF indicates a low detector resolution. Note that, since we are dealing only with resolution properties at this point, we have assumed for simplicity that d(x, y) and  $q_0(x, y)$  have been normalized appropriately so that differences in units can be neglected in the above equations (otherwise a gain factor should be included).

It is useful to break the input and output distributions into sinusoidal components of fixed frequencies using Fourier analysis. We write their two-dimensional Fourier Transforms as  $\tilde{q}_o(u,v) = FT\{q_0(x,y)\}$  and  $\tilde{d}(u,v) = FT\{d(x,y)\}$ , where

$$\widetilde{z}(u,v) = FT\{z(x,y)\} = \int_{-\infty}^{\infty} \int_{-\infty}^{\infty} z(x,y)e^{-2\pi i(ux+vy)}dxdy$$
 (3.12)

and

$$z(x, y) = FT^{-1} \{ \tilde{z}(u, v) \} = \int_{-\infty}^{\infty} \int_{-\infty}^{\infty} \tilde{z}(u, v) e^{2\pi i (ux + vy)} dx dy .$$
 (3.13)

Description of the input and output distributions into their spatial frequency contributions is useful since the convolution theorem states that if two functions are convolved in the spatial domain, then they are multiplied in the spatial frequency domain (and vice-versa), which greatly simplifies Eq. (3.11) to

$$\widetilde{d}(u,v) = \widetilde{q}_0(u,v) \cdot OTF(u,v) , \qquad (3.14)$$

where the optical transfer function (OTF) is the Fourier Transform of the PSF, *i.e.*,  $OTF(u,v) = FT\{p(x,y)\}$ . The role of the imaging system can thereby be seen as a "spatial frequency filter". A perfect system transfers all spatial frequencies equally; real systems, however, will be unable to reproduce high spatial frequency sinusoids due to their imperfect resolution capabilities. The two-dimensional *Modulation Transfer Function MTF*(u,v) is defined as

$$MTF(u,v) = |OTF(u,v)|, \qquad (3.15)$$

and gives a complete description of the resolution properties of a system. It is especially useful by the fact that if a detector has many separate blurring mechanisms, the total MTF is given by the product of each individual MTF.

If an imaging system is isotropic, the one-dimensional OTF

$$OTF(f) = OTF(u,0) \tag{3.16}$$

contains the same information as the 2-D OTF and is given by

$$OTF(u,0) = \int_{-\infty}^{\infty} \left\{ \int_{-\infty}^{\infty} p(x,y) dx \right\} e^{-2\pi i u x} dx = FT_{1D} \left\{ LSF(x) \right\}, \qquad (3.17)$$

where the 1-D Fourier Transform is defined as

$$FT_{1D}\{z(x)\} = \int_{-\infty}^{\infty} z(x)e^{-2\pi i x} dx$$
 (3.18)

and the Line Spread Function as

$$LSF(x) = \int_{-\infty}^{\infty} p(x, y')dy'. \qquad (3.19)$$

The one-dimensional modulation transfer function (MTF) is defined as the magnitude of the OTF

$$MTF(f) = |OTF(f)|, \qquad (3.20)$$

which removes information about the phase of the OTF. The MTF is the quantity which is usually used to describe the resolution of a detector. Note that the PSF is defined to have unit area, indicating that the MTF is equal to unity at zero spatial frequency. A

perfect detector will perfectly reproduce all spatial frequencies of the input and will be unity at all spatial frequencies (since the Fourier Transform of a delta-function PSF is a constant). In a practical detector, the MTF typically decreases with increasing spatial frequency due to imperfect resolution. The higher the MTF at a particular spatial frequency, the better it can reproduce that frequency in the image. One way to experimentally measure the MTF of a detector is to measure its response to an infinitesimally thin "line" input. The image of the line is blurred by the detector, and its profile corresponds to the LSF. The magnitude of the one-dimensional Fourier Transform of the LSF, normalized such that MTF(0) = 1, is the detector MTF.

#### 3.2.3.2 Noise Power Spectrum

In the previous section we analyzed the input and output characteristics of a detector in the spatial frequency domain. The MTF was seen to describe how an input sinusoid of a given spatial frequency is transferred by the system. The assumption made in the analysis was that the input and output were deterministic. In reality, however, x-ray images contain noise. An image d(x,y) is only one realization of all possible images. For this reason it can be described by a random variable D(x,y). The set of all possible d(x,y) is called the *ensemble* of D(x,y), and the  $n^{th}$  realization of D(x,y) is denoted by  $d_n(x,y)$ . In the following we make the same assumptions about linearity and shift invariance as in the previous section. Furthermore, we make the assumption that the distributions are *wide-sense stationary* (WSS), *i.e.*, their first and second order statistical properties do not vary with position. We also make the assumption of *ergodicity*, which

means that statistics can be obtained in two equivalent ways: a) by measuring the fluctuations at many (x,y) positions in a single image or b) by obtaining many realizations (n=1..N) of the same image.

Ideally, a uniform input to a detector will produce a uniform output. In reality, however, there will be fluctuations in the output. If we gather enough statistics about these fluctuations, we can obtain some parameters to describe them. Since we have assumed that the noise is ergodic, the mean and variance can be found by averaging over both (or either) (x,y) and n:

$$\overline{d}(x,y) = \left\langle \lim_{X,Y \to \infty} \frac{1}{2X} \frac{1}{2Y} \int_{-X-Y}^{X-Y} dx dy d_n(x,y) \right\rangle_n$$
(3.21)

and

$$\sigma^{2}(x,y) = \left\langle \lim_{X,Y \to \infty} \frac{1}{2X} \frac{1}{2Y} \int_{-X-Y}^{X} dx dy \left( \Delta d_{n}(x,y) \right)^{2} \right\rangle_{n}, \qquad (3.22)$$

where  $\Delta d_n(x, y) \equiv d_n(x, y) - \overline{d}_n$  and  $\langle \rangle_n$  denotes the average over n.

The mean and variance describe first-order statistics, but do not describe correlations which may occur either between successive images or between neighbouring positions. Although both types of correlation are possible in medical imaging detectors, in this work we are interested only in the latter; *i.e.* we assume that successive images are independent of each other. The spatial correlations between two points separated by  $(\Delta x, \Delta y)$  can be described by the *autocovariance* function (ACF), defined as

$$\gamma(\Delta x, \Delta y) = \left\langle \lim_{X,Y \to \infty} \frac{1}{2X} \int_{-X-Y}^{X} \int_{-X-Y}^{X} dx dy \Delta d_n(x, y) \Delta d_n(x + \Delta x, y + \Delta y) \right\rangle_n . \tag{3.23}$$

The ACF only depends on the separation  $(\Delta x, \Delta y)$ , not on the absolute location of the points, since as mentioned above we have assumed that the noise is ergodic. The ACF is large for two points which are strongly correlated, and is small otherwise. The variance is simply a special case of the ACF, since

$$\sigma^2 = \gamma(0,0) \quad . \tag{3.24}$$

In analogy with the MTF, it is useful to break the variance down into contributions from sinusoids of various spatial frequencies. The Fourier Transform of the fluctuations,

$$\Delta \tilde{d}(u,v) = FT \{ \Delta d(x,y) \}, \tag{3.25}$$

contains information about the phase of the fluctuations. Noise typically has random phase, and thus this quantity is not a good descriptor of image noise. Typically the *Noise Power Spectrum* (NPS) is used, which is defined as

$$NPS(u,v) = \left\langle \lim_{X,Y \to \infty} \frac{1}{2X} \frac{1}{2Y} \left| FT \left\{ \Delta d(x,y) \right\}^2 \right\rangle_n. \tag{3.26}$$

The absolute value operator removes the phase information. It is useful to find the equivalent of the NPS in position space. This can be found if Eq. (3.26) is re-written as

$$NPS(u,v) = \left\langle \lim_{X,Y\to\infty} \frac{1}{2X} \frac{1}{2Y} \left[ FT\{\Delta d(x,y)\} \right] \left[ FT\{\Delta d(x,y)\} \right]^* \right\rangle_{\pi}, \qquad (3.27)$$

which, using the convolution theorem, is equivalent to

$$FT^{-1}\left\{S(u,v)\right\} = \left\langle \lim_{X,Y\to\infty} \frac{1}{2X} \frac{1}{2Y} \Delta d(x,y) \otimes \otimes \Delta d^*(x,y) \right\rangle_{n}$$

$$= \left\langle \lim_{X,Y\to\infty} \frac{1}{2X} \frac{1}{2Y} \int_{-X}^{X} \int_{-Y}^{Y} dx' dy' \Delta d(x',y') \Delta d^*(x'-x,y'-y) \right\rangle_{n} . \tag{3.28}$$

For real and ergodic d(x, y), using Eq. (3.23) this becomes

$$NPS(u, v) = FT\{\gamma(x, y)\}, \qquad (3.29)$$

i.e., the ACF and the NPS are Fourier Transform pairs. Thus if noise is perfectly random, then the NPS will be constant over all spatial frequencies which is referred to as white noise. If, on the other hand, there are spatial correlations in the noise, then the NPS will decrease with increasing spatial frequency. It is also of note that

$$\sigma^2 = \gamma(0,0) = \int_{-\infty}^{\infty} \int_{-\infty}^{\infty} NPS(u,v) du dv , \qquad (3.30)$$

which shows explicitly that the NPS describes how the variance of an image is distributed into spatial frequency components. The NPS is commonly used to describe the noise properties of a detector, analogously to how the MTF describes the resolution properties of a detector.

Often a one-dimensional representation of the NPS is used for clarity. Ideally this could be done by taking the NPS along a single axis, i.e., NPS(f) = NPS(u,0). A problem with this definition is that at very low spatial frequencies, noise from both the u and the v axes contribute to the noise which artificially inflates the low-frequency values

in the 1-D NPS. Williams *et al*<sup>7</sup> have studied various approaches to solving this problem. They demonstrate that a reasonable solution is to take a thick slice of the 2D NPS near, but not on, the *u*-axis.

#### 3.2.3.3 Detective Quantum Efficiency

In the previous sections the imager has been treated as a black box which converts an input distribution of x-ray quanta  $q_0(x, y)$  into an output distribution d(x, y). The output "signal" in the spatial frequency domain is given by

$$signal_{out}(f) = \overline{d} \cdot OTF(f)$$
, (3.31)

where OTF(f) is the optical transfer function and  $\overline{d}$  is the large-area signal. If we define the total noise of the output by its standard deviation (the square root of the variance), then the output "noise" as a function of spatial frequency is given by

$$noise_{out} = \sqrt{NPS(f)} . (3.32)$$

Using these definitions the signal-to-noise ratio (SNR) of the output is given by

$$SNR_{out}(f) = \frac{\overline{d} \cdot OTF(f)}{\sqrt{NPS(f)}}.$$
(3.33)

The output SNR contains the total noise of the output, which contains the noise of the input. A quantity which describes the SNR transfer characteristics of a detector is called the Detective Quantum Efficiency (DQE), defined as<sup>8,9</sup>

$$DQE(\overline{q}, f) = \left| \frac{SNR_{out}(f)}{SNR_{in}(f)} \right|^{2}, \qquad (3.34)$$

where  $SNR_{in}(f)$  is the signal-to-noise ratio of the incident x-rays. Since x-rays obey Poisson counting statistics, the variance is equal to the mean which gives the input SNR

$$SNR_{in}(f) = \frac{\overline{q}_0}{\sqrt{\overline{q}_0}} = \sqrt{\overline{q}_0} \quad , \tag{3.35}$$

where  $\overline{q}_0$  is the average fluence incident on the detector. This leads to an expression for the DOE:

$$DQE(\overline{q}_0, f) = \frac{\overline{d}^2 \cdot MTF^2(f)}{\overline{q}_0 \cdot NPS(f)} = \frac{MTF^2(f)}{\overline{q}_0 \cdot \left(\frac{NPS(f)}{\overline{d}^2}\right)},$$
(3.36)

where we have used MTF(f) = |OTF(f)|. The DQE governs how the system transfers the SNR of the input into the SNR of the final image, and is the quantity most widely used to describe the physical image quality characteristics of a detector. A high DQE over a wide range of spatial frequencies indicates good imaging characteristics. Measurement of the DQE requires separate measurements of the MTF, the NPS, and the average fluence (x-rays per unit area) incident on the detector. If the DQE is due only to the fluctuations of quanta within the detector, it is said to be quantum limited and in this case does not depend on the incident fluence.

## 3.2.4 Transfer characteristics of digital detectors

In the previous sections of this Chapter we have summarized how linear systems theory can be used to describe image quality in terms of the MTF, NPS and DQE. We have described the image signal as  $\overline{d}(x, y)$ , a continuous function of spatial position. In this section we describe digital detectors, where the signal is sampled by a discrete rectangular grid of spacing  $\Delta x$  and  $\Delta y$ . <sup>10</sup>

There are usually a number of "analog" processes that occur in a digital x-ray detector before the information is digitized. The incident distribution of x-ray quanta  $q_0(x, y)$  can undergo a variety of interactions with the detector, often producing other types of quanta, for example optical photons for the case of phosphor-based detectors. These interactions will be explored in the following Chapter. The analog image q(x, y) refers to the distribution just prior to digitization. To convert the analog image at a point  $(x_m, y_n)$  into a digital value, some kind of measuring aperture must be used. In practice this aperture will have a finite size, and may have a non-uniform response about its centre. This response can be described by an aperture function A(x, y). For example, for a uniform square aperture of finite size a the aperture function can be written as

$$A(x,y) = a^{2} rect\left(\frac{x}{a}\right) rect\left(\frac{y}{a}\right), \qquad (3.37)$$

where the rect function is defined as

$$rect(x) = \begin{cases} \frac{1}{a}, |x| \le a/2 \\ 0, |x| > a/2 \end{cases}$$
 (3.38)

A digital image is formed by sampling the analog image at an array of points  $(x_m, y_n) = (m\Delta x, n\Delta y)$  to form a discrete image  $d_{mn}$ . Each point corresponds to an integration of the analog image over the measuring aperture, *i.e.*,

$$d_{mn} = \int_{-\infty}^{\infty} \int_{-\infty}^{\infty} q(x, y) A(x - x_m, y - y_n) dx dy , \qquad (3.39)$$

which can be re-written as a convolution

$$d_{mn} = q(x, y) \otimes \otimes A(x, y) \Big|_{x_{-1}, y_{-1}}.$$
 (3.40)

In Eq. (3.40) it can be seen that the analog image q(x, y) is both blurred by the detecting aperture and sampled at discrete points  $(x_m, y_n)$ . It is convenient to conceptually separate these effects into two separate stages. The *presampling image*  $d_{pre}(x, y)$  is defined as the image which has been blurred by the aperture but prior to sampling, *i.e.*,

$$d_{nre}(x, y) = q(x, y) \otimes \otimes A(x, y) . \tag{3.41}$$

If we could arrange so that the distance between samples were infinitesimally small, then the digital image would effectively be continuous and would be equal to the presampling image. In practice, the digital image is a discrete version of the presampling image, corresponding to the points  $(x_m, y_n) = (m\Delta x, n\Delta y)$ , and can be represented by the expression

$$d_{mn} = \overline{d}_{pre}(x, y) \cdot \mathrm{III}(x, y; \Delta x, \Delta y) = \overline{d}(x, y) \otimes \otimes A(x, y) \cdot \mathrm{III}(x, y; \Delta x, \Delta y) \ , \ (3.42)$$

where the *comb* function  $\mathbf{H}(x, y; \Delta x, \Delta y)$  is a two-dimensional string of delta functions

$$III(x, y; \Delta x, \Delta y) = \sum_{n = -\infty}^{\infty} \sum_{n = -\infty}^{\infty} \delta(x - m\Delta x) \delta(y - n\Delta x) , \qquad (3.43)$$

which effectively "picks out" the presampling signal at the sampling points.

#### 3.2.4.1 Digital Modulation Transfer Function

If the digital detector is given a delta-function input, the analog processes will typically introduce blurring (for example the scattering of x-rays within the detector), leading to an analog point spread function p(x, y) and a corresponding analog OTF  $OTF(u, v) = FT\{p(x, y)\}$ . The presampling PSF is the analog PSF which is blurred by the effect of the detecting aperture, i.e.,

$$p_{\text{nes}}(x, y) = p(x, y) \otimes \otimes A(x, y). \tag{3.44}$$

The Fourier Transform of this expression defines the presampling OTF

$$OTF_{pre}(u, v) = OTF(u, v) \cdot \tilde{A}(u, v)$$
, (3.45)

where  $\tilde{A}(u,v)$  is the Fourier Transform of the aperture response function. From Eq. (3.42), the digital PSF is given by

$$p_{mn} = p_{pre}(x, y) \cdot \Pi(x, y; \Delta x, \Delta y). \tag{3.46}$$

Since in practice the LSF is usually measured instead of the PSF, the digital LSF is similarly defined as

$$l_{mn} = l_{pre}(x, y) \cdot III(x; \Delta x). \tag{3.47}$$

Since the Fourier Transform of a comb function  $III(x; \Delta x)$  is another comb function  $III(f, 1/\Delta x)$ , this leads to the digital OTF<sup>10</sup>

$$OTF_{dig}(f) = OTF_{pre}(f) \otimes \left[ III \left( u; \frac{1}{\Delta x} \right) \right].$$
 (3.48)

The digital MTF is then defined as

$$MTF_{dig}(f) = \left| OTF_{dig}(f) \otimes \left[ III \left( f; \frac{1}{\Delta x} \right) \right] \right|.$$
 (3.49)

This shows that sampling of the presampling LSF with spacing  $\Delta x$ , shown in Fig. 3.5(a), results in a repetition of the presampling OTF in the spatial frequency domain shown in Fig. 3.5(b). The repetitions are sometimes called the *aliases* of the OTF. The Nyquist frequency,  $f_N = 1/(2\Delta x)$ , is also shown and represents the mid-point between the aliases. The repetition itself does not cause any problems, as long as one is only interested in frequencies below  $f_N$ .

The problem occurs if there is *overlap* between the aliases, which results in high frequencies disguising as lower frequencies in the MTF as seen in Fig. 3.5(c). This effect is called *aliasing* and occurs in undersampled digital detectors. If the analog signal is sampled with a moving aperture, the spacing between samples can be made small enough

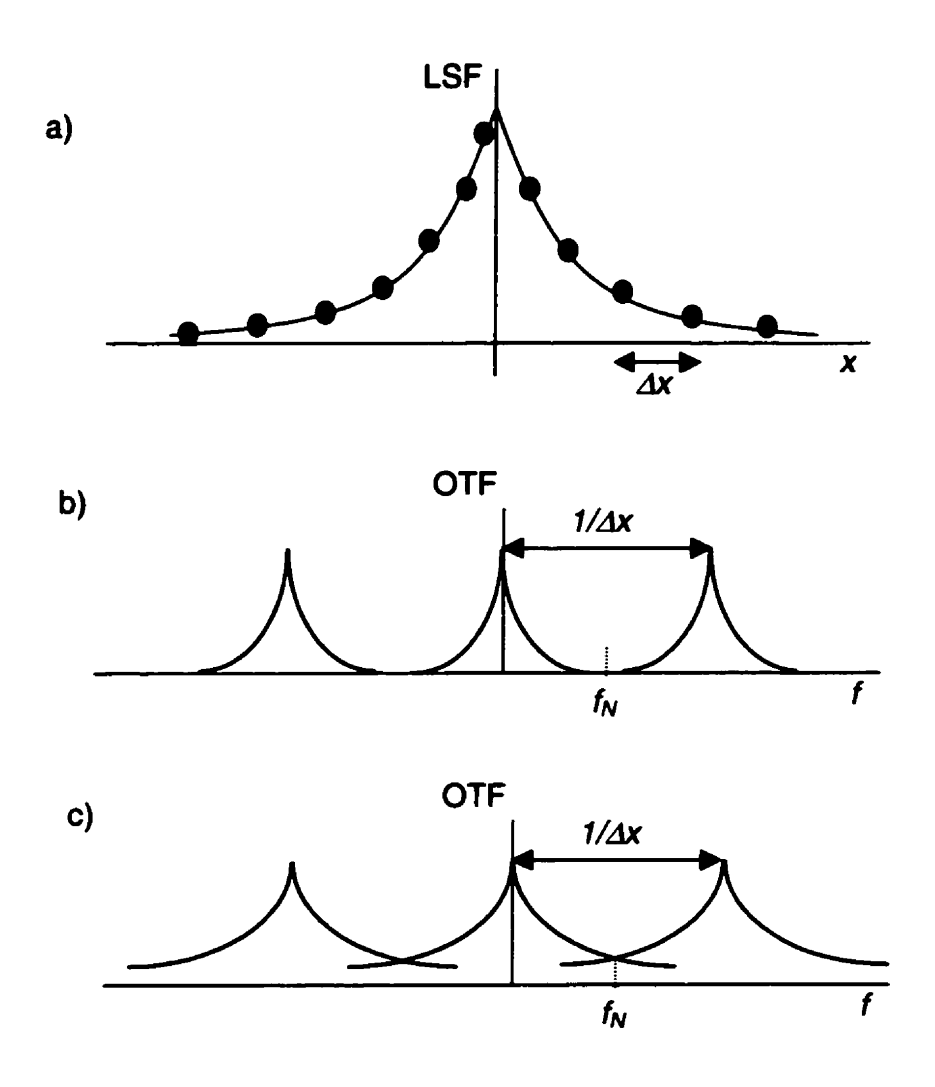


Figure 3.5: Schematic representation of (a) undersampling of LSF in cartesian space, (b) corresponding repetition of OTF in frequency space, and (c) aliasing due to the overlap of the OTF.

that the overlaps between aliases are negligible. A rule of thumb is that the sampling frequency must be smaller than the Nyquist frequency, which is equivalent to saying that the spacing between samples must be at least half the size of the measuring aperture. In many modern digital detectors, the digital signal is sampled using a grid of square pixels with size a and pitch (i.e. centre-to-centre spacing) p. Since physically the condition  $p \ge a$  must be true for such detectors, it is not possible to have two samples per pixel size. For this reason these detectors are inherently undersampled.

For undersampled digital detectors, the definition of the MTF must be approached with caution because the condition of shift invariance is broken. <sup>10</sup> Consider an experiment in which one wishes to measure an LSF. The setup is such that the thin collimated line of x-rays falls in the centre of a column of pixels. The resulting digital LSF is shown schematically in Fig. 3.6 (a). The digital MTF is also shown and is seen to increase at high spatial frequencies relative to the presampling MTF because of aliasing. Now consider that the experiment is repeated, except this time the line of x-rays is shifted and falls in between two adjacent columns of pixels. The digital LSF and MTF will now be different, as can be seen in Fig. 3.6 (b). In general, any shift (except shifts equal to an integer number of pixels) will lead to a different MTF.

One way to generalize the MTF for digital systems is to average the digital MTF over all possible phases. This MTF is referred to as the "expectation MTF" (EMTF). <sup>10</sup> Although the EMTF gives a phase-independent description, it does not describe the degradation of a single sinusoid by a detector. For this reason the presampling MTF is usually used as a descriptor of the resolution of a digital imaging system.

Conceptually, the presampling LSF can be constructed by measuring the digital LSF at many phases. A more convenient method is to use the angulated-slit technique. 11,12 Here the input line is tilted slightly relative to the pixel grid, as shown

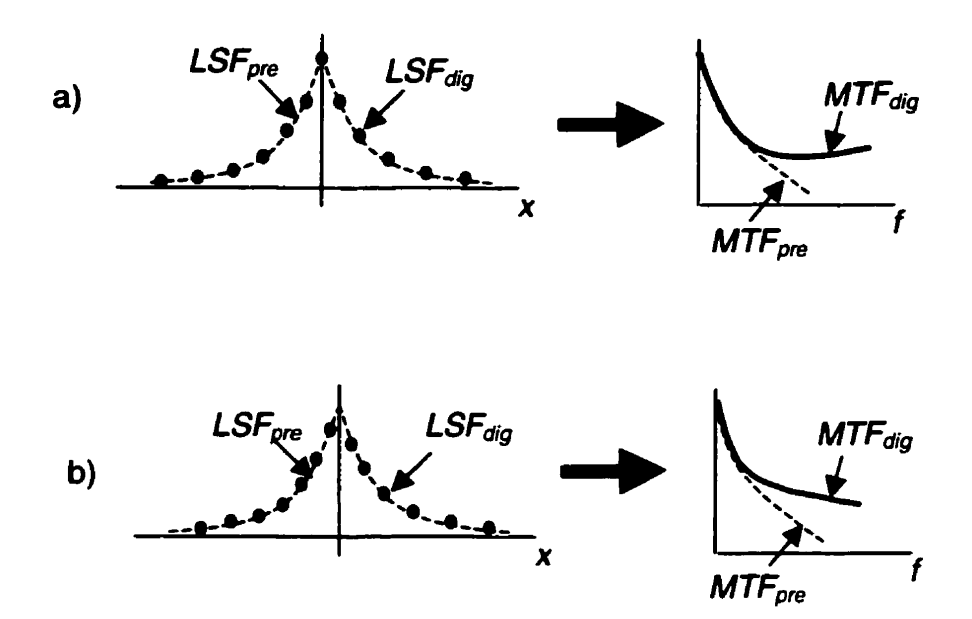


Figure 3.6: Digital LSF is measured with input line incident on (a) the centre of a row of pixels and (b) between two rows of pixels. Also shown are the corresponding digital MTFs (the dashed lines correspond to the presampling LSFs and MTFs).

LSF values from each row are recorded and used to piece together a finely sampled version of the presampling LSF (a smaller tilt angle results in a finer sample spacing). Fourier transformation then leads to the presampling MTF.

#### 3.2.4.2 Digital Noise Power spectrum

The NPS of a digital detector is affected in the same way as the MTF, i.e., it is repeated at regular intervals in the spatial frequency domain which can be expressed as 7.10

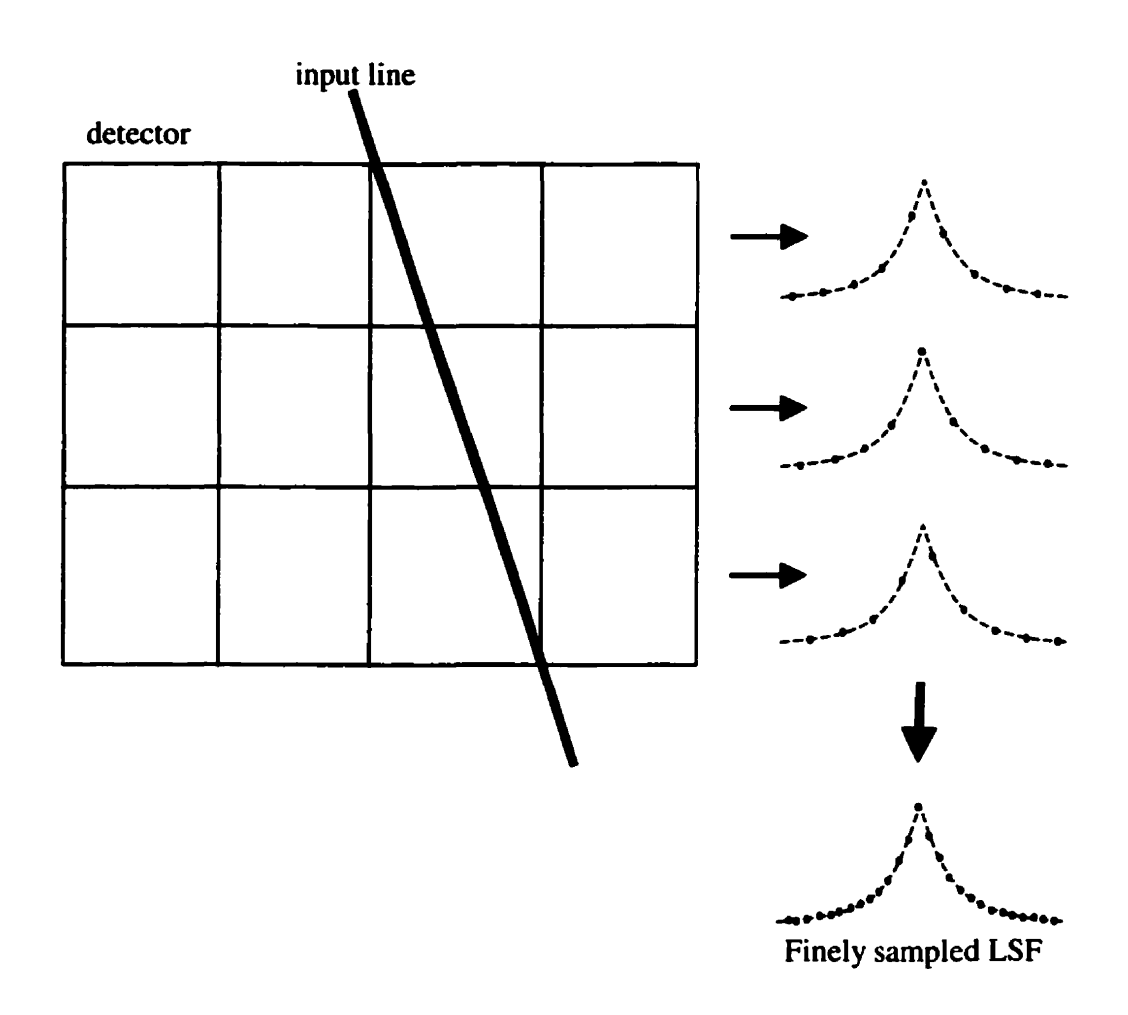


Figure 3.7: Angulated slit technique to determine the presampling LSF of an undersampled digital detector. The input line is slightly tilted relative to the pixel grid (tilt is exaggerated here for clarity), and the digital LSF values for each row are recorded. These values are pieced together to build a finely sampled version of the presampling LSF.

$$NPS_{dig}(u,v) = NPS_{pre}(u,v) \otimes \otimes \left[ \prod \left( u; \frac{1}{\Delta x} \right) \prod \left( v; \frac{1}{\Delta y} \right) \right]. \tag{3.50}$$

If the detector is undersampled, high noise frequencies can be disguised as low frequencies in the aliased NPS. Experimentally the *digital NPS*, which includes the effects of aliasing, is used as a measure of the noise properties of a digital detector.

#### 3.2.4.3 Digital Detective Quantum Efficiency

The DQE of a detector is a description of its signal-to-noise transfer properties for each spatial frequency. The "signal" and "noise" as a function of spatial frequency are aliased in undersampled digital detectors, and it is not clear how these should be defined in the DQE. If the signal is defined as the response of the detector due to a single sinusoid of a given frequency, it will be different than if it were defined as the response due to an input consisting of equal contributions from all spatial frequencies. This is because the assumption of shift-invariance is not held in undersampled digital detectors.

The *presampling* MTF correctly gives the response of the detector to a sinusoidal input of a given frequency. <sup>10</sup> In the output, a sinusoidal would be obscured by the *aliased* NPS for that given frequency, and thus a reasonable definition for the digital DQE is

$$DQE(\overline{q}_{0}, f) = \frac{MTF_{pre}^{2}(f)}{\overline{q}_{0} \cdot \left(\frac{NPS_{dig}(f)}{\overline{d}^{2}}\right)}.$$
(3.51)

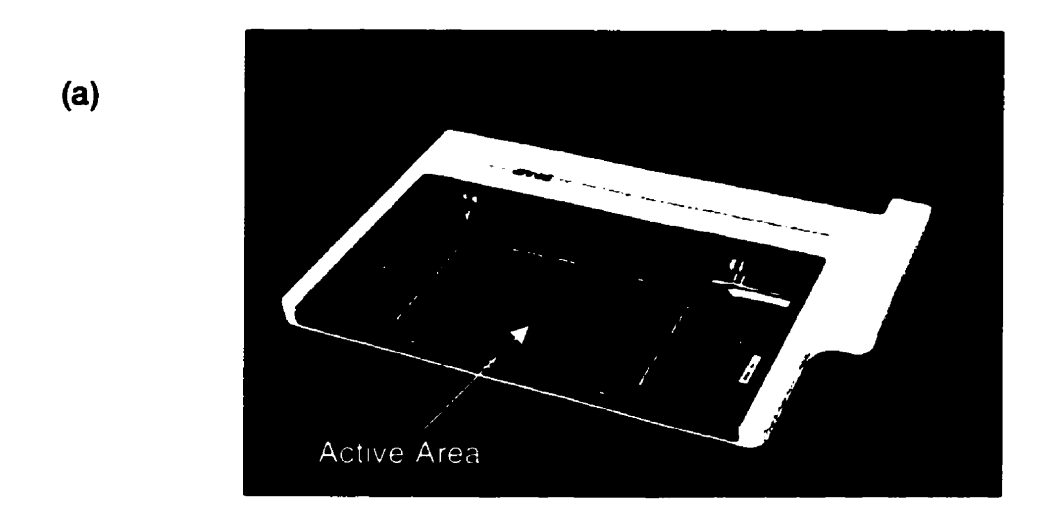
where  $MTF_{pre}(f)$  is the presampling MTF of the detector, which can be conveniently measured using the angulated slit technique, and  $NPS_{dig}(f)$  is the digital NPS of the

detector (which contains the aliased components which can not be removed). A drawback to this definition is that in practice the input to the detector will not consist of a single sinusoid but will contain many spatial frequencies. In fact, the signal and noise transfer properties of the detector will depend on the input to the detector since the particular input will determine how much aliasing is present. It is not possible to obtain an input-independent measure of the signal-to-noise properties of a digital detector. The definition of Eq. (3.51) is most commonly used as a measure of image quality for digital detectors.

# 3.3 Materials and Methods

# 3.3.1 Description of detector

The direct-detection AMFPI detector that we have used is a prototype a-Se based flat panel detector developed by ANRAD Corporation.<sup>13,14</sup> The detector has been designed for interventional mammography, and we are investigating its use and design modification for portal imaging. It is incorporated into a compact cassette, and is shown with the front cover removed in Fig. 3.8(a). A 200 µm a-Se layer is vacuum deposited directly onto an a-Si:H thin-film transistor (TFT) substrate. A coplanar bias electrode with a thickness of 450 nm has been evaporated onto the top surface of the a-Se layer which allows the application of a potential (up to 3000 V) across the a-Se. Above the electrode, there is a 40 µm polymer for electrical insulation. In order to use the detector at megavoltage energies, we have placed a 1.2 mm Cu plate in contact with the polymer, shown schematically in Fig. 3.8(b). Because we are unsure about the effect of pressure on



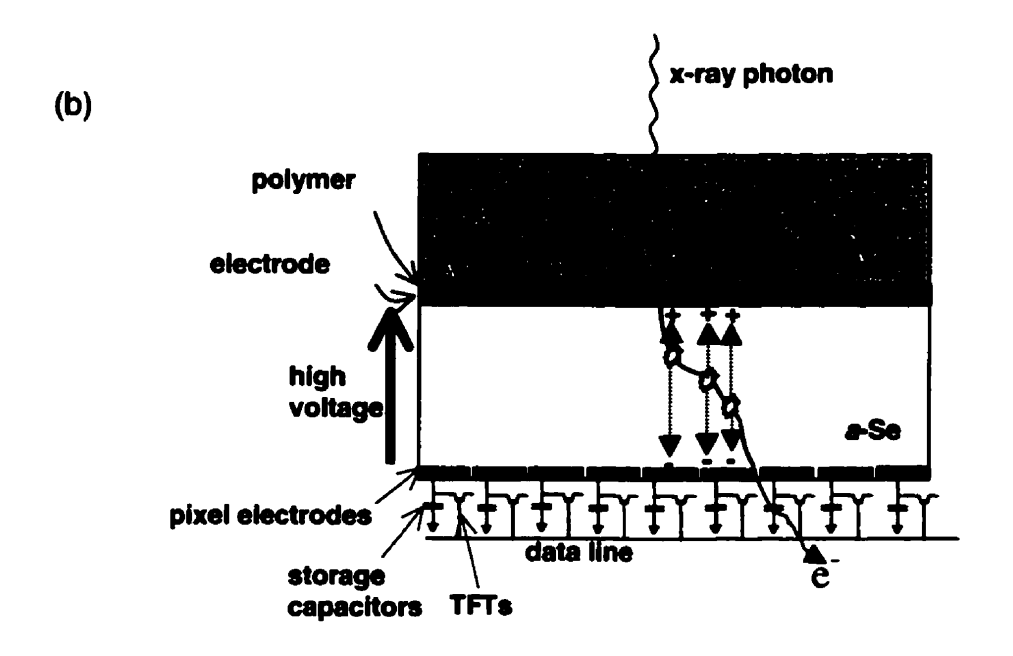
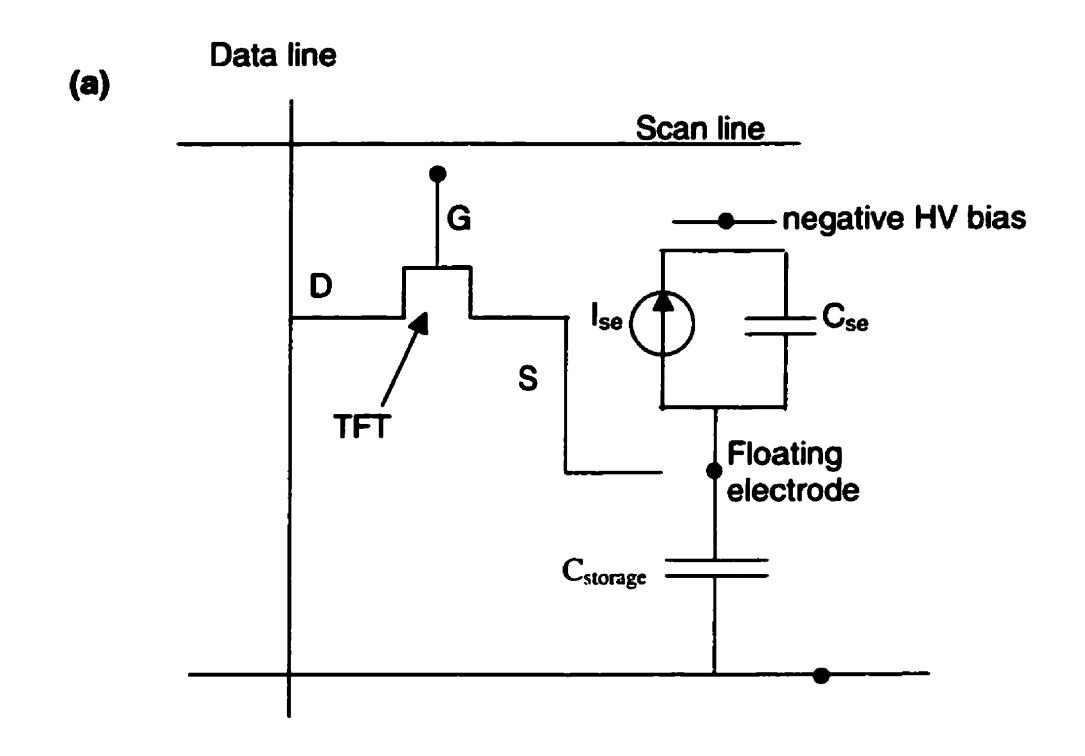


Figure 3.8: (a) Picture of direct-detection AMFPI with cover removed (b) Schematic diagram showing interaction of x-rays with the direct-detection AMFPI.

top of the flat-panel, a holding device was built to place the metal plate on the panel without actually resting on it. The device consists of two elbow-shaped nylon frames on opposite sides of the plate with the lower part of the elbow attached to the plate. The upper parts of the elbow have small nylon adjustment screws that rest on the casing surrounding the active area to allow the metal plate to be lowered right above the panel without applying pressure on it. The metal plate was smaller than the active area to avoid any contact with the edges of the panel and the casing. A paper thin sheet of plastic was placed between the plate and the panel to avoid scratching.

The TFT array has an active area of  $8.7 \text{ cm} \times 8.7 \text{ cm}$  and has  $1024 \times 1024 \text{ pixels}$  with an  $85 \,\mu\text{m}$  pitch. Each pixel comprises a common electrode, a pixel electrode, a  $0.68 \,\text{pF}$  storage capacitor and a TFT which acts as a switch as shown in Fig. 3.9(a). A micrograph of a pixel is also shown in Fig. 3.9(b). The source (S) and the drain (D) of each transistor are connected to the storage capacitance and to a data line, respectively, while the gate (G) is connected to a scan line.

The image formation process is as follows. X-rays interact with the metal/a-Se detector, and create electron-hole pairs within the a-Se layer (Fig. 3.8(b)). The charges drift in the applied electric field and are collected by the pixel electrodes at the surface, where they are integrated by the storage capacitors which are directly connected to the pixel electrodes. As opposed to other designs, which collect the holes, this design collects the electrons by applying a negative polarity on the top electrode. The capacitor thus becomes increasingly negative during irradiation, which allows for a self-limiting collection process. When a positive potential is placed on the gate of the transistor, the



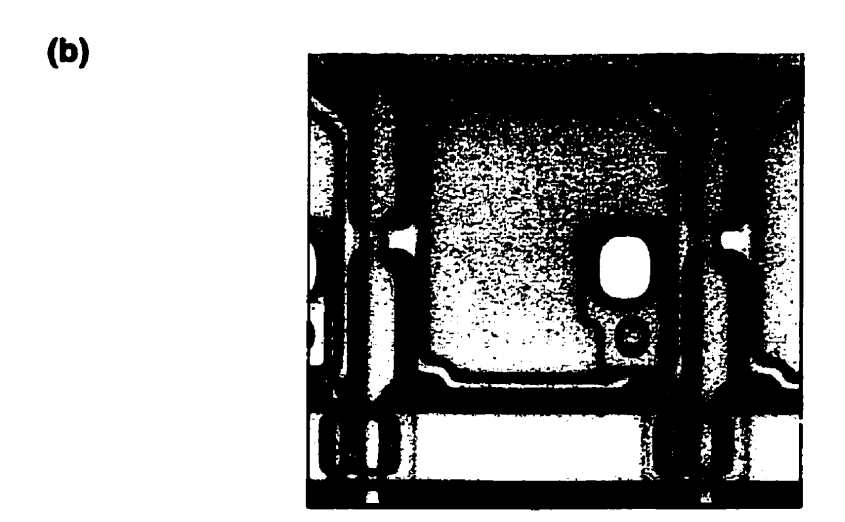


Figure 3.9: (a) Schematic diagram and (b) micrograph of a pixel in the direct-detection AMFPI.

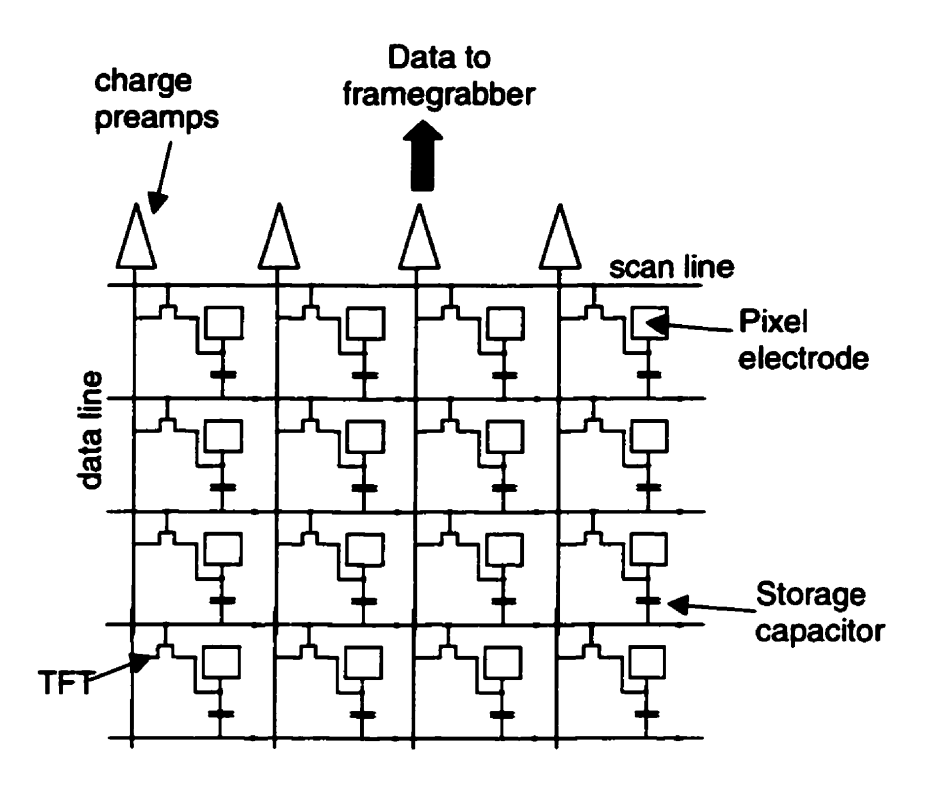


Figure 3.10: (a) Schematic diagram of the active matrix.

TFTs of one scan line are made conducting and the charges stored in the storage capacitance flow into the data lines to charge pre-amplifiers which are located at the end of the data lines as shown in Fig. 3.10. This action also automatically resets each individual pixel by putting the collecting electrode to ground. The process is repeated for each scan line to allow the reading of the two-dimensional image.

Other detectors, 15 which collect holes rather than electrons, are not self-limiting and require an independent reset of the device after each acquisition. The difficulty, however, with collecting the electrons is that their mobility is on the order of 100 times

lower than that of holes, meaning that they have a larger probability of falling into deep traps. This problem has been solved through the use of proprietary multi-layer a-Se in the detector. 14

Multichannel amplifiers and scan driver circuits are attached to the array to read out the collected charge. The amplifiers have various gain settings between 0.29 mV/fC and 8 mV/fC, with each setting having a linear dynamic range of 78 dB, 13-bit A/D conversion resolution, and an electronic noise of approximately 1600 electrons. Image data is transferred from the cassette to an interface module and a frame grabber (Genesis, Matrox Inc.) installed in a host computer by a high-speed serial link.

#### 3.3.2 Sensitivity

We explored various gain settings of the flat panel detector and found that saturation was achieved very quickly for the high settings. We thus chose the lower gain of 0.29 mV/fC for our measurements. Furthermore, although it was possible to attain applied electric fields up to 15 V/μm, we used a lower field of 5 V/μm to further decrease the system gain (a lower electric field results in more recombination of electron-hole pairs).

Prior to the measurements, ten offset images and ten flood-field images were acquired and averaged. These were used in subsequent images to correct for non-uniformities in the a-Se layer, and variable offsets and gains of the amplifiers.

#### Chapter 3 DQE measurements of a direct AMFPI at megavoltage energies

Measurements were performed on a Clinac 2300 EX (Varian Medical Systems, Palo Alto, CA) medical linear accelerator (linac) which has photon energies of 6 MV and 15 MV.

The sensitivity of the detector was measured by taking a series of uniform images, and taking the average pixel value in a  $5 \times 5$  cm<sup>2</sup> central region of interest. The detector was placed at an SSD of 140 cm, and various images were acquired with different monitor unit (MU) settings.\* The MUs were then converted to dose in water by measuring the dose in a solid water phantom (plastic material with x-ray interaction cross-sections very close to those of liquid water) with the same SSD as the detector and at depth of dose maximum. Sensitivity measurements were repeated with various dose rates ranging from 200 MU/min to 600 MU/min.

In order to investigate dark signal, *i.e.*, charges generated in the a-Se in the absence of radiation due to thermal fluctuations, we acquired images without radiation for various collection times. We also explored ghosting artifacts in a qualitative manner by irradiating high contrast objects and observing whether they were still visible in subsequent images.

<sup>\*</sup>A medical linear accelerator's output is measured in monitor units (MU), determined by ionization chambers in the linac head which are calibrated such that 1 MU results in a dose of 1 cGy (10<sup>-2</sup> J/kg) at the depth of maximum dose in water, at 100 cm away from the source with a field size of 10×10 cm<sup>2</sup>.

#### 3.3.3 Modulation Transfer Function

The measurement of MTF at megavoltage energies has been described in a number of works. <sup>16-20</sup> LSF images were acquired by collimating the beam with two lead blocks (25 cm × 5 cm × 10 cm) separated by 25 µm with shims. The blocks were placed on a motion stage which allows linear translation to within 0.05 mm, and the assembly was placed on the treatment couch as shown in Fig. 3.11. The gantry was rotated to 90° and the detector was placed directly behind the blocks (a separation between the blocks and the detector is shown in Fig. 3.11 for clarity). The legs of the stage were adjusted so

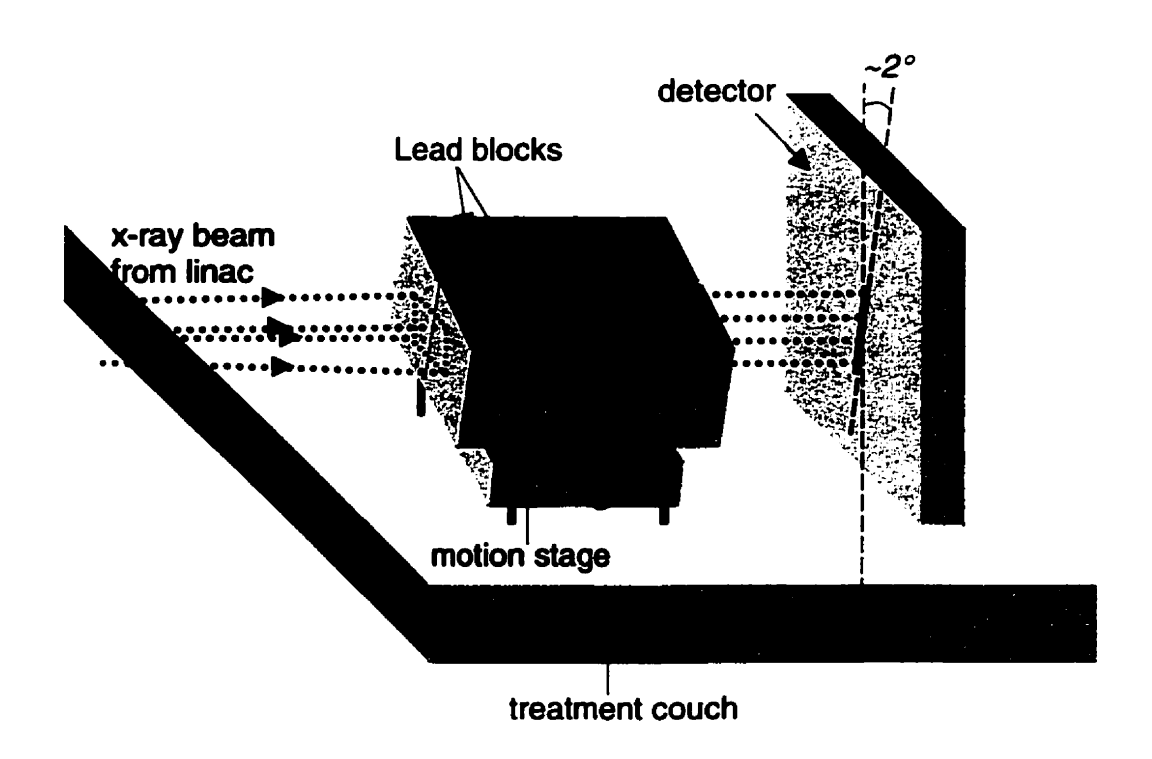


Figure 3.11: Experimental setup for LSF/MTF measurements.

that the blocks were tilted by approximately 2° relative to the pixelated grid of the detector. The motion stage was first leveled coarsely, and then was translated until maximum transmission through the blocks was achieved.

Images of the slit were taken with the 6 and 15 MV beams of the linear accelerator to form the line spread functions (LSFs). Background trends were removed by acquiring similar images with the slit translated by 5 mm so that it no longer faced the radiation beam, and subtracting these background images from the LSF images. The presampling LSFs were then constructed using the angulated slit technique described in Section 3.2.4.1. Although most of the background signal was removed from the subtraction, any remaining background was subtracted (typically less than about 3% of the signal). The LSFs were folded about their centre and averaged to reduce statistical uncertainty. The magnitude of the Discrete Fourier Transforms were calculated and normalized to unity at zero spatial frequency to determine the presampling MTFs.

# 3.3.4 Noise Power Spectrum

The detector was irradiated with 10 uniform fields for 6 and 15 MV beams, and the images were corrected with the offset and gain corrections. Since we were unsure of the extent of radiation damage to the electronics outside of the sensitive area, we limited our field size to  $10 \times 10 \text{ cm}^2$  at the detector surface. For this reason, and also because our metal plate did not cover the entire image area, we extracted a central  $800 \times 800$  pixel region from each uniform exposure to avoid penumbral effects. Each field was further subdivided into 16 sub-images for analysis. The two-dimensional NPS was calculated

#### Chapter 3 DQE measurements of a direct AMFPI at megavoltage energies

from the difference between sub-images and averaged.<sup>7</sup> The NPS of the difference images was used to correct for any low-frequency trends not completely removed from the image correction procedure. The resulting NPS was divided by two to account for the increased noise due to the subtraction of images. In order to obtain a one-dimensional NPS from the two-dimensional NPS, we extracted a 4×4 slice on either side of the central axis.<sup>21</sup> The spatial frequencies were taken as  $f = \sqrt{u^2 + v^2}$ , and the resulting NPS values were sorted into bins of 0.1 cycles/mm width. We compared other techniques of extracting the 1-D NPS and found that the results were essentially the same.

# 3.3.5 Detective Quantum Efficiency

We calculated the DQE using Eq. (3.51). Evaluation requires knowledge of the fluence (photons per unit area) incident on the detector surface. 18.22 Although direct measurement of this quantity is not possible, it can be approximately calculated from dose in water. The dose in solid water at the plane of the detector was measured at the same SSD as the flat-field NPS measurements, and at the relevant depth of maximum dose for the given energy (6 or 15 MV). In order to convert these doses to fluence, we used the Monte Carlo code EGSnrc<sup>23</sup> (discussed in Chapter 4) to calculate fluence-to-dose ratios for the given geometry. For these simulations we used 6 MV and 15 MV spectra generated by our treatment planning system which produce the correct measured percent depth dose curves. We obtained fluence-to-dose factors of 7.51×10<sup>-8</sup> cGy·mm²/photon (6 MV) and 1.11×10<sup>-7</sup> cGy·mm²/photon (15 MV). The estimation of fluence from dose is not necessarily very precise; for example our fluence-to-dose factor

is within 15-20% of those used by Munro and Bouius<sup>20</sup> which is at least partially due to the difference in energy spectra between linear accelerators.

#### 3.4 Results and Discussion

The sensitivity curves we obtained for the flat-panel detector are shown in Fig. 3.12. The curves are linear within experimental uncertainties with a slope of  $(344 \pm 2)$ counts/cGy, and a latitude of about 4 cGy. Larger sensitivities are possible with larger electric fields and/or gain settings, at the expense of the latitude. The sensitivity of the detector was found to be the same for both 6 and 15 MV beams. This is in agreement with the fact that  $W_{\pm}$  is independent of x-ray energy in the megavoltage energy regime, as discussed in Chapter 2. We also found that the sensitivity is unaffected by the dose rate for the repetition-rate settings of our linear accelerator. This is because virtually all recombination is due to initial recombination which, as opposed to general recombination, is independent of dose rate.<sup>24</sup> We investigated the effect of dark current for various accumulation times and found that it was negligible for up to 1 minute accumulation, which is much larger than typical acquisition times which are on the order of 1-2 seconds. We found little evidence of ghosting artifacts, and only saw faint outlines for very high contrast objects at very high doses, which is not likely to pose a problem in megavoltage imaging where contrasts are typically inherently low.

The measured presampling MTF curves are shown in Fig. 3.13 for the 6 and 15 MV beams. The MTF is degraded at the higher energy due to the increased lateral transport of high energy radiation within the detector. The results of the NPS

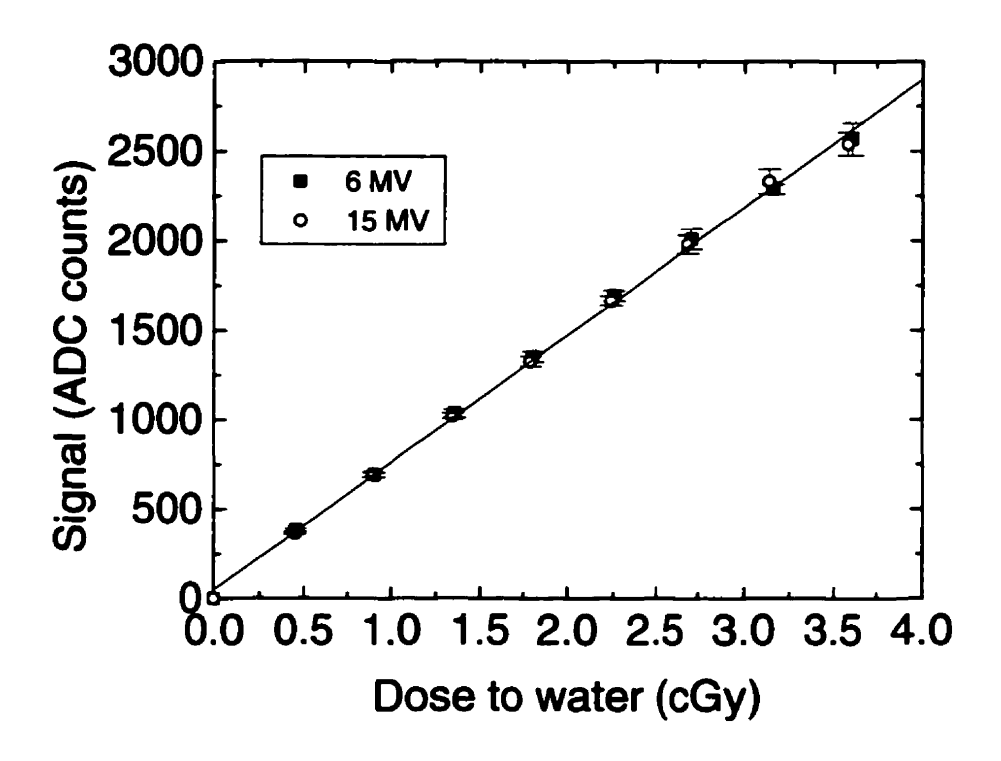


Figure 3.12: Sensitivity curve for the IMAM detector for 6 and 15 MV photon beams. Signal (ADC counts) is plotted versus dose measured in water at depth of dose maximum, with the same SSD as the detector.

measurements are shown in Fig. 3.14. The results are presented for a dose of 1 cGy; for other doses the NPS was found to be proportional to dose indicating that the detector is quantum limited at these doses (down to at least 0.5 cGy). Contrary to the case of diagnostic energies, where the NPS has been observed to be white for a-Se flat-panel detectors, 25 the NPS decreases with increasing spatial frequency at megavoltage energies. This must be due to correlations in the noise, which will be explored in Chapter 4. This effect is useful since it partially counter-balances some of the degradation of the DQE caused by the MTF.

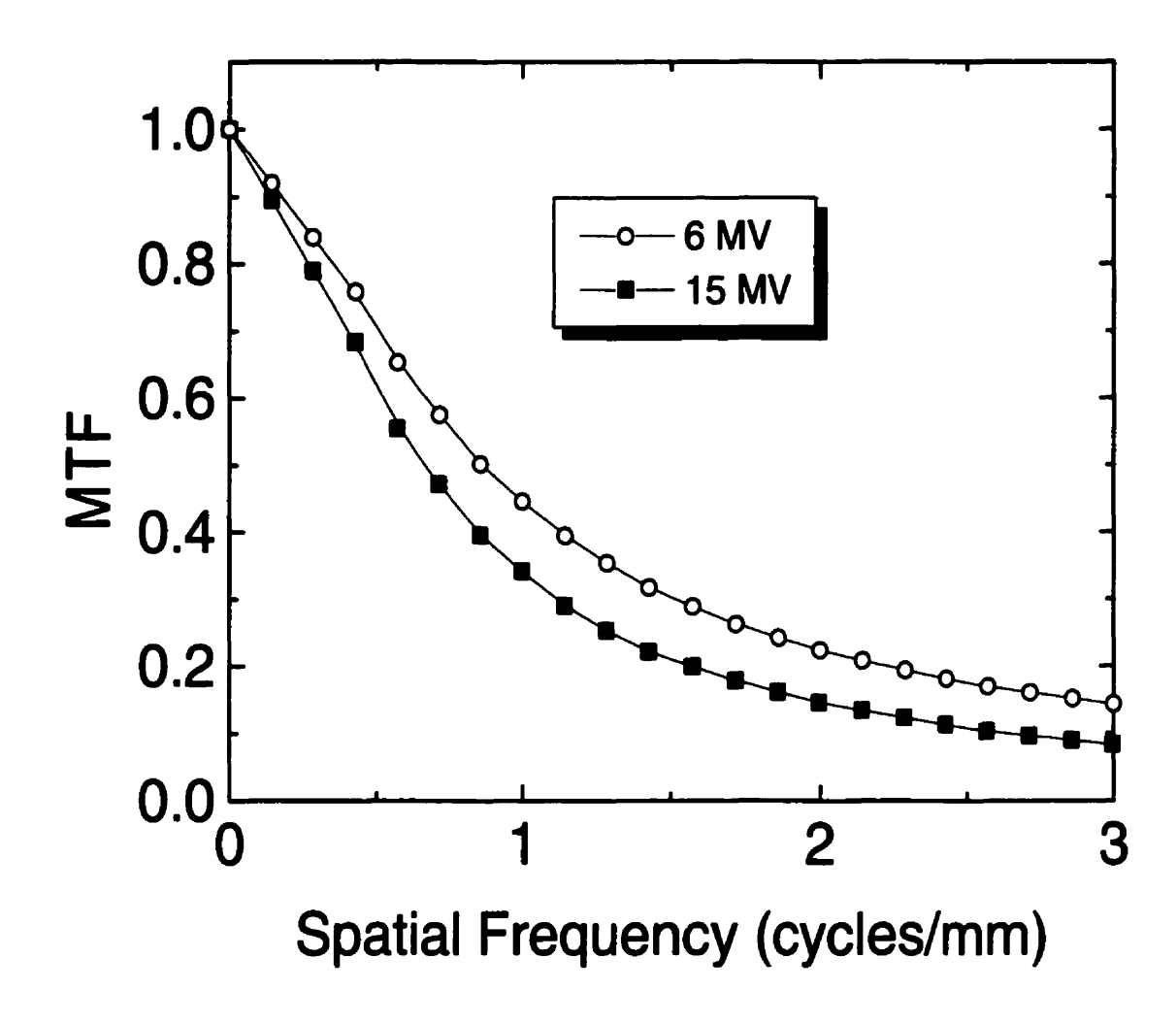


Figure 3.13: Presampling Modulation Transfer Function for the metal/a-Se AMFPI for 6 MV and 15 MV beams.

The measured DQE are shown in Fig. 3.14. A result which may seem surprising is the fact that the DQE is higher (and the NPS lower) for the 15 MV beam than for the 6 MV beam. We will see in Chapter 4 that our theoretical description of the DQE also predicts this. A possible explanation is that at high energies the total photon cross-section increases slightly with energy due to pair production. The opposite has been observed for

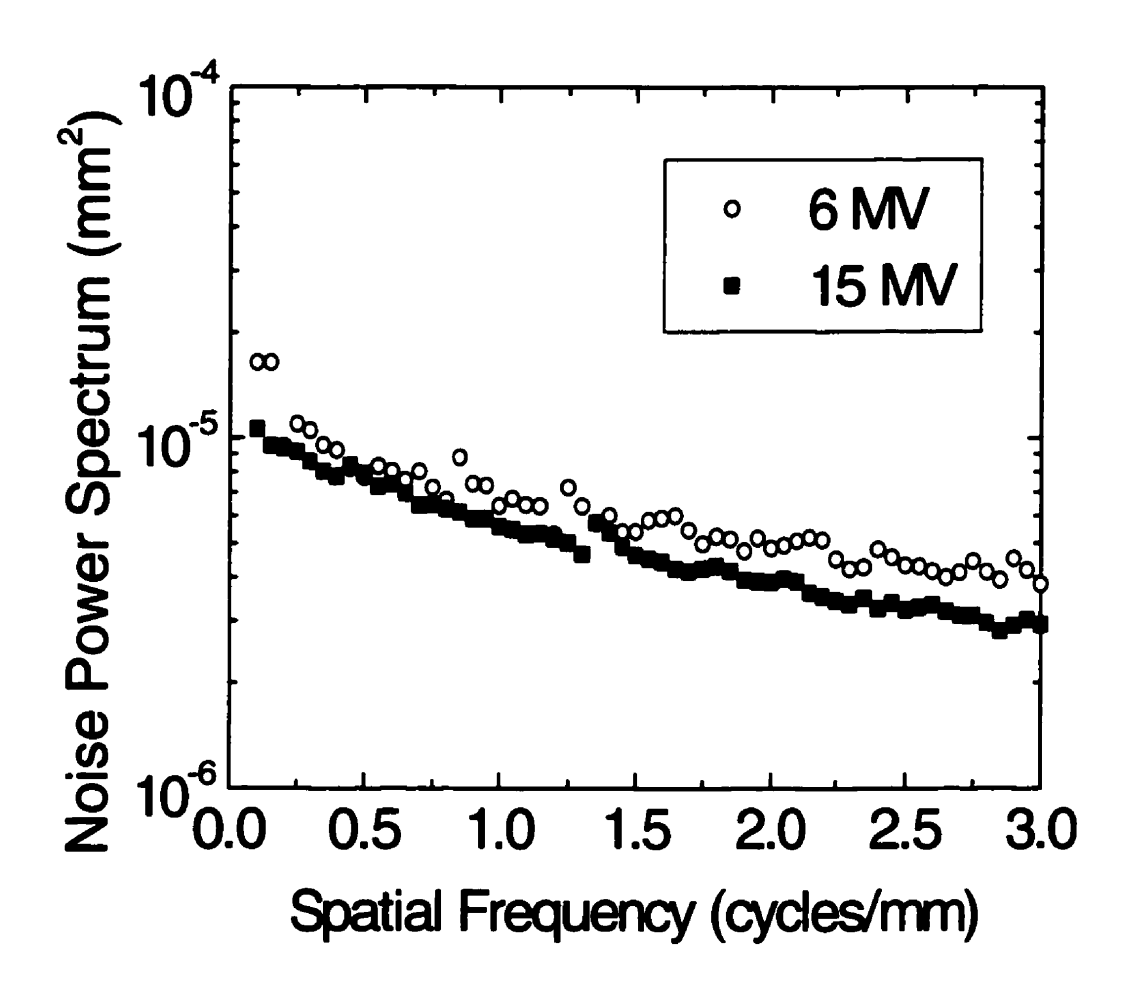


Figure 3.14: Measured Noise Power Spectrum for the metal/a-Se AMFPI for 6 MV and 15 MV beams.

an indirect AMFPI using a different linear accelerator,<sup>20</sup> however, and further investigation should be pursued into this matter.

In Fig. 3.16, we show the DQE we have measured for the direct AMFPI plotted against the indirect AMFPI measured by Munro and Bouius.<sup>20</sup> The DQE depends on the determination of fluence. Unfortunately, there is always a large uncertainty in the determination of fluence in these types of measurements, and the comparisons should be

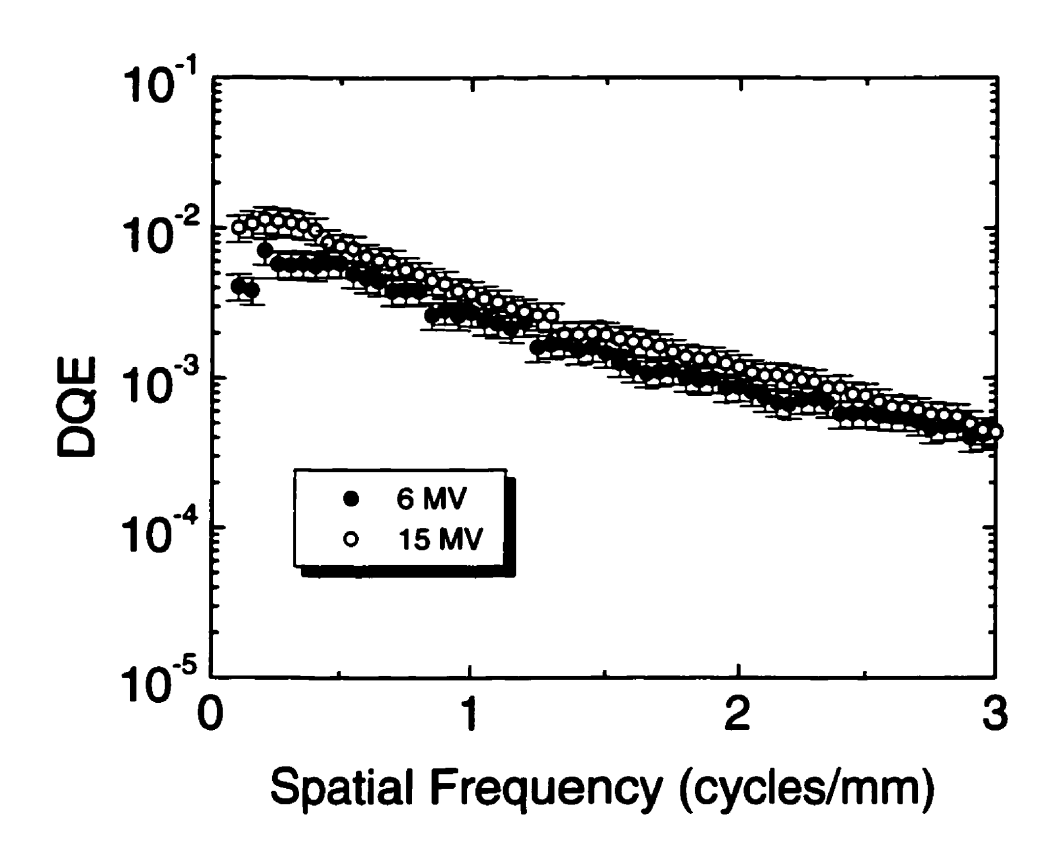


Figure 3.15: Measured Detective Quantum Efficiency for the metal/a-Se AMFPI for (a) 6 MV and (b) 15 MV beams.

studied with caution. Furthermore, the detectors have different mass thicknesses and pixel pitch which may substantially affect the DQE. Our direct detector has a mass thickness of 87 mg/cm<sup>2</sup> and pixel pitch of 85 µm while the indirect detector to which we compare has a mass thickness of 134 mg/cm<sup>2</sup> and pixel pitch of 750 µm. It can be seen that our detector has a lower DQE at zero spatial frequency, but there is a cross-over at about 0.3 cycles/mm after which the DQE of our detector becomes larger. The zero-frequency DQE of the direct AMFPI could be increased substantially by using a larger

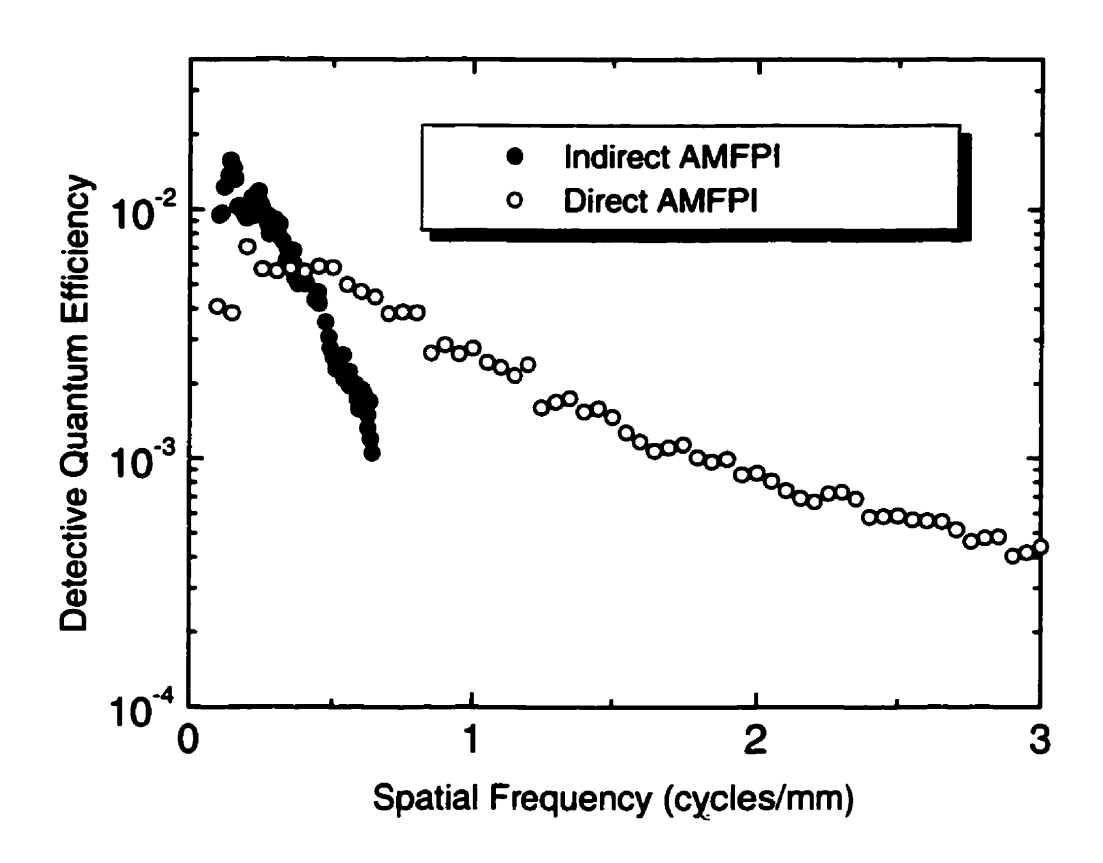


Figure 3.16: Detective Quantum Efficiency for the metal/a-Se based direct AMFPI compared to a metal/phosphor based indirect AMFPI.

a-Se layer, whereas the rapid drop-off with spatial frequency for the indirect AMFPI might be improved by using a smaller pixel pitch. These design characteristics must be explored further before a real comparison of direct vs indirect AMFPI detectors for portal imaging can be made. This will be explored in Chapter 4.

# 3.5 Conclusions

We have measured the sensitivity, MTF, NPS, DQE of a direct-detection AMFPI for megavoltage imaging. The detector consists of a 1.2 copper plate above a 200 µm a-Se layer with an a-Si:H TFT structure. The results for the DQE show that this detector exhibits very good imaging characteristics at megavoltage energies, and that these could be improved significantly with a larger a-Se thickness.

# 3.6 References

- [1] I.A. Cunningham, "Applied linear systems theory" in *Handbook of Medical Imaging*, Chapter 2 edited by R.L. Van Metter (SPIE, Bellingham, 2000).
- [2] J.C. Dainty and R. Shaw, Image Science (Academic Press, New York, 1974).
- [3] P. Sprawls, "X-ray imaging concepts: basic considerations" in *Proceedings of the 1991 AAPM Summer School: Specification, Acceptance Testing and Quality Control of Diagnostic X-ray Imaging Equipment* edited by J.A. Siebert, G.T. Barnes, and R.G. Gould (AAPM, New York, 1991).
- [4] R.N. Bracewell, The Fourier Transform and its applications (McGraw-Hill, 1978).
- [5] G.M. Jenkins and D.G. Watts, *Spectral analysis and its applications* (Holden-Day, San Francisco, 1968).
- [6] R.B. Blackman and J.W.Tukey, The measurement of power spectra (from the point of view of communications engineering) (Dover, New York, 1958).
- [7] M.B. Williams, "Noise power spectra of images from digital mammography detectors," Med. Phys. **26** 1279-1293 (1999).

#### Chapter 3 DQE measurements of a direct AMFPI at megavoltage energies

- [8] R. Shaw, "Absolute measures of optical instrumentation in medicine," Proc. SPIE. **70** 359-363 (1975).
- [9] R.F. Wagner and E.P. Muntz, "Detective Quantum Efficiency (DQE) analysis of xeroradiographic images," Proc. SPIE **70** 162-165 (1979).
- [10] J.T. Dobbins, "Effects of undersampling on the proper interpretation of modulation transfer function, noise power spectra, and noise equivalent quanta of digital imaging systems," Med. Phys. 22 171-181 (1995).
- [11] P.F. Judy, "The line spread function and modulation transfer function of a computed tomographic scanner," Med. Phys. 3 233-236 (1976).
- [12] H. Fujita, K. Doi and M.L. Giger, "Investigation of basic imaging properties in digital radiography," Med. Phys. 12 713-720 (1985).
- [13] A. Debrie, B. Polischuk, H. Rougeot, M. Hansroul, E. Poliquin, M. Caron, K. Wong, Z. Shukri and J.-P. Martin, "Quantitative analysis of performance of selenium flat-panel detector for interventional mammography," SPIE Physics of Medical Imaging 3977 417-425 (2000).
- [14] B. Polischuk, H. Rougeot, K. Wong, A. Debrie, E. Poliquin, M. Hansroul, J.P. Martin, T. Truong, M. Choquette, L. Laperriere, and Z. Shukri, "Direct conversion detector for digital mammography," SPIE Physics of Medical Imaging 3659 417-425 (1999).
- [15] D.L. Lee, L.K. Cheung, E.F. Palecki and L.S. Jeromin, "A new digital detector for projection radiography," Proc. SPIE 2432 237-249 (1995).
- [16] R.T. Droege and B.E. Bjarngard, "Metal screen-film detector MTF at megavoltage x-ray energies," Med. Phys. 6 515-518 (1979).

#### Chapter 3 DQE measurements of a direct AMFPI at megavoltage energies

- [17] R.T. Droege and B.E. Bjarngard, "Influence of metal screens on contrast in megavoltage x-ray imaging," Med. Phys. 6 487-493 (1979).
- [18] P. Munro, J.A. Rawlinson and A. Fenster, "Therapy imaging: a signal-to-noise analysis of metal plate/film detectors," Med. Phys. 14 975-984 (1987).
- [19] T. Falco and B.G. Fallone, "Characteristics of metal-plate/film detectors at therapy energies: I. Modulation Transfer Function," Med. Phys. **25** 2455-2462 (1998).
- [20] P. Munro and D.C. Bouius, "X-ray quantum limited portal imaging using amorphous silicon flat-panel arrays," Med. Phys. **25** 689-702 (1998).
- [21] J.T. Dobbins, D.L. Ergun, L. Rutz, D.A. Hinshaw, H. Blume and D.C. Clark, "DQE(f) of four generations of computed radiography acquisition devices," Med. Phys. 22 1581-1593 (1995).
- [22] T. Falco and B.G. Fallone, "Characteristics of metal-plate/film detectors at therapy energies: II. Detective Quantum Efficiency," Med. Phys. 25 2463-2468 (1998).
- [23] I. Kawrakow and D.W.O. Rogers, "The EGSnrc Code System: Monte Carlo Simulation of Electron and Photon Transport," NRCC Report PIRS-701 (2000).
- [24] D. Mah, J.A. Rowlands and J.A. Rawlinson, "Sensitivity of amorphous selenium to x rays from 40 kVp to 18 MV: Measurements and implications for portal imaging," Med. Phys. 25 444-456 (1998).
- [25] W. Zhao, I. Blevis, S. Germann and J.A. Rowlands, "Digital radiology using active matrix readout of amorphous selenium: Construction and evaluation of a prototype real-time detector," Med. Phys. **24** 1834-1843 (1997).

| 4.1 Introduction   | . 142         |
|--|---------------|
| 4.2 Background   | . 142         |
| 4.3 Theory   | . 147         |
| 4.3.1 Motivation for a new cascade equation                              | . 147         |
| 4.3.2 Derivation of a cascade equation for non-elementary stages         | . 149         |
| 4.3.3 Special cases of the non-elementary cascade equation               | . <i>15</i> 8 |
| 4.3.4 DQE of metal/phosphor detectors at megavoltage energies            | . <i>160</i>  |
| 4.3.5 DQE of metal/a-Se detectors at megavoltage energies                | . 164         |
| 4.3.6 DQE of direct and indirect AMFPI detectors at megavoltage energies | . 166         |
| 4.4 Materials and Methods  | . 167         |
| 4.4.1 Monte Carlo simulations of energy deposition                       | . 167         |
| 4.4.2 Monte Carlo simulations of optical transport within a phosphor     | . 170         |
| 4.4.3 DQE calculations   | . 172         |
| 4.5 Results and Discussion   | . 174         |
| 4.6 Conclusion   | . 181         |
| 4.7 References   | . 182         |

# 4.1 Introduction

In Chapter 3, measurements of the DQE for a prototype direct detection AMFPI were compared to the DQE of a prototype indirect detection AMFPI. The thickness, pixel size and pixel pitch of these detectors were different which made comparison difficult. To understand the effect that these detector characteristics have on image quality, it would be useful to have a theoretical description of the DQE. This can be approached using linear systems cascade analysis. We discuss this theoretical formalism in Section 4.2, and in Section 4.3 we extend the formalism so that we can apply it to megavoltage imaging. We use our formalism in conjunction with Monte Carlo techniques to calculate the DQE for direct and indirect AMFPIs which we compare to experimental results.

## 4.2 Background

The interaction of x-rays with a detector is governed by stochastic processes and as such affects the signal and noise of the final images. Furthermore, x-ray quanta may create other types of quanta, such as optical photons, which are also governed by stochastic processes. For this reason it is important to understand how the interactions of quanta within a detector affects the image quality.

Quanta have infinitesimal extent and can be described in a natural fashion using delta functions. They are treated in this manner in the theory of point processes.<sup>1,2</sup> We are often interested in two quantities: the average spatial distribution of quanta  $\overline{q}(r)$  (i.e., the expectation value of finding a quantum at a given location), and the noise power

spectrum NPS(f) which describes the statistical fluctuations about the average distribution. For calculation of these quantities it is possible to use a statistical analysis based on multivariate moment generating functions (MMGF) rather than point processes to describe the interaction processes.

Rabbani et al<sup>3,4</sup> have used an MMGF analysis to calculate the average and noise power spectra of quanta for two special cases. If the quanta undergo a pure amplification process, where the number of quanta changes but their locations do not, then the average and NPS of the distribution after the interaction,  $\overline{q}_{out}(r)$  and  $NPS_{out}(f)$ , are given in terms of the average and NPS before the interaction,  $\overline{q}_{in}(r)$  and  $NPS_{in}(f)$ , by the transfer relations

$$\overline{q}_{nut}(r) = \overline{g} \cdot \overline{q}_{in}(r) , \qquad (4.1)$$

$$NPS_{out}(f) = \overline{g}^{2} NPS_{in}(f) + \sigma_{g}^{2} \overline{\Phi}_{in} , \qquad (4.2)$$

where  $\overline{g}$  is the average amplification gain,  $\sigma_g^2$  is the variance of the gain, and  $\overline{\Phi}_{in}$  is the broad-area fluence at the input, *i.e.*, the zero-frequency component of the average distribution of input quanta

$$\overline{\Phi}_{in} = FT \{ \overline{q}_{in}(r) \}_{r=0}. \tag{4.3}$$

A special case of an amplification stage occurs if quanta have a probability  $\eta$  of being detected and  $1-\eta$  of not being detected. This is sometimes called a *binary selection* stage and is described by Eqs. (4.1) and (4.2) with  $\overline{g} = \eta$  and  $\sigma_g^2 = \eta(1-\eta)$ .

If quanta undergo a *pure dislocation process*, *i.e.*, they are dislocated to new locations but the number of quanta is conserved, then the transfer relations are given by

$$\overline{q}_{out}(r) = \overline{q}_{in}(r) \otimes p(r)$$
, (4.4)

$$NPS_{out}(f) = \left(NPS_{in}(f) - \overline{\Phi}_{in}\right)MTF^{2}(f) + \overline{\Phi}_{in}, \qquad (4.5)$$

where p(r) is the probability that a quantum scatters a distance r and  $MTF(f) \equiv FT\{p(r)\}$ . This shows that for a pure dislocation process, sometimes called stochastic blurring, the correlated noise is filtered by the square of the MTF while the uncorrelated part is not.

If quanta undergo many interactions within a detector consisting of pure amplifications or dislocations, then the expressions for the signal and noise can be cascaded as many times as necessary. This has been incorporated into a linear-systems cascade analysis framework by Cunningham<sup>5</sup> which has proven useful in the prediction of the signal and noise properties of various imaging modalities. In this framework the detector is conceptually subdivided into a series of stages. If a stage involves interaction of quanta, then it can be one and only one of either a) a pure amplification stage or b) a pure dislocation stage. At some stage in the detector the quanta must be converted to a physical signal which can be described by an average  $\overline{d}(r)$  and a noise power spectrum NPS(f). In cascade analysis, a stage involving a physical signal can be classified as either a) a deterministic blurring (or linear filter) stage, where the signal is blurred in a

deterministic fashion by a point spread function p(r) (perhaps by a physical aperture). This stage is described by the cascade equations

$$\overline{d}_{out}(r) = \overline{d}_{in}(r) \otimes p(r) , \qquad (4.6)$$

$$NPS_{out}(f) = NPS_{in}(f) \cdot MTF^{2}(f) , \qquad (4.7)$$

where  $MTF(f) = FT\{p(r)\}$ . Note that unlike an elementary dislocation stage the whole NPS is filtered by the square of the MTF; b) a noisy gain stage which may, for example, occur if the signal is fed through a noisy amplifier. In this case the cascade equations are given by

$$\overline{d}_{out}(r) = \overline{g} \cdot \overline{d}_{in}(r) , \qquad (4.8)$$

$$NPS_{out}(f) = \overline{g}^2 NPS_{in}(f) + \sigma_g^2 \overline{\Phi}_{in} , \qquad (4.9)$$

where  $\overline{g}$  and  $\sigma_g^2$  are the average and variance of the gain (although the cascade equations governing this stage have the same form as the equations for a pure amplification stage, the former is for a physical detector signal while the latter is for the multiplication of quanta through stochastic interaction processes); c an additive noise stage, where an independent noise source with noise power spectrum  $NPS_{add}(f)$  is simply added to the NPS of the previous stage, *i.e.*,

$$\overline{d}_{out}(r) = \overline{d}_{in}(r) \tag{4.10}$$

$$NPS_{out}(f) = NPS_{in}(f) + NPS_{add}(f) ; (4.11)$$

or d) an aliasing stage. If the signal is defined as the presampling signal and the NPS is replicated in the Fourier domain, then the cascade equations are given by

$$\overline{d}_{out}(r) = \overline{d}_{in}(r) , \qquad (4.12)$$

$$NPS_{out}(f) = \sum_{n=-\infty}^{\infty} NPS_{in}(f - \frac{n}{d}) . \qquad (4.13)$$

Once the image formation is delineated as a sequence of stages, the DQE at the  $i^{th}$  stage can be calculated from the expression

$$DQE_{i}(f) = \frac{\left|FT\left\{\overline{d}_{i}(r)\right\}\right|^{2}}{\overline{\Phi}_{0}NPS_{i}(f)},$$
(4.14)

where  $\overline{d}_i(r)$  is the average signal at the  $i^{th}$  stage produced by a delta-function input at the zeroth stage  $\overline{q}_0(r) = \overline{\Phi}_0 \delta(r)$  and where  $\overline{\Phi}_0$  is the average input fluence. This can be rewritten as

$$DQE_{i}(f) = \frac{\overline{g}_{1}^{2}\overline{g}_{2}^{2}...\overline{g}_{i}^{2}MTF_{1}^{2}(f) \cdot MTF_{2}^{2}(f)...MTF_{i}^{2}(f)}{NPS_{i}(f)\overline{\Phi}_{0}},$$
(1)

where the numerator is the squared product of all gains and MTFs for each stage up to the  $i^{th}$  stage. Note that the order of the stages is important, as the cascade equations for the NPS do not all commute.

# 4.3 Theory

#### 4.3.1 Motivation for a new cascade equation

The interaction of quanta with a detector may involve multiple amplifications and dislocations. In some cases, it may not be possible to clearly delineate a sequence of elementary stages from these interactions. Barrett *et al*<sup>1</sup> have used the theory of correlated point processes to develop a more general approach, where a single quantum may create many secondaries which are each dislocated to different positions. In this formalism, they assume that the secondaries are not correlated to each other. They note that this is a good approximation for many interaction processes unless there is some physical mechanism coupling the secondaries, such as space charge.

It is possible that even though secondaries are not correlated by a physical coupling mechanism, that they can be correlated for other reasons. Consider as an example the interaction of x-rays at diagnostic energies with a phosphor screen. The simplest situation which can occur is that an x-ray interacts with the screen and deposits its energy locally, creating many optical quanta at the point of interaction. This process can be modeled as an elementary amplification stage. It is possible, however, that a fluorescent x-ray created at the initial interaction point deposits energy at another location in the phosphor. In this case, the optical photon "secondaries" created by the incident x-ray consist of two groups: those created at the primary interaction site and those created at the fluorescent reabsorption site. The optical photons in the first group are spatially correlated to the optical photons in the second group. This correlation is due to the fact

that the optical photons are created at different points along the track of ionizing radiation through matter, not because they are coupled by any physical mechanism such as a force.

The problem of fluorescent reabsorption has been described by Cunningham<sup>2</sup> using a parallel cascade formalism. In his analysis there are three paths that the ionizing radiation may follow: 1) the incoming x-ray deposits all of its energy at the interaction point, 2) the incoming x-ray deposits part of its energy at the interaction point, and the rest escapes the phosphor in the form of a fluorescent x-ray, and 3) the incoming x-ray deposits part of its energy at the interaction point, and the rest is deposited at another location by a fluorescent x-ray. In his work, the paths are analyzed individually and used to calculate the noise power spectrum using the parallel cascade formalism.

In situations where the number of possible paths that the ionizing radiation can take is large, it may not be feasible to use the parallel cascade approach. Consider, for example, megavoltage imaging with a metal/phosphor detector. As shown in Fig. 4.1, x-rays interact with the detector and create a complex shower of ionizing photons, electrons and positrons. The ionizing electrons and positrons create many optical photons along their paths through a large number of discrete collisions. The number of possible paths that these particles can undergo is very large, and these paths are typically calculated using Monte Carlo techniques. If we consider all of the optical photon "secondaries" created by a given interacting x-ray, we can not treat their locations as uncorrelated since they all depend on the particular path an ionizing particle takes through the phosphor. For example, it can be seen in Fig. 4.1 that the position of the  $(i+2)^{th}$  photon depends on the position of the  $(i+1)^{th}$  photon, which in turn depends on the

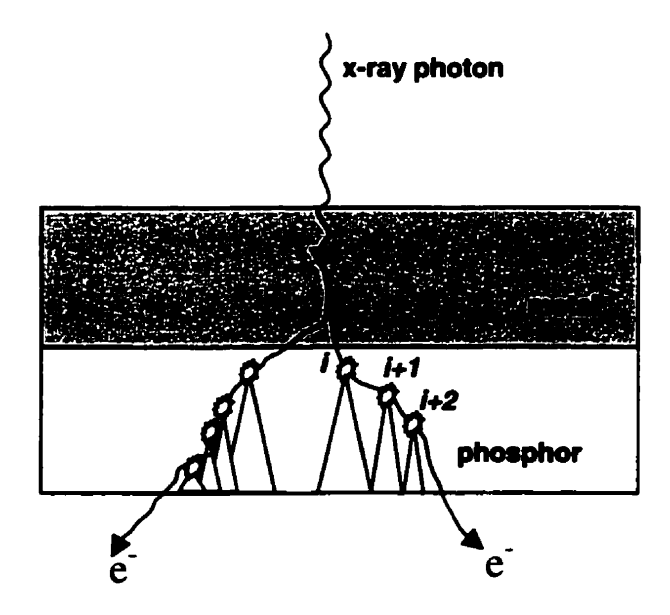


Figure 4.1: Schematic diagram showing the interaction of a megavoltage x-ray photon with a metal/phosphor detector. The x-ray creates a cascade of ionizing photons, electrons, and positrons which subsequently create optical photons along their paths. The locations of the ith, (i+1)th, (i+2)th, etc. optical photons are correlated to one another. The optical photons created scatter within the phosphor until they either they escape or they are absorbed.

position of the  $i^{th}$  photon, etc. In principle, the reason for the spatial correlation is the same as for the case of fluorescent reabsorption; the only difference is that the number of possible paths is greatly increased, making the solution using parallel cascades a difficult task. For this reason, we develop a new complimentary approach using multivariate moment generating function (MMGF) analysis to derive a cascade equation which can be easily evaluated using Monte Carlo simulations.

# 4.3.2 Derivation of a cascade equation for non-elementary stages

The goal is to derive equations for the signal and noise transfer for a stage involving multiple amplification and dislocation processes, where secondaries generated by the same input quantum may be correlated to each other. We follow the steps in the derivation of Rabbani  $et\ al^3$  closely to clearly identify the differences between our work and theirs.

Consider Fig. 4.2, where the input and output image planes are subdivided into pixels. The sets of random variables  $\{x_i\}$  and  $\{y_i\}$  represent the number of input and output quanta at each pixel, respectively. The goal is to calculate the multivariate moment-generating function (MMGF) of the output and express it in terms of the MMGF of the input which is defined as

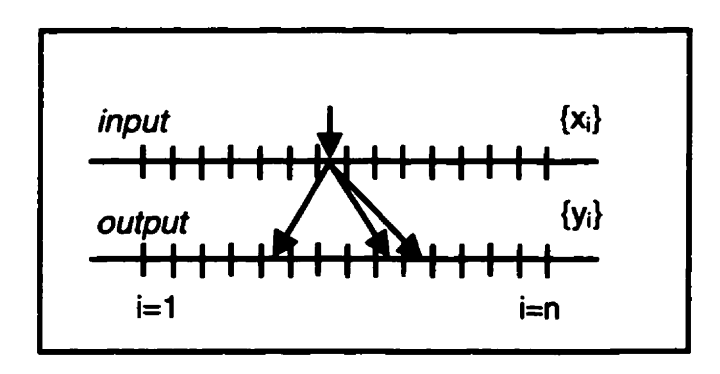


Figure 4.2: Schematic diagram showing the pixelization of the input and output plane used in the statistical analysis.

$$X(s) = \sum_{a_1} \dots \sum_{a_n} s_1^{a_1} \dots s_n^{a_n} \Pr\{x_1 = a_1, \dots, x_n = a_n\}, \qquad (4.15)$$

where  $Pr\{x_1 = a_1,...,x_1 = a_n\}$  denotes the probability that the input consists of  $a_1$  quanta at pixel 1,  $a_2$  quanta at pixel 2, etc. Statistical quantities such as the mean, variance and covariance can then be calculated from the MMGFs.

In their work, Rabbani *et al* derive the MMGF for pure amplification processes by defining the set of probabilities  $\{a_i(m)\}$  that an input quantum at the  $i^{th}$  pixel produces m output quanta. They have a separate derivation for pure dislocation processes by defining the set of probabilities  $\{p_j^{(i)}\}$  that a quantum originating from the  $i^{th}$  pixel scatters to the  $j^{th}$  pixel. In the situation we wish to consider, however, an input quantum can undergo any variety of processes, and thus the output it produces may consist of multiple correlated quanta spread out over various pixel locations in the output plane. This is the main difference between this work and that of Rabbani *et al*. To generalize the notation, we represent the output distribution, due to a *single* input quantum at pixel i, by the set of random variables  $\{g_j^{(i)}\}$ . We assume that the set  $\{g_j^{(i)}\}$  is shift invariant with respect to i, and can thus be represented by  $\{g_{i-j}\}$ .

The MMGF for the distributions represented by  $\{g_{i-j}\}$  is

$$Y(s \mid x_i = 1) = \sum_{g_{i-1}} \dots \sum_{g_{i-n}} s_1^{g_{i-1}} \dots s_n^{g_{i-n}} \Pr\{y_{i-1} = g_{i-1}, \dots, y_{i-n} = g_{i-n} \mid x_i = 1\} . \quad (4.16)$$

The summation can be re-ordered, yielding

$$Y(s \mid x_i = 1) = \sum_{g_1} ... \sum_{g_n} s_1^{g_{1-i}} ... s_n^{g_{n-i}} \Pr\{y_{i-1} = g_{i-1}, ..., y_{i-n} = g_{i-n} \mid x_i = 1\}, \quad (4.17)$$

where  $Pr\{y_{i-1} = g_{i-1}, ..., y_{i-n} = g_{i-n} \mid x_i = 1\}$  is independent of *i* due to the assumption of shift-invariance.

As previously described, each incident quantum will produce many output quanta. If we assume that the distribution of quanta produced by one input quantum is independent of the distributions produced by the other input quanta, then the MMGF for a *specific* input distribution of input quanta is given by

$$Y(s \mid x_1 = a_1, ..., x_1 = a_n) = [Y(s \mid x_1 = 1)]^{a_1} ... [Y(s \mid x_n = 1)]^{a_n}.$$
(4.18)

Note that we have merely assumed that the input quanta are independent, but there can still be correlations between the quanta in a given output distribution  $g_i$ . We obtain for a general input the output MMGF

$$Y(s) = \sum_{a_1} ... \sum_{a_n} [Y(s \mid x_1 = 1)]^{a_1} ... [Y(s \mid x_n = 1)]^{a_n} \Pr\{x_1 = a_1, ..., x_n = a_n\}, \quad (4.19)$$

which leads to

$$Y(s) = X(Y(s \mid x_1 = 1),...,Y(s \mid x_n = 1))$$
 (4.20)

Eq. (4.20) gives the output MMGF in terms of the MMGF of the input and the MMGF of the output produced by a single input quantum. Following Rabbani *et al*, we use the expression for the mean value and the covariance of  $y_i$ , which are given by

$$\overline{y}_{i} = \frac{\partial Y(s)}{\partial s_{i}} \bigg|_{s=1} = \sum_{k} \frac{\partial X(s)}{\partial s_{k}} \frac{\partial Y(s \mid x_{k} = 1)}{\partial s_{i}} \bigg|_{s=1}$$
(4.21)

and

$$cov(y_{i}, y_{j}) = \frac{\partial^{2} Y(s)}{\partial s_{i} \partial s_{j}} \Big|_{s=1} - \overline{y}_{i} \overline{y}_{j}$$

$$= \sum_{i} \sum_{k} \frac{\partial X(s)}{\partial s_{i} \partial s_{k}} \frac{\partial Y(s \mid x_{k} = 1)}{\partial s_{i}} \frac{\partial Y(s \mid x_{l} = 1)}{\partial s_{i}} \Big|_{s=1} + \sum_{k} \frac{\partial X(s)}{\partial s_{k}} \frac{\partial^{2} Y(s \mid x_{k} = 1)}{\partial s_{j} \partial s_{i}} \Big|_{s=1} - \overline{y}_{i} \overline{y}_{j}$$

$$(4.22)$$

The derivatives of the input MMGF are known to be

$$\frac{\partial X(s)}{\partial s_i}\bigg|_{s=1} = \overline{x}_i \tag{4.23}$$

and

$$\frac{\partial^2 X(s)}{\partial s_j \partial s_k}\bigg|_{s=1} = \operatorname{cov}(x_j, x_k) + \overline{x}_j \overline{x}_k - \overline{x}_j \delta_{jk} , \qquad (4.24)$$

where  $\delta_{ik}$  is the Kronecker delta function defined as

$$\delta_{jk} = \begin{cases} 1 & \text{if } j = k \\ 0 & \text{if } j \neq k \end{cases}.$$

The derivatives of Eqs. (4.21-4.22) can be expressed in terms of the  $\{g_i\}$  distributions as

$$\frac{\partial Y(s \mid x_k = 1)}{\partial s_i} \bigg|_{s=1} = \sum_{g_1} ... \sum_{g_k} g_{k-i} \Pr\{y_{k-1} = g_{k-1}, ..., y_{k-n} = g_{k-n} \mid x_k = 1\} , \quad (4.25)$$

and

$$\frac{\partial^{2} Y(s \mid x_{k} = 1)}{\partial s_{i} \partial s_{j}} \bigg|_{s=1} = \sum_{g_{1}} ... \sum_{g_{n}} g_{k-i} g_{k-j} \Pr\{y_{k-1} = g_{k-1}, ..., y_{k-n} = g_{k-n} \mid x_{k} = 1\}.$$
 (4.26)

In the work of Rabbani *et al*, these derivatives are expressible in terms of values such as the mean and variance of the amplification process for the case of a pure amplification or in terms or the probability of scattering to a new pixel for the case of a pure dislocation process.

In terms of our more general approach, we must carefully interpret  $\{g_k^{(i)}\}$  to evaluate the derivatives. Suppose we have N input quanta incident at the  $i^{th}$  pixel, labeled by m=1..N. Note that label m is simply an index used for notational convenience, not a label distinguishing one quantum from another. Using this notation, a particular realization of the distribution of output quanta produced by the  $m^{th}$  input quantum can be represented by  $g_{k-i}^{(m)}$ . Assuming we could construct a set of all possible  $g_{k-i}^{(m)}$  then we can re-write Eqs. (4.25) and (4.26) as

$$\left. \frac{\partial Y(s \mid x_k = 1)}{\partial s_i} \right|_{s=1} = \left\langle g_{k-i}^{(m)} \right\rangle_m \tag{4.27}$$

and

$$\frac{\partial^2 \mathbf{Y}(\mathbf{s} \mid \mathbf{x}_k = 1)}{\partial s_i \partial s_j} \bigg|_{\mathbf{s} = \mathbf{I}} = \left\langle g_{k-i}^{(m)} g_{k-j}^{(m)} \right\rangle_m . \tag{4.28}$$

where  $\langle \rangle_m$  denotes an average over the set, *i.e.*, over m=1..N as N tends to infinity. The expectation value and the covariance of the output are then given by

$$\overline{y}_i = \sum_{k} \overline{x}_k \left\langle g_{k-i}^{(m)} \right\rangle_m , \qquad (4.29)$$

and

$$\operatorname{cov}(y_i, y_j) = \sum_{l} \sum_{k} \left( \operatorname{cov}(x_k, x_l) - \overline{x}_k \delta_{kl} \right) \left\langle g_{k-i}^{(m)} \right\rangle_m \left\langle g_{l-j}^{(m)} \right\rangle_m + \sum_{k} \overline{x}_k \left\langle g_{k-i}^{(m)} g_{k-j}^{(m)} \right\rangle. \tag{4.30}$$

#### 4.3.2.1 Transfer relation for the Average distribution of quanta

In the limit of infinitely small pixels the average input and output distributions of quanta become continuous distributions of quanta per unit area as a function of position r, which we will write as  $\overline{q}_{in}(r)$  and  $\overline{q}_{out}(r)$ . Eq. (4.29) becomes a convolution and thus can be re-written as

$$\overline{q}_{out}(r) = \overline{q}_{in}(r) \otimes \langle g^{(m)}(r) \rangle_{-}, \qquad (4.31)$$

where  $g^{(m)}(r)$  is a particular realization of the spatial distribution of quanta produced by a single input quantum. If we define an average amplification gain as

$$\overline{g} = \int dr \langle g^{(m)}(r) \rangle_m , \qquad (4.32)$$

and a normalized point spread function

$$\overline{p}(r) = \frac{\left\langle g^{(m)}(r) \right\rangle_m}{\int dr \left\langle g^{(m)}(r) \right\rangle_m} , \qquad (4.33)$$

then the average output distribution can be re-written as

$$\overline{q}_{out}(r) = \overline{g} \cdot \overline{q}_{in}(r) \otimes \overline{p}(r) , \qquad (4.34)$$

which in the Fourier domain becomes

$$FT\{\overline{q}_{out}(r)\} = \overline{g} \cdot FT\{\overline{q}_{in}(r)\} \cdot MTF(f) , \qquad (4.35)$$

where  $MTF(f) \equiv FT\{\overline{p}(r)\}$ . The zero-frequency component of this distribution is the broad-area fluence, i.e.,

$$\overline{\Phi}_{out} = FT \{ \overline{q}_{out}(r) \}_{f=0}. \tag{4.36}$$

It follows that the transfer relation for this average fluence is

$$\overline{\Phi}_{out} = \overline{g}\overline{\Phi}_{in} \quad . \tag{4.37}$$

#### 4.3.2.2 Transfer relation for the Noise Power Spectrum

The noise power spectrum (NPS) is valid under wide-sense stationary (WSS) conditions, *i.e.*,  $\bar{x}_i = \bar{x}$  for all *i*. Under WSS conditions we can re-write the covariance  $cov(y_i, y_j) = R_y^{i-j}$  to indicate that it only depends on the difference *i-j*. From Eq. (4.30), this leads to

$$R_{y}^{i-j} = \sum_{k} \sum_{l} R_{x}^{k-l} \left\langle g_{k-i}^{(m)} \right\rangle_{m} \left\langle g_{l-j}^{(m)} \right\rangle_{m} - \overline{x} \sum_{k} \left\langle g_{k-i}^{(m)} \right\rangle_{m} \left\langle g_{k-j}^{(m)} \right\rangle_{m} + \overline{x} \sum_{k} \left\langle g_{k-i}^{(m)} g_{k-j}^{(m)} \right\rangle_{m} , \quad (4.38)$$

which in the limit of infinitesimal pixels becomes

$$R_{y}(r) = \int \int R_{x}(r_{1} - r_{2}) \langle g^{(m)}(r_{1} - r) \rangle_{m} \langle g^{(m)}(r_{2}) \rangle_{m} dr_{1} dr_{2}$$

$$- \overline{x} \int \langle g^{(m)}(r_{1} - r) \rangle_{m} \langle g^{(m)}(r_{1}) \rangle_{m} dr_{1}$$

$$+ \overline{x} \int \langle g^{(m)}(r_{1} - r) g^{(m)}(r_{1}) \rangle_{m} dr_{1} .$$

$$(4.39)$$

The noise power spectrum  $NPS_y(f)$  is defined as the Fourier Transform of  $R_y(r)$ , which leads to

$$NPS_{y}(f) = \iiint R_{x}(r_{1} - r_{2}) \langle g^{(m)}(r_{1} - r) \rangle_{m} \langle g^{(m)}(r_{2}) \rangle_{m} e^{-2\pi i r_{1}} dr_{1} dr_{2} dr$$

$$- \overline{x} \iiint \langle g^{(m)}(r_{1} - r) \rangle_{m} \langle g^{(m)}(r_{1}) \rangle_{m} e^{-2\pi i r_{1}} dr_{1} dr$$

$$+ \overline{x} \iiint \langle g^{(m)}(r_{1} - r) g^{(m)}(r_{1}) \rangle_{m} e^{-2\pi i r_{1}} dr_{1} dr$$

$$= \left| \langle FT \{ g^{(m)}(r) \} \rangle_{m} \right|^{2} (NPS_{x}(f) - \overline{x}) + \overline{x} \langle \left| FT \{ g^{(m)}(r) \right|^{2} \rangle_{m} .$$

$$(4.40)$$

We now modify the notation and write the transfer relation for the noise power spectrum as

$$NPS_{out}(f) = \overline{g}^2 MTF^2(f) \left( NPS_{in}(f) - \overline{\Phi}_{in} \right) + \overline{\Phi}_{in} S_g(f) , \qquad (4.41)$$

where  $NPS_{in}$  and  $NPS_{out}$  represent the input and output noise power spectra respectively, and

$$S_{g}(f) = \left\langle \left| FT \left\{ g^{(m)}(r) \right\} \right|^{2} \right\rangle_{m}. \tag{4.42}$$

## 4.3.3 Special cases of the non-elementary cascade equation

The transfer of average signal and noise for a stage which involves both amplifications and dislocations is given by Eqs. (4.34) and (4.41), and can be cascaded as many times as necessary. The equations involve the quantity  $S_g(f)$ , which requires a knowledge of the set of output distributions due to a single input quantum,  $\{g^{(m)}(r)\}$ . In future sections we will use Monte Carlo techniques to calculate the set. In certain simple cases, however,  $S_g(f)$  can be determined in a straightforward fashion as described below.

#### 4.3.3.1 Pure amplification stage

If the process consists of a pure amplification stage, then the  $\{g^{(m)}(r)\}$  will not depend on spatial position r and thus

$$S_{g}(f) = \left\langle \left(g^{(m)}\right)^{2}\right\rangle_{m}. \tag{4.43}$$

This can be expressed in terms of the average gain

$$\overline{g} = \left\langle g^{(m)} \right\rangle_m \tag{4.44}$$

and the variance of the gain

$$\sigma_g^2 = \left\langle \left( g^{(m)} \right)^2 \right\rangle_m - \left\langle g^{(m)} \right\rangle_m^2 , \qquad (4.45)$$

to yield

$$S_{g}(f) = \overline{g}^{2} + \sigma_{g}^{2}$$
 (4.46)

Since in this case MTF(f) = 1 then Eqs. (4.34) and (4.41) become the familiar cascade equations for a pure amplification stage,<sup>3</sup>

$$\overline{q}_{inut}(r) = \overline{g} \cdot \overline{q}_{in}(r) , \qquad (4.47)$$

$$NPS_{out}(f) = \overline{g}^{2} NPS_{in}(f) + \sigma_{g}^{2} \overline{\Phi}_{in} . \qquad (4.48)$$

#### 4.3.3.2 Pure dislocation stage

In the case of a pure dislocation stage, each output  $g^{(m)}(r)$  will consist of a delta function at a position  $r^{(m)}$ , and thus

$$S_{g}(f) = \left\langle \left| FT \left\{ \delta(r - r^{(m)}) \right\} \right|^{2} \right\rangle_{m} = 1 , \qquad (4.49)$$

which leads to the standard cascade equations for an elementary dislocation stage,3

$$\overline{q}_{out}(r) = \overline{q}_{in}(r) \otimes \overline{p}(r) \tag{4.50}$$

$$NPS_{out}(f) = \left(NPS_{in}(f) - \overline{\Phi}_{in}\right)MTF^{2}(f) + \overline{\Phi}_{in}, \qquad (4.51)$$

since  $\overline{g} = 1$ .

## 4.3.4 DQE of metal/phosphor detectors at megavoltage energies

#### 4.3.4.1 DQE neglecting Lubberts effect

In this section we focus on phosphor-based megavoltage x-ray detectors, although the principles are applicable to other megavoltage detectors. A fraction of x-ray photons interact with the detector, generating a complex shower of high-energy photons, electrons and positrons. These ionizing particles lead to the creation of many optical photons along their paths within the phosphor layer. The positions of these photons are correlated, as previously discussed in Section 4.3.1. The optical photons then scatter within the phosphor until they either they escape or are absorbed. These processes are shown schematically in Fig. 4.1.

In other works, the DQE of phosphor-based detectors at megavoltage energies has been calculated using cascade analysis consisting of elementary stages. Two approaches have been taken. Bissonnette *et al*<sup>8,9</sup> have divided the interactions into the following stages: 1) detection of x-rays by the phosphor, modeled as a binary selection process with probability  $\eta_1$ ; 2) scatter of ionizing radiation within the detector, modeled as an elementary dislocation with MTF  $T_2(f)$ ; 3) deposition of energy and creation of optical quanta, modeled as an elementary amplification with gain  $\overline{g}_3$  and variance  $\sigma_3^2$ ; 4) spread of optical quanta, modeled as an elementary dislocation stage with MTF  $T_4(f)$ ; and 5) loss of optical photons in the phosphor, a binary selection process with probability  $\eta_5$ .

The remaining stages which they used were specific to the mechanism of detection of optical photons (e.g., lens/mirror combination, CCD camera, etc), which we are not including in this work. The DQE calculated from these stages is given by

$$DQE(f) = \frac{\eta_1 \eta_5^2 \overline{g}_3^2 T_2^2(f) T_4^2(f)}{\eta_5^2 \left\{ \left[ \overline{g}_3^2 + \sigma_3^2 - \overline{g}_3 \right] T_4^2(f) + \overline{g}_3 \right\} + \eta_5 (1 - \eta_5) \overline{g}_3} \approx \eta_1 \frac{\overline{g}_3^2}{\overline{g}_3^2 + \sigma_{g_3}^2} T_2^2(f) , \quad (4.52)$$

where the approximation is made because  $\overline{g}_3 >> 1$ , *i.e.*, many optical photons are created per interacting x-ray (typically on the order of  $10^4$ ).

Since the scattering of ionizing radiation and the creation of optical photons occurs simultaneously, it is not clear why stage 2) should be placed before stage 3) in the analysis used to calculate Eq. (4.52). Drake *et al*<sup>10</sup> have taken the opposite approach and interchanged stages 2) and 3). In their work the steps become 1) x-ray interaction (binary selection with probability  $\eta_1$ ), 2) energy deposition and creation of optical photons (amplification stage with average gain  $\overline{g}_2$  with variance  $\sigma_{g_2}^2$ ), 3) total spread of high energy radiation and of optical quanta with a combined MTF of  $T_3(f)$ , and 4) loss of optical quanta in the phosphor (binary selection with probability  $\eta_4$ ). This leads to a different DQE than that of Bissonnette *et al*, and is given by

$$DQE(f) = \frac{\eta_1 \eta_4^2 \overline{g}_2^2 T_3^2(f)}{\eta_4^2 \left\{ \left[ \overline{g}_2^2 + \sigma_{g_2}^2 - \overline{g}_2 \right] T_3^2(f) + \overline{g}_2 \right\} + \eta_4 (1 - \eta_4) \overline{g}_2} \approx \eta_1 \frac{\overline{g}_2^2}{\overline{g}_2^2 + \sigma_2^2}, (4.53)$$

where we have again made the approximation that the optical photon gain is much larger than unity. Note that Eq. (4.53) predicts a DQE which is essentially independent of spatial frequency, which was not directly observed in the work of Drake et al because their DQE included effects of the lens/CCD system which dominated their DQE.

To solve the apparent problem of applying cascade analysis to megavoltage imaging, we may use the new transfer equations we have developed, given by Eqs. (4.34) and (4.41), to delineate the following stages: 1) x-ray interaction (binary selection with probability  $\eta_1$ ), 2) deposition of energy and creation of optical photons along the path of ionizing radiation (a non-elementary stage including multiple amplifications and dislocations, with parameters  $\overline{g}_2$ ,  $T_2(f)$ , and  $S_{g_2}(f)$ ), 3) spread of optical photons (elementary dislocation stage with MTF  $T_3(f)$ ), and 4) loss of optical photons (binary selection with probability  $\eta_4$ ). Using these stages, we use Eqs. (4.34) and (4.41) to obtain an expression for the DQE

$$DQE(f) = \frac{\eta_1 \eta_4^2 \overline{g}_2^2 T_2^2(f) T_3^2(f)}{\eta_4^2 \left[ \left[ S_{g_2}(f) - \overline{g}_2 \right] T_3^2(f) + \overline{g}_2 \right] + \eta_4 (1 - \eta_4) \overline{g}_2} \approx \eta_1 \frac{\overline{g}_2^2}{S_{g_2}(f)} T_2^2(f) . \quad (4.54)$$

Note that this DQE is similar to Eq. (4.52), with the  $\overline{g}^2 + \sigma_g^2$  term replaced by the frequency-dependent  $S_g(f)$  term. Thus our formalism predicts a spatial frequency dependence to Swank noise (i.e., noise due to the deposition of energy in the phosphor<sup>11</sup>).

In the approximation of many optical quanta per interacting x-ray, which is typically an excellent approximation, it be seen from Eqs. (4.52), (4.53) and (4.54) that the only parameters which are needed to evaluate the DQE depend on the deposition of energy in the phosphor (since the number of optical photons created is proportional to the energy deposition). Energy deposition in any material can be calculated using publicly

available Monte Carlo codes such as EGSnrc.<sup>12</sup> Implementation of this code to calculate the DQE will be described in Section 4.4.2.

#### 4.3.4.2 DQE including Lubberts effect

In the previous subsection we assumed that the transport of optical photons is not affected by the depth at which they were created. In practice, optical photons which are created farther away from the surface have less chance of escaping than those created near the surface; in addition they will also scatter more within the phosphor before escaping. This depth-dependence, referred to as the *Lubberts effect*, <sup>13</sup> is more likely to be important for thick phosphors. There are two possible approaches to include this effect. Van Metter *et al* <sup>14</sup> have used an MMGF analysis to modify the equations for cascade analysis of elementary stages to include the Lubberts effect. Their approach is only applicable to a series of elementary stages and in general is not applicable to our formalism. We thus we have chosen to include the Lubberts effect by explicitly modeling the transport of optical photons using Monte Carlo methods.

To accommodate this change, stages 2-4 in our cascade analysis are grouped together resulting in the following sequence of stages: 1) interaction of x-rays with probability  $\eta_1$ , 2) creation of optical photons along the tracks of ionizing radiation, and subsequent transport of the photons until they reach the phosphor surface (generalized stage with parameters  $\overline{g}_2$ ,  $T_2(f)$ , and  $S_{g_2}(f)$ ). These stages result in the DQE

$$DQE(f) = \frac{\eta_1 \overline{g}_2^2 |T_2(f)|^2}{S_{g_2}(f)} . {(4.55)}$$

Although this expression looks identical to Eq. (4.54), the terms represent different stages. Evaluation of this expression now requires not only Monte Carlo calculations of energy deposition in the phosphor, but also Monte Carlo modeling of optical transport. The specifics will be described in section 4.4.2.

#### 4.3.5 DQE of metal/a-Se detectors at megavoltage energies

In this section we apply the previous analysis to metal/a-Se detectors. We divide the signal formation into the following stages: 1) X-ray interaction with the detector, a binary selection stage with quantum efficiency  $\eta_1$ ; 2) Creation of electron-hole pairs along the track of ionizing radiation. This is the same as for metal/phosphor detectors except that electron-hole pairs are created instead of optical photons. The number of pairs  $n_{\pm}$  is given by

$$n_{\pm} = \frac{E_{abs}}{W_0} , \qquad (4.56)$$

where  $E_{abs}$  is the energy absorbed by the a-Se, and  $W_0 \approx 5$  eV is the energy required to create an electron-hole pair. <sup>15</sup> This is treated as a non-elementary stage with parameters  $\overline{g}_2$ ,  $T_2(f)$ , and  $S_{g_2}(f)$ ; 3) Escape from recombination. Some of the pairs recombine, as described in Chapter 2, and consequently do not contribute to the detectable signal. This is treated as a binary selection process with probability  $\eta_3$ . We assume that the electron-hole pairs drift parallel to the applied electric field with negligible deviation,

which has been shown to be an excellent approximation.<sup>16</sup> The DQE calculated from these stages is given by

$$DQE(f) = \frac{\eta_1 \eta_3^2 \overline{g}_2^2 T_2^2(f)}{\eta_3^2 S_{g_1}(f) + \eta_3 (1 - \eta_3) \overline{g}_2} \approx \eta_1 \frac{\overline{g}_2^2}{S_{g_2}(f)} T_2^2(f) , \qquad (4.57)$$

where, once again, the approximation comes from the fact that many electron-hole pairs are produced per interacting x-ray.

The stages for the metal/phosphor and metal/a-Se detectors are seen to be very similar. One of the main difference between phosphor and a-Se detectors is that optical photons in phosphor spread before being detected, whereas the electron-hole pairs in a-Se, to a good approximation, do not. In the limit of many quanta created per interacting x-ray, however, this difference is not manifested in the expression for the DQE. This is because even though the resolution of phosphors is degraded by the spreading of quanta, the scattered optical quanta are correlated to their point of origin which results in a NPS which decreases with increasing spatial frequency. This cancels out the degradation of the DQE caused by the MTF.

Evaluation of Eq. (4.57) requires calculation of the spatial positions of electronhole pairs along the tracks. Since the number of pairs is proportional to the energy deposited in a-Se, this can be accomplished using EGSnrc as long as we make the following assumptions: 1) the amount of recombination does not depend on the energy of ionizing particles, and 2) the amount of recombination does not depend on the depth of interaction in the a-Se. It was shown in Chapter 2 that these conditions are satisfied at megavoltage energies. The second condition would lead to an effect similar to the

Lubberts effect in phosphors. The fact that this limitation is not present in a-Se may be an important advantage over using phosphors, and will be explored later in this Chapter.

## 4.3.6 DQE of direct and indirect AMFPI detectors at megavoltage energies

The DQE of metal/phosphor and metal/a-Se detectors have been derived in Sections 4.3.4 and 4 3.5, respectively. We refer to these expressions as the analog DQE, i.e., the DQE that these detectors would have if the distribution of optical photons or electron-hole pairs could be perfectly detected. In a simple model of AMFPI detectors, these distributions of quanta are integrated over square pixels of size a with centre-to-centre spacing (pixel pitch) p. The stages can be delineated as follows: 1) Integration over pixels, described as a deterministic blurring stage. In our simple model the aperture response function is a rect function, which leads to a sinc function degradation in the spatial frequency domain; 2) aliasing due to digitization; and 3) addition of electronic noise. This is modeled as an additive noise component with NPS  $S_e(f)$ . Incorporation of these stages into the analysis lead to the DQE

$$DQE(f) = \frac{\eta_1 \overline{g}_2^2 T_2^2(f) \operatorname{sinc}^2(af)}{\sum_{g_2}^{\infty} S_{g_2}(f - \frac{n}{p}) \operatorname{sinc}^2(a(f - \frac{n}{p})) + \frac{S_{el}(f)}{\eta_1 \eta_1^2 a^4 \overline{\Phi}_0}}.$$
 (4.58)

Although the equation is the same for both direct and indirect AMFPIs, the terms  $\overline{g}_2^2$ ,  $T_2(f)$  and  $S_g$ , represent different physical processes. For direct detection they are

calculated from the spatial distribution of energy deposition in a-Se. For indirect detection, they can either be calculated from energy deposition within the phosphor if the Lubberts effect can be neglected, or they can be calculated from a full Monte Carlo simulation including optical transport if the Lubberts effect can not be neglected.

Eq. (4.58) depends on the pixel size a. In direct-detection systems, charges which fall within the spacing between pixel electrodes may accumulate, tending to repel further accumulation and thus leading to charges deviating towards the pixel electrodes. This results in a larger "effective" pixel size  $a_{coll}$ , which will modify Eq. (4.58) by replacing a with  $a_{coll}$ .<sup>17</sup>

#### 4.4 Materials and Methods

#### 4.4.1 Monte Carlo simulations of energy deposition

#### 4.4.1.1 Brief description of EGSnrc

Evaluations of the expressions for the DQE require knowledge of how energy is deposited in the detector. The best way to accomplish this is with a Monte Carlo code. In Chapter 2 we described a Monte Carlo code which we have written to calculate track structures. We have chosen not to use this code here since it was written for the specific task of calculating track structures and would have required major modifications. We have instead used EGSnrc, 12 which is freely available and widely used by the scientific

community. Although it can not calculate track structures, it is excellent for calculations of energy deposition in complex geometries.

Since the simulation of each collision, which we have implemented in our track structure code, is time consuming and not necessary for energy deposition calculations, EGSnrc uses a "condensed history" technique for transport of electrons and positrons, where many collisions are grouped together into a single interaction. The effective energy transfer and direction change are sampled from the appropriate multiple scattering distributions. This approximation is justified when particles undergo may collisions which individually only slightly affect the transport. This simplification introduces a *step length* parameter into the transport. Although the results are dependent on the step length, routines have been implemented to properly choose this parameter during simulations.

EGSnrc allows the user to define their geometry with a *user code*. Photons, electrons or positrons can be sent into the geometry, and the showers of ionizing particles they create are followed until all photons fall below a value PCUT and all electrons and positrons fall below a value ECUT (both parameters are user-defined, and are typically about 10 keV). The geometry can be separated into regions, and the user can keep track of the energy deposited in each of these regions in the user code.

#### 4.4.1.2 DQE simulations using EGSnrc

In order to evaluate the theoretical DQE for a-Se, we used EGSnrc to model the detector as a Cu plate above a layer of a-Se. The a-Se was modeled as atomic Se with a density of 4.27 g/cm<sup>3</sup> to match the density of the amorphous state. Modeling a-Se in this

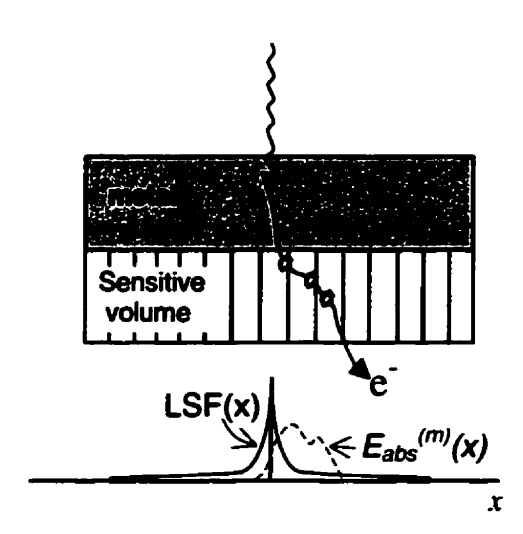


Figure 4.3: Schematic diagram showing modeling of detector using EGSnrc.

manner is adequate since we are only calculating energy deposition, not track structures as in Chapter 2.

We divided the a-Se layer into thin 0.1 mm strips as shown schematically in Fig. 4.3. A thin beam of N =  $10^6$  photons was set to be incident on the detector, with energy sampled from the 6 MV or 15 MV spectra used by our treatment planning system. For each photon history, the distribution of energy deposited in each strip  $E_{dep}^{(m)}(x)$  (m=1..N) was scored in the EGSnrc user code, and converted to  $g_2^{(m)}(x) = E_{dep}^{(m)}(x)/W_0$  where  $W_0 = 5$  eV (the actual value was not important since it cancels out in the expression for the DQE). The average of  $g_2^{(m)}(x)$  over all histories (normalized to unit area) produced the LSF which was used to calculate  $T_2(f)$ , and Eq.

(4.42) was used to calculate  $S_{r_2}(f)$ . The value for the gain  $\overline{g}_2$  was simply evaluated from the distributions  $g_2^{(m)}(x)$  by

$$\overline{g}_2 = \left\langle \int g_2^{(m)}(x) dx \right\rangle_m , \qquad (4.59)$$

and the fraction of x-rays which deposited energy gave the value for  $\eta_1$ .

For situations where the Lubberts effect could be neglected, energy deposition for metal/phosphor detectors was calculated in the same way as for a-Se except the a-Se layer was replaced by  $Gd_2O_2S$ :Tb with a reduced density of 3.67 g/cm<sup>3</sup> as described by Jaffray  $et\ al^{18}$  to account for air pockets. For thick phosphors where the Lubberts effect could not be neglected the phosphor was not only subdivided in the x plane but also in the z plane. The bin size in the z-direction ranged from 0.01 mm to 0.1 mm depending on the phosphor thickness. For each x-ray history, the energy deposited in each (x,z) bin was recorded in a text file. This text file was used as input to the optical transport code which is described in the following section.

### 4.4.2 Monte Carlo simulations of optical transport within a phosphor

We have written a Monte Carlo code which simulates optical transport in a phosphor. It is based on a code first described by Radcliffe *et al*<sup>19</sup> and later by Kausch *et al*.<sup>20</sup> The phosphor layer is assumed to consist of phosphor grains within a plastic binder. Optical photons scatter at the grain/binder interface, which is modeled by

randomly sampling an optical scattering length S from an exponential distribution  $\exp(-S/\overline{S})$ . The parameter  $\overline{S}$  is taken to be 25  $\mu$ m which represents the typical spacing between phosphor grains (this and all other parameters in the simulations are the same as used by Radcliffe et al<sup>19</sup> which gave reasonable results). The angular scattering is assumed to be isotropic.

For each optical photon history, an absorption length is sampled from an exponential distribution  $\exp(-T/\overline{T})$  where the parameter  $\overline{T}$  is taken to be 4 cm. If, for a particular history, the total pathlength of a photon exceeds the absorption length, it is absorbed within the phosphor and the history is terminated.

If a photon reaches the metal, it can either be absorbed by the metal or can reflect back into the phosphor. The reflectance of the metal is assumed to be 0.5. To accomplish this, a random number uniformly distributed between number between 0 and 1 is generated; if it is greater than 0.5, it is reflected whereas if the random number is less than 0.5 it is absorbed by the metal.

If a photon reaches the phosphor/air interface, one of two situations can occur. If  $\sin \theta \ge n_2/n_1$ , where  $\theta$  is the angle of incidence relative to the normal, then the photon undergoes total internal reflection and is reflected back into the phosphor for further transport. If  $\sin \theta < n_2/n_1$ , on the other hand, the photon escapes the phosphor and is detected.

The initial positions (x,z) of the optical photons are taken from the EGSnrc simulations, and the initial directions are sampled from an isotropic angular distribution.

For each optical photon, the transport is continued until either it is absorbed or it escapes the phosphor. The x-coordinate of the escaped photons is recorded to build the set  $g_2^{(m)}(x)$ . The quantities  $T_2(f)$ ,  $S_{p_1}(f)$ , and  $\overline{g}_2$  are then calculated from  $g_2^{(m)}(x)$ .

#### 4.4.3 DQE calculations

We first ran simulations to compare the DQE predicted by the equations of Bissonnette *et al* and Drake *et al* to the DQE predicted by our formalism (without Lubberts effect since this effect was not included in the other works) for a 1 mm Cu plate and a 134 mg/cm<sup>2</sup> Gd<sub>2</sub>O<sub>2</sub>S:Tb phosphor detector.

Most experimental data for the DQE of metal/phosphor detectors are for systems with read-out stages which severely degrade the DQE, such as lens assemblies, and thus the intrinsic DQE of the metal/phosphor is masked in these measurements. Munro *et al*<sup>21</sup> have measured the DQE for a 1 mm Cu plate and 400 mg/cm<sup>2</sup> Gd<sub>2</sub>O<sub>2</sub>S:Tb phosphor with x-ray film, and have shown that the resulting DQE is not significantly affected by presence of the film. For this reason their measured DQE can be taken as the intrinsic DQE of metal/phosphor. To verify our theory against this data, we ran simulations for the DQE for this detector. The thick phosphor used in their experiment, however, required us to include the Lubberts effect in our calculations.

To compare to experimental data for AMFPI detectors, we calculated the DQE using Eq. (4.58) for two detectors. The first detector was our direct-detection AMFPI described in Chapter 3, *i.e.*, 1.2 mm Cu above 200  $\mu$ m a-Se. We are unsure of the effective pixel size  $a_{coll}$ ; the real pixel size of the detector is approximately 75  $\mu$ m, but its

effective pixel size has been estimated to be approximately 80  $\mu$ m.<sup>22</sup> Over the range of spatial frequencies we have considered, we have found that varying  $a_{coll}$  from 75  $\mu$ m to 80  $\mu$ m in Eq. (4.58) does not create a significant difference in the DQE, and thus we have used  $a_{coll}$  = 75  $\mu$ m in our calculations. Since the detector was quantum limited over the doses used, we set  $S_{el}(f)$  = 0 in Eq. (4.58). The second detector to which we compared our simulations was the prototype indirect-detection AMFPI described by Munro and Bouius.<sup>23</sup> This detector has a 1.5 mm Cu plate above a 134 mg/cm<sup>2</sup> Gd<sub>2</sub>O<sub>2</sub>S:Tb phosphor, and a 0.75 mm pixel pitch. This detector was also shown to be quantum limited and thus we set  $S_{el}(f)$  = 0.

To allow comparison between direct and indirect AMFPI detectors, we calculated the DQE for mass thicknesses of 67, 134, 358, 721, and 947 mg/cm<sup>2</sup>. Mass thicknesses (*i.e.*, the product of thickness and density) were used instead of physical thicknesses for comparison between the different absorbing materials since x-ray absorption is proportional to this quantity (there is very little atomic number dependence at megavoltage energies<sup>24</sup>).

#### 4.5 Results and Discussion

Results of the DQE calculations using our theoretical formalism for the 1 mm Cu plate and a 134 mg/cm<sup>2</sup> Gd<sub>2</sub>O<sub>2</sub>S:Tb phosphor are shown in Fig.4.4, along with the DQE curves we have calculated using the equations of Bissonnette *et al* and Drake *et al*. For this thickness the x-ray quantum efficiency was calculated to be 0.0198, and the average optical photon gain to be 1.73×10<sup>4</sup> with an associated standard deviation of 1.66×10<sup>4</sup>, values similar to those calculated by Bissonnette *et al*. Although all three DQE curves have the same value at zero frequency, they exhibit very different spatial frequency dependencies. It can be seen that the DQE derived in this work lies between that predicted by the cascade stages of Drake *et al* and that predicted by the stages of Bissonnette *et al*. This is the result of correlations between the locations of the optical photons along the track of ionizing radiation.

Comparison of our theory (including Lubberts effect) to the experimental measurements of Munro et al are shown in Fig. 4.5, and excellent agreement is observed. Also shown are the DQE calculated using the cascade analysis of Bissonnette et al and Drake et al, but comparison is difficult since their equations do not include the Lubberts effect. The curve of Drake et al does not decrease with spatial frequency, and thus does not agree with experiment. The curve of Bissonnette et al has better agreement with experiment but underestimates the DQE; inclusion of the Lubberts effect in their model would only serve to decrease their DQE even further. This indicates that our

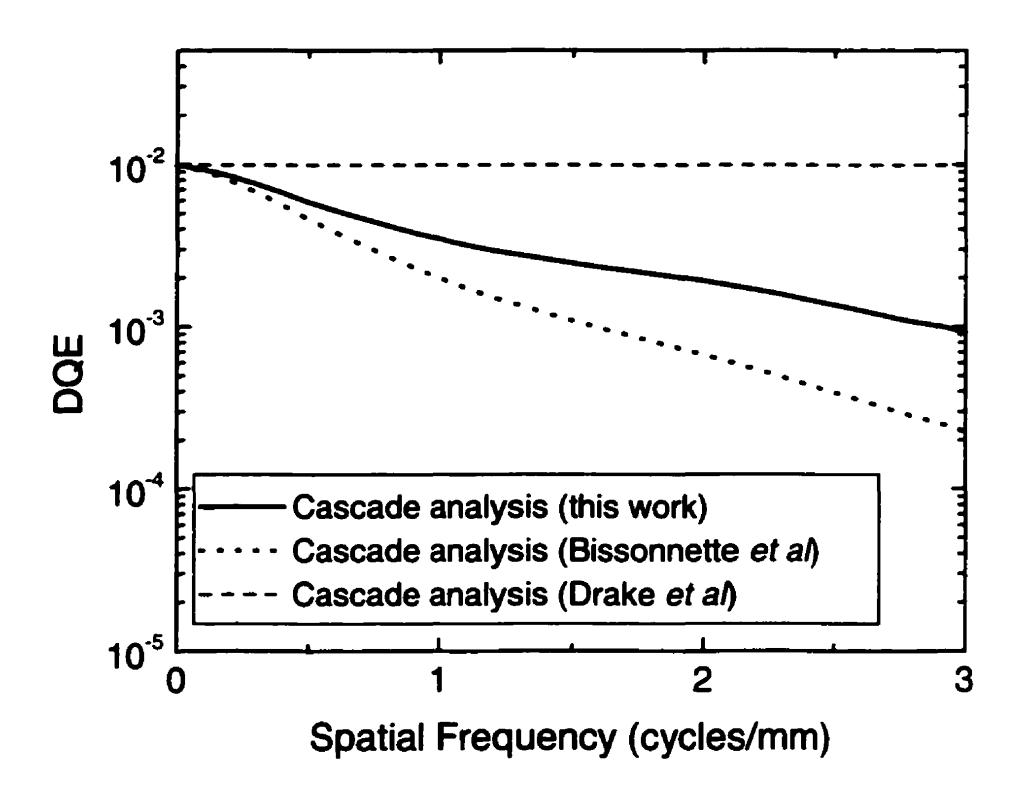


Figure 4.4: DQE for a 6MV x-ray beam interacting with a 1 mm Cu front plate above a 134 mg/cm<sup>2</sup>  $Gd_2O_2S$ : Tb phosphor calculated using the cascade analysis developed in this work (without taking the Lubberts effect into account) compared to the DQE calculated using the cascade analysis of Bissonnette et al<sup>8</sup> and of Drake et al<sup>10</sup>.

formalism provides a good description of the DQE of megavoltage metal/phosphor detectors.

Comparison between theory and our measurements for the MTF of the directdetection AMFPI which we described in Chapter 2 are shown in Fig. 4.6 and comparison for the DQE are shown in Fig. 4.7. The theoretical MTF and DQE agree very closely with the measured values for 6 MV, but underestimate the measured values

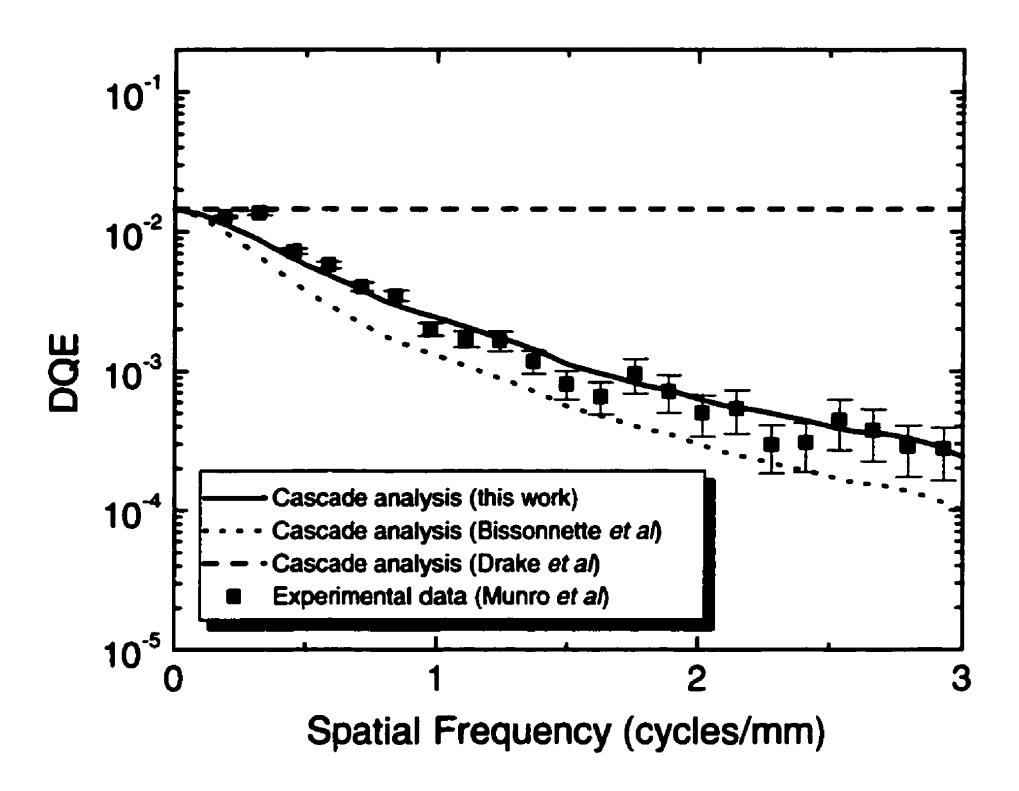


Figure 4.5: DQE for a 6MV x-ray beam interacting with a 1 mm Cu front plate above a 400 mg/cm2  $Gd_2O_2S$ : Tb phosphor calculated using the cascade analysis developed in this work (with the Lubberts effect taken into account) compared to the experimental measurements of Munro et al<sup>21</sup>. Also shown are the DQE calculated using the cascade analysis of Bissonnette et al<sup>8</sup> and of Drake et al<sup>10</sup>.

for 15 MV. We believe that this is due to the fact that 1.2 mm of Copper is insufficient for full buildup at 15 MV, and thus the simulations are more sensitive to the low energy portion of the spectrum which is not well known. For our simulation for the DQE of the indirect-detection AMFPI of Munro and Bouius, we obtained zero-frequency values which were about 10% low compared to experiment. We attributed this due to the fact that their flat panel is above a glass substrate. We added this substrate in our Monte Carlo

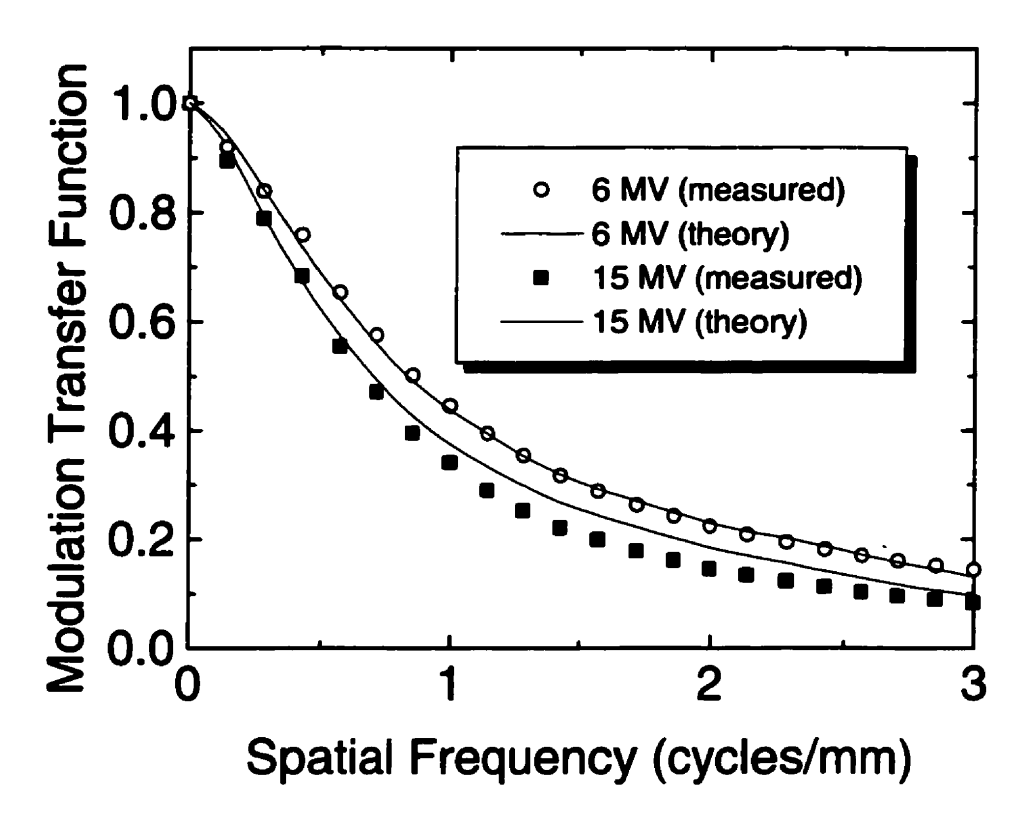


Figure 4.6: Theoretical calculations of MTF for the directdetection MTF compared to measured values, for 6 MV and 15 MV x-ray beams.

simulations, where we approximated it as 0.2 mm of Si (we found that the results did not vary substantially with Si thickness). The results are shown in Fig. 4.8, and show good agreement with experiment. The spatial frequency dependence of the DQE is dominated by aliasing of the NPS due to the large 0.75 mm pixel size. For this reason we have found that the DQE calculated from the model of Bissonnette *et al* fit the experimental data equally well since the aliasing overpowered any differences in the analog DQE.

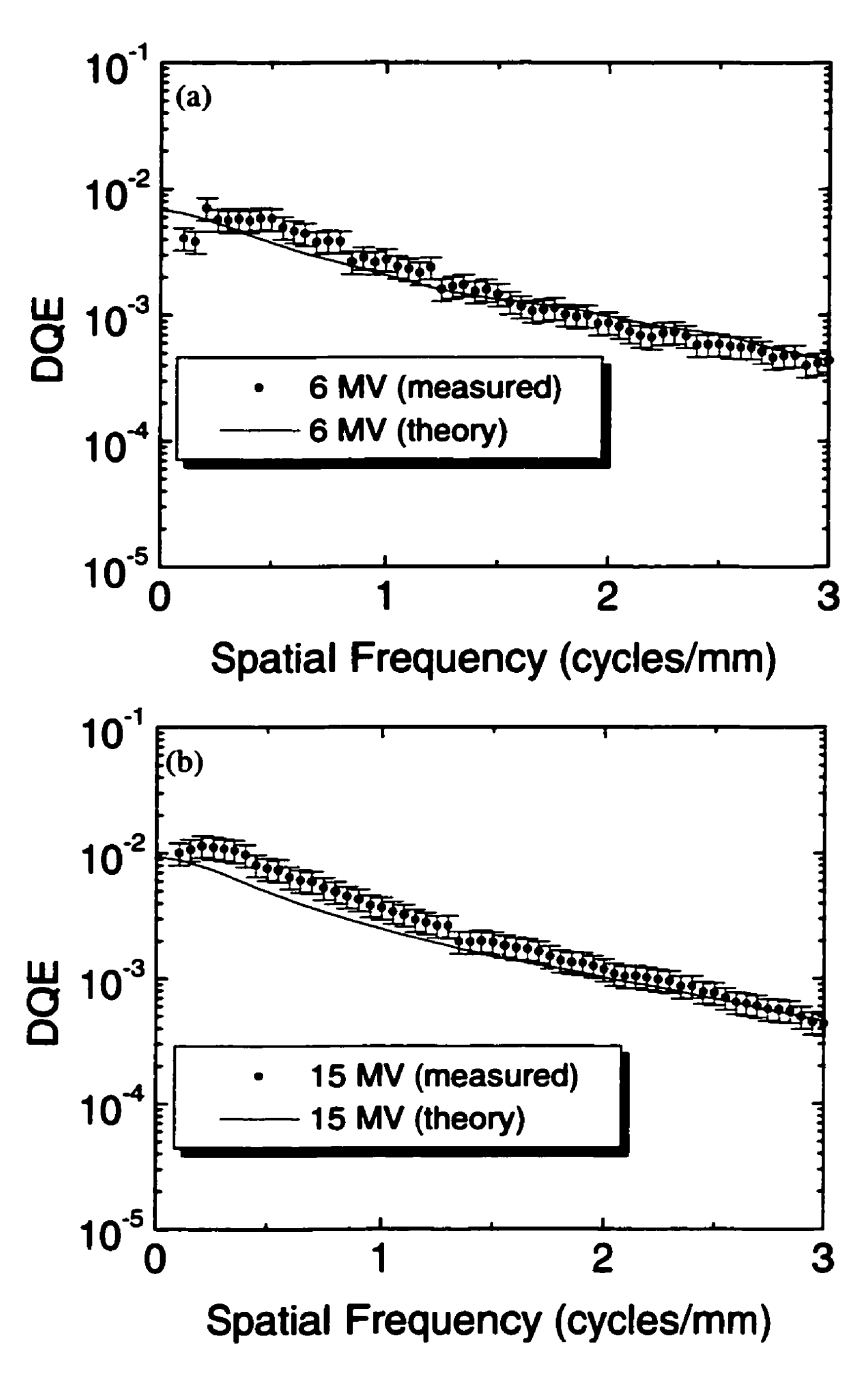


Figure 4.7: Theoretical calculations of DQE for the direct-detection MTF compared to measured values, for (a) 6 MV and (b)  $15 \, \text{MV} \, x\text{-rays}$ .

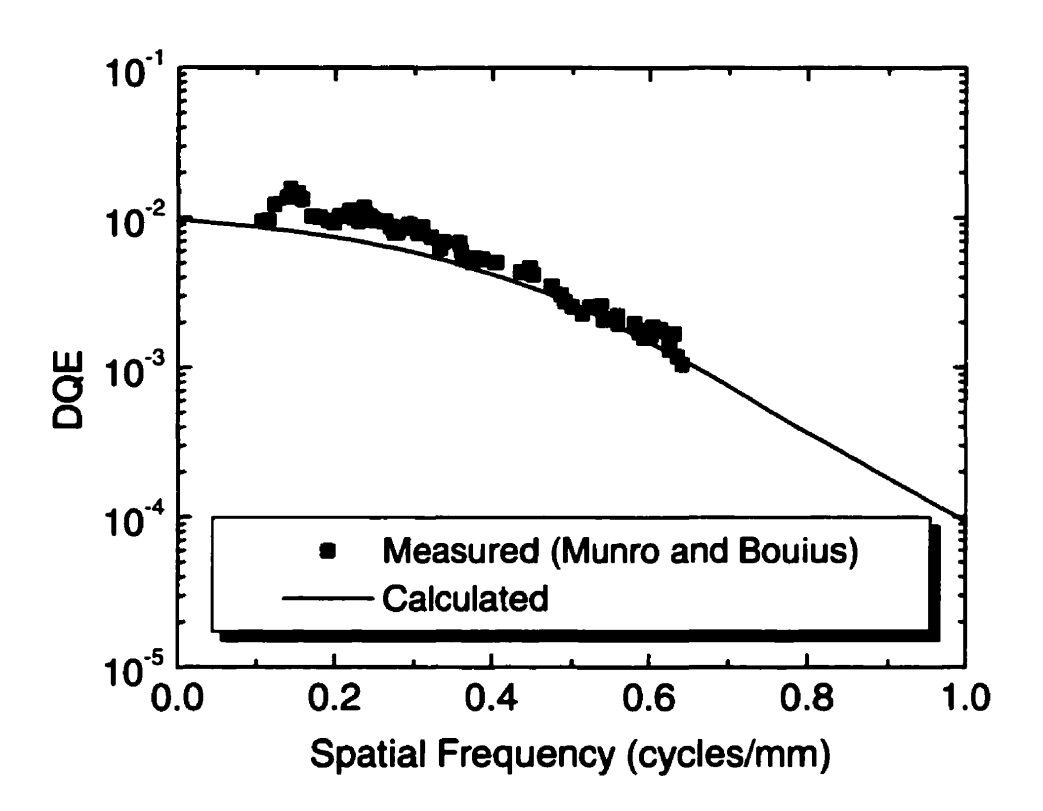


Figure 4.8: Theoretical calculations of DQE for the indirectdetection DQE compared to measured values described by Munro and Bouius.<sup>23</sup>

In Fig. 4.9 we show calculations for the inherent DQE of metal/a-Se and metal/phosphor detectors for various mass thicknesses. For low mass thicknesses, the DQE is essentially the same because the degradation due to the lower MTF of phosphors is counterbalanced by a corresponding loss in the NPS. Higher thicknesses lead to higher absorption of x-rays, and thus higher zero-frequency DQE, but also more scattering of ionizing radiation within the detector. For a-Se, this loss of resolution does not

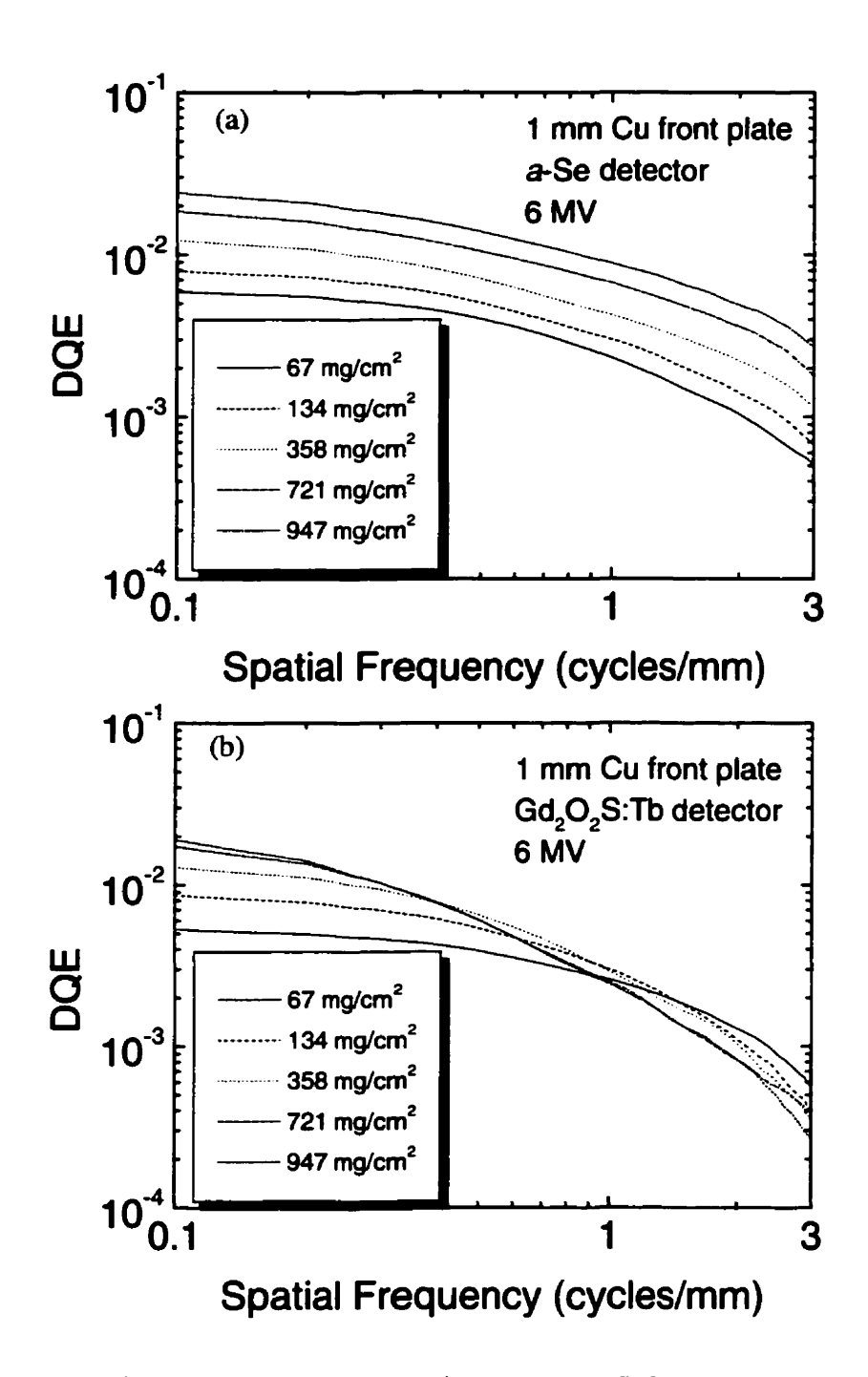


Figure 4.9: Theoretical calculations of DQE for various mass thicknesses for (a) direct-detection and (b) indirect-detection AMFPIs. Calculations are for 6 MV with a 1 mm Cu front plate.

significantly affect the DQE because of the correlations among the locations of the electron-hole pairs along the tracks of ionizing radiation described in our theory; thus the highest possible a-Se thickness should be used. Although the same holds for phosphors, the Lubberts effect begins to be important at large thicknesses which strongly degrades the DQE. Further increase of phosphor thickness above about 358 mg/cm<sup>2</sup> leads to high-frequency degradation of the DQE while not substantially improving the zero-frequency DQE. Experiments with high a-Se thicknesses are needed to confirm this prediction.

#### 4.6 Conclusion

We derive a generalized cascade equation for stages which involve both amplifications and dislocations. The equation simplifies to the usual equations for pure amplification and pure dislocation stages but is sufficiently general to be useful for more complicated cases where Monte Carlo techniques can be used to describe the interactions.

We apply our formalism to the case of megavoltage imaging with both phosphor-based and a-Se based detectors. In this case, it is not appropriate to separate the processes into pure amplification and pure dislocation stages. We evaluate the quantities in our cascade equation using Monte Carlo techniques, and our results show excellent agreement with experiment. We believe that the theory will be useful for other applications which can not be fully subdivided into elementary processes. We show with our theory that for small mass thicknesses the DQE is the same for direct and indirect AMFPIs, whereas for large mass thicknesses there should be advantages to using direct-detection AMFPIs for megavoltage imaging.

#### 4.7 References

- [1] H.H. Barrett, R.F. Wagner and K.J. Myers, "Correlated point processes in radiological imaging," Proc. SPIE. **3032** 110-124 (1997).
- [2] I.A. Cunningham, "Linear-systems modeling of parallel cascaded stochastic processes: the NPS or radiographic screens with reabsorption of characteristic x-radiation," Proc. SPIE **3336** 220-230 (1998).
- [3] M. Rabbani, R. Shaw and R. Van Metter, "Detective quantum efficiency of imaging systems with amplifying and scattering mechanisms," J. Opt. Soc. Am. 4A 895-901 (1987).
- [4] M. Rabbani and R. Van Metter, "Analysis of signal and noise propagation for several imaging mechanisms," J. Opt. Soc. Am A 7 1156-1164 (1989).
- [5] I.A. Cunningham, "A spatial-frequency dependent quantum accounting diagram and detective quantum efficiency model of signal and noise propagation in cascaded imaging systems," Med. Phys. 21 417-427 (1994).
- [6] J.H. Siewerdsen, L.E. Antonuk, Y. El-Mohri, J. Yorkston and W. Huang, "Signal, noise power spectrum, and detective quantum efficiency of indirect-detection flat-panel imagers for diagnostic radiology," Med. Phys. 25 614-628 (1998).
- [7] W. Zhao and J.A. Rowlands, "Digital radiology using active matrix readout of amorphous selenium: Theoretical analysis of detective quantum efficiency," Med. Phys. 24 1819-1833 (1997).
- [8] J.P. Bissonnette, I.A. Cunningham, D.A. Jaffray, A. Fenster and P. Munro, "A quantum accounting and detective quantum efficiency analysis for video-based portal imaging," Med. Phys. **24** 815-826 (1997).

- [9] J.-P. Bissonnette, I.A. Cunningham and P. Munro, "Optimal phosphor thickness for portal imaging," Med. Phys. 24 803-815 (1997).
- [10] D.G. Drake, D.A. Jaffray and J.W. Wong, "Characterization of a fluoroscopic imaging system for kV and MV radiography," Med. Phys. 27 898-905 (2000).
- [11] R.K. Swank, "Absorption and noise in x-ray phosphors," J. Appl. Phys. 44 4199-4203 (1973).
- [12] I. Kawrakow and D.W.O. Rogers, "The EGSnrc Code System: Monte Carlo Simulation of Electron and Photon Transport," NRCC Report PIRS-701 (2000).
- [13] G. Lubberts, "Random noise produced by x-ray fluorescent screens," J. Opt. Soc. Am. **58** 1475-1483 (1968).
- [14] R. Van Metter and M. Rabbani, "An application of multivariate moment-generating functions to the analysis of signal and noise propagation in radiographic screen-film systems," Med. Phys. 17 65-71 (1990).
- [15] W. Que and J.A. Rowlands, "X-ray photogeneration in amorphous selenium: Geminate versus columnar recombination," Phys. Rev. B **51** 10500-10507 (1995).
- [16] W. Que and J.A. Rowlands, "X-ray imaging using amorphous selenium: Inherent spatial resolution," Med. Phys. 22 365-374 (1995).
- [17] G. Pang, W. Zhao and J.A. Rowlands, "Digital radiology using active matrix readout of amorphous selenium: Geometric and effective fill factors," Med. Phys. 25 1636-1646 (1998).
- [18] D.A. Jaffray, J.J. Battista, A. Fenster and P. Munro, "Monte Carlo studies of x-ray energy absorption and quantum noise in megavoltage transmission radiography," Med. Phys. 22 1077-1088 (1995).

- [19] T. Radcliffe, G. Barnea, B. Wowk, G. Rajapakshe and S. Shalev, "Optimization of metal/phosphor screens for on-line portal imaging," Med. Phys. 21 227-235 (1994).
- [20] C. Kausch, B. Schreiber, F. Kreuder, R. Schmidt and O. Dossel, "Monte Carlo simulations of the imaging performance of metal plate/phosphor screens used in radiotherapy," Med. Phys. **26** 2113-2124 (1999).
- [21] P. Munro, J.A. Rawlinson and A. Fenster, "Therapy Imaging: A signal-to-noise analysis of a fluoroscopic imaging system for radiotherapy localization," Med. Phys. 17 763-772 (1990).
- [22] A. Debrie, B. Polischuk, H. Rougeot, M. Hansroul, E. Poliquin, M. Caron, K. Wong, Z. Shukri and J.-P. Martin, "Quantitative analysis of performance of selenium flat-panel detector for interventional mammography," SPIE Physics of Medical Imaging 3977 417-425 (2000).
- [23] P. Munro and D.C. Bouius, "X-ray quantum limited portal imaging using amorphous silicon flat-panel arrays," Med. Phys. **25** 689-702 (1998).
- [24] H.E. Johns and J.R. Cunningham, *The Physics of Radiology* (Thomas, Springfield, 1983).

# Chapter 5: Effect of front plate on image quality

| 5.1 Introduction   | 185 |
|--|-----|
| 5.2 Background: the effect of scattered radiation on image quality | 187 |
| 5.3 Materials and Methods  | 189 |
| 5.3.1 Description of Electrostatic probe a-Se detector             | 189 |
| 5.3.2 Measurement of Scatter Fraction                              |     |
| 5.3.3 Monte Carlo simulations of SF and SPR                        | 193 |
| 5.4 Results and Discussion   | 195 |
| 5.4.1 SF and SPR: comparison of simulations with experiment        | 195 |
| 5.4.2 Effect of front plate on DQE, contrast and DSNR              |     |
| 5.5 Conclusions  |     |
| 5.6 References   |     |

#### 5.1 Introduction

In Chapter 4 we have developed a formalism to calculate the DQE of direct and indirect AMFPI detectors at megavoltage energies. We have used this formalism to compare these types of detector for various thicknesses of the sensitive layer (i.e., a-Se or phosphor layer) on the DQE. In these comparisons we have used a fixed front plate of 1 mm Cu.

As previously discussed in Chapter 1, the use of a front plate in portal imaging has become customary since its first use in metal/film detectors. The plate acts as a

buildup layer, providing electronic equilibrium in the detector. It increases the fraction of x-rays which contribute to the signal, resulting in an increase in the broad-area detective quantum efficiency DQE(0), but also reduces the resolution, *i.e.*, a decrease in the modulation transfer function MTF(f) due to lateral radiation transport within the plate. The presence of the front plate also increases contrast by preferentially decreasing the contribution of scattered radiation, which has a lower average energy than the primary beam.

The sensitive layers of AMFPI detectors are thicker than film, which inherently increases the number of interacting x-rays. Typically a front plate equivalent to about 1-1.5 mm of Cu has been used for these detectors.<sup>2</sup> There have been very little studies, however, on how the front plate thickness affects the image quality for thick detectors. Wowk *et al*<sup>3</sup> have studied the effect of the front plate on the spatial-frequency dependent DQE(f) for thick phosphors, but in their model they assumed that the quantum noise was white, and they did not take the influence of patient scatter into account. In this Chapter we explore the effect of the front plate thickness on the DQE using the methods developed in Chapter 4, and we also explore the influence of the front plate on scatter rejection using Monte Carlo simulations. To confirm the scatter simulations, we measure the scatter fraction (SF) using a prototype *a*-Se based detector which uses an electrostatic probe to scan the surface charge distribution.

## 5.2 Background: the effect of scattered radiation on image quality

To model the effect of scatter, consider the example of a circular object embedded in a water-equivalent phantom, as in Fig. 2.1.<sup>4,5</sup> The difference in signal caused by the object,  $\Delta \overline{d}$ , determines the visibility of the object in the final image. The contrast C compares this difference to the signal itself,

$$C = \frac{\Delta \overline{d}}{\overline{d}} , \qquad (5.1)$$

and the differential signal-to-noise ratio DSNR compares it to the image noise  $\sigma$ ,

$$DSNR = \frac{\Delta \overline{d}}{\sigma_d} \quad . \tag{5.2}$$

The signal is comprised of a portion due to the primary beam,  $\overline{d}_p$ , and a portion due to the scattered beam,  $\overline{d}_s$  i.e.,

$$\overline{d} = \overline{d}_n + \overline{d}_s . ag{5.3}$$

Assuming the presence of the object only changes  $\overline{d}_p$ , but does not significantly alter  $\overline{d}_s$ . then  $\Delta \overline{d} \approx \Delta \overline{d}_p$  does not depend on the presence of scatter. By Eq. (5.1), the *contrast* reduction factor (i.e., the decrease in contrast due to scatter) is given by

$$\frac{C_s}{C_{ns}} = \frac{\overline{d}_p}{\overline{d}_p + \overline{d}_s} = 1 - SF \quad , \tag{5.4}$$

where  $C_s$  and  $C_{ns}$  are the contrast with and without scatter, respectively, and the scatter fraction SF is defined as

$$SF = \frac{\overline{d}_s}{\overline{d}_p + \overline{d}_s} . ag{5.5}$$

Using the same assumption, a similar factor can be found for the reduction in DSNR. In the presence of scatter, the standard deviation in the signal  $\sigma_d$  is given by

$$\sigma_d = \sqrt{\sigma_{d_p}^2 + \sigma_{d_z}^2} , \qquad (5.6)$$

since scatter and primary signals are mutually exclusive. In the absence of scatter, this simply becomes  $\sigma_d = \sigma_{d_a}$ . By Eq. (5.2), this leads to the DSNR reduction factor

$$\frac{DSNR_s}{DSNR_{ns}} = \frac{1}{\sqrt{1 + SPR}} , \qquad (5.7)$$

where  $DSNR_s$  and  $DSNR_{ns}$  are the DSNR with and without the presence of scatter, and the scatter-to-primary ratio SPR is defined as

$$SPR = \frac{\sigma_{d_r}^2}{\sigma_{d_p}^2} \ . \tag{5.8}$$

These factors, SF and SPR, describe how scattered radiation affects image quality in terms of the contrast and differential signal-to-noise ratio. For a digital display system, the loss in contrast can often be compensated by contrast-enhancing algorithms as long as the DQE is adequate. The loss in DSNR, however, must be compensated by an increase in dose. The increase in dose at a depth of  $d_{max}$  in the patient is given approximately by

$$\frac{D_s}{D_{ns}} = 1 + SPR \quad , \tag{5.9}$$

where  $D_s$  and  $D_{ns}$  are the dose with and without the presence of scatter, respectively.

#### 5.3 Materials and Methods

#### 5.3.1 Description of Electrostatic probe a-Se detector

The scatter measurements have been performed on a prototype detector developed by our group<sup>6,7</sup> (these measurements were not possible with the flat panel detector due to its limited area which limits the field size). The basic principle of operation is that a uniform positive charge distribution is first applied to the a-Se surface, which sets up an applied field across the layer. Electron-hole pairs generated by irradiation drift in this field and partially neutralize the surface charge above the location where they were created. The resulting surface charge distribution above the a-Se is scanned with an electrostatic probe to form a two-dimensional image.

The detector consists of a light-tight box with a  $20 \times 20 \text{ cm}^2$  frame which holds various metal/a-Se plates. These plates consist of a-Se which is directly deposited on a metal substrate, and the metal faces the radiation beam to act as a front plate. Scanning is performed by a servo-motor operated two-dimensional motion stage, which is controlled by a two axis microprocessor-based motion controller (Unidex11, Aerotech, Inc., Pittsburgh, PA) capable of 2  $\mu$ m positional accuracy. An electrostatic coupling probe (Trek Inc., model P0766/344, Medina, NY), with an aperture width of 200  $\mu$ m and the

capability to measure potentials up to 3000 V, is installed on this stage and is positioned at a distance of approximately 100 µm from the a-Se surface. The probe output is digitized via a 16-bit analog-to-digital converter (ADC488/16A, Iotech). The stage motion and data acquisition are controlled by a commercial package (LABVIEW, National Instruments, Inc., Austin, TX) on a 486 Personal Computer.

Also installed on the motion detector is a scorotron, which consists of three fine conducting wires set to a high potential (6550 V) above a wire mesh grid set to 2100 V. The wires cause electrical breakdown of the surrounding air, resulting in negatively charged carriers (mostly CO<sub>3</sub>). These carriers subsequently drift in the electric field created by the grid towards the a-Se surface, where they become trapped. To charge the plate, the motion controller sweeps the scorotron (which is 2 mm above the a-Se surface) three times across the plate, resulting in an even accumulation of charge on the a-Se surface. After this procedure, a surface potential equal to the grid potential (2100 V) is achieved.

After irradiation, the remaining surface voltage distribution is measured by scanning the probe over a 13"×13" ROI in a raster fashion, with a measurement sample of  $200\times200$  points (approximately 650  $\mu$ m intervals).

#### 5.3.2 Measurement of Scatter Fraction

As previously discussed, the SF and SPR were measured using the probe-based detector. The measurement of the voltage at the surface of the a-Se layer represents the signal. A sensitivity curve was first obtained to linearize this signal. The imager was

placed under the 6 MV beam of a Clinac 2300 C/D linear accelerator, such that the distance between the source-to-receptor distance (SRD) was 172 cm. For each measurement point, the plate was charged to an initial voltage  $V_o$  of 2100 V via corona charging. The imager was then exposed with a  $10 \times 10 \text{ cm}^2$  field to an increasing number of monitor units (MU), and the resulting average plate voltage in a  $5 \times 5 \text{ cm}^2$  ROI at the centre of the plate was measured with the scanning electrostatic coupling probe. Since the dose deposited in the a-Se is directly proportional to the number of monitor units, plots of plate voltage versus relative dose to the a-Se were obtained. The calibration was performed for the following front plates: a) 1.0 mm copper, b) 1.5 mm copper, c) 2.0 mm aluminum, and d) 1.0 mm tungsten, each with a 300  $\mu$ m a-Se layer.

To measure the scatter fraction, a polystyrene phantom was placed at a source-to-surface distance (SSD) of 100 cm. The plate voltage remaining in the central ROI after a fixed monitor unit (MU) irradiation (approximately 7 MU, depending on the plate), V'(A), was measured with the probe for field sizes A varying from  $2 \times 2$  cm<sup>2</sup> to  $20 \times 20$  cm<sup>2</sup>, and converted to the linearized signal (i.e., relative dose) D'(A) with the sensitivity curve. The lower limit to the field size was determined by the size of the beam penumbra which interfered with the ROI, and the upper limit by the size of the phantom. This was repeated three times for each of the four plates; the standard deviation of the trials was used to estimate the uncertainty. The curve D'(A) was then extrapolated to zero-area field by the use of a weighted second-order polynomial to find the contribution of the primary beam, D'(O). The curve was subsequently normalized to D'(O) so that the relative dose at zero-field was unity.

In calculating the scatter fraction, it is only the effects of patient scatter which must be considered. However, D'(A) is expected to increase not only due to an increase in patient scatter with field size but also to an increase in scatter from the linear accelerator jaws. To correct for this, the same experiment was repeated in the absence of the phantom. The resulting curve  $D_c(A)$ , also normalized to unity at zero field, represents the increase in a-Se dose with field size which is *not* due to patient scatter. Consequently, the dose variation with field size due purely to the effects of patient scatter, D(A), is approximately given by<sup>5</sup>

$$D(A) = \frac{D'(A)}{D_c(A)} . {(5.10)}$$

From the corrected curve, the scatter fraction for a  $20 \times 20$  cm<sup>2</sup> can then be calculated. Since D(20) represents the total dose, and D(0) the primary dose, then the difference represents the scatter dose. From Eq. (5.5), the scatter fraction is then given by

$$SF(20) = \frac{D(20) - D(0)}{D(20)}. (5.11)$$

The scatter fraction was measured in this fashion for each of the four plates. One factor in this measurement which is arbitrary is the amount of MUs used. Assuming the dose-response curve accurately linearizes the signal, this factor should make no difference. To check the validity of this technique, however, the experiment was repeated with different MUs to expose the plate, both with and without the presence of the phantom.

#### 5.3.3 Monte Carlo simulations of SF and SPR

User codes were written for EGSnrc<sup>8</sup> to model the quantities SF and SPR for the a-Se detector; the geometry is shown in Fig. 5.1. X-ray photons originate from a point source with a direction sampled such that all photons are incident with even probability onto a square  $20 \times 20$  cm<sup>2</sup> field defined at a source-to-surface distance (SSD) of 100 cm. The photon energy is sampled from a 6 MV or 15 MV spectrum taken from our treatment planning system. The change of spectrum with angle and the beam profile are not considered since we only calculate energy deposition close to the central axis where these effects are not important. A 20 cm water phantom is defined at SSD = 100 cm. The detector is modeled as a metal plate over an a-Se layer in the same fashion as in the DQE simulations of Chapter 4, and is placed at a specified air gap away from the phantom. The sensitive region of interest (ROI) in which dose is scored is defined as the central  $5 \times 5$  cm<sup>2</sup> of the detector.

Primary photons and scattered particles originating from the polystyrene slab are labeled in the EGSnrc code with the use of the LATCH variable. This was accomplished by determining which photons were about to undergo either Rayleigh, photoelectric, Compton or pair production interactions. Once the LATCH variable is attached to a particle, it is passed to all of the progeny of that particle. In this way we could distinguish between the dose due to the primary and the scattered radiation.

For each history, the energy deposited in the central ROI of the detector by primary photons and by scattered radiation were scored with separate variables. When N

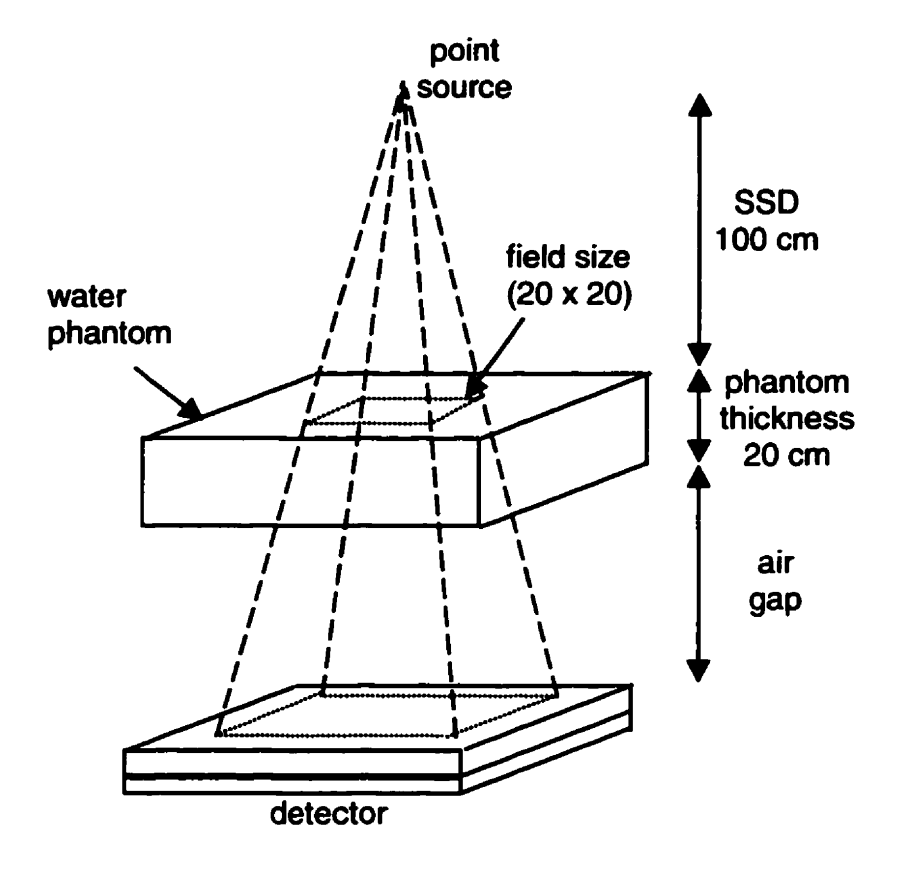


Figure 5.1: Schematic diagram of the EGSnrc user code geometry to simulate the SF and SPR.

histories were completed, the average and standard deviation in the energy deposited due to the primary and scattered beams were calculated and used to calculate the SF and SPR.

The energy cutoffs used in the simulations were 10 keV, i.e., PCUT=10 keV and ECUT=521 keV. These values proved to be a good balance between accuracy and computer time. Rayleigh scattering was neglected since it did not significantly affect the results. The number of histories were divided into 10 batches, with sufficient histories to achieve standard deviations of less than 5%. Simulations required between 8 and 24 hours on an SGI workstation (IRIS INDIGO, Silicon Graphics, Mountainview, CA).

For the phosphor detectors, we have proceeded in a manner similar to the a-Se detector except we corrected the signal for the effect of light transport since energy deposited in the top of the phosphor layer does not contribute as much to the signal as energy deposited near the bottom of the layer. To accomplish this, we first run the optical transport code discussed in Chapter 4 for the phosphor thickness in question, and determine the fraction of visible photons which escape the layer as a function of depth in the phosphor. We find a best-fit curve for these functions and use this analytical expression to weigh the energy deposited depending on the depth directly in the EGSnrc simulations. The rest of the calculations proceed the same as for the case of a-Se.

#### 5.4 Results and Discussion

#### 5.4.1 SF and SPR: comparison of simulations with experiment

The results of SF and SPR simulations for a metal/a-Se detector for a 20 cm phantom and a  $20 \times 20$  cm<sup>2</sup> field are shown in Fig. 5.2. The SF decreases with plate thickness. This is because the plate preferentially attenuates scatter which is of lower average energy and stops electrons originating from the patient. Both factors are seen to decrease with metal thickness. The lower density metals have a smaller SF and SPR for a given thickness because they have lower x-ray attenuation coefficients.

The sensitivity curves for the probe-based detector are shown in Fig. 5.3. The curve is seen to be non-linear. This arises because as electron-hole pairs are created during x-ray exposure, they neutralize the surface charge which results in a lower applied

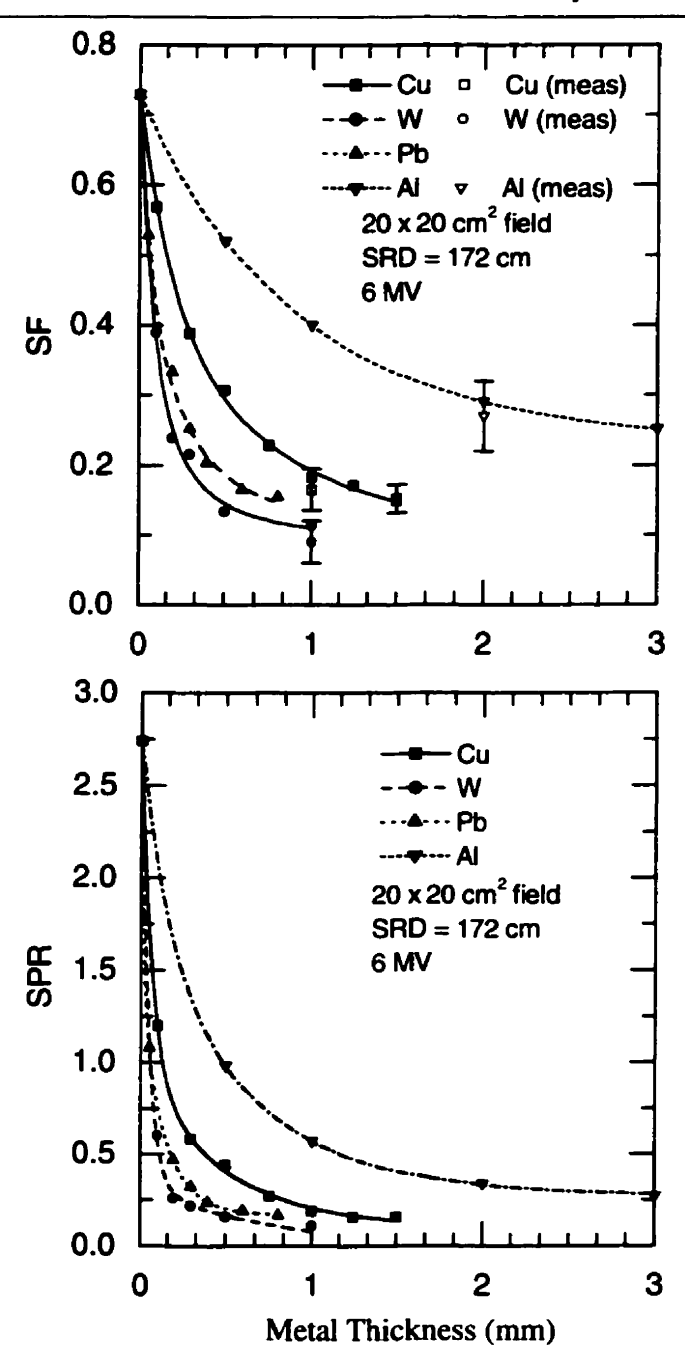


Figure 5.2: a) SF and b) SPR for a 20×20 cm<sup>2</sup> field versus metal thickness for various metals, generated by EGSnrc, with a 20 cm phantom and SRD of 172 cm. Empty points (with error bars) correspond to measured values.

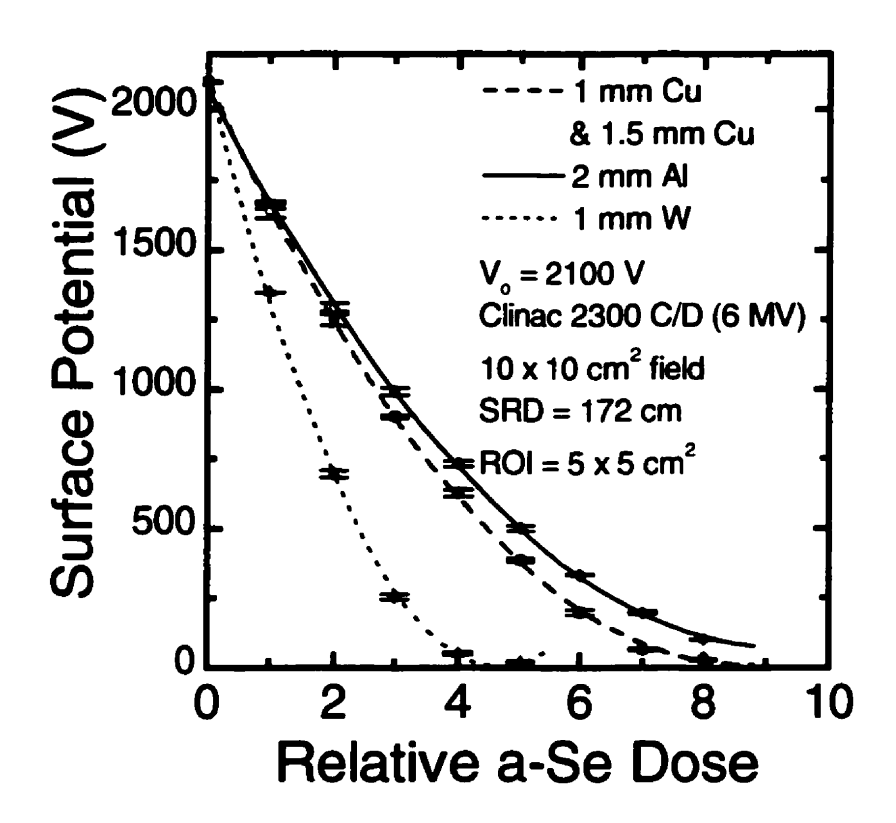


Figure 5.3: Measurements of surface potential versus relative absorbed dose to a-Se, with four plates. Only one curve is shown for 1.0 mm Cu and 1.5 mm Cu plates, since they were identical within experimental uncertainties. Measured on a Clinac 2300 C/D (6 MV, SRD=172 cm).

field and a corresponding increase in  $W_{\pm}$  as the image is being acquired.<sup>7</sup> The curve for 1 mm Cu and 1.5 mm Cu were found to be the same within experimental uncertainties and therefore only one is shown for clarity.

The change in surface potential with field size with and without a 20 cm phantom at SRD of 172 cm was measured for the four plates. The potential was converted to

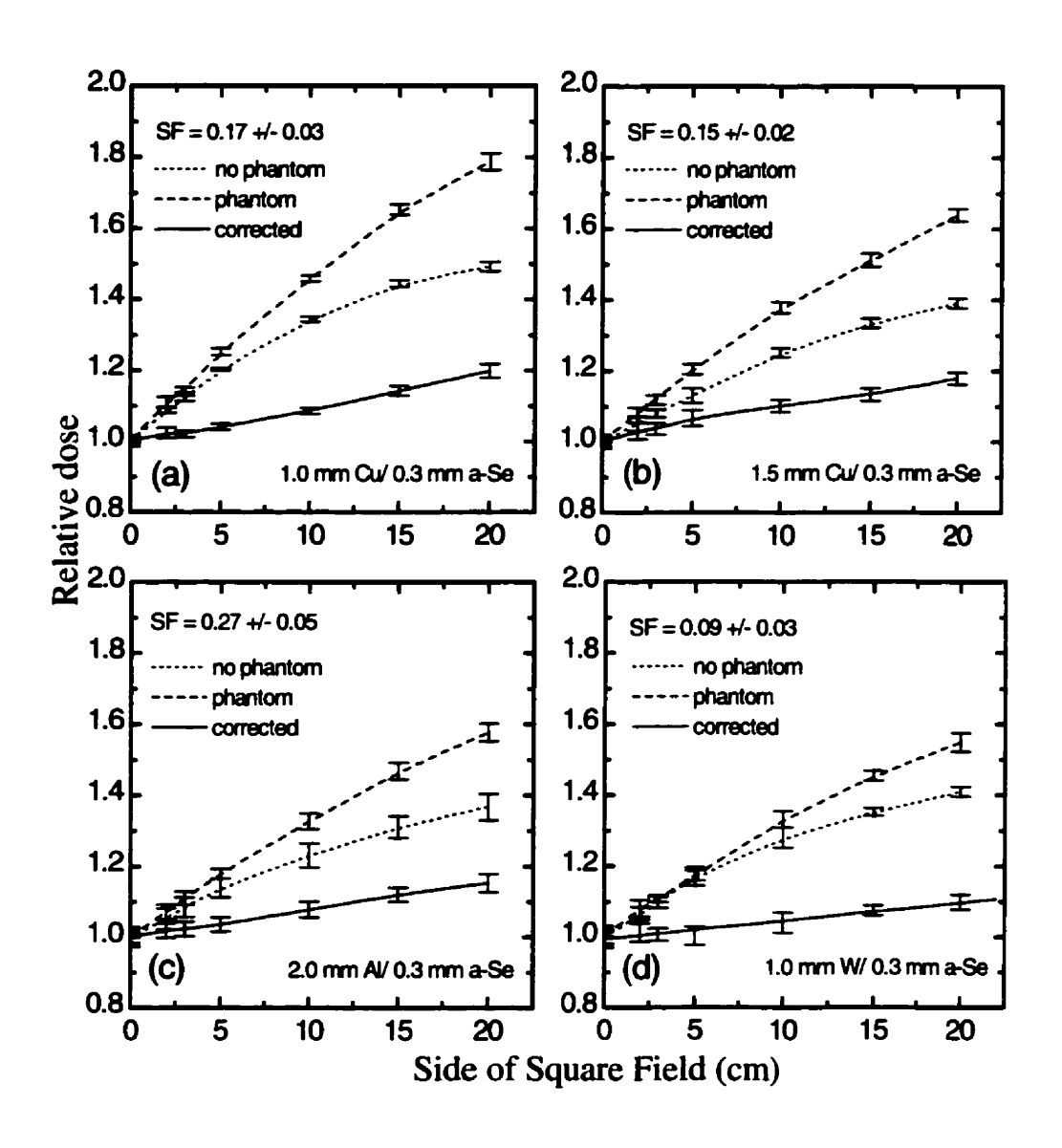


Figure 5.4: Measurements of relative dose to a-Se versus field size with phantom, without phantom and the corrected curve which represents the change due to patient scatter only. Measured on a Clinac 2300 C/D (6 MV), SRD = 172 cm, 20 cm polystyrene phantom.

relative dose using the sensitivity curves (Fig. 5.3). The curves of relative dose to a-Se versus field size, with and without phantom, and the corrected curve which represents the change in dose due to phantom scatter, are shown in Fig. 5.4. From these the scatter fractions were calculated, and are plotted for comparison with the Monte Carlo simulations in Fig. 5.2(a). It is seen that the measurements agree with the simulations within experimental uncertainties. The results were identical when different combinations of Monitor Units were used to expose the a-Se, as long as it was within the practical dynamic range of the plate.

### 5.4.2 Effect of front plate on DQE, contrast and DSNR

The dependence of DQE on front plate thickness is shown for metal/phosphor and metal/a-Se detectors in Fig. 5.5 and Fig. 5.6, respectively, for a 6 MV beam. Graphs are included for various mass thicknesses ranging from 67 mg/cm<sup>2</sup> to 721 mg/cm<sup>2</sup>. It is seen that the zero-frequency DQE increases with front plate thickness, but plateaus at a thickness of about 1 mm Cu. This occurs because although more x-rays interact with the detector for a larger front plate, once the thickness reaches the maximum range of electrons in the metal it serves only to attenuate the photon beam. Although the zero-frequency DQE increases with front plate thickness, there is a corresponding decrease in the DQE at higher frequencies. This occurs because larger thicknesses lead to more lateral scatter of radiation within the detector which degrades the MTF.

For small thicknesses of the sensitive layer, about 1 mm Cu seems to be optimal for metal/a-Se and metal/phosphor detectors, depending of course on the spatial

frequencies of interest. At larger mass thicknesses, however, the front plate worsens the DQE because it degrades the higher frequencies without significantly increasing the low frequencies.

The contrast degradation ratio for a 6 MV beam (for a representative 20 cm phantom, 10 cm air gap and 20×20 cm<sup>2</sup> field size) is plotted versus front plate thicknesses for various a-Se and phosphor mass thicknesses in Fig. 5.7. The contrast is seen to increase substantially with front plate thickness, because it filters out the lower-energy scatter component of the beam. The increase starts to saturate at about 1 mm Cu. The same trends are also seen in Fig. 5.8 for the DSNR degradation ratio, except the DSNR starts to saturate at about 0.4 mm Cu. Another feature of note is that the contrast is more affected by scattered radiation for the metal/phosphor detector than for the metal/a-Se detector; this is because the Gd<sub>2</sub>O<sub>2</sub>S:Tb has a higher atomic number than a-Se, meaning that the low-energy scattered radiation has a higher photoelectric interaction cross-section with the detector.

As discussed in Section 5.2, the degradation of contrast due to scatter is important in fixed-display detectors such as film while in digital detectors it can often be improved using contrast-enhancing algorithms. The degradation of DSNR, on the other hand, can only be recovered by increasing the dose. Taking the DSNR as the important parameter, we interpret our results in the following way: for a 6 MV beam, about 1 mm Cu is optimal for detector thicknesses less than about 100 mg/cm<sup>2</sup> (i.e., about 0.3 mm of a-Se or Gd<sub>2</sub>O<sub>2</sub>S:Tb), while for larger detector thicknesses about 0.4 mm Cu is optimal. These numbers are generalities, of course, and the actual optimal thickness depends on the mass

thickness of the detector in question and on the relative importance of contrast, DSNR and DQE at various spatial frequencies on image quality for a particular task.

The DQE for the 15 MV beam are shown in Figs. 5.9 and 5.10. The same trends observed for the 6 MV beam are still relevant. The contrast and DSNR degradation factors for the 15 MV beam are shown in Figs 5.11 and 5.12, respectively. It is seen that much larger thicknesses are needed to filter out the scattered beam at 15 MV than at 6 MV beam because of the higher penetration of x-rays at these energies; saturation has still not been reached at thicknesses as large as 4 mm. A 6 MV beam is typically used for portal imaging, however, and the detector design is more likely to be suited for this energy than for 15 MV.

## 5.5 Conclusions

We have run simulations of the DQE, scatter fraction and scatter-to-primary ratio for various metal/a-Se and metal/phosphor thicknesses using Monte Carlo methods. We have measured the SF for a metal/a-Se detector to validate our simulations. We have found that although 1 mm Cu is adequate for small detector thicknesses, for a-Se or phosphor thicknesses greater than about 300 µm a smaller front plate of about 0.4 mm Cu may be optimal for a 6 MV beam. We have generated graphs which can be used for more specific optimizations depending on the imaging task.

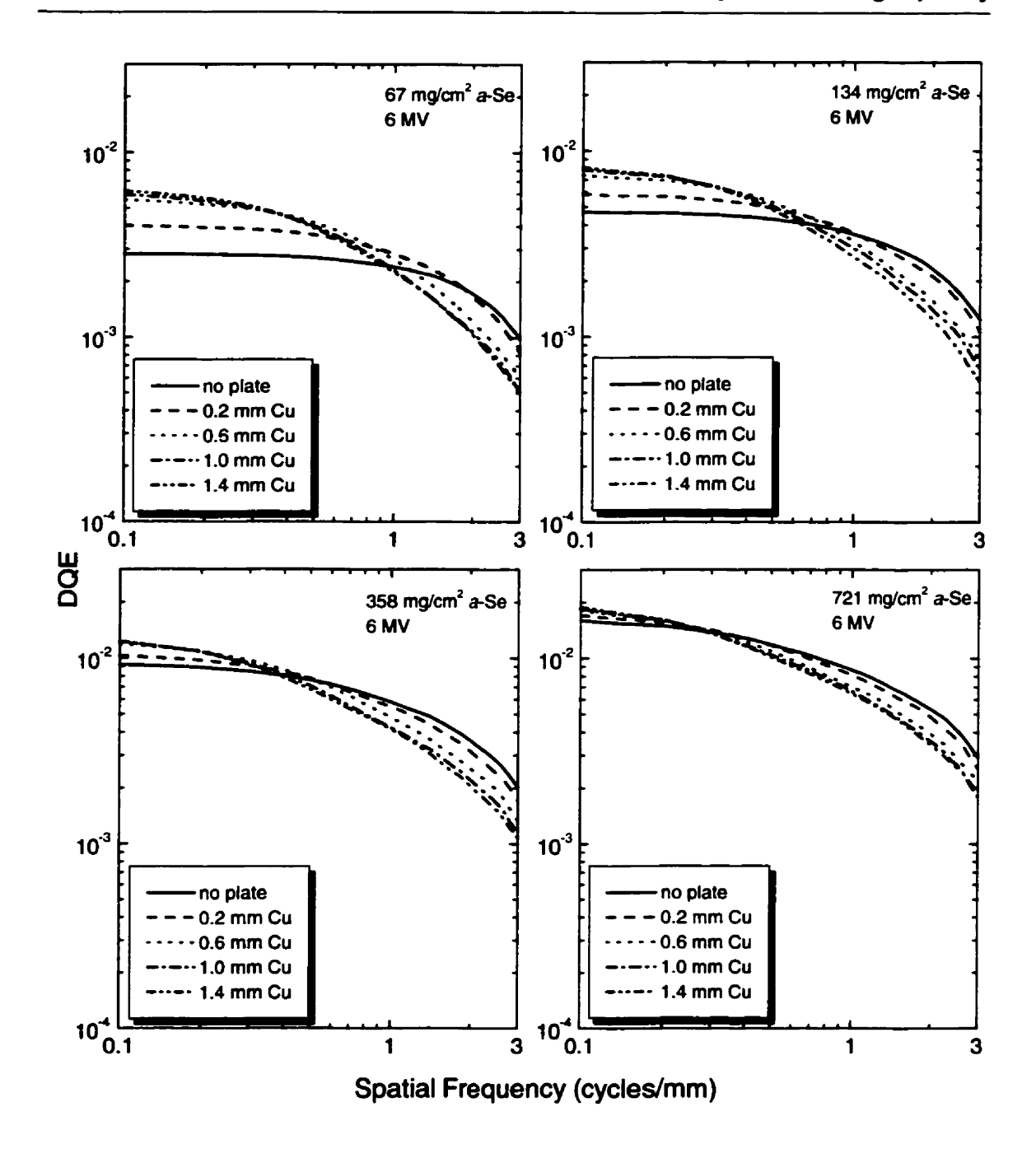


Figure 5.5: DQE of metal/a-Se detectors at 6 MV for various front plate (copper) and a-Se thicknesses.

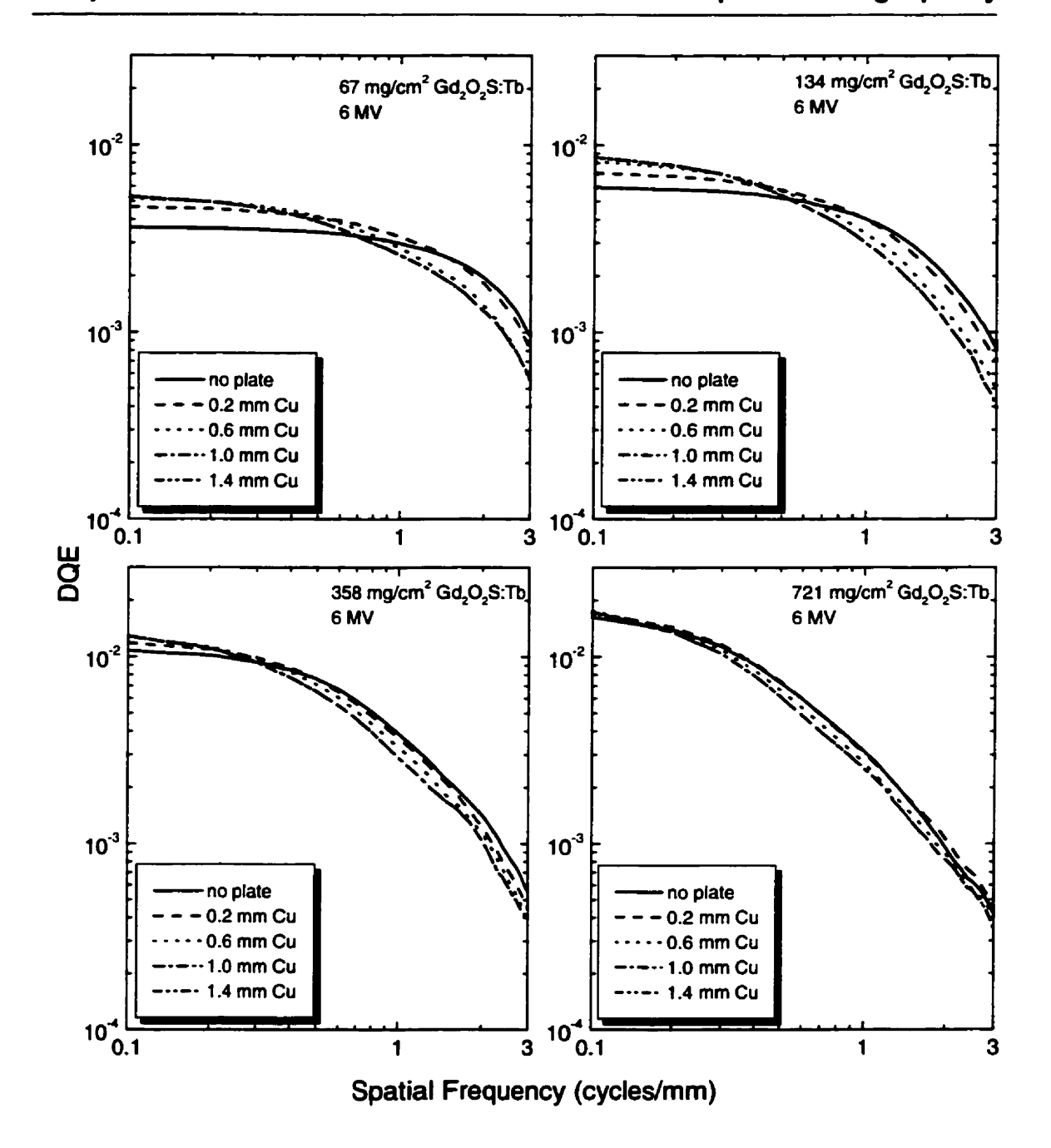


Figure 5.6: DQE of metal/phosphor detectors at 6 MV for various front plate (copper) and  $Gd_2O_2S$ : Tb thicknesses.

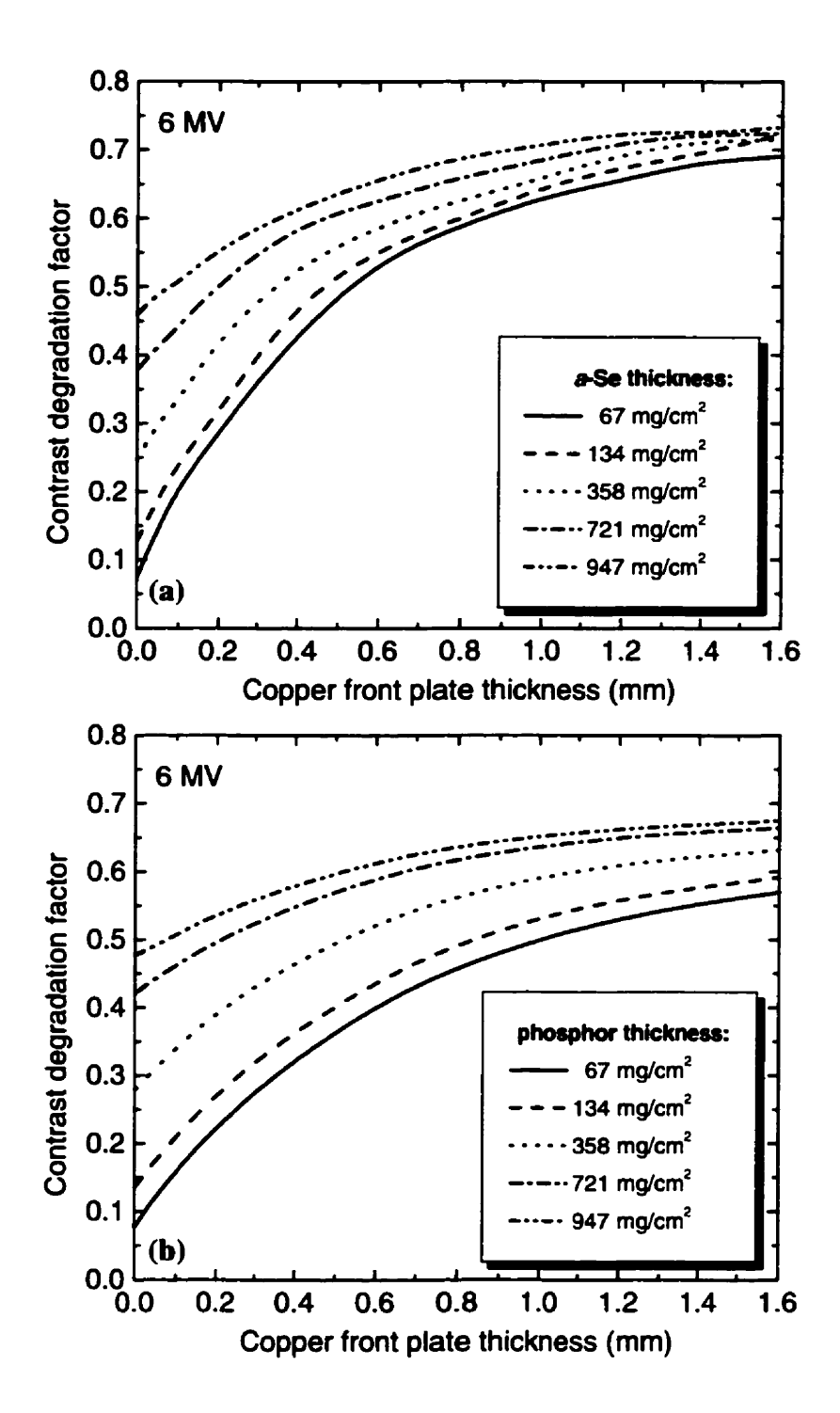


Figure 5.7: Contrast degradation factor of (a) metal/a-Se and (b) metal/phosphor detectors at 6 MV plotted versus front plate (copper) thickness, for various sensitive layer thicknesses.

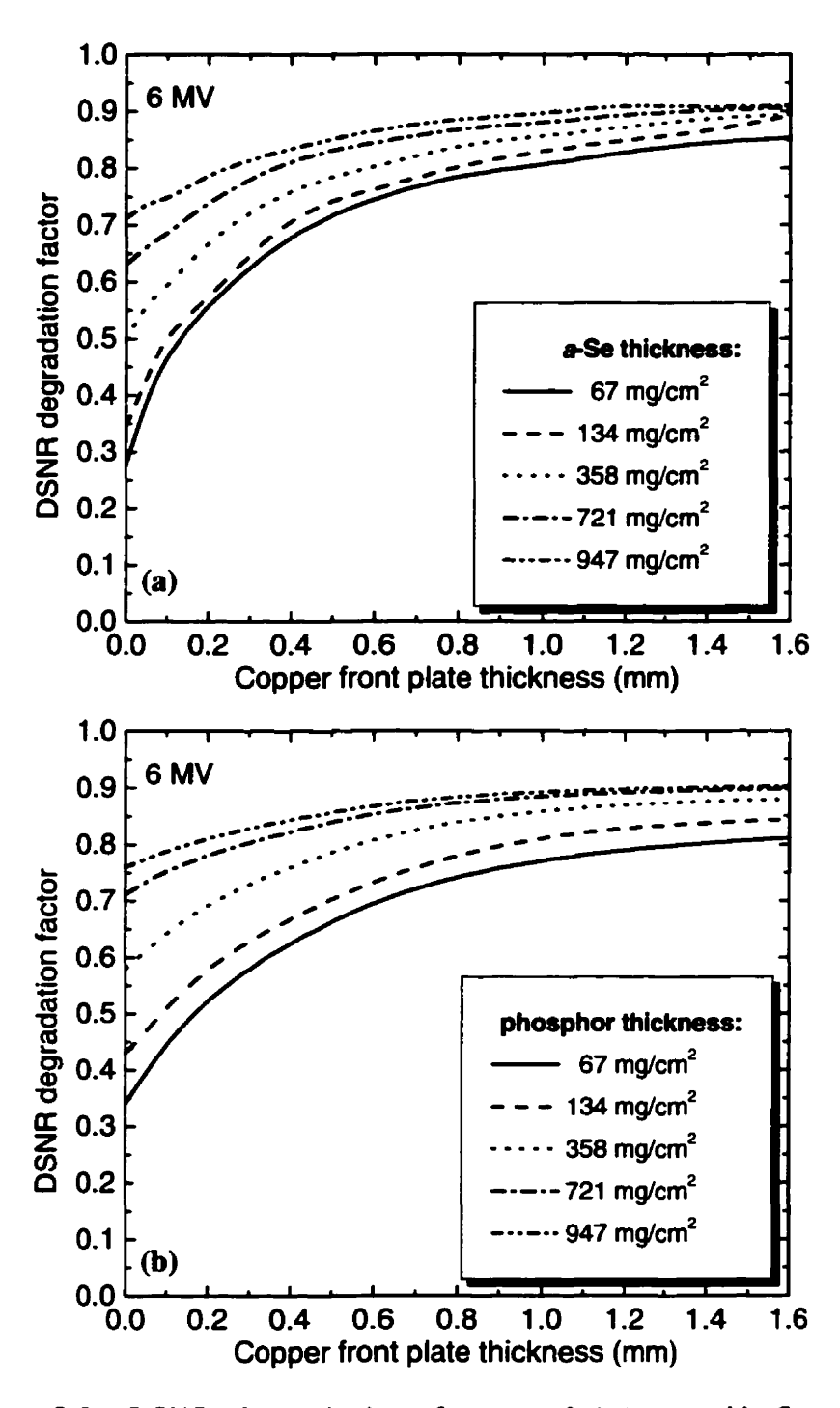


Figure 5.8: DSNR degradation factor of (a) metal/a-Se and (b) metal/phosphor detectors at 6 MV plotted versus front plate (copper) thickness, for various sensitive layer thicknesses.

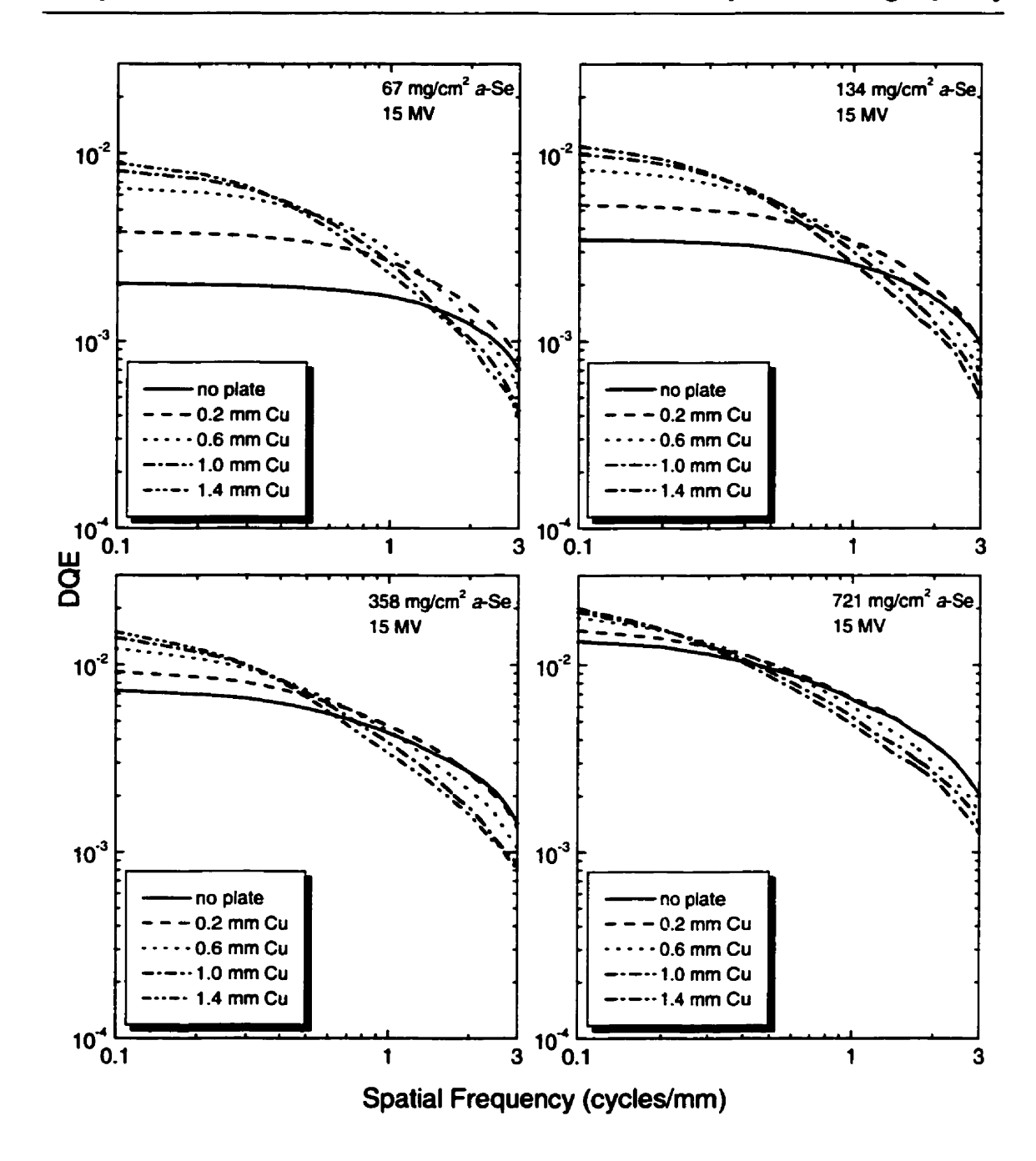


Figure 5.9: DQE of metal/a-Se detectors at 15 MV for various front plate (copper) and a-Se thicknesses.

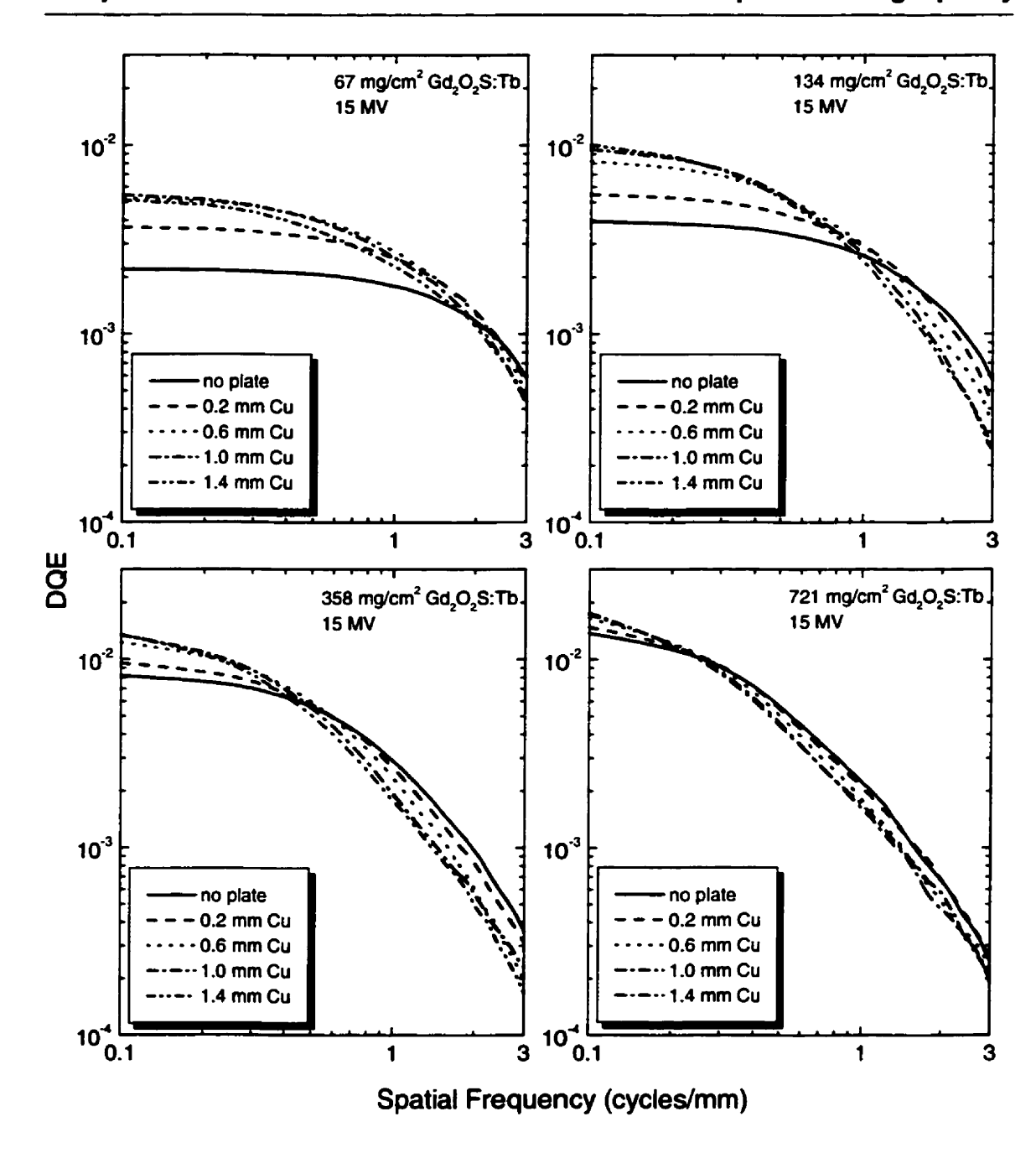


Figure 5.10: DQE of metal/phosphor detectors at 15 MV for various front plate (copper) and  $Gd_2O_2S$ : Tb thicknesses.

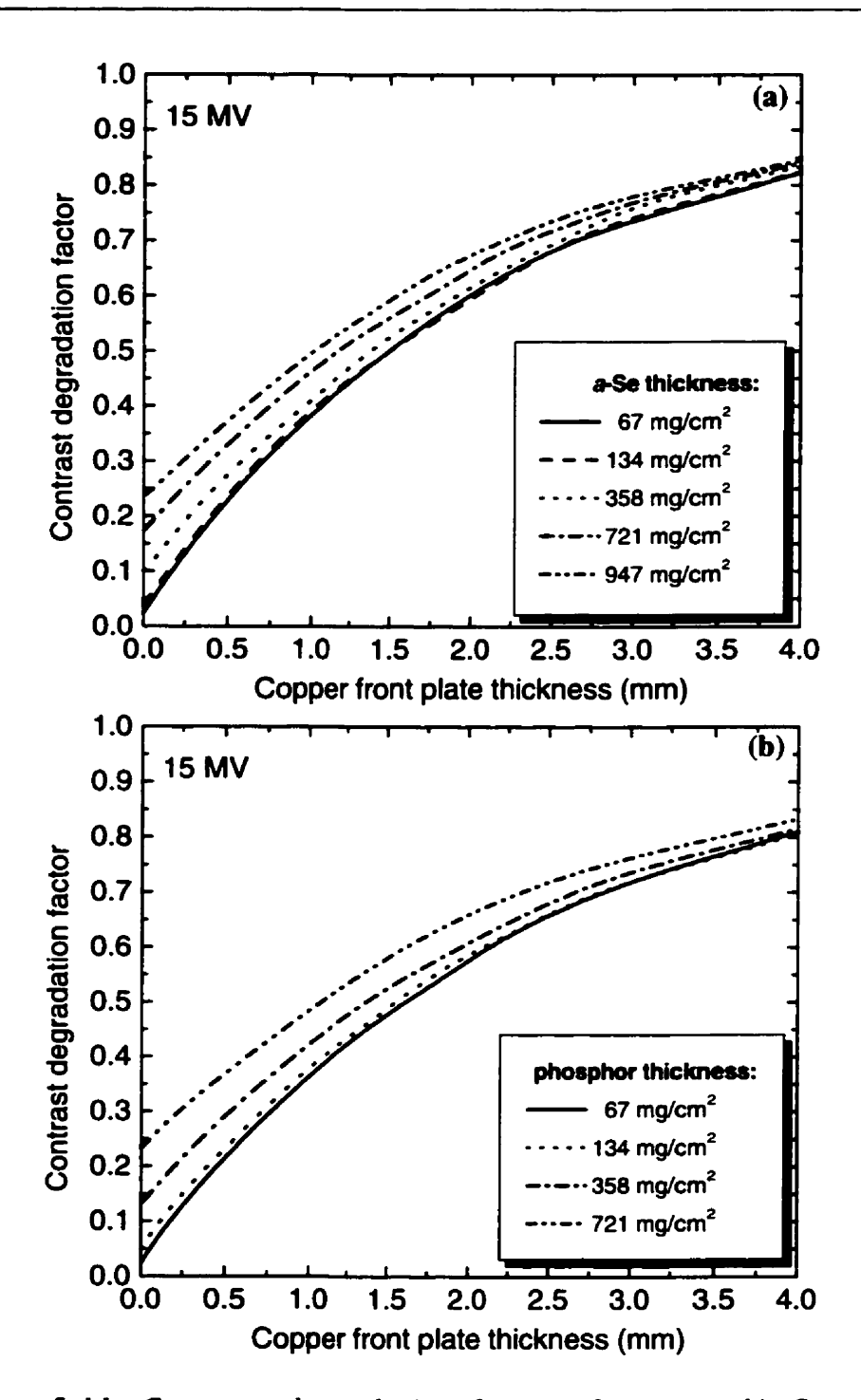


Figure 5.11: Contrast degradation factor of (a) metal/a-Se and (b) metal/phosphor detectors at 15 MV plotted versus front plate (copper) thickness, for various sensitive layer thicknesses.

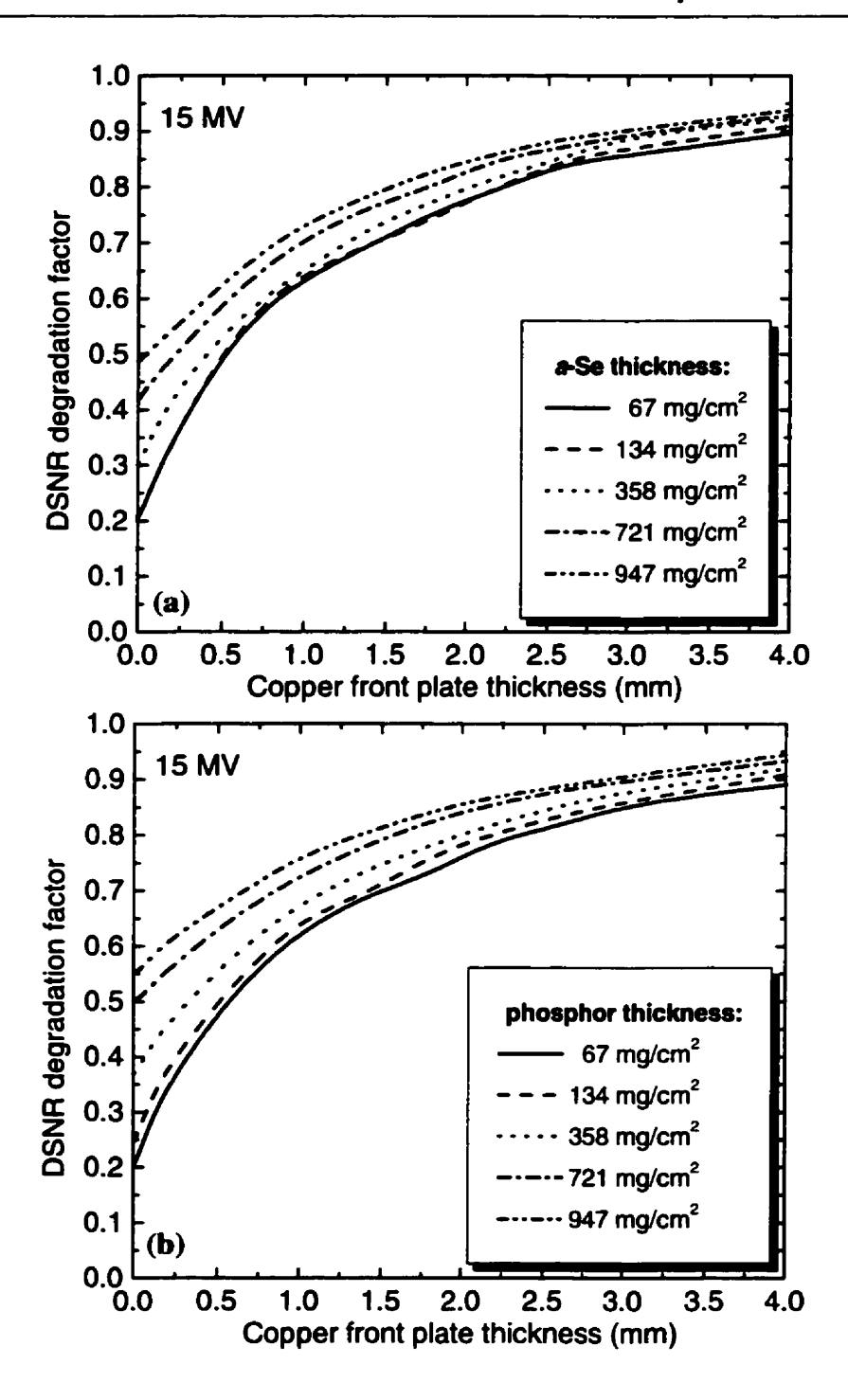


Figure 5.12: DSNR degradation factor of (a) metal/a-Se and (b) metal/phosphor detectors at 15 MV plotted versus front plate (copper) thickness, for various sensitive layer thicknesses.

### 5.6 References

- [1] R.T. Droege and B.E. Bjarngard, "Influence of metal screens on contrast in megavoltage x-ray imaging," Med. Phys. 6 487-493 (1979).
- [2] A.L. Boyer, L. Antonuk, A. Fenster, M. Van Herk, H. Meertens, P. Munro, L.E. Reinstein and J. Wong, "A review of electronic portal imaging devices (EPIDs)," Med. Phys. 19 1-16 (1992).
- [3] B. Wowk, T. Radcliffe, K. Leszczynski, S. Shalev and R. Rajapakshe, "Optimization of metal/phosphor screens for on-line portal imaging," Med. Phys. 21 227–235 (1994).
- [4] W. Swindell, E.J. Morton, P.M. Evans and D.G. Lewis, "The design of megavoltage projection imaging systems: some theoretical aspects," Med. Phys. 18 855-866 (1991).
- [5] D.A. Jaffray, J.J. Battista, A. Fenster and P. Munro, "X-ray scatter in megavoltage transmission radiography: physical characteristics and influence on image quality," Med. Phys. 21 45-60 (1993).
- [6] B.G. Fallone and T. Falco, "Megavoltage imaging method using a combination of a photoreceptor with a high energy photon converter and intensifier," U.S. Patent (1997).
- [7] T. Falco, H. Wang and B.G. Fallone, "Preliminary study of a metal/a-Se-based portal detector," Med. Phys. 25 814-823 (1998).
- [8] I. Kawrakow and D.W.O. Rogers, "The EGSnrc Code System: Monte Carlo Simulation of Electron and Photon Transport," NRCC Report PIRS-701 (2000).

# **Chapter 6: Conclusions**

We have developed a theory for the quantitative description of the signal produced by x-rays in a-Se. This has involved the calculation of cross-sections for the creation of multiple electron-hole pairs, the development of a single-collision photon/electron Monte Carlo transport code, and simulations of electron-hole pair recombination along these tracks. We have shown that the electron-hole pairs are created in spurs with energy-dependent radii, which governs the observed energy dependence of the pair creation energy  $W_{\pm}$ . We find that  $W_{\pm}$  depends on the thickness of a-Se at megavoltage energies, but not on the front plate thickness.

We have measured the sensitivity, MTF, NPS, and DQE of an a-Se based direct-detection AMFPI for megavoltage imaging. The detector consists of a 1.2 copper plate above a 200 µm a-Se layer with an a-Si:H TFT structure. The results for the DQE show that this detector exhibits very good imaging characteristics at megavoltage energies, and that these could be improved significantly with a larger a-Se thickness.

We derive a generalized cascade equation for stages which involve both amplifications and dislocations. The equation simplifies to the usual equations for pure amplification and pure dislocation stages but is sufficiently general to be useful for more complicated cases where Monte Carlo techniques can be used to describe the interactions.

Chapter 6: Conclusions

We apply our formalism to the case of megavoltage imaging with both phosphor-based and a-Se based detectors. In this case, it is not appropriate to separate the processes into pure amplification and pure dislocation stages. We evaluate the quantities in our cascade equation using Monte Carlo techniques, and our results show agreement with experiment. We believe that the theory will be useful for other applications which can not be fully subdivided into elementary processes. We show with our theory that for small mass thicknesses the DQE is the same for direct and indirect AMFPIs, whereas for large mass thicknesses there should be advantages to using direct-detection AMFPIs for megavoltage imaging.

We model the effect of scatter rejection by the front plate using Monte Carlo techniques, and confirm our simulations with measurements using a prototype electrostatic probe-based detector. Taking both the DQE and scatter rejection into account, we find that the front plates typically used for portal imaging (~1mm) are optimal for small a-Se/phosphor thicknesses, but that for larger a-Se/phosphor thicknesses (greater than about 300 µm) a smaller front plate (0.4 mm) could lead to better image quality.

#### **BIBLIOGRAPHY**

The numbers in square brackets indicate the page(s) where the items have been referenced in the thesis.

- L.E. Antonuk, Y. El-Mohri, W. Huang, K.-W. Jee, J. Siewerdsen, M. Maolinbay, V. Scarpine, H. Sandler and J. Yorkston, "Initial Performance Evaluation of an indirect-detection, active matrix flat-panel imager (AMFPI) prototype for megavoltage imaging," Int. J. Rad. Onc. Biol. Phys. 42 437-452 (1998). [p. 3]
- L.E. Antonuk, Y. El-Mohri, J.H. Siewerdsen and J. Yorkston, "Empirical investigation of the signal performance of a high-resolution, indirect detection, active matrix flat-panel imager (AMFPI) for fluoroscopic and radiographic operation," Med. Phys. 24 51-70 (1997). [p. 3]
- J.C. Ashley, "Interaction of low-energy electrons with condensed matter: stopping powers and inelastic mean free paths from optical data," J. Elect. Spect. Rel. Phenom., 46 199-214 (1988). [p. 40]
- H.H. Barrett, R.F. Wagner and K.J. Myers, "Correlated point processes in radiological imaging," Proc. SPIE. 3032 110-124 (1997). [p. 142]
- W.M. Bartczak and A. Hummel, "Computer simulation of ion recombination in irradiated nonpolar liquids," J. Chem. Phys 87 5222-5228 (1987). [p. 78]
- M.G. Bell and W.Y. Liang, "On determination of the dielectric functions of a-Se and trig-Se by electron energy loss spectroscopy," in 5th International Conference on Amorphous and Liquid Semiconductors. 1973. [p. 52, 56, 60]
- H. Bethe, "Theory of the passage of fast corpuscular rays through matter," Annal der Physik 5 325 (1930). [p. 34]
- J.P. Bissonnette, I.A. Cunningham, D.A. Jaffray, A. Fenster and P. Munro, "A quantum accounting and detective quantum efficiency analysis for video-based portal imaging," Med. Phys. 24 815-826 (1997). [p. 160]

- J.-P. Bissonnette, I.A. Cunningham and P. Munro, "Optimal phosphor thickness for portal imaging," Med. Phys. 24 803-815 (1997). [p. 160]
- R.B. Blackman and J.W.Tukey, The measurement of power spectra (from the point of view of communications engineering) (Dover, New York, 1958). [p. 107]
- I.M. Blevis, D.C. Hunt and J.A. Rowlands, "Measurement of x-ray photogeneration in amorphous selenium," J. Appl. Phys. 85 7958-7963 (1999). [p. 15,16,45,81]
- J.W. Boag, "Xeroradiography (review)," Phys. Med. Biol. 18 3-37 (1973). [p. 2,15]
- N. Bohr, Mat.Fys.Medd.K.Dan.Vidensk.Selsk. 18 1 (1948). [p. 64]
- G. Borasi and R. Cubeddu, "Some remarks on selenium plates for xeroradiography," J. Appl. Phys. 48 1375-1379 (1977). [p. 14]
- A.L. Boyer, L. Antonuk, A. Fenster, M. Van Herk, H. Meertens, P. Munro, L.E. Reinstein and J. Wong, "A review of electronic portal imaging devices (EPIDs)," Med. Phys. 19 1-16 (1992). [p. 6, 186]
- R.N. Bracewell, *The Fourier Transform and its applications* (McGraw-Hill, 1978). [p. 107]
- C.F. Carlson, U.S. Patent 221776 (1938). [p. 2]
- D.E. Cullen, S.T. Perkins and S.M. Seltzer, Tables and Graphs of Electron Interaction Cross Sections from 10 eV to 100 GeV Derived from the LLNL Evaluated Electron Data Library (EEDL), Z = 1 100, Lawrence Livermore National Laboratory (1991). [p. 26, 71]
- D.E. Cullen, S.T. Perkins and S.M. Seltzer, Tables and graphs of photon-interaction cross sections from 10 eV to 100 GeV derived from the LLNL evaluated photon data library (EPDL), parts A&B, Lawrence Livermore National Laboratory (1989). [p. 21, 61]

- I.A. Cunningham, "Applied linear systems theory" in *Handbook of Medical Imaging*, Chapter 2 edited by R.L. Van Metter (SPIE, Bellingham, 2000). [p. 96]
- I.A. Cunningham, "Linear-systems modeling of parallel cascaded stochastic processes: the NPS or radiographic screens with reabsorption of characteristic x-radiation," Proc. SPIE 3336 220-230 (1998). [p. 142, 148]
- I.A. Cunningham, "A spatial-frequency dependent quantum accounting diagram and detective quantum efficiency model of signal and noise propagation in cascaded imaging systems," Med. Phys. 21 417-427 (1994). [p. 4, 144]
- J.C. Dainty and R. Shaw, Image Science (Academic Press, New York, 1974). [p. 96]
- A. Debrie, B. Polischuk, H. Rougeot, M. Hansroul, E. Poliquin, M. Caron, K. Wong, Z. Shukri and J.-P. Martin, "Quantitative analysis of performance of selenium flat-panel detector for interventional mammography," SPIE Physics of Medical Imaging 3977 417-425 (2000). [p. 122, 173]
- J.T. Dobbins, "Effects of undersampling on the proper interpretation of modulation transfer function, noise power spectra, and noise equivalent quanta of digital imaging systems," Med. Phys. 22 171-181 (1995). [p. 113, 116, 118, 119]
- J.T. Dobbins, D.L. Ergun, L. Rutz, D.A. Hinshaw, H. Blume and D.C. Clark, "DQE(f) of four generations of computed radiography acquisition devices," Med. Phys. 22 1581-1593 (1995). [p. 131]
- J.L. Donovan, "X-ray sensitivity of selenium," J. Appl. Phys. **50** 6500-6504 (1979). [p. 14]
- D.G. Drake, D.A. Jaffray and J.W. Wong, "Characterization of a fluoroscopic imaging system for kV and MV radiography," Med. Phys. 27 898-905 (2000). [p. 161]

- R.T. Droege and B.E. Bjarngard, "Influence of metal screens on contrast in megavoltage x-ray imaging," Med. Phys. 6 487-493 (1979). [p. 5, 185]
- R.T. Droege and B.E. Bjarngard, "Metal screen-film detector MTF at megavoltage x-ray energies," Med. Phys. 6 515-518 (1979). [p. 129]
- T. Falco and B.G. Fallone, "Characteristics of metal-plate/film detectors at therapy energies: I. Modulation Transfer Function," Med. Phys. **25** 2455-2462 (1998). [p. 129]
- T. Falco and B.G. Fallone, "Characteristics of metal-plate/film detectors at therapy energies: II. Detective Quantum Efficiency," Med. Phys. **25** 2463-2468 (1998). [p. 131]
- T. Falco, H. Wang and B.G. Fallone, "Preliminary study of a metal/a-Se-based portal detector," Med. Phys. 25 814-823 (1998). [p. 7, 189]
- B.G. Fallone and T. Falco, "Megavoltage imaging method using a combination of a photoreceptor with a high energy photon converter and intensifier," U.S. Patent (1997). [p. 7, 189]
- B.G. Fallone and M. Lachaine, "X-ray interactions in a-Se based diagnostic and portal imagers," Proceedings of the Chicago 2000 World Congress on Medical Physics and Biomedical Engineering 3294-76031.pdf (2000). [p. 7]
- U. Fano and J.W. Cooper, "Spectral distribution of atomic oscillator strengths," Reviews of modern physics 40 441-507 (1968). [p. 41]
- W.D. Fender, "Quantification of the xeroradiographic discharge curve," SPIE 70 364-371 (1975). [p. 14]
- H. Fiedler and F. Laugwitz, "Zur Quantenausbeute elektroradiographischer Selenschichten," J. Signal AM 9 229-235 (1981). [p. 14]

- E. Fourkal, M. Lachaine and B.G. Fallone, "Signal formation in a-Se based x-ray detectors," Phys. Rev. B 63, 195204 (2001). [p. 7]
- H. Fujita, K. Doi and M.L. Giger, "Investigation of basic imaging properties in digital radiography," Med. Phys. 12 713-720 (1985). [p. 118]
- R.N. Hamm, J.E. Turner, R.H. Ritchie and H.A. Wright, "Calculation of heavy-ion tracks in liquid water," Radiat. Res. 104 S5-S20 (1985). [p. 56]
- C. Haugen and S.O. Kasap, "Langevin recombination of drifting electrons and holes in stabilized a-Se (Cl-doped a-Se: 0.3% As)," Philos. Mag. B 71 91-96 (1995). [p. 43]
- C. Haugen, S.O. Kasap and J. Rowlands, "Charge transport and electron-hole pair creation energy in stabilized a-Se x-ray photoconductors," J. Phys. D 32 200-207 (1999). [p. 86]
- J. Hirsch and H. Jahankhani, "The carrier yield in a-Se under electron bombardment," J. Phys.: Condens. Matter 1 8789 (1989). [p. 15, 44, 85]
- G. Jaffé, "Columnar ionization," Le Radium 10 126-134 (1913). [p. 15, 44]
- D.A. Jaffray, J.J. Battista, A. Fenster and P. Munro, "Monte Carlo studies of x-ray energy absorption and quantum noise in megavoltage transmission radiography," Med. Phys. 22 1077-1088 (1995). [p. 6, 170]
- D.A. Jaffray, J.J. Battista, A. Fenster and P. Munro, "X-ray scatter in megavoltage transmission radiography: physical characteristics and influence on image quality," Med. Phys. 21 45-60 (1993). [p. 186]
- G.M. Jenkins and D.G. Watts, *Spectral analysis and its applications* (Holden-Day, San Francisco, 1968). [p. 102]

- H.E. Johns and J.R. Cunningham, *The Physics of Radiology* (Thomas, Springfield, 1983). [p. 1, 22, 23, 173]
- W. Jones and N. March, *Theoretical solid state physics, Vol. 1* (Dover, New York, 1973). [p. 52]
- P.F. Judy, "The line spread function and modulation transfer function of a computed tomographic scanner," Med. Phys. 3 233-236 (1976). [p. 118]
- S.O. Kasap, V. Aiyah., B. Polischuk and A. Baillie, "X-ray sensitivity of stabilized a-Se for x-ray imaging with electrostatic readout," J. Appl. Phys. 83 2879-2887 (1998). [p. 14]
- C. Kausch, B. Schreiber, F. Kreuder, R. Schmidt and O. Dossel, "Monte Carlo simulations of the imaging performance of metal plate/phosphor screens used in radiotherapy," Med. Phys. **26** 2113-2124 (1999). [p. 170]
- I. Kawrakow and D.W.O. Rogers, "The EGSnrc Code System: Monte Carlo Simulation of Electron and Photon Transport," NRCC Report PIRS-701 (2000). [p. 66, 71, 73, 131, 163, 165, 167]
- C.A. Klein, "Band gap dependence and related features of radiation ionization energies in semiconductors," J. Appl. Phys. **39** 2029 (1968). [p. 42]
- J.C. Knights and E.A. Davis, "Photogeneration of charge carriers in amorphous selenium," J. Phys. Chem. Solids 35 543-554 (1975). [p. 17]
- H.A. Kramers, "On a modification of Jaffé's theory of column ionization," Physica (Utrecht) 18 665-675 (1952). [p. 44]
- S. Kubsad, R. Mackie, B. Gehring, D. Misisco, B. Paliwal, M. Mehta and T. Kinsella, "Monte Carlo and convolution dosimetry for stereotactic radiosurgery," Int. J. Rad. Onc. Biol. Phys. **19** 1027-1035 (1990). [p. 86]

- G.J. Kutcher, G.S. Mageras and S.A. Leibel, "Control, correction and modeling of setup errors and organ motion," Semin. Radiat. Oncol 5 143-145 (1995). [p. 5]
- M. Lachaine and B.G. Fallone, "Calculation of inelastic cross-sections for the interaction of electrons with amorphous selenium," J. Phys. D 33 551-555 (2000). [p. 7]
- M. Lachaine and B.G. Fallone, "Cascade analysis for medical imaging detectors with stages involving both amplification and dislocation processes," Med. Phys. 28, 501-507 (2001). [p. 8]
- M. Lachaine and B.G. Fallone, "Characteristics of direct and indirect active matrix flatpanel portal imagers," Proceedings of the Chicago 2000 World Congress on Medical Physics and Biomedical Engineering, Chicago IL 3295-53559.pdf (2000). [p. 8]
- M. Lachaine and B.G. Fallone, "Design characteristics of direct and indirect active matrix flat panel portal imagers," Radiology and Oncology 35, 67-75 (2001). [p. 8]
- M. Lachaine and B.G. Fallone, "Front plate optimization of an a-Se based portal imager," Proceedings of the conference of the Canadian Organization of Medical Physicists (COMP), Charlottetown, PEI 165-167 (1997). [p. 8]
- M. Lachaine and B.G. Fallone, "Front-plate optimization of an a-Se based portal imager," Med. Phys. (abstract) 24 1207 (1997). [p. 8]
- M. Lachaine and B.G. Fallone, "Monte Carlo detective quantum efficiency and scatter studies of a metal/a-Se portal detector," Med. Phys. 25 1186-1194 (1998). [p. 8]
- M. Lachaine and B.G. Fallone, "Monte Carlo optimization of a metal-plate/a-Se portal imager," Med. Phys. (abstract) 24 1003 (1997). [p. 8]
- M. Lachaine and B.G. Fallone, "Monte Carlo simulations of recombination in amorphous selenium," Proceedings of the Canadian Organization of Physicists in Medicine 92-94 (1999). [p. 7]

- M. Lachaine and B.G. Fallone, "Monte Carlo simulations of x-ray induced recombination in amorphous selenium," J. Phys. D 33 1417-1423 (2000). [p. 7]
- M. Lachaine and B.G. Fallone, "Quantitative analysis of signal formation in a-Se based diagnostic imagers," Proceedings of the Chicago 2000 World Congress on Medical Physics and Biomedical Engineering 3769-22590.pdf (2000). [p. 7]
- M. Lachaine, E. Fourkal and B.G. Fallone, "Investigation into the physical properties of direct and indirect active matrix flat panel imagers for radiotherapy," Medical Physics (submitted). [p. 8]
- M. Lachaine, E. Fourkal and B.G. Fallone, "Detective quantum efficiency of a direct-detection active matrix flat panel imager," Med. Phys. (in press) 28 (2001). [p. 7]
- P. Langevin, "Recombinaison et mobilités des ions dans les gaz," Ann. Chim. Phys. 28 287-433 (1903). [p. 43]
- J.A. Laverne and S.M. Pimblott, "Energy loss distributions in hydrocarbons," J. Phys. Chem. 99 10541-10548 (1995). [p. 61]
- D.L. Lee, L.K. Cheung, E.F. Palecki and L.S. Jeromin, "A new digital detector for projection radiography," Proc. SPIE 2432 237-249 (1995). [p. 126]
- G. Lubberts, "Random noise produced by x-ray fluorescent screens," J. Opt. Soc. Am. 58 1475-1483 (1968). [p. 163]
- D. Mah, J.A. Rowlands and J.A. Rawlinson, "Sensitivity of amorphous selenium to x rays from 40 kVp to 18 MV: Measurements and implications for portal imaging," Med. Phys. 25 444-456 (1998). [p. 15, 16, 46, 61]
- P. Munro, "Portal imaging technology: Past, present and future," Semin. Radiat. Oncol. 5 115-133 (1995). [p. 6]

- P. Munro and D.C. Bouius, "X-ray quantum limited portal imaging using amorphous silicon flat-panel arrays," Med. Phys. **25** 689-702 (1998). [p. 7, 132, 135, 173]
- P. Munro, J.A. Rawlinson and A. Fenster, "Therapy Imaging: A signal-to-noise analysis of a fluoroscopic imaging system for radiotherapy localization," Med. Phys. 17 763-772 (1990). [p. 129]
- P. Munro, J.A. Rawlinson and A. Fenster, "Therapy imaging: a signal-to-noise analysis of metal plate/film detectors," Med. Phys. 14 975-984 (1987). [p. 129]
- L. Onsager, "Initial recombination of ions," Phys. Rev. 54 554 (1938). [p. 20]
- D.M. Pai and R.C. Enck, "Onsager mechanisms of photogeneration in amorphous selenium," Phys. Rev. B 11 5163-5174 (1975). [p. 20]
- G. Pang, W. Zhao and J.A. Rowlands, "Digital radiology using active matrix readout of amorphous selenium: Geometric and effective fill factors," Med. Phys. **25** 1636-1646 (1998). [p. 167]
- S.T. Perkins, D.E. Cullen, M.H. Chen, J.H. Hubbell, J.Rathkopf and J.Scofield, *Tables and Graphs of Atomic Subshell and Relaxation Data Derived from the LLNL Evaluated Atomic Data Library (EADL)*, Z = 1-100, (1991). [p. 18, 23, 24, 36, 69, 70, 73]
- B. Polischuk, H. Rougeot, K. Wong, A. Debrie, E. Poliquin, M. Hansroul, J.P. Martin, T. Truong, M. Choquette, L. Laperriere, and Z. Shukri, "Direct conversion detector for digital mammography," SPIE Physics of Medical Imaging 3659 417-425 (1999). [p. 122]
- W. Que and J.A. Rowlands, "X-ray imaging using amorphous selenium: Inherent spatial resolution," Med. Phys. 22 365-374 (1995). [p. 165]
- W. Que and J.A. Rowlands, "X-ray photogeneration in amorphous selenium: Geminate versus columnar recombination," Phys. Rev. B **51** 10500-10507 (1995). [p. 15, 44, 84]

- M. Rabbani, R. Shaw and R. Van Metter, "Detective quantum efficiency of imaging systems with amplifying and scattering mechanisms," J. Opt. Soc. Am. 4A 895-901 (1987). [p. 143]
- M. Rabbani and R. Van Metter, "Analysis of signal and noise propagation for several imaging mechanisms," J. Opt. Soc. Am A 7 1156-1164 (1989). [p. 143]
- T. Radcliffe, G. Barnea, B. Wowk, G. Rajapakshe and S. Shalev, "Optimization of metal/phosphor screens for on-line portal imaging," Med. Phys. 21 227-235 (1994). [p. 170]
- R.H. Ritchie and W. Brandt, "Primary processes and track effects in irradiated media" in *Radiation research: biomedical, chemical and physical perspectives* edited by O.F. Nygaard, H.I. Adler, and W.K. Sinclair (Academic Press, New York, 1975). [p. 156]
- H.H. Rossi and M. Zaider, *Microdosimetry and its applications* (Springer, New York, 1995). [p. 29, 37]
- J.A. Rowlands and D.M. Hunter, "X-ray imaging using amorphous selenium: photoinduced discharge (PID) readout for digital general radiography," Med. Phys. 22 1983-2005 (1995). [p. 3]
- R.M. Schaffert, U.S. Patent 2666144 (1950). [p. 2]
- R. Shaw, "Absolute measures of optical instrumentation in medicine," Proc. SPIE. 70 359-363 (1975). [p. 111]
- J.H. Siewerdsen, L.E. Antonuk, Y. El-Mohri, J. Yorkston and W. Huang, "Signal, noise power spectrum, and detective quantum efficiency of indirect-detection flat-panel imagers for diagnostic radiology," Med. Phys. **25** 614-628 (1998). [p. 3]
- J.H. Siewerdsen, L.E. Antonuk, Y. El-Mohri, J. Yorkston, W. Huang and J.M. Boudry, "Empirical and theoretical investigation of the noise performance of indirect detection,

active matrix flat-panel imagers (AMFPIs) for diagnostic radiology," Med. Phys. **24** 71-89 (1997). [p. 144]

- P. Sprawls, "X-ray imaging concepts: basic considerations" in *Proceedings of the 1991 AAPM Summer School: Specification, Acceptance Testing and Quality Control of Diagnostic X-ray Imaging Equipment* edited by J.A. Siebert, G.T. Barnes, and R.G. Gould (AAPM, New York, 1991). [p. 1, 96, 98]
- R.K. Swank, "Absorption and noise in x-ray phosphors," J. Appl. Phys. 44 4199-4203 (1973). [p. 162]
- W. Swindell, E.J. Morton, P.M. Evans and D.G. Lewis, "The design of megavoltage projection imaging systems: some theoretical aspects," Med. Phys. 18 855-866 (1991). [p. 187]
- R. Van Metter and M. Rabbani, "An application of multivariate moment-generating functions to the analysis of signal and noise propagation in radiographic screen-film systems," Med. Phys. 17 65-71 (1990). [p. 163]
- R.F. Wagner and E.P. Muntz, "Detective Quantum Efficiency (DQE) analysis of xeroradiographic images," Proc. SPIE 70 162-165 (1979). [p. 111]
- M.B. Williams, "Noise power spectra of images from digital mammography detectors," Med. Phys. **26** 1279-1293 (1999). [p. 111]
- L. Wolfe, L. Kalisher and B. Considine, "Cobalt-60 treatment field verification by xeroradiography," A. J. R. 18 1973 (1973). [p. 6]
- B. Wowk, T. Radcliffe, K. Leszczynski, S. Shalev and R. Rajapakshe, "Optimization of metal/phosphor screens for on-line portal imaging," Med. Phys. **21** 227–235 (1994). [p. 186]

- W. Zhao, I. Blevis, S. Germann and J.A. Rowlands, "Digital radiology using active matrix readout of amorphous selenium: Construction and evaluation of a prototype real-time detector," Med. Phys. **24** 1834-1843 (1997). [p. 3, 133]
- W. Zhao and J.A. Rowlands, "Digital radiology using active matrix readout of amorphous selenium: Theoretical analysis of detective quantum efficiency," Med. Phys. 24 1819-1833 (1997). [p. 3, 144]
- W. Zhao and J.A. Rowlands, "X-ray imaging using amorphous selenium: Feasibility of a flat panel self-scanned detector for digital radiology," Med. Phys. 22 1595-1604 (1995). [p. 3]